

Earth and Planetary Science

Volume 2 · Issue 2 · October 2023 ISSN 2810-9732





Honorary Editor-in-Chief

Zheng-Xiang Li

Curtin University, Australia

Editor-in-Chief

Albert Galy

CRPG - CNRS - Université de Lorraine, France

Associate Editor

Maria Gritsevich

Finnish Geospatial Research Institute (FGI), Finland

Editorial Board Members

Angelo De Santis, Italy	Xiaojun Xu, China
Yangting Lin, China	Karoly Nemeth, Hungary
Ross Mitchell, China	Shaunna M. Morrison, United States
Ian M. Coulson, Canada	Stavro L. Ivanovski, Italy
Andrea Brogi, Italy	Alessandro Mura, Italy
Michele Paternoster, Italy	Chengmin Zhang, China
Chi Pui Tang, China	Luka Č. Popović, Serbia
Pál Sümegi, Hungary	Xuanmei Fan, China
Long Xiao, China	Kebiao Mao, China
Yazhou Yang, China	Xiaoping Zhang, China
Sandor Gulyas, Hungary	Rui Li, China
David C Fernández-Remolar, China	Armél Zacharie Ekoa Bessa, Cameroon
Jean-Louis Vignerresse, France	Lidong Dai, China
Marek Tulej, Switzerland	

Volume 2 Issue 2 • October 2023 ISSN 2810-9732 (Online)

Earth and Planetary Science

Honorary Editor-in-Chief

Zheng-Xiang Li

Editor-in-Chief

Albert Galy



Contents

Research Articles

- 1 **Petrochemistry of Phyllites from Patharkhola, Lesser Kumaun Himalaya with Reference to Tectonic Implications**
Haritabh Rana Harel Thomas Aman Soni Satyam Shukla
- 10 **Geophysical Evaluation of Agricultural Potential of Orlu and Environs Using Landsat Imagery**
Chukwuebuka N. Onwubuariri Chidimma O. Ikeme Lebe A. Nnanna Boniface I. Ijeh Chidiebere C. Agoha
Cynthia C. Nwaeju Obinna C. Dinneya Festus U. Nwaneho
- 21 **Some Remarks about Asteroid Impact Triggered “Bioaerosol” Escape during a Putative Microbial Exchange between Early Earth and Mars**
Balázs Bradák
- 33 **Revisiting Recent Amplitude and Phase Variations of the Chandler Wobble and Free Core Nutation**
Zinovy Malkin
- 38 **Contribution to the Knowledge of Twenty Members of the Lagenid Benthic Foraminifera in the Southern Tethys**
Haidar Salim Anan
- 55 **Facies and Hydrocarbon Reservoir Rock Characterization of the Paleozoic Rocks of Peshawar Basin, northwest Pakistan**
Sajjad Ahmad Sohail Raza Suleman Khan
- 68 **Interpretation of Geothermal Magnetic Depths, Physicochemical Parameters and Heavy Metals Determination of Lamurde Hot-spring in the North-Eastern Benue Trough, Nigeria**
Mukaila Abdullahi Yunis B. Valdón Fartisinha P. Andrew Adamu Usman Abba Ibrahim Maigari
- 75 **Results of the Application of Direct-search Mobile Technology in the Exploration Blocks of Shakal and Halabja (Kurdistan)**
Mykola Yakymchuk Arzu Javadova Ignat Korchagin

Review

- 86 **Origin of the Moon and Lunar Water**
Nick Gorkavyi



RESEARCH ARTICLE

Petrochemistry of Phyllites from Patharkhola, Lesser Kumaun Himalaya with Reference to Tectonic Implications

Haritabh Rana Harel Thomas* Aman Soni Satyam Shukla

Department of Applied Geology, Dr. Harisingh Gour Vishwavidyalaya (A Central University), Sagar (M.P.), 470003, India

ARTICLE INFO

Article history

Received: 17 April 2023

Revised: 27 May 2023

Accepted: 31 May 2023

Published Online: 21 July 2023

Keywords:

Phyllites

Geochemistry

Tectonic settings

Almora

ABSTRACT

Phyllites from Patharkhola, Lesser Kumaun Himalaya have been studied to investigate the geochemical characteristics of these rocks and their formation processes and mechanism of emplacement. Petrographically, phyllites have been showing the mineral assemblages as Biotite (25% approx.)-chlorite (25% approx.)-muscovite (20% approx.)-quartz (10% approx.)-feldspar (10% approx.)-sericite (5% approx.). Geochemically, the analysed four samples of phyllites have high SiO_2 and Al_2O_3 values. Phyllites with higher alumina have more enrichment of trace elements. The enrichment of Zr and depletion of Y and Nb indicate preferential survival of zircon in extreme weathering conditions. The HFSE has shown variation in the ratios due to decoupling with the major oxides. The enrichment of LREE and depletion of HREE suggest mixing of the terrigenous sediments with the concomitant magma. Discrimination plots to classify the tectonic settings suggested that the phyllites of Patharkhola have formed in active continental margins.

1. Introduction

The Himalaya, arc-shaped mountain belt covering the whole boundary of northern India is an example of an intercontinental collision between Indian and Asian plates around 55 Ma ago ^[1-7]. The structure, stratigraphy and tectonics of the Lesser Kumaun Himalaya have been described by Auden ^[8]; Valdiya ^[9,10]; Thomas & Thomas ^[11]; Thomas & Thomas ^[12]; Joshi et al. ^[13]; Joshi et al. ^[14]; Rana and Thomas ^[15]. The Almora group of rocks forms a part of the Lesser Himalayas bounded by North and South Almora thrust ^[9]. Almora Crystallines are disposed of in the form of a broad asymmetrical synformal nappe with

its axis trending in NW-SE direction plunging due, south east. These comprise chiefly metamorphic derivatives of pelitic, semi-pelitic and psammitic sediments. The area of investigation, around Patharkhola, District Almora, forms the southern limb of Almora Crystallines ^[15-17] lying between longitude 79°09'E to 79°17'56"E and latitude 29°47'42"N to 29°56'69"N with an approximate area of around 120 square kilometres (Figure 1). The main rock types exposed in the area are gneisses, schists and phyllites. In this paper, the authors discuss the geochemical characteristics of phyllites to understand their process of formation.

*Corresponding Author:

Harel Thomas,

Department of Applied Geology, Dr. Harisingh Gour Vishwavidyalaya (A Central University), Sagar (M.P.), 470003, India;

Email: harelthomas@gmail.com

DOI: <https://doi.org/10.36956/eps.v2i2.842>

Copyright © 2023 by the author(s). Published by Nan Yang Academy of Sciences Pte. Ltd. This is an open access article under the Creative Commons Attribution-NonCommercial 4.0 International (CC BY-NC 4.0) License. (<https://creativecommons.org/licenses/by-nc/4.0/>).

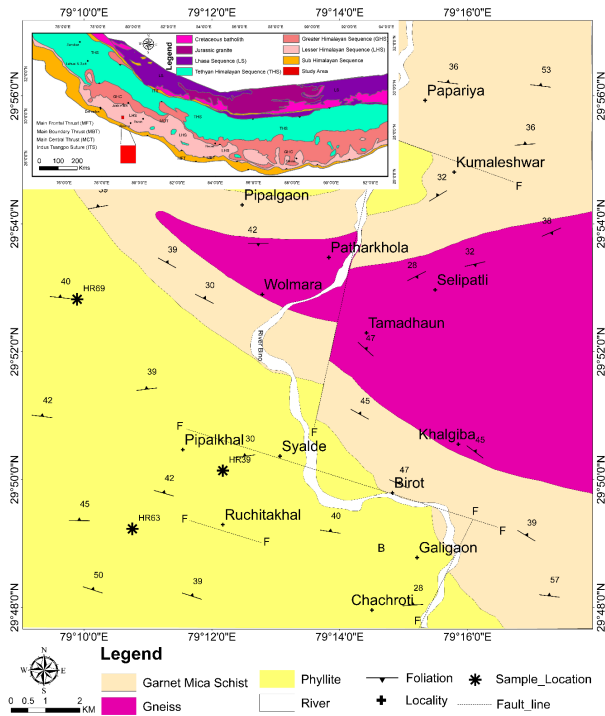


Figure 1. Detailed geological map around Patharkhola Kumaun Lesser Himalaya Uttarakhand India modified after Thomas and Thomas (2003) ^[12].

2. Geological Setting

In the Kumaun region, the Lesser Himalayan sequence is delineated by MCT from the Higher Himalayan in the north and by MBT from the Siwaliks in the south ^[18]. The Almora group of rocks forming the largest nappe dominantly consists of metapelites and meta-psammite. The sequence of these rocks has shown amphibolite grade of metamorphism ^[19] with maximum P-T estimates as 575 °C and 8 kbar. These metapelitic rocks are considered to be of Precambrian age ^[1,16,20]. In Kumaun Himalaya, the Munsyari gneisses of Almora Group were dated 1830

± 200 Ma. Old ^[21] by Rb/Sr isotopic data. Islam et al. ^[22] proposed Proterozoic granitoids of Lesser Himalaya be grouped into older clusters of 2200-1800 Ma and younger clusters of 1400-1200 Ma age. Kohn et al. ^[23] proposed a U-Pb zircon age of 1830 ± 50 Ma for the Paleoproterozoic edge arc of Lesser Himalayas. Mandal et al. ^[24] dated biotite augen gneiss for U-Pb zircon date as 1878 ± 2.4 Ma. The metamorphic terrain of Lesser Himalayas exhibits multiple deformation patterns and polyphase metamorphism ^[25], which is well exposed in the central part of Almora nappe. Phyllites are widely distributed in the area under investigation (Figure 1); exposed in the NW, S to SW and in the western part of the area. The phyllites are grey, greenish grey, brownish and greyish green and at places become compact and siliceous. At a few places, phyllites show more increase in the silica content giving a quartzitic appearance to these phyllites. The phyllites are composed of chlorite, mica, quartz and feldspar. At some localities, these phyllites exhibit iron enrichment or chlorite knots too. The phyllites are characterised by well-developed schistosity (S_2). At some localities, the colour bands in siliceous phyllites show bedding planes (S_1). Best exposures of crushed phyllites can be observed near villages Ruchiakhal, Syalde and Deghat. Phyllites of the area are highly folded ^[12]. Fold structures such as gentle folds, asymmetrical folds and chevron folds are well exposed at several places and can be easily seen on the motor road leading to Udaipur around Chachroti, Galigaon, Kueta and from Ruchiakhal to Pipalkhal. At a few localities, ptygmatic folds are also found associated with the quartz vein intruded in phyllites. Phyllites showing asymmetrical folds are exposed along the road to Ruchiakhal village (Figure 2). Chevron folds are commonly observed in this rock type (Figure 3). The phyllites of the area under investigation show a strike of WNW-ESE dipping towards the northern directions.



Figure 2. Asymmetrical fold developed in phyllite. Location Ruchiakhal Village.



Figure 3. Chevron fold exposed in phyllite. Location Ruchiakhal road.

3. Petrography

The dominant mineral assemblage of phyllites is biotite (25% approx.)-chlorite (25% approx.)-muscovite (20% approx.)-quartz (10% approx.)-feldspar (10% approx.)-sericite (5% approx.) along with ilmenite and magnetite as accessories. The preferred orientation of chlorite and micas defines the well-developed schistosity. Elongated grains of quartz and feldspar run parallel to the schistosity planes.

Chlorite shows yellowish green to light green pleochroism, first order interference colour is usually observed occurring as tiny specks which are fibrous in nature. It shows preferred orientation marking the schistosity along with the mica minerals. Two variants of muscovite have been distinguished based on the grain size and grain relationship with other minerals. Muscovite I show preferred orientation marking the schistosity along with the biotite and chlorite grains. Muscovite II showing angular relationship with the other mica grains has been observed due

to the rock heterogeneities as feldspar and quartz have high strength behaviour as compared to phyllosilicate, due to which some of the mica grains have rotated during the deformation process. Biotite based on mutual relationship and relation with schistosity, two different variants have been recognized. Biotite I along with muscovite I and chlorite grains defines the schistosity (Figures 4-6).

Quartz usually fine grained occurs with feldspar and biotite grains aligned parallel to the schistosity plane. Recrystallized quartz showing wavy extinction and inclusions of sericite and chlorite is observed at a few places.

Feldspar, both orthoclase and plagioclase feldspar is observed. Plagioclase feldspar mostly albite to oligoclase is observed to have anorthite content as An_{06} to An_{12} , measured during the microscopic study. At most of the places, both feldspars are showing alteration towards sericitization.

Sericite usually occurs as alteration products in feldspar (both orthoclase and plagioclase) along with in some grains of quartz.

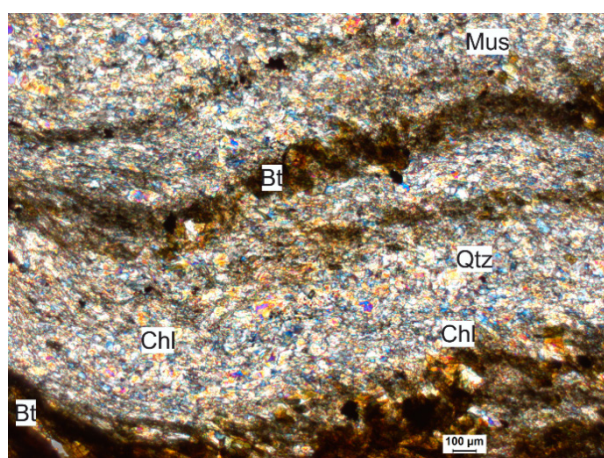


Figure 4. Mineral association of biotite, chlorite, muscovite and quartz in phyllite (HR39) under cross nicol. (Abbreviations are after Whitney and Evans, 2010) ^[26].

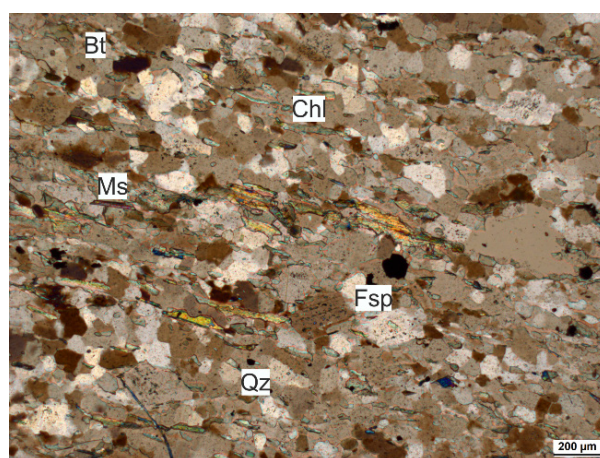


Figure 5. Phyllite (HR63) shows a mineral assemblage of biotite, muscovite, chlorite, feldspar and quartz (Abbreviations are after Whitney and Evans, 2010) ^[26].

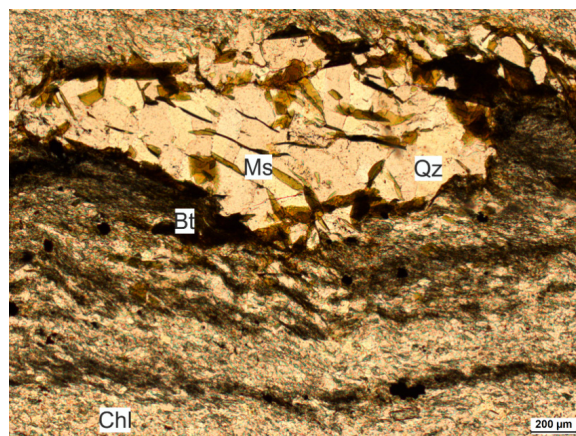


Figure 6. Phyllite (HR92) shows a mineral assemblage of chlorite, biotite, muscovite and quartz (Abbreviations after Whitney and Evans, 2010) ^[26].

4. Geochemistry and Petrogenesis

Four samples of phyllites analyzed by X-ray fluorescence method (XRF) and Inductively Coupled Plasma-mass Spectrometry (ICP-MS) method, respectively, at the Wadia Institute of Himalayan Geology, Dehradun are tabulated in Table 1.

The SiO_2 and Al_2O_3 content varies from 65.81 to 79.9% and from 10.13 to 16.82%, respectively. The FeO^T content varies from 3.15 to 10.97%. The average Na_2O and K_2O content in the phyllites is 3.38% and 3.25%, respectively. The average $\text{K}_2\text{O}/\text{Na}_2\text{O}$ ratio of these rocks is 0.96 which is usually four times less than the mean value of PAAS standard [27]. TiO_2 content of the rocks varies from 0.13

to 0.83%, respectively. The $\text{K}_2\text{O}/\text{Al}_2\text{O}_3$ ratio is higher as compared to the $\text{Na}_2\text{O}/\text{Al}_2\text{O}_3$ ratio, clearly differentiated from igneous rocks [28] (Figure 7). Even though metamorphism may alter the original chemistry, changes are themselves related to plate tectonic environments and bulk composition should still reflect the tectonic settings. K and Na being mobile are easily affected by low grade metamorphism, but phyllites being dominantly composed of biotite along with a subordinate amount of feldspar compensate for K and Na in the system. It is evident that all samples fall within the field specified for sedimentary rock. Figure 8 [29] shows that the phyllites dominantly fall in the wacke-arkose field with higher $\text{SiO}_2/\text{Al}_2\text{O}_3$ ratio as compared to $\text{Fe}_2\text{O}_3/\text{K}_2\text{O}$. The plots between SiO_2 versus

Table 1. Major oxides, REE, trace elements and CIPW norm of phyllites.

Sample No.	HR69	HR39	HR63	HR97	Sample No.	HR69	HR39	HR63	HR97
					Trace elements				
SiO_2	73.41	65.81	79.9	73.79	Sc	2	8	3	11
Al_2O_3	15.85	16.82	10.13	12.3	V	9	59	11	42
Fe_2O_3	1.67	4.69	1.77	5.28	Cr	219	199	474	2605
FeO	1.48	4.17	1.57	5.69	Co	128	45	443	343
MnO	0.04	0.07	0.01	0.08	Ni	175	132	398	2227
MgO	0.2	1.13	0.12	0.8	Cu	4	28	19	37
CaO	0.57	0.69	0.22	0.58	Zn	49	87	12	51
Na₂O	3.59	2.74	4.23	2.98	Ga	15	19	4	10
K₂O	4.64	3.44	2.13	2.8	Rb	350	136	65	116
TiO₂	0.13	0.69	0.24	0.83	Sr	69	82	87	95
P₂O₅	0.26	0.04	0.03	0.03	Y	34	36	18	28
Total	101.84	100.29	100.35	105.16	Zr	50	367	133	511
FeO/MgO	7.4	3.69	13.083	7.112	Nb	14	21	4	17
K₂O/Na₂O	1.292	1.255	0.503	0.939	Ba	173	737	498	649
Na₂O/Al₂O₃	0.226	0.162	0.417	0.242	Pb	36	21	11	18
Rare Earth Elements					Th	4	24	8	25
La	12.413	76.69	21.965	102.22	U	BDL	6.6	BDL	2.8
Ce	21.874	146.17	55.35	178.17					
Er	1.575	8.263	1.758	4.72					
Tm	0.22	1.214	0.277	0.694					
Yb	1.32	7.71	1.723	4.31					
Lu	0.18	1.04	0.24	0.56					
LREE	58.485	356.902	109.613	419.558					
HREE	9.266	39.208	8.167	23.42					
REE total	67.751	396.11	117.78	442.978					
LREE/HREE	6.311	9.102	13.421	17.914					
La/Eu	17.582	31.0234	22.231	49.429					
Eu/Lu	3.922	2.376	4.116	3.692					

other oxides are shown in Figure 9. The plot of SiO_2 versus Na_2O , CaO , Al_2O_3 , MgO and MnO shows regression of more than 0.5. In general, phyllites having Al_2O_3 values of more than 15% show higher trace elements contents. The plot of SiO_2 versus trace elements is shown in Figure 10. The enrichment of Zr and depleted Y, Nb values indicate the preferential survival of zircon in extreme weathering conditions due to the decoupled behaviour of Y and Nb as compared to Zr. Ni and Cr show higher values as compared to PAAS. Co values are ranging from 45 to 343 ppm. The Ni/Co ratio ranges from 0.8 to 6.5 Ni shows a wide range of values with respect to Co whose values are clustered. In terms of ratios of trace elements, variability has been observed as Co/Th is on higher side due to higher values of Co as compared to Th while Sc/Th is on the lower side as the Sc is consistently low as compared to Th. HFSE ratios have shown quite a variability as the Zr/Nb ratio ranges from 3.5 to 33.2 while the Zr/Y ratio shows 1.4 to 18.2. This is due to decoupling of the HFSE in the major oxides.

The REE data of phyllites shows enrichment of LREE and depletion of HREE. The LREE ranges from 58.4 to 419.5 while the HREE ranges from 8.2-39.2. The rare earth data for the selected phyllitic assemblage were normalized to chondrites [30]. Their values are plotted in Figure 11, and it shows slightly steeper to almost flatter light rare earth element (LREE) pattern with La/Eu ratio of 30.06, a relatively flat to a slightly enriched heavy rare earth element (HREE) pattern with Eu/Lu ratio of 3.05.

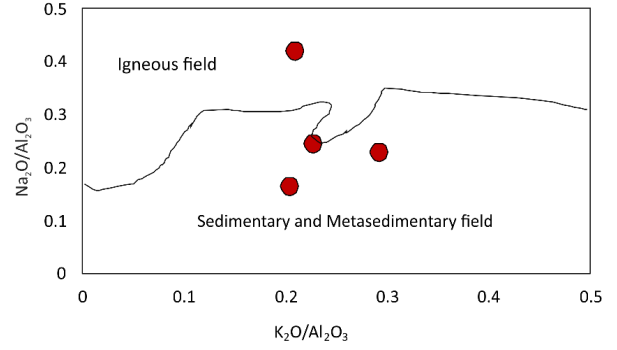


Figure 7. $\text{K}_2\text{O}/\text{Al}_2\text{O}_3$ versus $\text{Na}_2\text{O}/\text{Al}_2\text{O}_3$ after Garrels and Mackenzie (1971) [28].

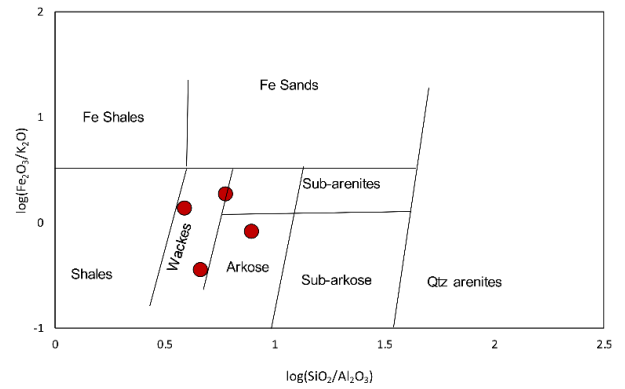


Figure 8. $\log(\text{SiO}_2/\text{Al}_2\text{O}_3)$ versus $\log(\text{Fe}_2\text{O}_3/\text{K}_2\text{O})$ after Herron (1988) [29] for classification of terrigenous sediments and shales.

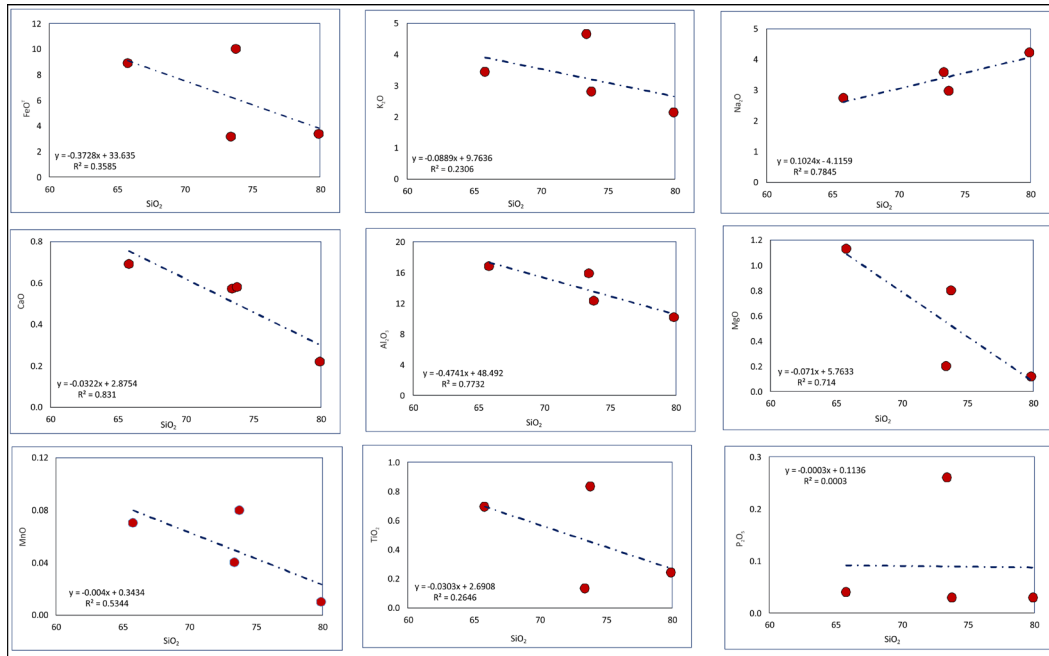


Figure 9. Harker variation diagram of Silica versus major oxides.

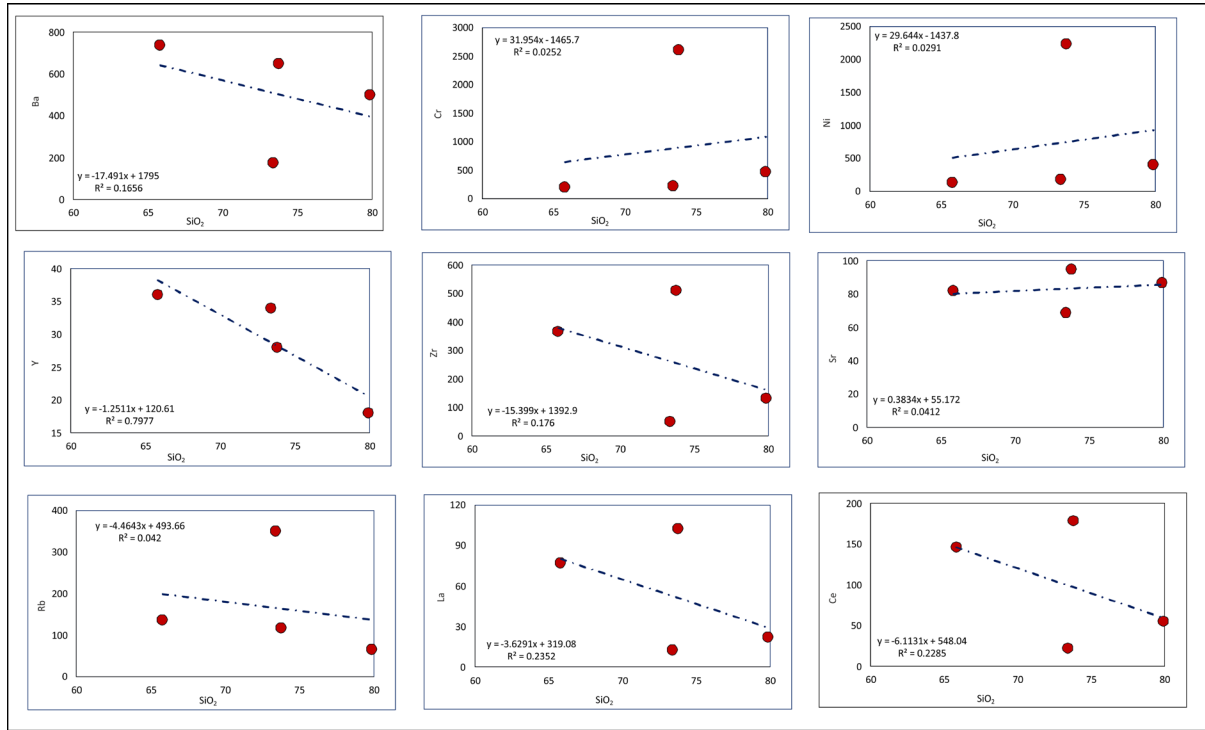


Figure 10. Harker variation diagram of Silica versus trace elements.

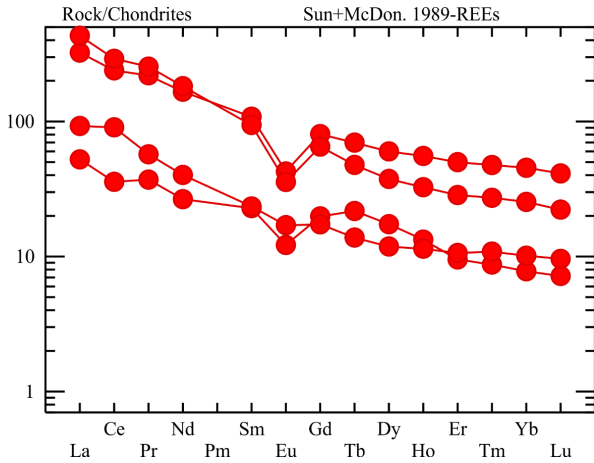


Figure 11. Chondrite normalised plot for Phyllites, Patharkhola, Sun and McDonough, 1989^[30].

5. Tectonic Implications

Studies have traditionally shown that geochemistry plays a crucial role as a sensitive indicator in determining the provenance of sedimentary and metasedimentary rocks and also to constrain the tectonic setting in which they were deposited^[31-34]. Trace elements such as Co, Sc, Ni, Zr, Th, La and others are used for tectonic environment discrimination due to their fractionation and low mobility in sedimentary environments. Bhatia^[31] proposed ternary plots of Sc-Th-Zr/10 and Sc-La-Th. The process of col-

lisional tectonics and deformation is formed during the mechanism of orogeny or plate convergence leading to the formation of continental arc or active continental margin settings. These depositional environments forming in these regions are usually underlain by thick and elevated continental crust^[32]. Geochemical composition of phyllites is plotted in these ternary plots. Figures 12 and 13 falls in the active continental margin and passive margin continental settings. The plot of SiO_2 versus $\text{K}_2\text{O}/\text{Na}_2\text{O}$ (Figure 14) shows that phyllites of Patharkhola have been formed in the active continental margin.

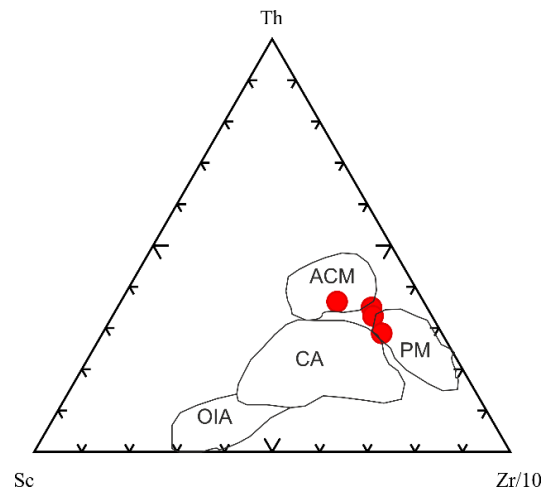


Figure 12. Th-Sc-Zr/10 tectonic setting discrimination ternary diagrams (after Bhatia & Crook 1986)^[32].

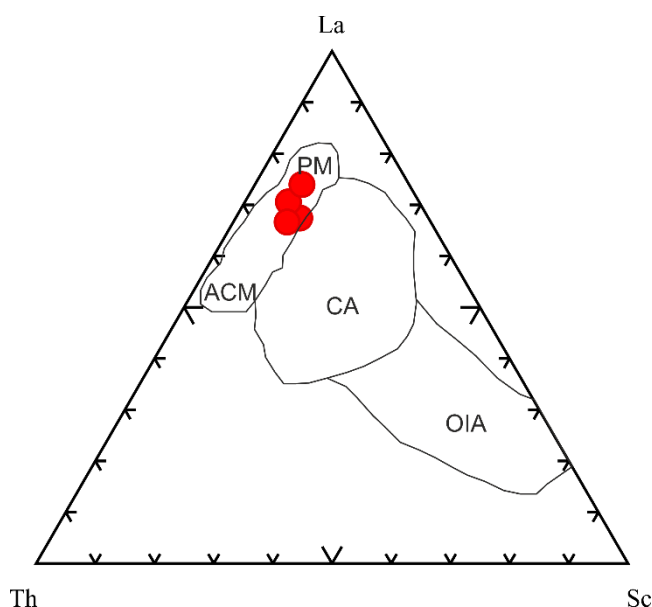


Figure 13. La-Th-Sc tectonic setting discrimination ternary diagram after Bhatia & Crook (1986) ^[32].

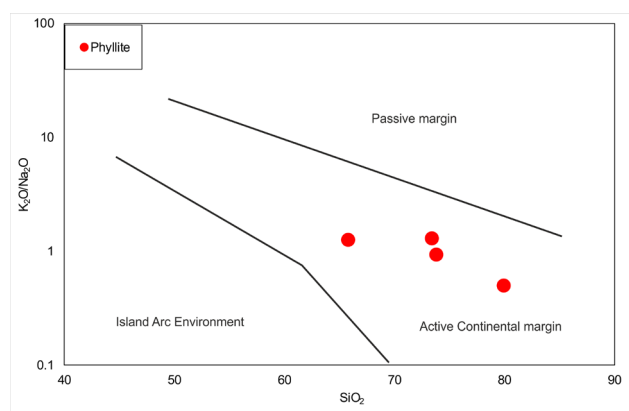


Figure 14. SiO₂ versus K₂O/Na₂O for Patharkhola rocks after Roger and Korsch 1986 ^[33].

6. Discussion & Conclusions

Phyllites exposed in the western part of the Patharkhola area of District Almora exposed in the NW, S to SW. They are grey, greenish grey, brownish and greyish green in colour, fine-grained and thinly foliated. Phyllites of the area are highly folded showing gentle folds, asymmetrical folds and chevron folds. Along with all these, ptygmatic folds are also found associated with the quartz vein intruded in phyllites. Based on the mineral paragenesis, phyllites have been containing Chlorite-biotite-sericite-quartz-muscovite. Geochemically, the phyllites have high SiO₂ and Al₂O₃ values along with higher ratios of K₂O/Al₂O₃ and SiO₂/Al₂O₃. Phyllites with higher Al₂O₃ values have a strong association with trace elements in-

dicating their preponderance of K-feldspars and micas. The enrichment of Zr and depletion of Y and Nb indicate preferential survival of zircon in extreme weathering conditions. The HFSE has shown variation in the ratios due to decoupling with the major oxides. Fluids at magmatic arcs are usually marked by enrichment of LREE and LILE along with relative depletion of HFSE. The enrichment of LREE and depletion of HREE suggest mixing of the terrigenous sediments with the magma ^[33]. Discrimination plots to classify the tectonic settings suggested that the phyllites of Patharkhola have formed in active continental margins. The reliability of such diagrams is supported by the rock mineralogy as it is dominated by biotite along with a subordinate amount of feldspar. Such mineralogy guarantee that the K and Na were immobile at low grade metamorphism. This can be considered that the Lesser Himalayan rocks have subducted during the collisional processes leading to the formation of tholeiitic magma followed by a mixing of melt and crustal contamination. Afterwards, the exhumation of the asthenosphere is associated with arc magmatism.

Author Contributions

Author Haritabh Rana carried out the field work along with Aman Soni and Satyam Shukla as a part of his Ph.D. work under the supervision of Harel Thomas who conceptualized the work. All authors have read and agreed to the published version of the manuscript.

Funding

This research received no external funding.

Acknowledgement

The authors should like to put on record their candid thanks to the Head, Department of Applied Geology, Doctor Harisingh Gour Vishwavidyalaya, Sagar (M.P.) and the Department of Science and Technology, New Delhi, India for providing PURSE- Phase -II facilities for conducting present research work. The authors express sincere thanks to the reviewers for their critical and constructive reviews which significantly improved the focus and clarity of the manuscript.

Data Availability Statement

The data used for writing this manuscript have been attached in Table 1.

Conflict of Interest

All authors disclosed no any conflict of interest.

References

- [1] Gansser, A., 1964. *Geology of the Himalayas*. Wiley InterScience: New York. pp. 289-291.
- [2] Molnar, P., Tapponnier, P., 1975. Cenozoic tectonics of Asia: Effects of a continental collision: Features of recent continental tectonics in Asia can be interpreted as results of the India-Eurasia collision. *Science*. 189(4201), 419-426.
- [3] Yin, A., 2006. Cenozoic tectonic evolution of the Himalayan orogen as constrained by along-strike variation of structural geometry, exhumation history, and foreland sedimentation. *Earth-Science Reviews*. 76(1-2), 1-131.
- [4] Webb, A.A.G., Yin, A., Harrison, T.M., et al., 2011. Cenozoic tectonic history of the Himachal Himalaya (northwestern India) and its constraints on the formation mechanism of the Himalayan orogen. *Geosphere*. 7(4), 1013-1061.
- [5] Webb, A.A.G., 2013. Preliminary balanced palinspastic reconstruction of Cenozoic deformation across the Himachal Himalaya (northwestern India). *Geosphere*. 9(3), 572-587.
- [6] Mukherjee, S., Carosi, R., van der Beek, P., et al., 2015. Tectonics of the Himalaya: An introduction. *Special Publications*. 412(1), 1-3.
- [7] Mukherjee, S., Puneekar, J., Mahadani, T., et al., 2015. Intrafolial folds: Review and examples from the western Indian Higher Himalaya. *Ductile Shear Zones: From Micro- to Macro-scales*. John Wiley & Sons: Hoboken. pp. 182-205.
- [8] Auden, J.B., 1937. Structure of the Himalaya in Garhwal. *Records of Geological Survey of India*. 71, 407-433.
- [9] Valdiya, K.S., 1980. Stratigraphic scheme of the sedimentary units of the Kumaun Lesser Himalaya. *Stratigraphy and correlations of the lesser Himalayan formations*. Hindustan Publishing Corporation: Delhi. pp. 7-48.
- [10] Valdiya, K.S., 1980. *Geology of Kumaun Lesser Himalaya*. Wadia Institute of Himalayan Geology: Dehradun. pp. 291-295.
- [11] Thomas, T., and Thomas, H., 1992. Fold flattening and strain studies in a part of Almora Crystalline Zone, around Tamadhaun Kumaun Himalaya. *Indian Mining and Engineering Journal*. 5-7. Available from: https://www.researchgate.net/publication/372491354_Fold_Flattening_and_Strain_Studies_in_a_part_of_Almora_Crystalline_Zone_around_Tamadhaun_Kumaun_Himalaya
- [12] Thomas, T., Thomas, H., 2003. Fourier shape of the fold developed around Tamadhaun, district almora using a computer programm. *Gondwana Geological Magazine, Advances in Precambrian of Central India*. 7, 169-176. Available from: <https://www.gondwanags.org.in/>
- [13] Joshi, G., Agarwal, A., Agarwal, K.K., et al., 2017. Microstructures and strain variation: Evidence of multiple splays in the North Almora Thrust Zone, Kumaun Lesser Himalaya, Uttarakhand, India. *Tectonophysics*. 694, 239-248.
- [14] Joshi, M., Kumar, A., Ghosh, P., et al., 2018. North Almora Fault: A crucial missing link in the strike slip tectonics of western Himalaya. *Journal of Asian Earth Science*. 172, 249-263.
- [15] Rana, H., Thomas, H., 2018. *Geology of the Patharkhola area, Almora District, Uttarakhand (India): With special reference to the lithology and field relation*. Bulletin of Department of Geology. 20-21, 1-6.
- [16] Heim, A., Gansser, A., 1939. *Central Himalaya*. Hindustan Publishing: Delhi.
- [17] Kumar, G., Prakash, G., Singh, K.N., 1974. *Geology of the Deoprayag-Dwarahat area, Garhwal, Chamoli and Almora districts, Kumaun Himalaya, Uttar Pradesh*. Himalayan Geology. 4, 323-347.
- [18] Nakata, T., 1989. Active faults of the Himalaya of India and Nepal. *Geological Society of America Special Paper*. 232(1), 243-264.
- [19] Ghose, N.C., Chakrabarti, B., Singh, R.K., 1974. Structural and metamorphic history of the Almora group, Kumaun Himalaya, Uttar Pradesh. *Geology*. 4, 171-174.
- [20] Mehdi, S.H., Kumar, G., Prakash, G., 1972. Tectonic evolution of eastern Kumaun Himalaya: A new approach. *Himalayan Geology*. 2, 481-501.
- [21] Bhanot, V.B., Singh, V.P., Kansal, A.K., et al., 1977. Early Proterozoic Rb-Sr whole-rock age for central crystalline gneiss of higher Himalaya, Kumaun. *Journal of Geological Society of India*. 18(2), 90-91.
- [22] Islam, R., Ahmad, T., Khanna, P.P., 2005. An overview on the granitoids of the NW Himalaya. *Himalayan Geology*. 26(1), 49-60.
- [23] Kohn, M.J., Paul, S.K., Corrie, S.L., 2010. The lower Lesser Himalayan sequence: A Paleoproterozoic arc on the northern margin of the Indian plate. *Bulletin*. 122(3-4), 323-335.
- [24] Mandal, S., Robinson, D.M., Kohn, M.J., et al., 2016. Zircon U-Pb ages and Hf isotopes of the Askot klippe, Kumaun, northwest India: Implications for Paleoproterozoic tectonics, basin evolution and associated metallogeny of the northern Indian cratonic margin. *Tectonics*. 35(4), 965-982.

- [25] Joshi, M., Tiwari, A.N., 2009. Structural events and metamorphic consequences in Almora Nappe, during Himalayan collision tectonics. *Journal of Asian Earth Sciences*. 34(3), 326-335.
- [26] Whitney, D.L., Evans, B.W., 2010. Abbreviations for names of rock-forming minerals. *American Mineralogist*. 95(1), 185-187.
- [27] Condie, K.C., 1993. Chemical composition and evolution of the upper continental crust: Contrasting results from surface samples and shales. *Chemical Geology*. 104(1-4), 1-37.
- [28] Mackenzie, F.T., Garrels, R.M., 1971. *Evolution of sedimentary rocks*. Norton: New York.
- [29] Herron, M.M., 1988. Geochemical classification of terrigenous sands and shales from core or log data. *Journal of Sedimentary Research*. 58(5), 820-829.
- [30] Sun, S.S., McDonough, W.F., 1989. Chemical and isotopic systematics of oceanic basalts: Implications for mantle composition and processes. Geological Society, London, Special Publications. 42(1), 313-345.
- [31] Bhatia, M.R., 1983. Plate tectonics and geochemical composition of sandstones. *The Journal of Geology*. 91(6), 611-627.
- [32] Bhatia, M.R., Crook, K.A.W., 1986. Trace element characteristics of graywackes and tectonic setting discrimination of sedimentary basins. *Contribution to Mineralogy and Petrology*. 92(2), 181-193.
- [33] Roger, B.P., Korsch, R.J., 1986. Determination of tectonic setting of sandstone mudstone suites using SiO₂ content and K₂O/Na₂O ratio. *Journal of Geology*. 94(5), 635-650.
- [34] Madukwe, H.Y., Obasi, R.A., Fakolade, O.R., et al., 2015. Provenance, tectonic setting and source-area weathering of the coastal plain sediments, South West, Nigeria. *Science Research Journal (SCIRJ)*. 3(2), 20-31.



RESEARCH ARTICLE

Geophysical Evaluation of Agricultural Potential of Orlu and Environs Using Landsat Imagery

Chukwuebuka N. Onwubuariri^{1*} Chidimma O. Ikeme² Lebe A. Nnanna¹ Boniface I. Ijeh¹
 Chidiebere C. Agoha³ Cynthia C. Nwaeju⁴ Obinna C. Dinneya¹ Festus U. Nwaneho⁵

1. Department of Physics, Michael Okpara University of Agriculture, Umudike, 440101, Nigeria

2. Department of Microbiology, Federal University of Technology, Owerri, 340110, Nigeria

3. Department of Geology, Federal University of Technology, Owerri, 340110, Nigeria

4. Department of Mechanical Engineering, Nigeria Maritime University, Okereko, Delta State, 332105, Nigeria

5. Department of Physics, Federal University of Technology, Owerri, 340110, Nigeria

ARTICLE INFO

Article history

Received: 19 April 2023

Revised: 30 May 2023

Accepted: 5 June 2023

Published Online: 13 June 2023

Keywords:

Agriculture

Normalized Difference Vegetation Index (NDVI)

Lineaments

Drainage

Food

ABSTRACT

The scarcity of food afflicting third-world countries, particularly Nigeria, case study Orlu zone, Imo State, Nigeria, is intolerable, given the high rate of environmental degradation in the form of erosions, nation's poor economic state, insecurity, and extremely low per capita income of citizens, motivated this research. This research is tailored to a possible approach to combating the threat of food insecurity via geophysical investigation of agricultural potential areas and as well help in managing food insecurity ravaging the area, particularly in this post-COVID lockdown era. In this research, a geophysical approach—Landsat imagery and interpretation—was used to identify areas with high agricultural yielding potentials and how to exploit them for bumper agricultural harvests to sustain livelihood and alleviate the food crisis and food inflation ravaging the zone. Within the study area, the following data were collected: Normalized Difference Vegetation Index (NDVI) map, lineament map and drainage pattern map. They were interpreted, and areas with high agricultural yield potentials were mapped. Band ratios (3/4, 4/2, 3/1, 5/4) were generated to reduce the effects of shadowing and as well improve the features present. The NDVI values that indicate soil viability, generated within the study area range from -0.22 to 0.51.

1. Introduction

The use of the Landsat satellite has been consistent since the launching of the first satellite in 1972. The Na-

tional Aeronautics and Space Administration (NASA), on March 1, 2022, launched the most recent Geostationary Operational Environmental Satellite (GOES-T), which

*Corresponding Author:

Chukwuebuka N. Onwubuariri,

Department of Physics, Michael Okpara University of Agriculture, Umudike, 440101, Nigeria;

Email: onwubuariri.chukwuebuka@mouau.edu.ng

DOI: <https://doi.org/10.36956/eps.v2i2.844>

Copyright © 2023 by the author(s). Published by Nan Yang Academy of Sciences Pte. Ltd. This is an open access article under the Creative Commons Attribution-NonCommercial 4.0 International (CC BY-NC 4.0) License. (<https://creativecommons.org/licenses/by-nc/4.0/>).

will ensure and provide coverage of environmental and weather conditions and as well make predictions as it relates to weather. For about 50 years now, there has been a steady gathering of satellite imagery and this has led to the availability of the longest continuous archive of such imagery presently available ^[1].

Landsat can be applied in various aspects of life for different uses. Its benefits include ensuring water conservation and the safety of the public. It also provides a guide for field workers who are saddled with the decision of managing natural resources as it assists them in developing the proper developmental strategies and plans ^[2]. Irrespective of research carried out on Landsat imagery, the overall advantage of open access Landsat imagery is not so easy to predict as a result of many downstream and value-added uses.

Some analytical surveys were carried out in 2009 and 2012 to estimate the economic advantages of Landsat imagery employing the contingent method of assessment. There has been a series of case evaluations on Landsat by USGS in addition to the surveys Carried out by Miller and others ^[3]. A more quantitative approach was taken for these case studies, looking into the defined application of Landsat, its merit and demerit as appraised by the users. Specific examples of applications of imagery, advantages and drawbacks that arise from them give the details of users and uses as well.

The application of Landsat imagery in the investigation of agriculturally viable areas within Orlu and its environs, Nigeria is the focus of this research. Monitoring of agricultural production and food availability has become a major concern in Nigeria as the country's population continues to grow astronomically. According to the Food and Agriculture Organization (FAO) of the United Nations and the United Nations World Food Programme (WFP), Nigeria will face food insecurity and it is expected to last from June 2022 to August 2022 and possibly beyond. WFP and FAO ^[4] predicted a population of 19.4 million Nigerians across 21 States of the Federation including the Federal Capital Territory (FCT) to face food insecurity during the period, with 14.4 million people representing about 74.2% of the predicted population, already facing the crisis. It is worthy of note that tremendous improvements have been made in the last 50 years in agriculture with the practice of irrigation, crop rotation, fertilization, crop rotation and other technologies. These practices have contributed immensely to improving and increasing agricultural yield globally and Landsat imagery has played a huge role in informing management decisions, mostly at a global level in monitoring agricultural production or maximizing yield for a local field. This study investigates a number of agri-

cultural applications and uses of Landsat imagery, unraveling both the merits and drawbacks, if any, with respect to the use of this technology.

Location Study Area

The study area Orlu and its environs as seen in Figure 1, are located in Imo state, Southeastern Nigeria and it is defined with Longitude 6°40'0" E-7°10'0" E and Latitude 5°10'0" N-6°0'0" N. There are two pronounced seasons within the study area: The dry season, which spans between November and March, and the wet or rainy season, which is primarily experienced between April and October, having its peak in June and July. The vegetation of the area is monsoon and tropical Savannah. Plants like Palm trees, yams, cassava, cocoyam, maize, and other crops are frequently grown in the area.

2. Materials and Method

The study area was geophysically mapped using geologic and topographic maps. Physical observations of the vegetation, drainage, and lineaments within the study area were also made. Geomorphological activities such as top soil weathering were also considered because they have an impact on agricultural practices.

The national space research and development center agency (NSRDA) provided a seven-band Landsat Enhanced Thematic Mapper (ETM) image of Orlu and its environs. The same area was also imaged by the shuttle radar topographic mission (SRTM). Ground control points (GCPs) and Satellite orbit transformation were employed for the correction of imagery. These Image corrections were performed with the aid of geo-coded Landsat multispectral scanner (MSS), SPOT (Satellite Pour l'Observation de la Terre) Multispectral data (image to image geo-coding) and the Universal Transverse Mercator (UTM) coordinate system. Radiometric amendments were also carried out on each scene. Band 1 Enhanced Thematic Mapper (ETM) data which permeates water for bathymetric mapping across the coastline was used to differentiate soil vegetation and types of forest ^[5]. ETM Band 2 was used in the estimation of green reflectance from healthy plants, while Band 3 estimated the chlorophyll assimilation in vegetation. ETM Band 4 was employed perfectly in spotting the peaks in near-infrared reflectance of healthy green vegetation including water bodies/land borders. Soil moisture and vegetation were analyzed using the two mid-Infrared bands (Bands 5 and 7). They were also employed in making distinctions between rock and mineral types. The thermal-Infrared Band on ETM Band 6 was also used in analyzing soil moisture and vegetation ^[6].

difference between the bands. NDVI values are presented theoretically in the form of a ratio extending from -1 to 1 . Practically, high negative values indicate water, values around zero show bare soil, and values higher than 0.6 signifies dense green vegetation.

3.2 Lineaments

Lineaments deduced from satellite images are usually employed in revealing major azimuth arrays whose alignment offers a clue of an area's regional fractured setting^[8-10]. Geomorphologically, lineaments are described as mappable, common or complex linear surface attributes with fragments aligning rectilinearly or moderately in curvilinear form, having pronounced differences from adjacent patterns and apparently reflecting the subsurface peculiarities^[11]. Hobbs^[12] identified linear surface expressions as valleys, ridges, elevated area boundaries, rivers, coastlines, rock formation boundary lines, and fracture zones. The recognition of lineaments within an area is influenced by the types of outcrops observed within the area. The existence of thick vegetation, alluvial deposits, volcanic ashes, and human activities like landscape modification can pose some problems in the identification of lineaments.

3.3 Drainage Patterns

Howard^[13] postulated that examination and analysis of drainage expose the details of structural attributes and

lithology. The fundamental knowledge is that rivers flow from areas of high elevation to areas of low elevation along the maximum regional topographic gradient. There are different drainage forms and they include Dendritic, parallel, trellis, rectangular, radial/centrifugal, annular, and contorted^[14,13]. Drainage irregularities are described as unconformities from a dendritic pattern circumlocutory to the regional topographic gradient. These deviations result from structural or lithological incoherence^[15].

4. Results and Discussion

The Landsat 5-ETM data were treated and analyzed using different types of image boosting and modification processes. Band ratios for image modification and transformations were generated using IDRISI 32 calculator module^[16]. These ratios ($3/4$, $4/2$, $3/1$, $5/4$) were generated to reduce the effects of shadowing and to improve the detection of particular features. IDRISI 32 composite module was also in use to generate three band Red, Green, and Blue (RGB) color composites for image enhancement. The spectral qualities of images were improved via this method. Composites were generated in the following forms: RGB 357, RGB 751, RGB 752, and NDVI composite. These ratios generated were carefully analyzed alongside with digital elevation model to extract information and subsequently attribute the color patterns observed to that of color composites.

IDRISI 32 was used to generate a digital elevation model as seen in Figure 2 from Shuttle Radar Topographic

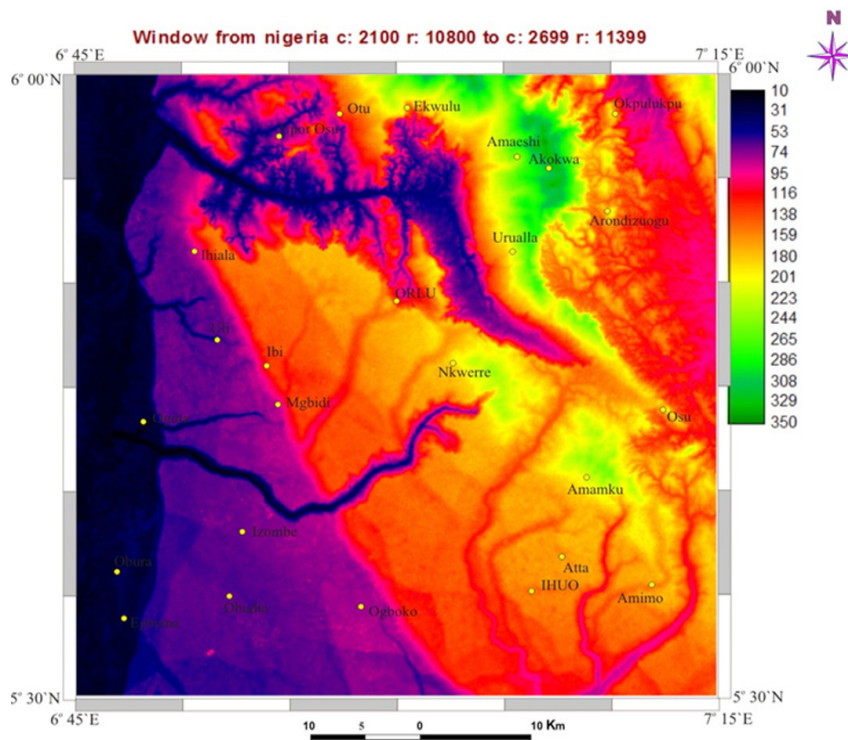


Figure 2. Digital elevation model (DEM) map.

Mission (SRTM) data using a color-shaded operation. Using the ERDAS and ArcView software, the DEM was converted into a contour map. Geomorphic units in the study area were identified using the DEM ^[17]. Based on the image texture and tone, three geomorphic units were identified: A portion of Orlu and Environs, a scarp slope, and a low-lying plain. The highest elevations are represented as green patches and are thought to be sandy ridges. This feature, visible in the upper right corner of Figure 2, is thought to be part of the Awka-Orlu Cuesta, which runs NE-SW. The scarp gradient of the ridge was recognized by the close packing of light green, yellow, and red colors, demonstrating an abrupt alteration in topography from 116 to 201 meters. There are numerous streams, gullies, and rivers on the slope. The interpretation of topographic high areas as characterized by top soil will be correct. Similarly, the highest elevation of the study area is depicted as green contours on the topographic map (Figure 3), which corresponds to the green patches on the DEM map in Figure 2. The study area's low-lying plain is depicted in blue on the DEM and topographic map. The ridge slope is similar to the one interpreted from the DEM imagery.

Linear features with a length of 1km or more were considered. The longer lineaments have the greatest potential for further development into gullies, limiting the amount

of land available for agriculture. Lineaments reveal three distinct groups of linear features. The most common direction is NE-SW, while others are N-S, E-W, and NW-SE. Figure 4 depicts the drainage map of the study area superimposed on the lineament map.

To prove the affiliation between geological formations and structural attributes, the interpreted lineaments (Figure 5) were submerged on the edge-enhanced map with a lineament density map (Figure 6) indicating a high-density fracture area east of Urualla and Orlu town. These lines indicate that the top soils used for agriculture have been weakened and therefore are carried away by runoff due to their loose nature, causing soil erosion. This consequently leads to non-availability of topsoil used for agriculture and its nutrients.

The Normalized Difference Vegetation Index (NDVI) is based on a plant's chlorophyll content, which indicates the amount of nutrients in the soil. The higher the chlorophyll content of plants, the more there are nutrients in the soil, implying that the area is very viable for agriculture ^[18]. Areas with low chlorophyll content have low soil nutrients or have been eroded as top soil used for agriculture has been washed away. NDVI was established to demarcate areas of vegetation and bare soil. Healthy plants were seen to have higher NDVI values due to their high reflectance

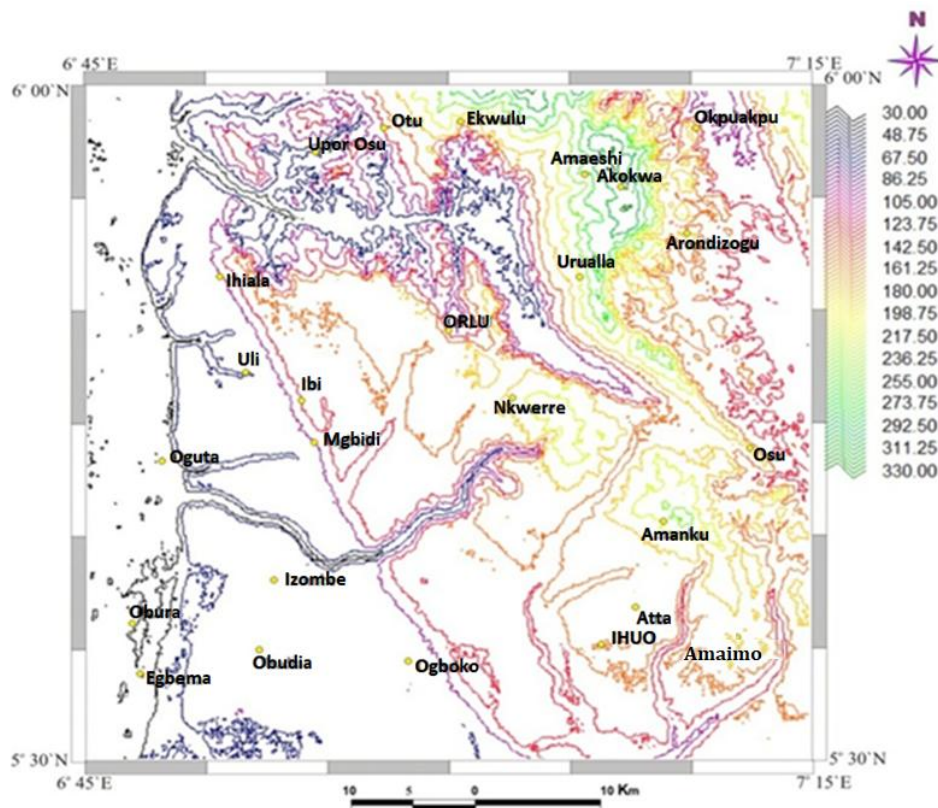


Figure 3. Topographical map of Orlu and Environs.

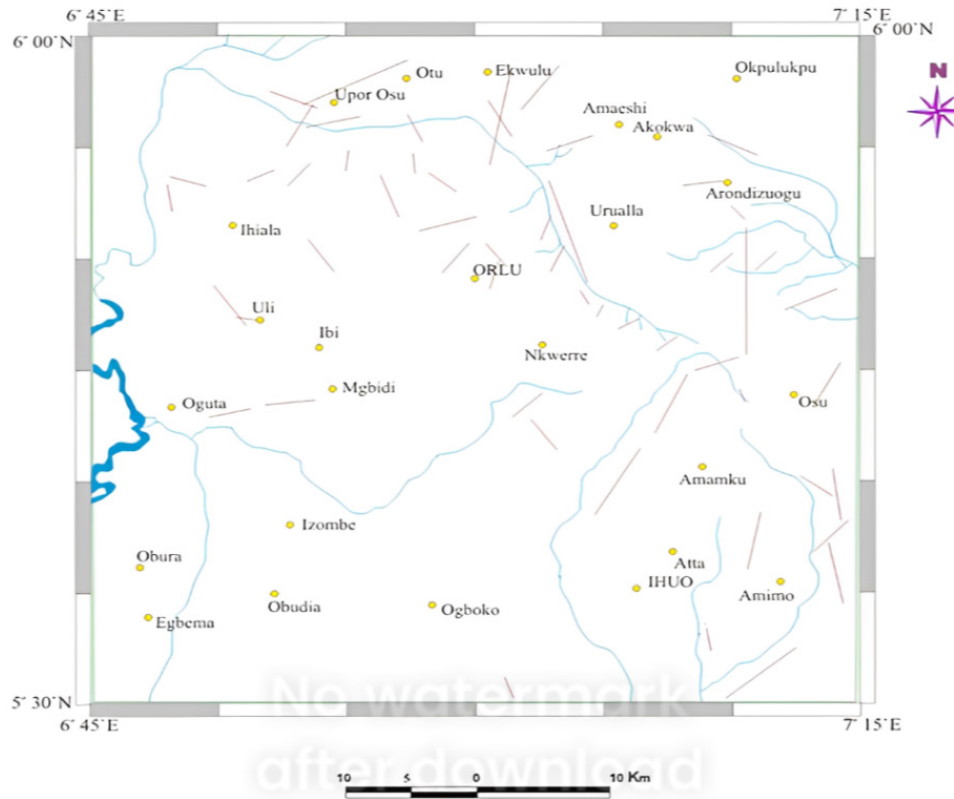


Figure 4. Lineament on drainage map.

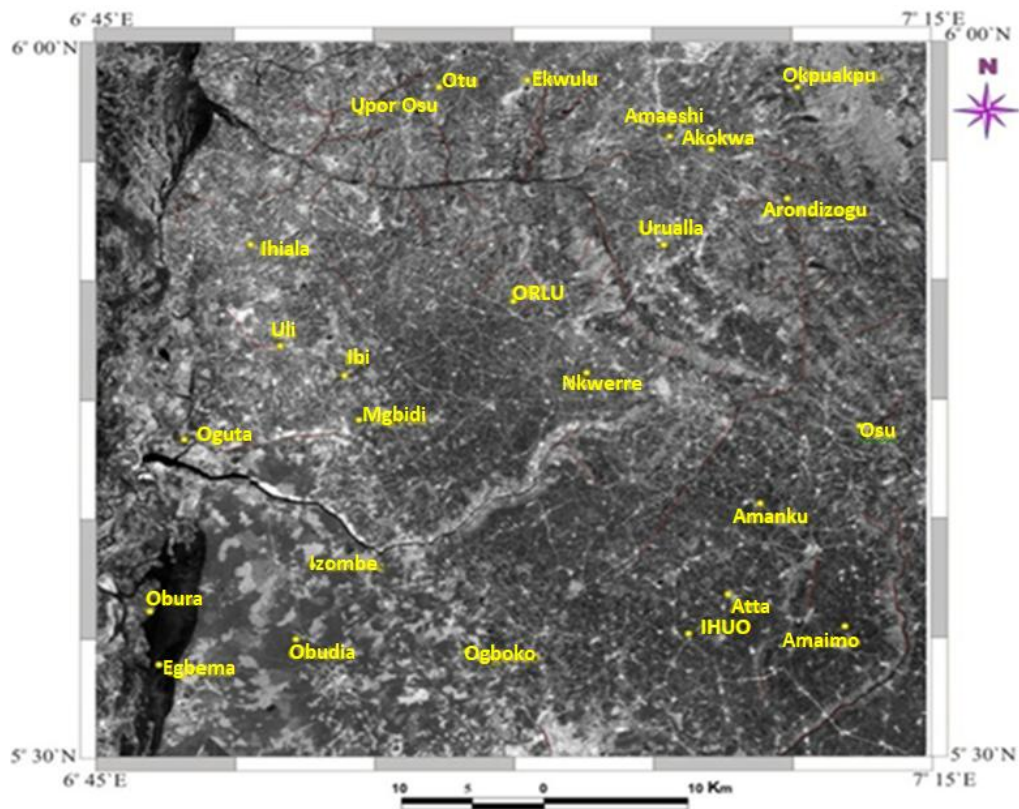


Figure 5. Lineament on edge enhanced band 5 map.

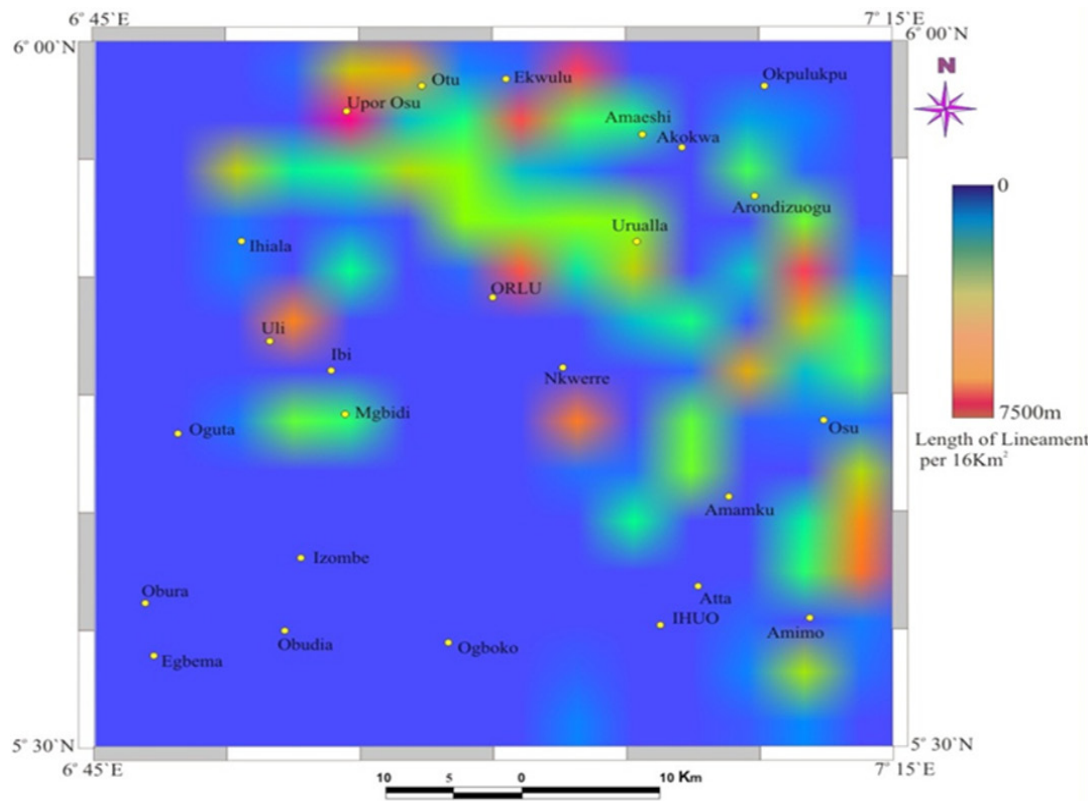


Figure 6. Lineament density map.

of infrared (band 4) light and relatively low reflectance of red (band 3) light. The NDVI is calculated using the formula in Equation (1).

A closer examination of the NDVI imagery (Figure 7) revealed that the brown areas with NDVI values between -0.22 and -0.01 correspond to bare or eroded soils. It is not recommended to conduct agricultural activities in such areas because crops will barely survive, let alone yield results. Yellow areas (0.01 - 0.19) correspond to sparsely vegetated areas. The lack of vegetation within the zones may indicate a lack of soil nutrients; though agricultural activities may be permitted only within the said area if significant soil remedial interventions can take place. This intervention to improve soil nutrients will undoubtedly be capital intensive, as crop yield may not justify the capital invested to make the soil viable, so agricultural activities are not recommended. Dense vegetation areas with NDVI values between 0.19 and 0.51 indicate high chlorophyll content. These are invariably natural agricultural viable areas, as indicated by the color green in Figure 7.

The dendritic configuration indicates that the underlying sediment is a single unit. Also, the dendritic pattern shows that the top lithology of the soil is soft and most

likely suitable and less energy-consuming during cultivation. Overburdens, sand, and other materials are included in this litho-unit. The RGB752 composite in Figure 8 is very descriptive because it distinguishes between the patterns. In Figure 2, the bare soil area, interpreted as a sandy ridge from the DEM, is rendered in lavender and magenta, while urban areas are represented in a lavender form.

The areas with vegetation are represented by green shades in RGB 357 and 752 as seen in Figures 10 and 8, indicating potentially agricultural high yield areas, which is consistent with NDVI as seen in Figure 7. Shades of blue indicate vegetated areas in RGB 751 (Figure 9), while light brown and light yellow indicates areas with no or little vegetation.

The unsupervised classification which is primarily based on image classification was carried out using ArcGIS. This classification depends on tonal differences as seen in Figure 11. Nine tonal features were observed in the study area. The blue and green colors in Figure 11 represent areas with mixed vegetation. Yellow areas were discovered in Orlu, Urualla, and Umueshi. This was previously interpreted as sand based on the DEM and color composites.

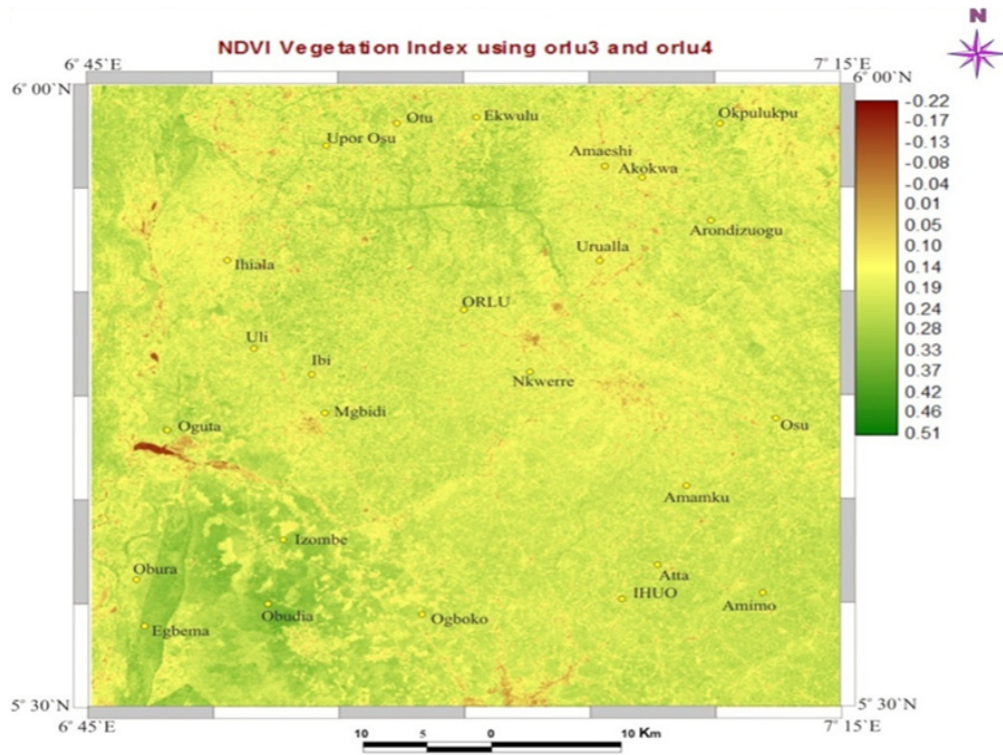


Figure 7. Normalized Difference Vegetation Index (NDVI).

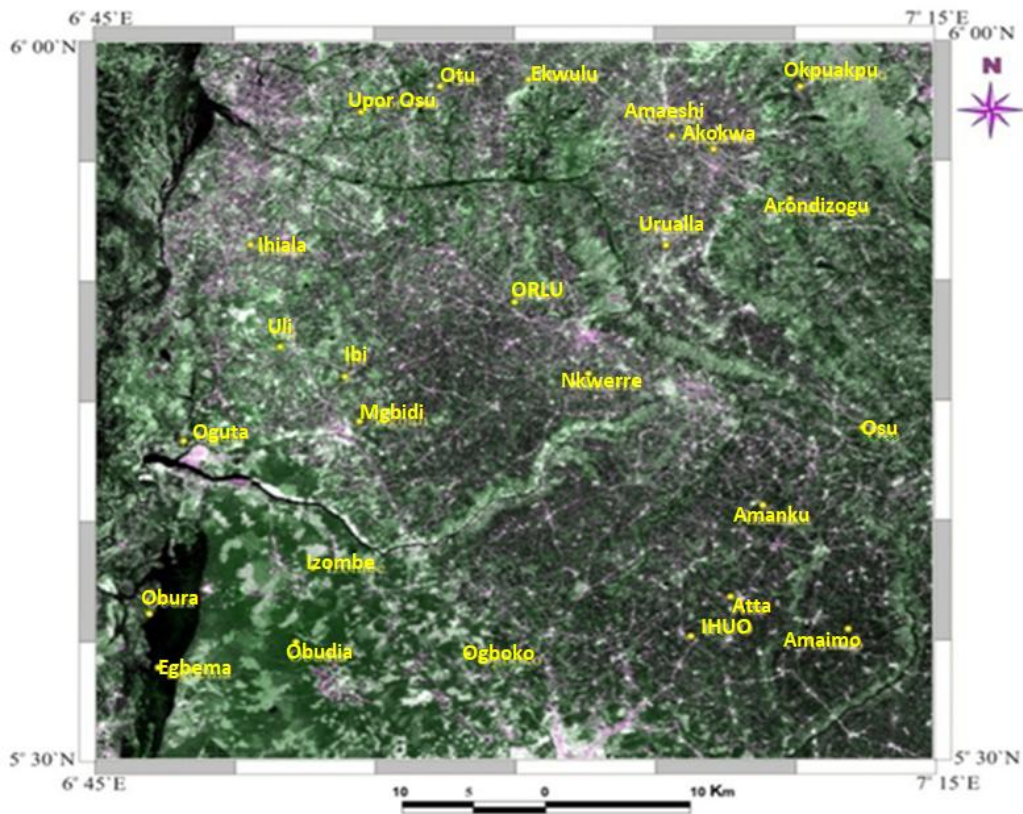


Figure 8. Colour composite RGB 752 map.

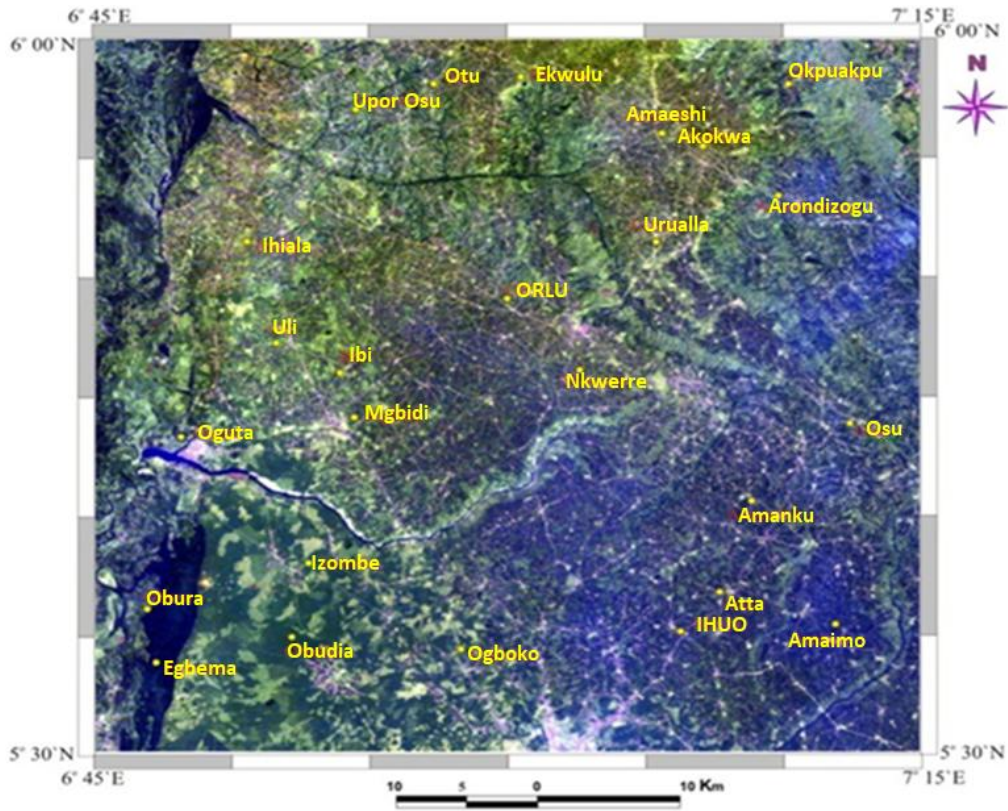


Figure 9. Colour composite RGB 751 map.

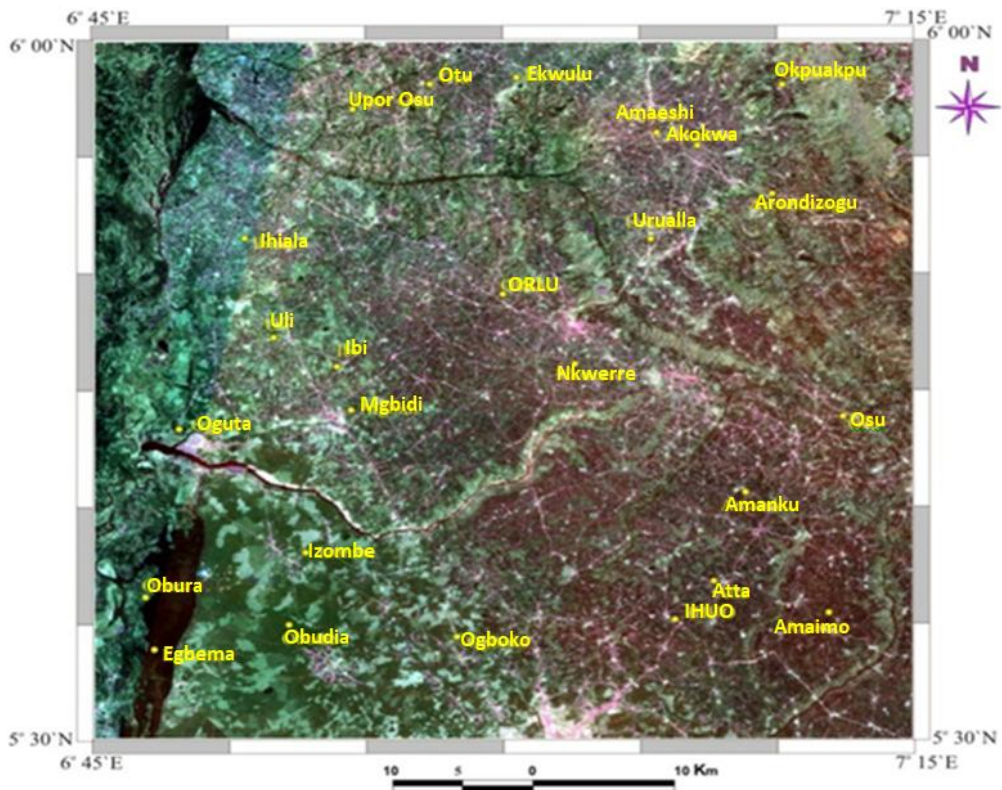


Figure 10. Colour composite RGB 357 map.

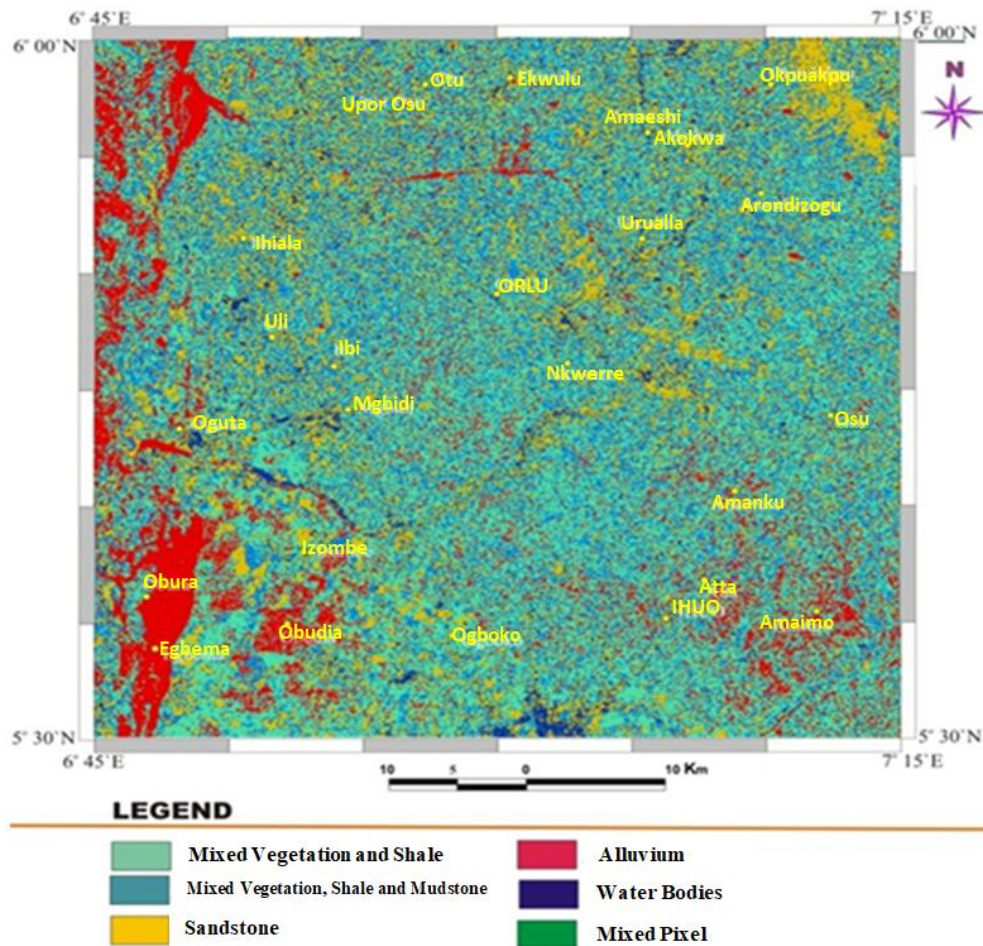


Figure 11. Unsupervised classification map.

5. Conclusions

Figures 2 and 3 from this study revealed the presence of a topographic high, which can easily aid runoff or washing away of top soil meant for agricultural activities. The presence of lineaments concentrating in the north-eastern part of the study area, as shown in Figures 4 and 6 respectively, revealed that erosion, which is a major factor affecting agricultural practices within the area, is structurally and lithologically controlled. It's possible that the lineaments provided a path for the top soil to migrate. This could also imply that the rivers and streams that serve as a source of water and irrigation in the area are structurally controlled. Hence agricultural practices should be discouraged in these areas to limit waste. Should agriculture be practiced in such locations, proper control measures must be put in place to ensure sustenance and preservation of agricultural input for appropriate yield. The study's findings also validate the existence of significant relationships between NDVI and crop yield, as shown in Figure 7, and which Figures 8, 9, and 10 agree with. Areas with high

NDVI values are areas best fit for agricultural practices as they are areas of high soil nutrients with minimal or no erosion threats as a result of topography or even lineaments.

To contribute to the resolution of Nigeria's impending food crisis, it is critical to take note of these areas identified as viable for agriculture and make proper use of them for crop yield while investing limited resources.

Author Contributions

Chukwuebuka N. Onwubuariri conceptualize this research and is the main editor of the manuscript; Chidimma O. Ikeme and Chukwuebuka N. Onwubuariri gathered all the data used for this research and as well interpreted them after they were being processed; Lebe A. Nnanna and Boniface I. Ijeh supervised the entire research; Chidiebere C. Agoha and Cynthia C. Nwaeju processed the acquired data; Obinna C. Dinneya and Festus U. Nwaneho did the literature review. All authors have read and agreed to the published version of the manuscript.

Data Availability Statement

Data will be made available on request.

Funding

This research received no external funding.

Conflict of Interest

There is no conflict of interest.

References

- [1] Leslie, C.R., Servina, L.O., Miller, H.M., 2017. Landsat and agriculture: Case studies on the uses and benefits of landsat imagery in agricultural monitoring and production. US Department of the Interior, US Geological Survey: Reston. pp. 27.
- [2] Serbina, L., Miller, H.M., 2014. Landsat and water: Case studies of the uses and benefits of Landsat imagery in water resources. US Department of the Interior, US Geological Survey. US Department of the Interior, US Geological Survey: Reston. pp. 61.
- [3] Miller, H.M., Richardson, L., Koontz, S.R., et al., 2013. Users, uses, and value of Landsat satellite imagery—Results from the 2012 survey of users. US Geological Survey Open-File Report. 1269, 51.
- [4] Hunger Hotspots FAO-WFP Early Warnings on Acute Food Insecurity June to September 2022 Outlook [Internet]. WFP and FAO; 2022. Available from: <https://www.wfp.org/publications/hunger-hotspots-fao-wfp-early-warnings-acute-food-insecurity-june-september-2022>
- [5] El-Hattab, M., Almogamal, W., 2019. Bathymetry mapping using landsat ETM+ data and field measurements for west coast of Yemen. Remote Sensing of Land. 3(1), 28-38.
- [6] Li, P., Jiang, L., Feng, Z., 2013. Cross-comparison of vegetation indices derived from Landsat-7 enhanced thematic mapper plus (ETM+) and Landsat-8 operational land imager (OLI) sensors. Remote Sensing. 6(1), 310-329.
DOI: <https://doi.org/10.3390/rs6010310>
- [7] Horel, Á., Zsigmond, T., 2023. Plant growth and soil water content changes under different inter-row soil management methods in a sloping vineyard. Plants. 12(7), 1549.
DOI: <https://doi.org/10.3390/plants12071549>
- [8] McElfresh, S.B., Harbert, W., Ku, C.Y., et al., 2002. Stress modeling of tectonic blocks at Cape Kamchatka, Russia using principal stress proxies from high-resolution SAR: New evidence for the Komandorskiy Block. Tectonophysics. 354(3-4), 239-256.
- [9] Casas, A.M., Cortes, A.L., Maestro, A., et al., 2000. LINDENS: A program for lineament length and density analysis. Computers & Geosciences. 26(9-10), 1011-1022.
- [10] Koike, K., Nagano, S., Kawaba, K., 1998. Construction and analysis of interpreted fracture planes through combination of satellite-image derived lineaments and digital elevation model data. Computers & Geosciences. 24(6), 573-583.
- [11] O'leary, D.W., Friedman, J.D., Pohn, H.A., 1976. Lineament, linear, lineation: Some proposed new standards for old terms. Geological Society of America Bulletin. 87(10), 1463-1469.
- [12] Hobbs, W.H., 1904. Lineaments of the Atlantic border region. Bulletin of the Geological Society of America. 15(1), 483-506.
- [13] Howard, A.D., 1967. Drainage analysis in geologic interpretation: A summation. AAPG Bulletin. 51(11), 2246-2259.
- [14] Deffontaines, B., Chorowicz, J., 1991. Principles of drainage basin analysis from multisource data: Application to the structural analysis of the Zaire Basin. Tectonophysics. 194(3), 237-263.
- [15] Singh, V.P., 2018. Hydrologic modeling: Progress and future directions. Geoscience Letters. 5(1), 1-18.
DOI: <https://doi.org/10.1186/s40562-018-0113-z>
- [16] Hussain, S., Mubeen, M., Karuppannan, S., 2022. Land use and land cover (LULC) change analysis using TM, ETM+ and OLI Landsat images in district of Okara, Punjab, Pakistan. Physics and Chemistry of the Earth, Parts a/b/c. 126, 103117.
DOI: <https://doi.org/10.1016/j.pce.2022.103117>
- [17] Omali, A.O., Kolawole, M.S., Ameh, E.G., 2019. Application of remote sensing techniques in the study of groundwater zonation of the rock in Lokoja Metropolis Central Nigeria. Journal of Mining and Geology. 54(2), 149-162.
- [18] Radočaj, D., Šiljeg, A., Marinović, R., et al., 2023. State of major vegetation indices in precision agriculture studies indexed in web of science: A review. Agriculture. 13(3), 707.
DOI: <https://doi.org/10.3390/agriculture13030707>



RESEARCH ARTICLE

Some Remarks about Asteroid Impact Triggered “Bioaerosol” Escape during a Putative Microbial Exchange between Early Earth and Mars

Balázs Bradák 

Laboratory of Exo-Oceanography, Faculty of Oceanology, Kobe University, 5-1-1 Fukaeminami-machi, Higashinada-ku, Kobe, 658-0022, Japan

ARTICLE INFO

Article history

Received: 17 May 2023

Revised: 28 June 2023

Accepted: 30 June 2023

Published Online: 10 July 2023

Keywords:

Early Earth

Early Mars

Panspermia

Escape phase

Asteroid impact

ABSTRACT

In general, Panspermia theory discusses the possibility of the spread of life in the universe. The migration of living organisms between planets is crucial in such a “fertilization” process. This study focuses on one particular case and phase of such migration: the possible material transport between the early Earth and Mars with a focus on the phase of escape, i.e., the ejection of a microorganism-containing material into space. Specific characteristics of asteroid impacts and one of the possible processes, which may be able to transfer microorganisms to space, were investigated. The comparison of the terrestrial and Martian paleoenvironment showed that theoretically, early Mars, similar to Earth, might allow biological evolution and might be able to harbor life. Determining various pressure zones regarding the survivability of the mechanical compression in the case of an impact and the characterization of specific physical parameters of the ejected debris lead to the identification of the pressure—mass/size conflict and the conclusion, which indicates two possible ways of material escape. The possibly “common” and known way is the material ejection close to ground zero. It guarantees big enough debris to protect its passengers during their travel. Still, the survival rate at/close to ground zero is supposedly low, and the heat and overpressure-related compression may sterilize the material even before boarding. An alternative way, discussed in this study, provides a higher chance of survival further from the impact center. Still, the possibility of the ejectile reaching the escaping velocity and the minimum required size is low. Although solving such a problem is out of the scope of this manuscript, searching for an ideal combination of various parameters is a possible challenge for future studies.

*Corresponding Author:

Balázs Bradák,

Laboratory of Exo-Oceanography, Faculty of Oceanology, Kobe University, 5-1-1 Fukaeminami-machi, Higashinada-ku, Kobe, 658-0022, Japan;

Email: bradak.b@port.kobe-u.ac.jp

DOI: <https://doi.org/10.36956/eps.v2i2.860>

Copyright © 2023 by the author(s). Published by Nan Yang Academy of Sciences Pte. Ltd. This is an open access article under the Creative Commons Attribution-NonCommercial 4.0 International (CC BY-NC 4.0) License. (<https://creativecommons.org/licenses/by-nc/4.0/>).

1. Introduction

The study presented here focuses on a particular segment of a Panspermia hypothesis-related theory, namely the research about the possibility of microbial exchange between early Earth and Mars.

Following the early pioneering studies ^[1,2], Rampelotto ^[3] suggested that the Panspermia hypothesis, the transfer of the “seeds of life” between planets, is one of the promising fields of astrobiological research. The proposed transfers between planets rely on a set of crucial steps, namely the escape, the transfer, and the landing phases ^[4]. Experiments and modeling have investigated all efforts. However, there are still numerous questions that need to be considered further, e.g., the paleoenvironment of the donor and the recipient planets, along with, e.g., appearance, as well the survival of a living organism in the case of, e.g., asteroid impact.

In particular, the potential material transfer between planetary bodies, especially Earth and Mars, has been the target of various studies from various aspects, including the role of asteroid impacts on bio-material production, the study of meteorites as a potential source of organic components, the search for the signs of microbial life, the search for the earliest marks of life, and the existence of LUCA—Last Universal Common Ancestor (see in detailed in Section 1.1). Among those studies, one focuses on the thorough research of the survival of a microorganism during the ejection, transfer, and landing phase of the transfer ^[5]. This study from Mileikowsky et al. ^[5] summarizes many aspects of the transfer, such as various factors of microbe survival, the size and number of unshocked meteorites, the possible transporters of microorganisms, and the approximate fraction of microbes. Their study concluded that viable transfer between Mars and Earth was highly probable. To provide additional information to their research, the early Martian and terrestrial paleoenvironment are compared below from the point of view of historical geology/planetary science. In addition, the possible survival of the shockwave-mechanical pressure and ejection of material further from ground zero, from the center of impact, are discussed.

1.1 Paleoenvironment on Early Earth and Mars and the Potential of Emerging Life

From the angle of the early Earth and Mars microbial exchange hypothesis, it seems essential to compare the early Martian and terrestrial paleoenvironment between approximately 4.6 to 2.5 Ga ago, to understand the potential for bioaerosols’ escape and transportation between the two planets (Figure 1). Both planets suffered a catastroph-

ic collision at their very early age, which might be responsible for the dichotomy, the sharp contrast between the northern and southern hemispheres of Mars (~4.5 to 4.47 Ga) ^[6], and the formation of the Earth’s Moon, described by the Theia hypothesis (~4.51 Ga) ^[7]. The Martian Northern Hemisphere has a significantly lower elevation compared to the Southern regions, which may have functioned as a hydrological and sedimentary basin, be the location of the Martian ocean and one of the potential regions of the emergence of life in subsequent Martian periods (see below) (Figure 1). Despite the dichotomy-forming impact and the one indicated by the crater retention age of the Hellas basin (3.97 to 4.06 Ga) ^[8], the mean impact flux during the pre-Noachian was significantly lower compared to the Noachian Late Heavy Bombardment (LHB) period (c.a. 10% of the LHB flux) ^[9]. Along with the lack of impact events, no marks of pre-Noachian plate tectonism and volcanism can be recognized, along with the missing significant surface erosion—even if the Fe/Mg phyllosilicates exposed on the Noachian surface ^[10] may indicate pre-Noachian subsurface weathering processes and the presence of water, or groundwater hydrothermal circulation ^[9,11]. The lack of impact and volcanic activity might have significantly influenced the (lack of the) formation of the pre-Noachian atmosphere. The pre-Noachian paleoclimate might be strongly influenced by the faint young Sun, which provided less solar flux ^[12], and the lack of volcanism (tectonism), which might play a key role in increasing CO₂, CH₄, NH₃, hydrogen sulfides, and aerosol content of the atmosphere ^[9].

Contrasting with the Martian pre-Noachian paleoenvironment, there are significant differences in Earth’s Hadean (~4.6 to 4 Ga) paleoenvironment. Following the Theia-collision, the formation of the global Hadean Ocean (~4.4 to 4.3 Ga), an aqueous planet with the possible appearance of proto-continental crusts and landmasses, set a different course in planetary evolution ^[13]. Compared to the pre-Noachian paleoenvironment, the rising crust-mantle cycle on Earth might help the formation of a CO₂ atmosphere, along with the global Hadean Ocean (and the lack of significant size landmass above sea level), which protected the CO₂ storage in continental rocks and its subduction into the mantle ^[14].

Despite the differences in the evolution of the two planets, there are common components that may have supported the emergence of life. Although there are some doubts about the existence of a Martian atmosphere in pre-Noachian (see above), a Noachian denser CO₂ atmosphere was formed by potentially volatile outgassing, which is expected to be efficient in pre-Noachian as well ^[12,15]. If it did exist, such outgassing made the Martian pre-Noachian

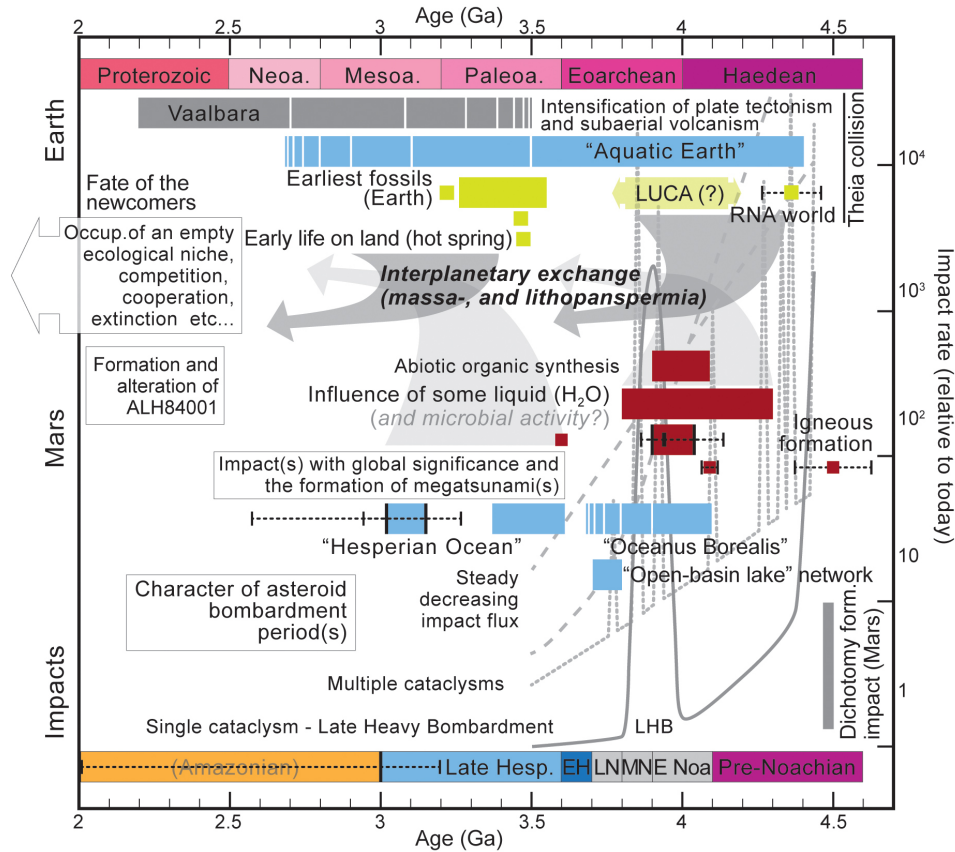


Figure 1. A chronological summary of various factors contributing to the possible microbial exchange between Mars and Earth.

atmosphere similar to the Hadean terrestrial atmosphere. In some sense, both the Martian and terrestrial paleoenvironment can be considered as “calm” as well, regarding the cold Martian world with the characteristic topographical dichotomy and without oceans, significant erosion and impact flux^[9], and Earth covered by global Hadean Ocean providing shelter for the emerging life^[13].

Among the possible paleoenvironmental similarities, there is one which may suggest similar abiogenesis in the early Mars and Earth: the mark of hydrothermal activity. Based on our current knowledge^[13], hydrothermal processes and environment might be the key to abiogenesis, providing components for prebiotic synthesis and molecules, and via the so-called RNA world around 4.36 Ga^[16], the building blocks of first cells and the so-called LUCA, i.e., the Last Universal Common Ancestor of life on Earth. The potential marks of hydrothermal processes were observed in the Martian environment as well^[11] suggesting the possible evolution of exo-LUCA (the extraterrestrial correspondent of LUCA), the appearance of extraterrestrial life via abiogenesis^[13]. Despite this hypothesis’s speculative nature and missing information to prove it, the pre-Noachian environment is considered one of the best

candidates for life’s emergence on Mars^[9].

Despite the ongoing argument about the natural, artificial, or organic origin of the identified features^[17-20], some studies suggest that there are apparent similarities between terrestrial magneto fossils and the phenomenon observed in the Martian meteorite^[19,20]. The one and currently only possible comparison of potential early Martian and terrestrial life is based on analyzing the mark of microbial life found in the Allan Hills (Antarctica) or ALH84001 meteorite^[17]. Unfortunately, a recent study has also seen some distinct mechanisms of abiotic organic synthesis, which possibly operated on early Mars (4.1 to 3.9 Ga) and questioned the features’ biogenic origin found in ALH84001^[21]. Regardless of the speculation about the possible fossils in ALH84001, it may provide some evidence about processes related to the appearance of some liquid (hydrothermal activity and/or weathering) around 4.3 to 3.8 Ga on Mars^[22] (Figure 1).

1.2 Possible Bioaerosol Escape from the Gravity Well of the Studied Planets

Following the introduction to the planetary environment of emerging life, the possible way of escape, the first

crucial step of life transportation^[4], needs to be discussed. There are some potential ways of high-altitude transport of microbes by bioaerosols (fine particles suspended in the air, containing or consisting of various microbes), including i) giant meteorite impacts and ii) volcanic eruptions^[4].

Following the “relatively calm” pre-Noachian/Hadean, the Noachian (Mars) and Archean (Earth) starts with the intense LHB impact event (~4.1 to 3.8 Ga). Like many components in the history of the young Solar system, there are arguments about the timing, nature, and even the existence of the LHB^[23,24]. Regardless that LHB appeared as an intense asteroid bombardment period with spike-like, periodic, or steady decline impact flux in the history of the planets, it might eject a significant amount of aerosols and water to the atmosphere^[25] carrying microbes to higher altitudes. The impacts seem to have some limitations in their sterilizing effect as well, leaving behind survivals in micro-habitats and the “deep biosphere” of the global ocean of the Hadean/Archean Earth^[13], and theoretically, if life did exist on Mars, e.g., in Ocean Borealis^[26]. The marks of such impacts can be identified on the surface of Mars, indicated by the crustal-scale Hellas, Isidis, and Argyre basins^[8,27]. Earth’s continuously changing surface makes identifying Archean age impact craters difficult. Still, indirect geochemical and petrographical evidence, such as the iridium abundance in the oldest sediments and the appearance of shocked quartz, suggest the escalation of extraterrestrial material influx by asteroid impacts^[28].

Although the impact flux significantly decreased during the Hesperian, some potential candidates could still lift bioaerosols to higher altitudes. The Martian paleoenvironment during the Hesperian (3.71 to 3.37 Ga) is characterized by the intensification of volcanism, changing wet and dry periods, permafrost, catastrophic floods, and a possible ocean in the Northern lowlands^[29,30]. Recently, a theory of large, planetary-scale impact(s) on Mars during the Late Hesperian triggered a scientific discussion^[31-33]. If such an impact existed, it provided a potential explanation for escaping various bioaerosols from Mars by ejecting microbe-containing material into space^[34].

Along with meteorite impacts, volcanic eruptions can also eject bioaerosols to high altitudes^[35] if the type of volcanism allows it. Most likely, eruptions with a higher Volcanic Explosivity Index have some chance of ejecting material into space. On Mars, volcanoes and volcanic regions are comprised mostly of basaltic rocks of various types and morphology^[27], which suggest volcanic activity ranging from the formation of effusive lava plains, shields, and lava flows to explosive eruptions (e.g., pyroclastic products around 4 Ga)^[36,37]. Compared to Mars, the volcanic activity on Archean Earth (4 to 2.5 Ga) had various

contributors. The appearance of one of the first super-craton, the continent-size Vaalbara (2.7 to 2.2 Ga)^[38], meant the slow ending of the marine “monopoly” on the Earth’s surface. The early continental evolution-controlled komatiite volcanism (3.5 to 1.5 Ga) was characterized by low-viscosity magma and created large volcanic flow fields^[39] along the island-arc volcanism^[40], which explosive eruptions might work as a supporter of ejection of early life developing on land (e.g., in hot spring deposits;^[41]) into higher atmospheric altitudes (Figure 1).

Some short speculation can be made about the becoming of the bioaerosol following the escape phase. It has been proven by recent experiments on ISS (International Space Station; Tanpopo or Dandelion mission) that microorganisms can survive a minimum of three years, exposed to outer space during interplanetary travel by using the surface cells killed by radiation, as a protective layer (so-called massapanspermia)^[42]. Such a shield might allow safe travel between Mars and Earth. Although the landing process on a recipient planet from the perspective of lithopanspermia (transfer of microbial passengers inside of asteroids) is well studied, there are only a few explanations about how bioaerosols might survive entry into the atmosphere^[5,42]. Many theories can be built about the fate of the microbes arriving in an “alien world”, e.g., the way of survival of a pre-Noachian/Noachian non-marine microorganism in the most likely ocean-dominated Hadean to (Eo)archean Earth^[13,43], or vice versa. Several questions can be raised regarding the possible interaction between the endemic microbial life on Earth^[44-46] and the cosmic newcomers. Such interaction might contain competition, cooperation^[47], and the occupation of empty paleoecological niche as well, but (as the writer Michael Ende told in his famous novel, the *Neverending Story*), this and the summary of the evolutionary consequences of such interactions are “another story and shall be told another time.”

This study aims to evaluate one critical problem during the first step of microbial transfer between planets, namely the character of an asteroid impact which can provide enough supporting energy to eject some material to leave the planet and does not destroy every living organism during the process.

2. Data and Data Analysis

2.1 Data Sources

The following datasets were used to analyze the potential bioaerosol transfer between Earth and Mars during their early period (older than 2.5-3 Ga). The impact crater data from early Earth is based on the simulation and dataset provided by Marchi et al.^[48,49]. Two sources were used

to collect impact crater data from Mars, including the study of Robbins and Hynek^[50] and Robbins et al.^[8].

Craters above 150 km diameter were used during the analysis, which crater size was possibly caused by a 10-20 km diameter size impactor. Mileikowsky et al.^[5] used this minimum impactor size to evaluate the potential natural transfer of viable microbes between Earth and Mars and roughly equal the size of the Chicxulub impact (~10 km). This collision caused the mass extinction at the boundary of the Cretaceous and Paleogene (ca. 66 Ma).

2.2 The Calculation of Key Parameters

The following equations were used to characterize the mass and the size of the ejectiles. The size of the impactor was determined based on the size of the impact crater, following the equation of Hughes^[51]:

$$\log D = (1.026 \pm 0.5) + (1.16 \pm 0.04) \log d \quad (1)$$

where d (diameter in km) is the impactor's size, and D (diameter in km) is the size of the crater created by the impact.

The impact energy was derived from the so-called Shoemaker formula, presented in the study of Shoemaker et al.^[52], including the impact angle factor:

$$D = 0.074 c_f (g_E/g)^{1/6} (W \rho_i/\rho_t)^{1/3.4} (\sin i)^{2/3} \quad (2)$$

where D (km) is the size of the impact crater, c_f is the so-called crater collapse factor: 1.3, g_E is the gravitational acceleration on Earth, g is the gravitational acceleration on other planets, where the crater was formed, ρ_i is the density of the impactor: 3.65 g/cm³^[53], ρ_t is the density of the rock at the target location: 2.86 g/cm³^[53], i (°) is the impact angle, defined as 45° in the case of this study, and W is the impact energy (kinetic energy of the impactor) in kilotons TNT equivalent.

The estimation of the peak overpressure, a key component during the characterization of various parameters of the ejectiles, is based on the review of Vijayaraghavan et al.^[54], summarizing the methods applied during the study of nuclear experiments:

$$P_{s0} = 6784 (W/R^3) + 93 (W/R^3)^{1/2} \quad (3)$$

where P_{s0} (bars) is the maximum (peak) blast overpressure, W is the yield of a nuclear explosion, which represents the kinetic energy of the impactor in this study in tons of TNT equivalent (see Equation (2)), and R (m) is the distance from "ground zero".

During the estimation of various characteristics of the ejectiles, some environmental conditions have to be considered regarding the survival and the successful transfer of the potential microorganism.

Melosh^[55] and Armstrong et al.^[53] suggested that the speed of the impactor (v_i) needs to be slightly more than double the second cosmic velocity to transfer the ejectile

out of the gravity well of the planet. For such reason, in this study, v_{iE} , the minimum impact speed on Earth, and v_{iM} , the minimum impact speed on Mars, were set to 22.4 and 10.1 km/s, respectively. Along with studying the ejectile characteristics of an impact characterized by the minimum impact speed, an additional, possibly limiting condition was also investigated. Meteorites with a 300 km diameter size and 30 km/s speed or above are considered to be able to evaporate the water in case of an impact in an ocean^[56]. Along with the use of the minimum impact speed, which can transfer bioaerosols in space (v_{iE} and v_{iM}), v_{iO} , the ocean evaporating impact speed on Earth (30 km/s) was also applied during the data analysis to compare the results in the case of a potential ocean evaporating impact. In addition, along with 15 km/s, 30 km/s impact velocity was also used in the study of Mileikowsky et al.^[5]. Such impact velocities represent the extreme ends of impactor speed which may appear in an impact with possible ejection of bioaerosols.

High temperature is a critical environmental component that endangers the microorganism's survival by sterilizing the bioaerosols during impact. Melosh^[55] and Mileikowsky et al.^[5] applied the following equation to determine the mass of the ejectile with temperature restriction (< 100 °C):

$$m_e(\sim E, M, E_o, M_o) = 1.2 \frac{P_{s0}}{\rho_t C_T v_i} \left[1 - \left(\frac{2v_e}{v_i} \right)^{1/3} \right] m_i \quad (4)$$

where m_eE and m_eM (kg) are the mass of the ejected, (non-)sterilized materials, in the case of collision of Earth or Mars and an impactor with v_{iE} , v_{iM} , and v_{iO} impact speeds, respectively (see the description above Equation (3)). m_eE_o and m_eM_o are the mass of the non-sterilized ejecta, in the case of a collision with an asteroid speeding up to 30 km/s, the potential minimal "ocean evaporating" speed. m_i is the weight of the projectile. During the determination of the mass, first, the volume of the impactor was calculated by the definition of the shape of the projectile as a theoretical sphere (with a diameter d , Equation (1)^[51]), and the mass of this theoretical sphere shape impactor was determined by the use of ρ_t AVG: 3.65 g/cm³ as its average density, based on the study of Britt and Consolmagno^[57] and Hughes^[51]. v_e is the speed of ejecta, equivalent to the second cosmic velocity on Earth and Mars, 11.186 and 5.022 km/s, respectively.

Along with temperature, pressure is another critical environmental component during an impact to be considered a potential limitation for microorganism survival. Based on the study of Hazael et al.^[58], a microorganism may survive in tens of GPa pressure, and the calculation of P_{s0} and P_{s0surv} allows us to define the characteristics of

ejectiles beyond the 1 GPa blast overpressure most likely survivable limit. P_{s0} (in Pa; please note that Equation (4) results are in bars) is the maximum (peak) blast overpressure. Along with calculating ejectile characteristics at peak blast overpressure, the pressure limiting factor for life was set to P_{s0surv} : 1 GPa^[5]. ρ_t is the rock density at the target location: 2.86 g/cm³^[53], and C_T is the velocity of sound in the target rock: 6×10^3 m/s.

The size of the ejected material during spallation is crucial for the survival of the microbes during the escape from the donor planet, during the interplanetary exchange, and during entering the atmosphere of the recipient planet. Based on Mileikowsky et al.^[5], the size of the ejected material needs to be bigger than 0.2 m in diameter to protect the microbes from heat during the impact and the escape phase.

The equation applied by Mileikowsky et al.^[5] was used to determine the average fragment diameter expected during spallation:

$$l_{AVG} = \frac{T}{\rho_t v_e^{2/3} v_i^{4/3}} d \quad (5)$$

where l_{AVG} is the ejected fragments' average size (diameter in m), and T is the tension fracture, equal to 0.1×10^9 Pa in basalt and other igneous rocks. As it is described in the previous equations, d is the size of the impactor (diameter in km), ρ_t is the density of the rock at the target location: 2.86 g/cm³^[53], v_e is the speed of the ejecta, and v_i is the speed of the impactor in various, analyzed in multiple cases (v_iE , v_iM and v_iO), as it is summarised at the description of Equation (4).

In addition to the average fragment size, possibly ejected from the donor planet, the maximum fragment size was also estimated^[5]:

$$l_{MAX} = \frac{m_w + 3}{2} l_{AVG} \quad (6)$$

where l_{MAX} is the maximum size (diameter in m) of the ejected fragments, l_{AVG} is the average fragment size (in m; Equation (5)), and m_w is the so-called Weibulls constant, which is 9.5 for basalt.

3. Results and Discussion

Some key characteristics of a potential asteroid impact that might be able to eject debris hijacked by living organisms need to be evaluated.

One of the critical environmental components is the peak overpressure wave which appears in the surroundings of the impact. Mileikowsky et al.^[5] describe that the pressure caused by the shockwave is zero at the surface, and even the pressure rises, there are near-surface microbes that may survive the impact. Inspired by the works of Melosh^[55] and Toon et al.^[25], which describe the evolution and effect of the shockwave, namely stress

pulse and mechanical pressure, different zones around the impact center were reconstructed. Based on the information about the survivable overpressure found in the study of Mileikowsky et al.^[5] and Hazael et al.^[58], four zones, namely the "Safe" survival zone, Critical zone, Quasi-sterile zone, and Sterile zone, were separated and calculate. Pressure below 1 GPa was considered safe; pressure between 1 and 10 GPa is critical for certain species, but there are potential survivals of extreme compression (e.g., the length of high-pressure exposure)^[58]. The Quasi-sterile zone was defined due to the decreasing number but still existing species that may survive extreme high-pressure exposure (e.g.,^[59]). The Sterile zone refers to pressure and region where the compression is too big and prevents the survival of known lifeforms.

As it is shown in Figure 2, in the case of a Chicxulub-size impact (with various impact velocities), living organisms even in less than 100 km distance from ground zero may survive the peak pressure of the impact (please note that only the pressure is examined here, without any other components of an impact). The survivability dramatically decreases, e.g., in the case of a 100 km diameter size impactor. The Safe survival zone is located out of c.a. 800-900 km (Earth) and c.a. 700 km (Mars) radius from ground zero and closer than 400 km (Earth) and c.a. 350 km (Mars) from the center of the impact (Quasi-sterile-, and Sterile zone) only a few (or none) possible survival species may be found on the planetary surface.

Regarding the mass and average size of the ejectiles, there are significant differences between the number of ejectiles at various peak pressures, under certain living organisms may survive the impact. In the case of a 100 km diameter impactor, c.a. 10^{33} kg ejectiles are expected in contrast to the c.a. 10^{16} - 10^{15} kg mass of ejectiles at the 10 GPa and 1 GPa peak pressure environment, respectively. It must be noted that compared to the estimation of Mileikowsky et al.^[5], who used 15 km/s impact speed, in the case of Figure 3a, 30 km/s was used. Setting the impact speed to the velocity of a "planet destroyer" asteroid shows the possible maximum ejected mass and resulted in such extreme ground zero ejected mass results. The estimation of Mileikowsky et al.^[5] feels more realistic, e.g., 8.3×10^{14} kg in the case of a 100 km diameter impactor colliding with Mars at the velocity of 15 km/s. As an additional comparison, the mass of Earth and Mars can be listed as c.a. 5.97×10^{24} and 6.39×10^{23} kg, respectively. Despite the extreme values, Figure 3a indicates the significant drop in ejected mass at the Critical pressure zone and Safe survival zone, compared to ground zero.

The average size of the ejectiles was calculated at the two extreme possibilities; one is the already suggested

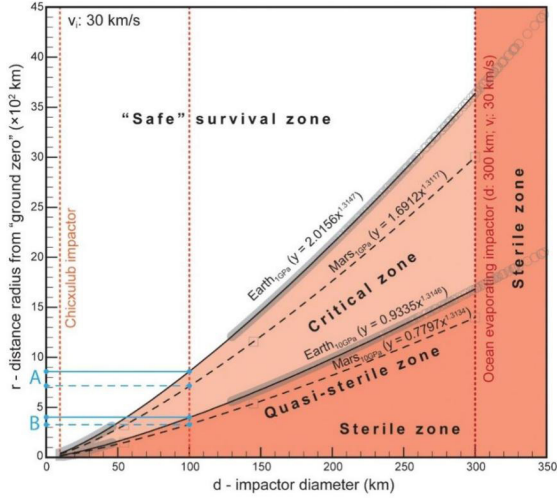


Figure 2. The distance of (non-)survivable pressure zones during a blast wave hit from ground zero of an asteroid impact. The 1 GPa and 10 GPa pressure limits of survivability are based on the study and review of Mileikowsky et al. [5] and Hazael et al. [58]. The blue solid and dashed lines indicate the minimum distance of Safe survival zone (A) and Critical zone (B) from ground zero, in the case of Earth (solid line) and Mars (dashed line), respectively. The solid lines indicate the calculation based on terrestrial impacts and Earth parameters; the dashed lines indicate the calculations based on Martian impact and the various Martian parameters.

maximum expected impact speed, a speed of an asteroid capable of evaporating oceans (Figure 3b, v_i), and the other end, the lowest impact speed which is capable of providing enough energy to transfer the debris out of the gravity well of the planets (Figure 3b, v_{MIN}). Decreasing average grain size can be recognized by the increase in the impact velocity. A collision with a 100 km diameter asteroid with v_{MIN} minimum velocity results in 50-60 m diameter debris ejected from Mars and c.a. 10 m diameter debris from Earth at ground zero. If the same impactor arrives with a 30 km/s impact speed, the size of ejectiles change to c.a. 10 m in the case of Mars and 7-8 m diameter in the case of Earth. Regarding the estimated asteroid size, the roughly 10 to tens-of-meter diameter asteroids feel capable of safely transferring microorganisms between early Earth and Mars. Still, some aspects must be considered during the evaluation of the results.

The comparison resulted in a contradicting result. As may be expected, the calculation of Mileikowsky et al. [5] showed decreasing average grain size by the decreasing impactor size (impact velocity was set to constant), most likely due to the decreasing impact energy with reducing asteroid size. It is also expected that further and further from ground zero, the average size of ejected debris is decreasing due to the decaying impact energy (stress wave) [55]. Example theoretical pressure zones, related to the 30 km/s

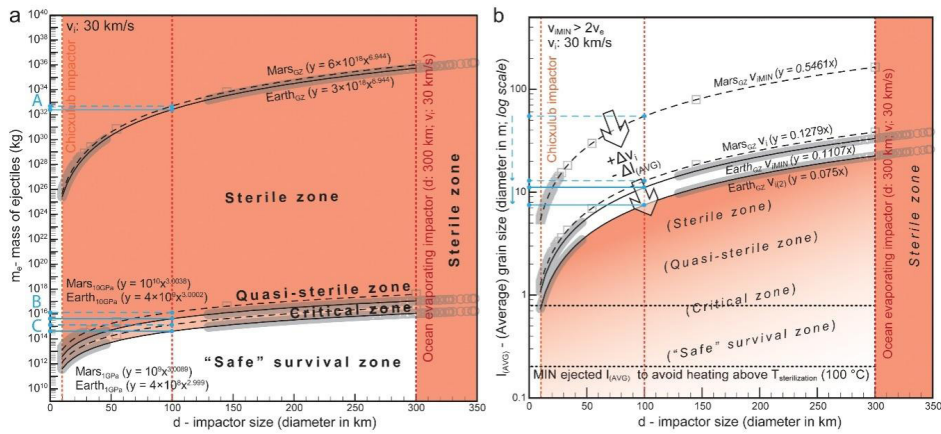


Figure 3. a) The mass of ejectiles at various distances from ground zero and b) the estimation of the average size of ejected fragments during various size asteroid impacts. The solid lines indicate the calculation based on terrestrial impacts and Earth parameters; the dashed lines indicate the calculations based on Martian impact and the various parameters of Mars. The arrows in Figure 3b show the decreasing average size of ejectiles. Earth_{GZ} and Mars_{GZ} lines mark the ejected mass and average grains size at ground zero. 1 GPa and 10 GPa indices indicate the ejection mass at the 1 GPa and 10 GPa pressure zones (the distances of those pressure zones from ground zero are summarized in Figure 2). The blue solid and dashed lines indicate the amount of ejected material at ground zero (A), at 10 GPa peak pressure at ground zero and/or at the minimum distance of the Critical zone (B), and at 1 GPa peak pressure at ground zero and/or at the Safe survival zone (C), in the case of Earth (solid line) and Mars (dashed line) respectively. Please note that in the case of Figure 3b, the indication of various zones only serves as a visual aid, indicating the decreasing grain size with increasing distance from ground zero in the case of the $v_i = 30$ km/s velocity impacts (Section 3 and Section 4; the pressure-mass/size conflict).

s velocity impacts are indicated in brackets (Figure 3b). In contrast, the result in this study demonstrates that impact speed significantly influences the average size of the ejectiles, i.e., higher impact velocity results in smaller size of ejectiles, which variable needs to be considered in further studies.

Along with the impactor's velocity, the size should also be discussed shortly. As an example, the effect of a theoretical 100 km diameter impactor was analyzed. As shown in Figure 3, the mass and average size decrease significantly with the decrease of the impactor size. In the first billion years, the initially high ratio of asteroid impacts reduced considerably^[14], along with the estimated size of the impactors (e.g.,^[48]). Such estimations suggest that the size of potential impactors, which may eject microorganism-containing debris in space when a simple living organism appears on Earth (and theoretically on Mars), was smaller than the example 100 km. Using a 20 km diameter size impactor (such size asteroid was used as maximum size impactor in, e.g.,^[5]), the ejected mass of material at 1 GPa and 10 GPa pressure is around 10^{12} - 10^{13} kg, and the average ejectile size is around 1 m diameter (at 30 km/s impact velocity) (Figure 3a).

The minimum ejectile size is the third size-related factor that needs to be considered. Please note that based on the explanation of Mileikowsky et al.^[5], if the size of the ejectile is bigger than 0.2 m or 0.8 m diameter, it prevents the inner part from heating up above 100 °C, which would sterilize the debris. Such heating appears at the impact and the time of entering the new planet's atmosphere following the transfer. Regarding the potential transfer between Earth and Mars with their early atmosphere, the 0.2 m or 0.8 m is a crucial minimum size limit, which must be kept in mind, even if the fall through the atmosphere is a relatively short period (few tens of seconds) and a heat shield, a compact, melted layer, forms around the meteorite^[5]. In addition, asteroids may break up during the transfer and landing phase, which may endanger the microorganisms' survival in smaller meteorites^[5].

The pressure-mass/size conflict

The determination of various pressure zones around the impact site, and their distance from ground zero, all together with the change in the ejected mass (even if the extreme 30 m/s impact velocity and 100 km diameter impactor size were used) and the supposed difference in decreasing average size of ejected debris moving further from the center of impact revealed a dilemma. Such a dilemma is closely related not only to the possible bioaerosol/microbe-containing material exchange between early Earth and Mars but applies, in general, to any case when

the escape of microorganisms from terrestrial (Earth-like) planets is discussed.

The size of impactors as a limiting factor during the transfer of microbes to another planet was discussed in detail in Mileikowsky et al.^[5]. In the case of Mars-Earth transfer, Category 1 meteorites are too small to provide a safe transfer to microorganisms.

This research adds a factor to the material ejection phase. The distances of the Safe-and Critical survival zone (Figure 2) raised the question that in such distances, there is enough impact energy left to lift big enough size and amount of debris (Figure 3) and eject it into space with possible living microbial content or not (Figure 4). A higher velocity and bigger size impactor certainly provides enough energy to fragment and eject bigger mass and size debris to space. Despite the expected surface and subsurface overpressure conditions, i.e., from 0 to ≤ 1 GPa overpressure^[5], the calculation in this study shows that even in the case of a 20 km diameter impactor, zones, where microorganisms may survive the mechanical pressure, are located in c.a. 100 km distance or further. The question is whether the impact has enough energy (regarding, e.g., the propagation and decay of the first stress wave-detached shock^[55]) to detach and eject materials into space, located in further distances (along with the non-shocked ejectiles from the neighbour of ground zero), or the ejected material is big enough to protect the microbes via the transfer.

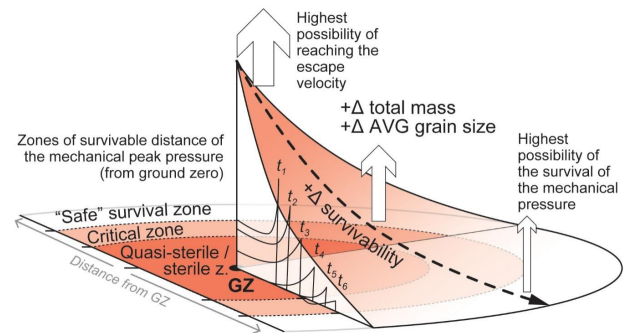


Figure 4. The visual explanation of the pressure-mass/size conflict. t1 to t6 curves indicate the variation of overpressure in the air with the distance at successive times^[60], and GZ marks the ground zero.

Similar to explosions, the characteristics of the peak overpressure-related shock front (blast wave) and the dynamic pressure (drag force associated with the strong wind accompanying the passage of the blast wave) at a certain distance from ground zero may be considered critical parameters during the evaluation of surface material detachment, lift and ejection further from ground zero^[60,61]. The detailed research of the surface waves, such as incident and reflected waves, and their interaction, including

the formation of a single wavefront by merging the two waves (so-called Mach or irregular region), may significantly contribute to understanding microbe-bearing material ejection in space. Still, it is beyond the scope of this study and most likely requires experiment-based complex simulations.

4. Conclusions and Summary

Along with the determination of various zones regarding the (microbial) survivability of the mechanical pressure triggered by the shockwave, the mass and average size of the ejectiles were estimated. The size of ejectiles in the case of a possible exchange between Earth and Mars falls between 10 to tens of km in the case of a 100 km impactor. The extreme ends of such scale represent the scale of various impact speeds, the minimum impact velocity required to trigger enough high escape velocity for the ejectiles, and a maximum high velocity, defined as 30 km/s. The estimated average ejectile size drops to a magnitude smaller size range in the case of smaller (20 km diameter) asteroids, which might be more common around 3.5 Ga ago, during the period when life appeared in the case of Earth and theoretically on Mars. Considering various physical effects on the ejectile, e.g., the potential further fragmentation of the debris during the transfer and landing phase, the smaller size may jeopardize the survival of the carried microbes.

The study of essential characteristics leads to a dilemma, named pressure-mass/size conflict, that is not simply related to the understanding of the possible microbial exchange between the early Earth and Mars, but any panspermia studies targeting asteroid impacts as potential contributors in the escape step of microbial transport.

The pressure-mass/size conflict originates from a contradiction related to the determined zones, indicating the distance where living organisms, most likely microorganisms in the case of early Earth and theoretically Mars, may survive the shockwave-triggered mechanical pressure and the size of the ejectiles which may carry microbes during the transfer between planets. It seems that some impacts with specific impact energy can eject the appropriate size debris, which may be a carrier for microorganisms during the transfer between early Earth and Mars. The only problem is that such impact energy may sterilize the sample by the mechanic pressure, and the zones where the shock wave triggered mechanical pressure is survivable on the surface are far from the impact center. At such a distance, the impact energy may not be enough to accelerate the ejectile speed to reach the escaping velocity and leave the planet's gravity well.

Although solving such a problem is out of the scope of

this manuscript, searching for an “ideal” combination of various parameters (e.g., impactor size, impact velocity, and so on) is a possible challenge for future studies. In closing words, at least two alternative ways of material ejection into space by asteroid impact can be considered. The possibly most discussed and known way is material ejection close to ground zero. It guarantees big enough debris to protect its passengers during their travel. Still, the survival rate at/close to ground zero is supposedly low, and the heat and overpressure-related compression may sterilize the material even before “boarding”. Another alternative way may provide a higher chance of survival, further from the center of impact. Still, the possibility of the ejectile reaching the escaping velocity and the minimum required size is low. Such ways may represent a scale's extreme ends regarding various factors that may influence the bioaerosol escape during an asteroid impact. One of the focuses of future studies can be the determination of an ideal way, an ideal escaping distance, where all the considered factors are in a setting that supports successful bioaerosol escape.

Funding

This research received no external funding.

Acknowledgement

I want to thank Simone Marchi for providing the early Earth impact dataset. It provided a strong foundation for the calculations.

I would like to thank the anonymous reviewers of this article for taking the time and effort to review the manuscript. I appreciate all of their valuable comments and suggestions, which helped improve this manuscript's quality.

Data Availability Statement

Data will be available upon request from the author.

Conflict of Interest

The author declares no conflict of interest.

References

- [1] Crick, F.H., Orgel, L.E., 1973. Directed panspermia. *Icarus*. 19(3), 341-346.
DOI: [https://doi.org/10.1016/0019-1035\(73\)90110-3](https://doi.org/10.1016/0019-1035(73)90110-3)
- [2] Mautner, M., 1979. Directed panspermia: A technical evaluation of seeding nearby solar systems. *Journal of British Interplanetary Society*. 32, 419-422.
- [3] Rampelotto, P.H. (editor), 2010. *Panspermia: A*

- promising field of research. *Astrobiology Science Conference 2010: Evolution and Life: Surviving Catastrophes and Extremes on Earth and Beyond*; 2010 Apr 20-26; League City, Texas.
- [4] Kawaguchi, Y., 2019. Panspermia hypothesis: History of a hypothesis and a review of the past, present, and future planned missions to test this hypothesis. *Astrobiology*. Springer: Singapore, 419-428.
DOI: https://doi.org/10.1007/978-981-13-3639-3_27
- [5] Mileikowsky, C., Cucinotta, F.A., Wilson, J.W., et al., 2000. Natural transfer of viable microbes in space: 1. From Mars to Earth and Earth to Mars. *Icarus*. 145(2), 391-427.
DOI: <https://doi.org/10.1006/icar.1999.6317>
- [6] Bottke, W.F., Andrews-Hanna, J.C., 2017. A post-accretionary lull in large impacts on early Mars. *Nature Geoscience*. 10(5), 344-348.
DOI: <https://doi.org/10.1038/ngeo2937>
- [7] Canup, R.M., Asphaug, E., 2001. Origin of the Moon in a giant impact near the end of the Earth's formation. *Nature*. 412(6848), 708-712.
DOI: <https://doi.org/10.1038/35089010>
- [8] Robbins, S.J., Hynek, B.M., Lillis, R.J., et al., 2013. Large impact crater histories of Mars: The effect of different model crater age techniques. *Icarus*. 225(1), 173-184.
DOI: <https://doi.org/10.1016/j.icarus.2013.03.019>
- [9] Andrews-Hanna, J., Bottke, W.B. (editors), 2017. Mars during the pre-Noachian. *Fourth International Conference on Early Mars: Geologic, Hydrologic, and Climatic Evolution and the Implications for Life*; 2017 Oct 2-6; Flagstaff, Arizona.
- [10] Carter, J., Poulet, F., Bibring, J.P., et al., 2013. Hydrous minerals on Mars as seen by the CRISM and OMEGA imaging spectrometers: Updated global view. *Journal of Geophysical Research: Planets*. 118(4), 831-858.
DOI: <https://doi.org/10.1029/2012JE004145>
- [11] Ehlmann, B.L., Mustard, J.F., Murchie, S.L., et al., 2011. Subsurface water and clay mineral formation during the early history of Mars. *Nature*. 479(7371), 53-60.
DOI: <https://doi.org/10.1038/nature10582>
- [12] Wordsworth, R.D., 2016. The climate of early Mars. *Annual Review of Earth and Planetary Sciences*. 44, 381-408.
DOI: <https://doi.org/10.1146/annurev-earth-060115-012355>
- [13] Camprubí, E., De Leeuw, J.W., House, C.H., et al., 2019. The emergence of life. *Space Science Reviews*. 215, 1-53.
DOI: <https://doi.org/10.1007/s11214-019-0624-8>
- [14] Zahnle, K., Arndt, N., Cockell, C., et al., 2007. Emergence of a habitable planet. *Space Science Reviews*. 129, 35-78.
DOI: <https://doi.org/10.1007/s11214-007-9225-z>
- [15] Grott, M., Morschhauser, A., Breuer, D., et al., 2011. Volcanic outgassing of CO₂ and H₂O on Mars. *Earth and Planetary Science Letters*. 308(3-4), 391-400.
DOI: <https://doi.org/10.1016/j.epsl.2011.06.014>
- [16] Benner, S.A., Bell, E.A., Biondi, E., et al., 2020. When did life likely emerge on Earth in an RNA-first process?. *Chem Systems Chem*. 2(2), e1900035.
DOI: <https://doi.org/10.1002/syst.201900035>
- [17] McKay, D.S., Gibson Jr, E.K., Thomas-Keppta, K.L., et al., 1996. Search for past life on Mars: Possible relic biogenic activity in Martian meteorite ALH84001. *Science*. 273(5277), 924-930.
DOI: <https://doi.org/10.1126/science.273.5277.924>
- [18] Bradley, J.P., Harvey, R.P., McSween Jr, H.Y., et al., 1997. No 'nanofossils' in martian meteorite. *Nature*. 390(6659), 454-455.
DOI: <https://doi.org/10.1038/37257>
- [19] Thomas-Keppta, K.L., Bazylinski, D.A., Kirschvink, J.L., et al., 2000. Elongated prismatic magnetite crystals in ALH84001 carbonate globules: Potential Martian magnetofossils. *Geochimica et Cosmochimica Acta*. 64(23), 4049-4081.
DOI: [https://doi.org/10.1016/S0016-7037\(00\)00481-6](https://doi.org/10.1016/S0016-7037(00)00481-6)
- [20] Friedmann, E.I., Wierzbos, J., Ascaso, C., et al., 2001. Chains of magnetite crystals in the meteorite ALH84001: Evidence of biological origin. *Proceedings of the National Academy of Sciences*. 98(5), 2176-2181.
DOI: <https://doi.org/10.1073/pnas.051514698>
- [21] Steele, A., Benning, L.G., Wirth, R., et al., 2022. Organic synthesis associated with serpentinization and carbonation on early Mars. *Science*. 375(6577), 172-177.
DOI: <https://doi.org/10.1126/science.abg7905>
- [22] Borg, L.E., Connelly, J.N., Nyquist, L.E., et al., 1999. The age of the carbonates in Martian meteorite ALH84001. *Science*. 286(5437), 90-94.
DOI: <https://doi.org/10.1126/science.286.5437.90>
- [23] Boehnke, P., Harrison, T.M., 2016. Illusory late heavy bombardments. *Proceedings of the National Academy of Sciences*. 113(39), 10802-10806.
DOI: <https://doi.org/10.1073/pnas.1611535113>
- [24] Bottke, W.F., Norman, M.D., 2017. The late heavy bombardment. *Annual Review of Earth and Planetary Sciences*. 45, 619-647.
DOI: <https://doi.org/10.1146/annurev-earth-063016-020131>
- [25] Toon, O.B., Zahnle, K., Morrison, D., et al., 1997.

- Environmental perturbations caused by the impacts of asteroids and comets. *Reviews of Geophysics*. 35(1), 41-78.
DOI: <https://doi.org/10.1029/96RG03038>
- [26] Baker, V.R., Strom, R.G., Gulick, V.C., et al., 1991. Ancient oceans, ice sheets and the hydrological cycle on Mars. *Nature*. 352(6336), 589-594.
DOI: <https://doi.org/10.1038/352589a0>
- [27] Carr, M.H., Head III, J.W., 2010. Geologic history of Mars. *Earth and Planetary Science Letters*. 294(3-4), 185-203.
DOI: <https://doi.org/10.1016/j.epsl.2009.06.042>
- [28] Ryder, G., Koeberl, C., Mojzsis, S.J., 2000. Heavy bombardment of the Earth at ~3.85 Ga: The search for petrographic and geochemical evidence. *Origin of the Earth and Moon*. University of Arizona Press: Tucson. pp. 475-492.
DOI: <https://doi.org/10.2307/j.ctv1v7zdrp.30>
- [29] Barlow, N.G., 2010. What we know about Mars from its impact craters. *Bulletin*. 122(5-6), 644-657.
DOI: <https://doi.org/10.1130/B30182.1>
- [30] Rapin, W., Dromart, G., Rubin, D., et al., 2021. Alternating wet and dry depositional environments recorded in the stratigraphy of Mount Sharp at Gale crater, Mars. *Geology*. 49(7), 842-846.
DOI: <https://doi.org/10.1130/G48519.1>
- [31] Rodriguez, J.A.P., Fairén, A.G., Tanaka, K.L., et al., 2016. Tsunami waves extensively resurfaced the shorelines of an early Martian ocean. *Scientific Reports*. 6(1), 1-8.
DOI: <https://doi.org/10.1038/srep25106>
- [32] Costard, F., Séjourné, A., Lagain, A., et al., 2019. The Lomonosov crater impact event: A possible mega-tsunami source on Mars. *Journal of Geophysical Research: Planets*. 124(7), 1840-1851.
DOI: <https://doi.org/10.1029/2019JE006008>
- [33] Turbet, M., Forget, F., 2019. The paradoxes of the Late Hesperian Mars ocean. *Scientific Reports*. 9(1), 5717.
DOI: <https://doi.org/10.1038/s41598-019-42030-2>
- [34] Gladman, B., Dones, L., Levison, H.F., et al., 2005. Impact seeding and reseeded in the inner solar system. *Astrobiology*. 5(4), 483-496.
DOI: <https://doi.org/10.1089/ast.2005.5.483>
- [35] Van Eaton, A.R., Harper, M.A., Wilson, C.J., 2013. High-flying diatoms: Widespread dispersal of microorganisms in an explosive volcanic eruption. *Geology*. 41(11), 1187-1190.
- [36] Mandon, L., Quantin-Nataf, C., Thollet, P., et al., 2020. Refining the age, emplacement and alteration scenarios of the olivine-rich unit in the Nili Fossae region, Mars. *Icarus*. 336, 113436.
DOI: <https://doi.org/10.1016/j.icarus.2019.113436>
- [37] Whelley, P., Matiella Novak, A., Richardson, J., et al., 2021. Stratigraphic evidence for early martian explosive volcanism in Arabia Terra. *Geophysical Research Letters*. 48(15), e2021GL094109.
DOI: <https://doi.org/10.1029/2021GL094109>
- [38] de Kock, M.O., Evans, D.A., Beukes, N.J., 2009. Validating the existence of Vaalbara in the Neoproterozoic. *Precambrian Research*. 174(1-2), 145-154.
DOI: <https://doi.org/10.1016/j.precamres.2009.07.002>
- [39] Mole, D.R., Fiorentini, M.L., Thebaud, N., et al., 2014. Archean komatiite volcanism controlled by the evolution of early continents. *Proceedings of the National Academy of Sciences*. 111(28), 10083-10088.
DOI: <https://doi.org/10.1073/pnas.1400273111>
- [40] Polat, A., 2012. Growth of Archean continental crust in oceanic island arcs. *Geology*. 40(4), 383.
DOI: <https://doi.org/10.1130/focus042012.1>
- [41] Djokic, T., Van Kranendonk, M.J., Campbell, K.A., et al., 2017. Earliest signs of life on land preserved in ca. 3.5 Ga hot spring deposits. *Nature Communications*. 8(1), 15263.
DOI: <https://doi.org/10.1038/ncomms15263>
- [42] Kawaguchi, Y., Shibuya, M., Kinoshita, I., et al., 2020. DNA damage and survival time course of deinococcal cell pellets during 3 years of exposure to outer space. *Frontiers in Microbiology*. 11, 2050.
- [43] Dong, J., Fischer, R.A., Stixrude, L.P., et al., 2021. Constraining the volume of Earth's early oceans with a temperature-dependent mantle water storage capacity model. *AGU Advances*. 2(1), e2020AV000323.
DOI: <https://doi.org/10.1029/2020AV000323>
- [44] Schopf, J.W., Kitajima, K., Spicuzza, M.J., et al., 2018. SIMS analyses of the oldest known assemblage of microfossils document their taxon-correlated carbon isotope compositions. *Proceedings of the National Academy of Sciences*. 115(1), 53-58.
DOI: <https://doi.org/10.1073/pnas.1718063115>
- [45] Homann, M., 2019. Earliest life on earth: Evidence from the Barberton Greenstone Belt, South Africa. *Earth-Science Reviews*. 196, 102888.
DOI: <https://doi.org/10.1016/j.earscirev.2019.102888>
- [46] Lepot, K., 2020. Signatures of early microbial life from the Archean (4 to 2.5 Ga) eon. *Earth-Science Reviews*. 209, 103296.
DOI: <https://doi.org/10.1016/j.earscirev.2020.103296>
- [47] Hibbing, M.E., Fuqua, C., Parsek, M.R., et al., 2010. Bacterial competition: Surviving and thriving in the microbial jungle. *Nature Reviews Microbiology*. 8(1), 15-25.

- DOI: <https://doi.org/10.1038/nrmicro2259>
- [48] Marchi, S., Bottke, W.F., Elkins-Tanton, L.T., et al., 2014. Widespread mixing and burial of Earth's Hadean crust by asteroid impacts. *Nature*. 511(7511), 578-582.
DOI: <https://doi.org/10.1038/nature13539>
- [49] Marchi, S., Drabon, N., Schulz, T., et al., 2021. Delayed and variable late Archaean atmospheric oxidation due to high collision rates on Earth. *Nature Geoscience*. 14(11), 827-831.
DOI: <https://doi.org/10.1038/s41561-021-00835-9>
- [50] Robbins, S.J., Hynek, B.M., 2012. A new global database of Mars impact craters ≥ 1 km: 1. Database creation, properties, and parameters. *Journal of Geophysical Research: Planets*. 117, E05004.
DOI: <https://doi.org/10.1029/2011JE003966>
- [51] Hughes, D.W., 2003. The approximate ratios between the diameters of terrestrial impact craters and the causative incident asteroids. *Monthly Notices of the Royal Astronomical Society*. 338(4), 999-1003.
DOI: <https://doi.org/10.1046/j.1365-8711.2003.06157.x>
- [52] Shoemaker, E.M., Wolfe, R.F., Shoemaker, C.S., 1990. Asteroid and comet flux in the neighborhood of Earth. *Global Catastrophes in Earth History; An Interdisciplinary Conference on Impacts, Volcanism, and Mass Mortality*. GeoScienceWorld: McLean. pp. 155-170.
DOI: <https://doi.org/10.1130/SPE247-p155>
- [53] Armstrong, J.C., Wells, L.E., Gonzalez, G., 2002. Rummaging through Earth's attic for remains of ancient life. *Icarus*. 160(1), 183-196.
DOI: <https://doi.org/10.1006/icar.2002.6957>
- [54] Vijayaraghavan, C., Thirumalaivasan, D., Venkatesan, R., 2012. A study on nuclear blast overpressure on buildings and other infrastructures using geospatial technology. *Journal of Computer Science*. 8(9), 1520.
DOI: <https://doi.org/10.3844/jcssp.2012.1520.1530>
- [55] Melosh, H.J., 1985. Ejection of rock fragments from planetary bodies. *Geology*. 13(2), 144-148.
Available from: <https://pubs.geoscienceworld.org/gsa/geology/article-abstract/13/2/144/188960/Ejection-of-rock-fragments-from-planetary-bodies?redirectedFrom=fulltext>
- [56] Wells, L.E., Armstrong, J.C., Gonzalez, G., 2003. Re-seeding of early Earth by impacts of returning ejecta during the late heavy bombardment. *Icarus*. 162(1), 38-46.
DOI: [https://doi.org/10.1016/S0019-1035\(02\)00077-5](https://doi.org/10.1016/S0019-1035(02)00077-5)
- [57] Britt, D.T., Consolmagno, G.J.S.J., 2003. Stony meteorite porosities and densities: A review of the data through 2001. *Meteoritics & Planetary Science*. 38(8), 1161-1180.
DOI: <https://doi.org/10.1111/j.1945-5100.2003.tb00305.x>
- [58] Hazael, R., Meersman, F., Ono, F., et al., 2016. Pressure as a limiting factor for life. *Life*. 6(3), 34.
DOI: <https://doi.org/10.3390/life6030034>
- [59] Burchell, M.J., Mann, J.R., Bunch, A.W., 2004. Survival of bacteria and spores under extreme shock pressures. *Monthly Notices of the Royal Astronomical Society*. 352(4), 1273-1278.
DOI: <https://doi.org/10.1111/j.1365-2966.2004.08015.x>
- [60] Glasstone, S., Dolan, P.J., 1977. The effect of nuclear weapons. United States Department of Defense and Energy Research and Development Administration. pp. 653.
- [61] Ben-dor, G., Igra, O., Elperin, T., 2001. Handbook of shock waves: Shock wave interactions and propagation. Academic Press: Cambridge. pp. 543.



RESEARCH ARTICLE

Revisiting Recent Amplitude and Phase Variations of the Chandler Wobble and Free Core Nutation

Zinovy Malkin*

Pulkovo Observatory, St. Petersburg, 196140, Russia

ARTICLE INFO

Article history

Received: 6 June 2023

Revised: 5 July 2023

Accepted: 18 July 2023

Published Online: 26 July 2023

Keywords:

Earth's rotation

Chandler wobble

Free core nutation

Amplitude

Phase variations

ABSTRACT

The paper is devoted to the analysis of two components of the Earth's rotation, Chandler wobble (CW) and free core nutation (FCN). They are oscillations with near-constant periods but variable amplitude and phase. The variations of the amplitude and phase of the CW and FCN have already been considered in the literature, and both showed similar behavior such as a recent significant decrease of the amplitude and large phase change. However, the CW and FCN amplitude and phase variations are, to a large extent, predicted for the current epochs, and their today's variations need regular updates with obtaining new observations. In this work, the CW and FCN parameters have been re-computed using the latest data and compared with the data published earlier. It was found that the currently obtained amplitude and phase variations generally agreed with the data published earlier. The main difference is that the epochs of the current minimum of amplitude and phase jump or both CW and FCN happened somewhat later than was predicted in previous publications. The delay is about two years for the CW relative to the prediction made in 2010 and about one year for the FCN with respect to the prediction made in 2022.

1. Introduction

The rotation of the Earth is a very complex process that consists of many free and forced modes. Analysis of the variations in the Earth's rotation plays an important role in our understanding of the physical processes in the Earth's surface, interior, atmosphere, and hydrosphere. Three main constituents of the Earth's rotation are movement of the rotation axis in terrestrial and celestial reference frames, and rotation around the rotation axis. In this paper,

some features of the first two processes will be discussed.

The movement of the Earth's rotation axis relative to the Earth's surface manifests itself as Polar motion (PM) and is observed through the coordinates of the terrestrial Pole X_p and Y_p in the conventional terrestrial reference frame ^[1]. The Chandler wobble (CW) discovered by Seth Carlo Chandler in 1891 ^[2,3] is one of the main and most complicated components of the Earth's rotation, and numerous papers were devoted to investigation of the CW

*Corresponding Author:

Zinovy Malkin,

Pulkovo Observatory, St. Petersburg, 196140, Russia;

Email: malkin@gaoran.ru

DOI: <https://doi.org/10.36956/eps.v2i2.873>

Copyright © 2023 by the author(s). Published by Nan Yang Academy of Sciences Pte. Ltd. This is an open access article under the Creative Commons Attribution-NonCommercial 4.0 International (CC BY-NC 4.0) License. (<https://creativecommons.org/licenses/by-nc/4.0/>).

variations, such as changes in the CW amplitude and phase. A brief overview of these studies is given ^[4-10] and papers cited therein. The main result ^[4] was detecting, for the first time, a large jump in the CW phase in the 2000s and a simultaneous deep minimum of the CW amplitude.

Free core nutation (FCN) is a component of the motion of the Earth's rotation axis in the conventional celestial reference frame ^[1]. The FCN is a free Earth's rotational mode caused by the misalignment of the rotational axis of the Earth's mantle and the rotational axis of the outer liquid core ^[11]. It is observed through the coordinates of the celestial Pole dX and dY in the conventional celestial reference frame ^[1]. Like CW, the FCN is an oscillation with highly variable amplitude and phase that was investigated in many studies ^[12-17] and papers cited therein. In a recent paper ^[18], a new minimum of the FCN amplitude and simultaneous large jump in the FCN phase was preliminary detected at the epoch around 2022.

It should be noted that the CW and FCN amplitude and phase variations ^[4,18] were obtained from analysis of the series of Earth orientation parameters (EOP) ended near the epochs of the investigated minima of the amplitude and phase jumps. Besides, both series used in these works are smoothed, the CW series to a lesser extent, and the FCN series to a larger extent. Under these circumstances, today's behavior of the CW and FCN could not be accurately predicted when these papers were published. Therefore, it is very desirable to revise the results ^[4,18] using the latest available observations, which is the primary goal of this study.

The paper is organized as follows. Section 2 describes the analysis of the CW variations, and Section 3 is devoted to the analysis of the FCN variations. Section 4 sums up the paper.

2. Chandler Wobble

The first step in the CW analysis was to extract the CW signal from the PM time series, removing all the trend, periodic, and quasi-periodic components beyond the CW frequency band. For this study, the CW signal was extracted from the IERS (International Earth Rotation and Reference Systems Service) Pole coordinates time series IERS C01^① using a band-pass digital filter based on the Fourier transform with the window 1.18...1.20 yr centered at the nominal CW period $P_{CW} = 1.19$ years. The IERS C01 series begins in 1846.0 and extends to the present (April

2023). It is sampled at 0.1 Besselian year (36.524 solar days) for the period 1846-1890 and 0.05 Besselian year (18.262 solar days) after 1890.0. Using this data, a new interpolated EOP series of the CW component of polar motion X_{CW} and Y_{CW} with 10 days step was constructed and used for further analysis. This series is shown in Figure 1. Epochs in all the plots in this paper are expressed in Besselian years.

For this work, PM (CW) series started with 1900.0 was used because the data before 1900 are less reliable. The whole IERS C01 series was considered ^[4], while in this study we are mostly interested in the CW behavior in recent years.

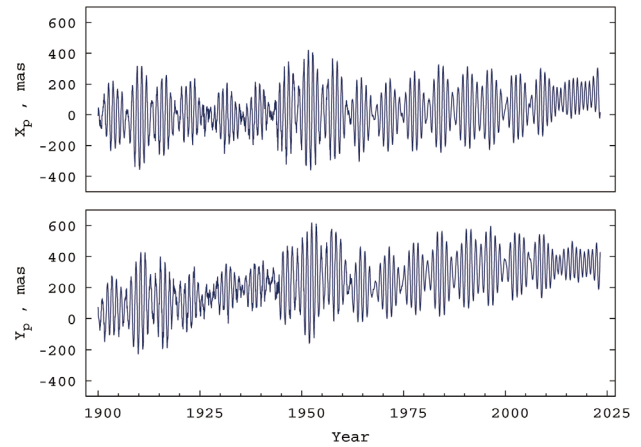


Figure 1. IERS C01 series.

A general CW model can be expressed as follows:

$$\begin{aligned} X_{CW} &= A_c \cos \phi - A_s \sin \phi, \\ Y_{CW} &= A_c \sin \phi + A_s \cos \phi, \\ A_c &= -X_{CW} \sin \phi + Y_{CW} \cos \phi, \\ A_s &= X_{CW} \cos \phi + Y_{CW} \sin \phi, \end{aligned} \quad (1)$$

where CW phase $\phi = 2\pi/P_{CW}(t-t_0)$, t is the epoch at which observed X_{CW} and Y_{CW} values are given, $t_0 = J2000.0$. Each group of Equation (1) corresponds to one epoch given in the CW series. Then the instant CW amplitude and phase at epoch t can be found as:

$$\begin{aligned} A_{CW} &= \sqrt{X_{CW}^2 + Y_{CW}^2} = \sqrt{A_c^2 + A_s^2}, \\ P_{CW} &= \arctan \frac{A_c}{A_s}. \end{aligned} \quad (2)$$

The results of this analysis are shown in Figure 2. For a better representation of the CW phase variations, the linear trend corresponding to the CW frequency was removed from the CW phase series. The results of the previous analysis ^[4] are also shown in these plots. Note that the IERS C01 EOP series, which was analyzed ^[4], ended in December 2008 (epoch 2009.0).

① https://datacenter.iers.org/data/latestVersion/EOP_C01_IAU2000_1846-now.txt

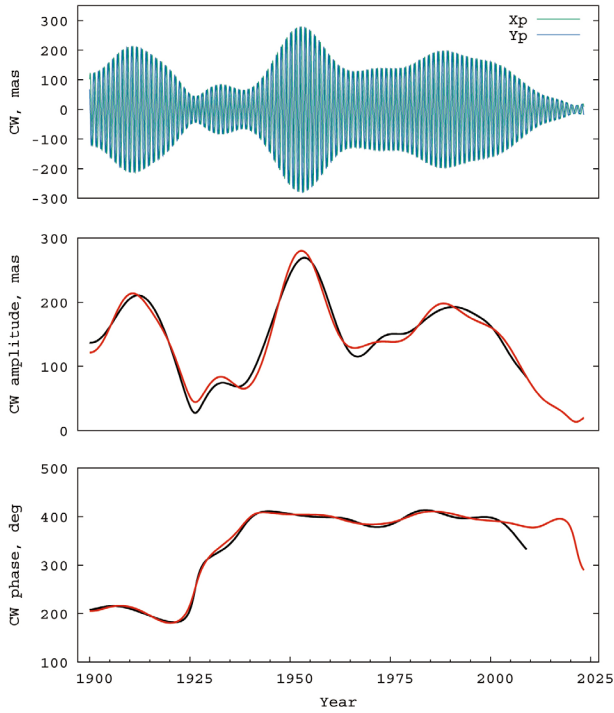


Figure 2. Chandler wobble (CW) series (upper panel), CW amplitude (middle panel), and CW phase minus linear drift (bottom panel). In the amplitude and phase plots, data from the previous publication are shown in black, and data obtained in this work are shown in red.

A well-known large CW phase jump in the 1920s is clearly visible in Figure 2, but we are mostly interested in the comparison of the second large CW phase jump epoch (after 2000.0) detected^[4] in this work. One can see that the present analysis revealed an even larger CW phase jump, but its epoch is later than was suggested^[4]. One of the reasons may be that the minimum of the CW amplitude was reached after 2010, at the epoch 2021.4 according to this work, which made the determination of the moment of the phase jump made in 2010 not very reliable.

Obtained results for CW variations are in good agreement with the results^[9] derived by a similar method of digital filtration of the IERS EOP series but using another filtering technique.

3. Free Core Nutation

The FCN amplitude and phase variations were studied using the ZM3 FCN model in the same way as it was done^[18]. First, the ZM2 celestial pole offset (CPO) model was constructed by the Gaussian smoothing and interpolation at daily intervals of the combined EOP series maintained by the International VLBI Service for Geodesy and Astron-

omy[®] (IVS). Figure 3 shows the ZM2 CPO model along with the underlying IVS CPO series.

Then the ZM3 model (FCN series) was evaluated using the following expression:

$$\begin{aligned} dX &= A_c \cos \phi - A_s \sin \phi + X_0, \\ dY &= A_c \sin \phi + A_s \cos \phi + Y_0, \end{aligned} \quad (4)$$

where $\phi = 2\pi/P_{FCN}(t - t_0)$, P_{FCN} is the FCN period equal to -430.21 solar days, t is the epoch at which observed dX and dY values are given, $t_0 = J2000.0$. The model parameters A_c , A_s , X_0 , and Y_0 are adjusted by the least square method for running 431-day intervals with one day shift. Each pair of Equation (3) corresponds to one CPO epoch given in the ZM2 series. The model parameters A_c , A_s , X_0 , and Y_0 were computed at the middle epoch of each 431-day interval.

The FCN contribution to the celestial pole motion at the same epochs is computed by using Equation (3) without the bias terms X_0 and Y_0 .

$$\begin{aligned} dX_{FCN} &= A_c \cos \phi - A_s \sin \phi, \\ dY_{FCN} &= A_c \sin \phi + A_s \cos \phi. \end{aligned} \quad (4)$$

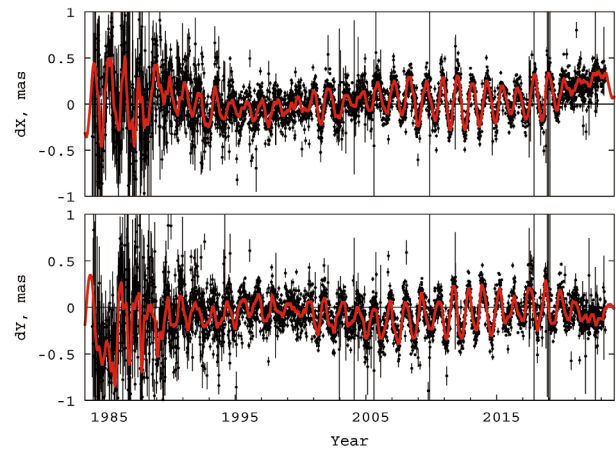


Figure 3. ZM2 FCN series (red line) and IVS combined series (black dots with error bars).

Then the instant amplitude A_{FCN} and phase P_{FCN} of the FCN signal can be computed as:

$$\begin{aligned} A_{FCN} &= \sqrt{dX_{FCN}^2 + dY_{FCN}^2} = \sqrt{A_c^2 + A_s^2}, \\ P_{FCN} &= \arctan \frac{A_c}{A_s}. \end{aligned} \quad (5)$$

Thus obtained the FCN amplitude and phase variations are shown in Figure 4. For a better representation of the FCN phase variations, the linear trend corresponding to the FCN frequency was removed from the FCN phase se-

© <https://ivsec.gsfc.nasa.gov/products-data/product-tables/bkg-products-eops.html>

ries. The results of the previous analysis^[18] are also shown in these plots. Note that the IVS EOP series^[18] ended in February 2022 (epoch 2022.13).

Results presented in Figure 4 confirmed the deep minimum of the FCN amplitude and FCN phase jump discussed^[18], but their epoch is later than was suggested^[18] by about one year. This epoch still cannot be accurately determined because the minimum of the FCN amplitude most probably is not reached yet. However, it can be noted that the current minimum of the FCN amplitude, which is ≈ 35 mas, is deeper than the previous minimum in about 1999.4, which was ≈ 55 mas.

One can also see in Figure 4 that the amplitude variations in the 1980s and at the beginning of the 1990s are substantially different for the previous and the current analysis. This can be explained by using different versions of the IVS CPO series^[18] and in this study. These series substantially differ at the beginning of the interval due to the low accuracy and instability of the CPO observations in this period. The most reliable CPO data begins in May 1993^[19].

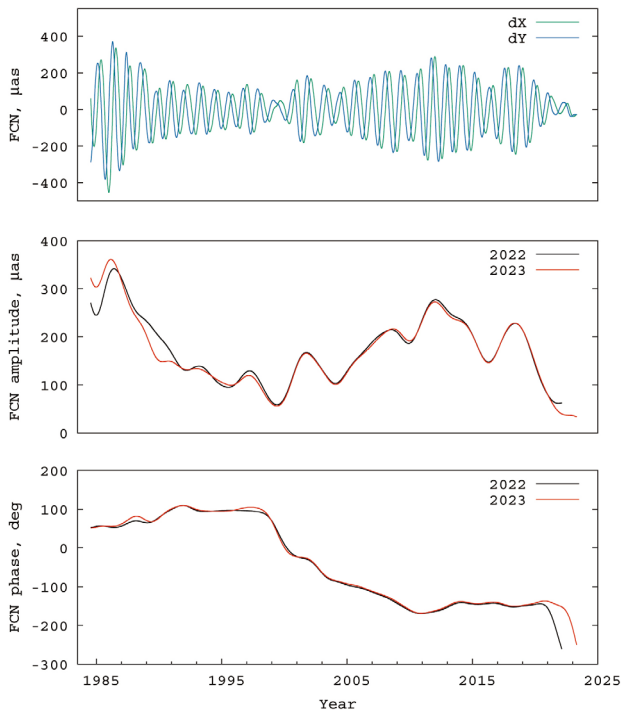


Figure 4. Free core nutation (FCN) series (upper panel), FCN amplitude (middle panel), and FCN phase minus linear drift (bottom panel). In the amplitude and phase plots, data from the previous publication are shown in black, and data obtained in this work are shown in red.

4. Conclusions

In this paper, a re-computation was made of the CW

and FCN amplitude and phase variations using the latest data of EOP observations. Obtained results were compared with the results of the prediction of the recent peculiarities in the CW and FCN behavior published earlier. The comparison confirmed the deep minima of the CW and FCN amplitude and simultaneous CW and FCN phase jumps, but the epochs of these events occurred to be later than predicted. Such a result could be expected because the recent amplitude and phase variations under investigation are detected near the end of the EOP series used for the study. Therefore, the addition of new data obtained during the last years allowed us to determine this epoch more accurately. Also, an edge effect in the data analysis can impact the accuracy of the obtained epochs of the minima of the CW and FCN amplitude and phase jumps.

It should be also noted that the phase of any physical oscillation is often less stable during the period of near-zero amplitude. This effect is also observed in both the case of CW and FCN.

It is important to bear in mind that the parts of the phase variation plots in Figures 2 and 4 close to horizontal do not mean that the phase of corresponding oscillation (CW or FCN) is constant, since the slope of the line on the plot directly depends on the linear drift corresponding to the CW (FCN) frequency which has been subtracted from the phase before plotting. Therefore, these periods simply correspond to the periods of linear phase change. However, the jumps and other disturbances in the plots correspond to the actual non-linear disturbances in the CW or FCN phase.

From results of the analysis of the CW and FCN series showed that in both cases the precise epochs of the current minima of the CW (to a lesser extent) and FCN (to a larger extent) amplitude and simultaneous phase jumps are still hardly possible. Re-computation of the CW and FCN series in two-three years with the addition of new observations will allow us to investigate these events in more detail.

Funding

This research received no external funding.

Acknowledgement

The author is grateful to the anonymous reviewers for their careful reading of the manuscript and useful comments. This research has made use of SAO/NASA Astrophysics Data System^③ (ADS). The figures were prepared using gnuplot^④.

③ <https://ui.adsabs.harvard.edu/>

④ <http://www.gnuplot.info/>

Data Availability Statement

IERS EOP series are available at <https://datacenter.iers.org/eop.php>. Author's FCN and CPO series used in this study are available at <http://www.gaoran.ru/english/as/per-sac/>. Other results derived from this work can be available from the author upon reasonable request.

Conflicts of Interest

The author states that there are no known conflicts of interest.

References

- [1] Petit, G., Luzum, B., 2010. IERS Technical Note No. 36. Verlag des Bundesamts für Kartographie und Geodäsie: Frankfurt am Main, Germany.
- [2] Chandler, S.C., 1891. On the variation of the latitude, I. *Astronomical Journal*. 11, 59-61.
- [3] Chandler, S.C., 1891. On the variation of the latitude, II. *Astronomical Journal*. 11, 65-70.
- [4] Malkin, Z., Miller, N., 2010. Chandler wobble: Two more large phase jumps revealed. *Earth, Planets and Space*. 62, 943-947.
DOI: <https://doi.org/10.5047/eps.2010.11.002>
- [5] Miller, N.O., 2011. Chandler wobble in variations of the Pulkovo latitude for 170 years. *Solar System Research*. 45, 342-353.
DOI: <https://doi.org/10.1134/S0038094611040058>
- [6] Chao, B.F., Chung, W.Y., 2012. Amplitude and phase variations of Earth's Chandler wobble under continual excitation. *Journal of Geodynamics*. 62, 35-39.
DOI: <https://doi.org/10.1016/j.jog.2011.11.009>
- [7] Zotov, L., Bizouard, C., 2012. On modulations of the Chandler wobble excitation. *Journal of Geodynamics*. 62, 30-34.
DOI: <https://doi.org/10.1016/j.jog.2012.03.010>
- [8] Vondrák, J., Ron, C., Chapánov, Y., 2017. New determination of period and quality factor of Chandler wobble, considering geophysical excitations. *Advances in Space Research*. 59(5), 1395-1407.
DOI: <https://doi.org/10.1016/j.asr.2016.12.001>
- [9] Zotov, L.V., Sidorenkov, N.S., Bizouard, C., 2022. Anomalies of the chandler wobble in 2010s. *Moscow University Physics Bulletin*. 77(3), 555-563.
DOI: <https://doi.org/10.3103/S0027134922030134>
- [10] Chen, W., Chen, Y., Ray, J., et al., 2023. Free decay and excitation of the chandler wobble: Self-consistent estimates of the period and quality factor. *Journal of Geodesy*. 97(4), 36.
DOI: <https://doi.org/10.1007/s00190-023-01727-z>
- [11] Dehant, V., Mathews, P.M., 2015. Precession, nutation and wobble of the earth. Cambridge University Press: Cambridge, UK.
- [12] Malkin, Z., Terentev, D., 2003. Parameters of the free core nutation from VLBI data. *Communications of the IAA RAS*. 149.
DOI: <https://doi.org/10.48550/arXiv.physics/0702152>
- [13] Gubanov, V.S., 2009. Dynamics of the Earth's core from VLBI observations. *Astronomy Letters*. 35, 270-277.
DOI: <https://doi.org/10.1134/S1063773709040070>
- [14] Malkin, Z., 2013. Free core nutation and geomagnetic jerks. *Journal of Geodynamics*. 72, 53-58.
DOI: <https://doi.org/10.1016/j.jog.2013.06.001>
- [15] Belda, S., Ferrándiz, J.M., Heinkelmann, R., et al., 2016. Testing a new free core nutation empirical model. *Journal of Geodynamics*. 94, 59-67.
DOI: <https://doi.org/10.1016/j.jog.2016.02.002>
- [16] Vondrák, J., Ron, C., 2017. New method for determining free core nutation parameters, considering geophysical effects. *Astronomy & Astrophysics*. 604(A&A), A56.
DOI: <https://doi.org/10.1051/0004-6361/201730635>
- [17] Cui, X., Sun, H., Xu, J., et al., 2020. Relationship between free core nutation and geomagnetic jerks. *Journal of Geodesy*. 94(4), 1-13.
DOI: <https://doi.org/10.1007/s00190-020-01367-7>
- [18] Malkin, Z., Belda, S., Modiri, S., 2022. Detection of a new large free core nutation phase jump. *Sensors*. 22(16), 5960.
DOI: <https://doi.org/10.3390/s22165960>
- [19] Malkin, Z.M., 2020. Statistical analysis of the results of 20 years of activity of the international VLBI service for geodesy and astrometry. *Astronomy Reports*. 64, 168-188.
DOI: <https://doi.org/10.1134/S1063772920020043>



RESEARCH ARTICLE

Contribution to the Knowledge of Twenty Members of the Lagenid Benthic Foraminifera in the Southern Tethys

Haidar Salim Anan ^{*}

Al Azhar University-Gaza, P.O. Box 1277, Palestine

ARTICLE INFO

Article history

Received: 27 May 2023

Revised: 11 July 2023

Accepted: 24 July 2023

Published Online: 14 August 2023

Keywords:

Paleontology

Lagenid foraminifera

Paleogeography

Tethys

ABSTRACT

The modern taxonomical consideration is used for twenty Lagenid benthic foraminiferal species which are belonging to eight genera from nine countries in the Southern Tethys: Chile, Argentina, Egypt, Tanzania, Jordan, Iraq, United Arab Emirates (UAE), Iran and Pakistan: *Nodosaria catenula* (Reuss) Iraq, *Pyramidulina robinsoni* (Futyan) Jordan, *Tollmannia costata* (d'Orbigny), *Tollmannia fingeri* Anan, sp. nov., *Percultazonaria fragaria* (Gümbel), *Percultazonaria tuberculata* (Plummer), *Lenticuzonaria argentinica* Anan, *Lenticuzonaria misrensis* Anan, *Percultalina misrensis* Anan, *Hemirobulina comma* (Roemer), *Hemirobulina curvatura* (Cushman), *Hemirobulina humilis* (Reuss), *Hemirobulina nammalensis* (Haque), *Hemirobulina pachygaster* Gümbel, *Vaginulinopsis argentinica* Anan, sp. nov., *Vaginulinopsis deserti* (Said & Kenawy), *Vaginulinopsis emiratensis* (Anan), *Vaginulina boukharyi* (Anan), *Vaginulina chilensis* Anan, sp. nov., and *Ramulina shreiffae* Anan, sp. nov. Nine species of these assemblage were recorded from Egypt (about 45%), 3 species from Chile (about 15%), 2 species from Argentina (about 10%), and one species (about 5%) from each of Tanzania, Jordan, Iraq, UAE, Iran and Pakistan. Four species are believed here to be new: *Tollmannia fingeri*, *Vaginulinopsis argentinica*, *Vaginulina chilensis* and *Ramulina shreiffae*.

1. Introduction

The present study aims at throwing light on the paleontology and biogeography of twenty small benthic foraminiferal species that were originally erected by many authors from nine countries in the Southern Tethys. Ten of them were erected originally from Egypt (Northeast Africa), while the other species were recorded from East

Africa (Tanzania), Southwest Asia (Jordan, Iraq, UAE, Iran, Pakistan) (Figure 1A) and South America (Chile, Argentina) (Figure 1B). Four out of them are believed here to be new: two species from Chile (*Tollmannia fingeri* and *Vaginulina chilensis*), one species from Argentina (*Vaginulinopsis argentinica*), and also the other one species from Egypt (*Ramulina shreiffae*).

*Corresponding Author:

Haidar Salim Anan,

Al Azhar University-Gaza, P.O. Box 1277, Palestine;

Email: profanan@gmail.com

DOI: <https://doi.org/10.36956/eps.v2i2.866>

Copyright © 2023 by the author(s). Published by Nan Yang Academy of Sciences Pte. Ltd. This is an open access article under the Creative Commons Attribution-NonCommercial 4.0 International (CC BY-NC 4.0) License. (<https://creativecommons.org/licenses/by-nc/4.0/>).

2. Material of Study

Rich and well-preserved twenty Lagenid foraminiferal species from nine countries in the Southern Tethys (South America, Northeast and Central East Africa, and Southwest Asia) made it possible to elucidate them with its modern taxonomical consideration. Following the Code of Zoological Nomenclature, a taxonomic revision of four species of them is re-described its morphological features, which are considered here as a new species. As noted by many researchers (e.g. Finger^[1]), the sample processing of foraminiferal specimens was processed from the sedimentary rock samples by (1) soaking in water or hydrogen peroxide until most of the sediment had disaggregated, (2) washing the residue over a standard 230-mesh (63- μ m openings) sieve, and (3) drying by funneling through fast-flow filter paper, followed by oven-drying at 30 °C, (4) specimens were then picked with a 000 sable hair brush and sorted by species onto 63 60-grid micropaleontological slides, from which primary types were selected and transferred onto single-hole slides for reference and imaging.

3. Systematic Paleontology

The taxonomy of Loeblich & Tappan^[2] is followed here. The twenty benthic foraminiferal species belonging to eight genera, which were recorded from the Maastrichtian to Ypresian of nine Southern Tethyan countries, and illustrated in Plate 1.

Order Foraminiferida Eichwald, 1830

Suborder Lagenina Delage & Hérouard, 1896

Genus *Nodosaria* Lamarck, 1812

Nodosaria catenula (Reuss, 1860) (Plate 1, Figure 1)

1860 *Dentalina catenula* Reuss^[3], p. 185, Plate 3, Figure 6.

1956 *Dentalina catenula* Reuss-Said & Kenawy^[17], p. 132, Plate 2, Figure 24.

2019 *Laevidentalina catenula* Reuss-Jaff & Lawa^[21], p. 12, Plate 1, Figure 21. • {illustrated specimen}.

Age, type locality and sample: Late Campanian-Early Maastrichtian, Dokan section, sample number DSH05-105 (Figure 2).

Remarks: *Nodosaria* differs from *Laevidentalina* by its elongate arcuate smooth test, rounded to fusiform proloculus, which is mostly apiculate. *Nodosaria catenula* was recorded from Austria (Northern Tethys) and later from both Egypt and Iraq (Southern Tethys).

Genus *Pyramidulina* Fornasini, 1894

Pyramidulina robinsoni (Futyan, 1976) (Plate 1, Figure 2)

1976 *Nodosaria robinsoni* Futyan^[4], p. 525, Plate 82, Figures 5, 6.

2006 *Nodosaria* sp. Pearson et al.^[9], p. 307, Plate 4, Figure 11.

2016 *Nodosaria limbata* d'Orbigny-Orabi & Zaky^[22], p. 188, Plate 3, Figure 1. •

Type locality and sample no.: North Gunna, Farafra Oasis, Egypt, sample 65 (Figures 3A, B).

Age: Thanetian.

Remarks: Anan^[23] introduced an evolutionary trend: The Middle Paleocene *Pyramidulina robinsoni* (Futyan) → Late Paleocene-Early Eocene *Pyramidulina leroyi* Anan^[24]. *Pyramidulina robinsoni*, so far, was recorded from Jordan, Egypt and Tanzania.

Genus *Tollmannia* Sellier de Civrieux & Dessauvagie,

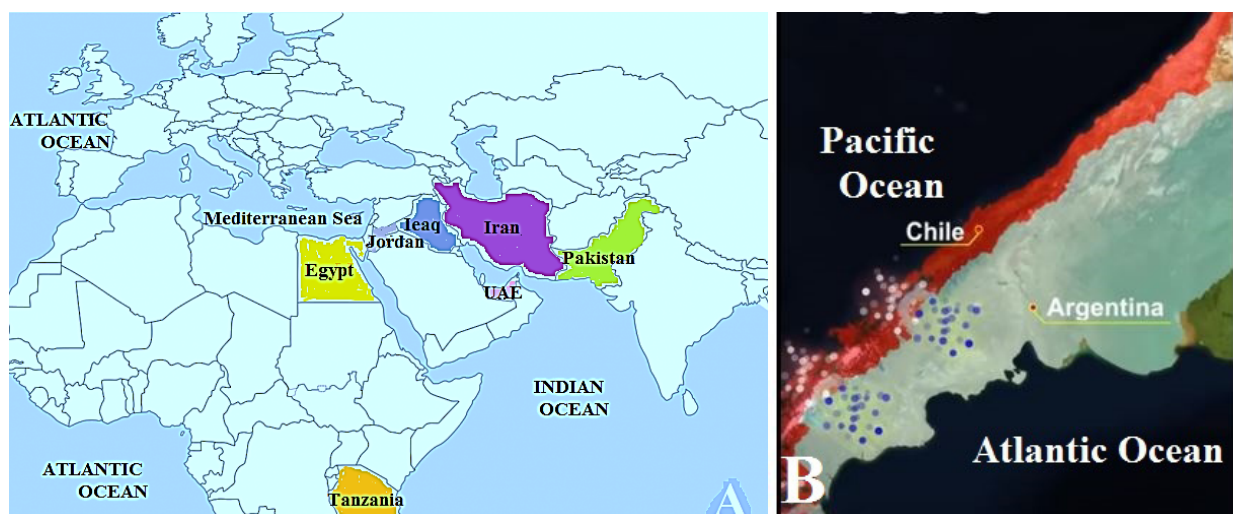


Figure 1. Location map of the Southern Tethys (A): Northeast Africa (Egypt), East Africa (Tanzania), Southeast Asia (Jordan, Iraq, UAE, Iran, Pakistan), and the southern Tethys (B): South America (Chile and Argentina).

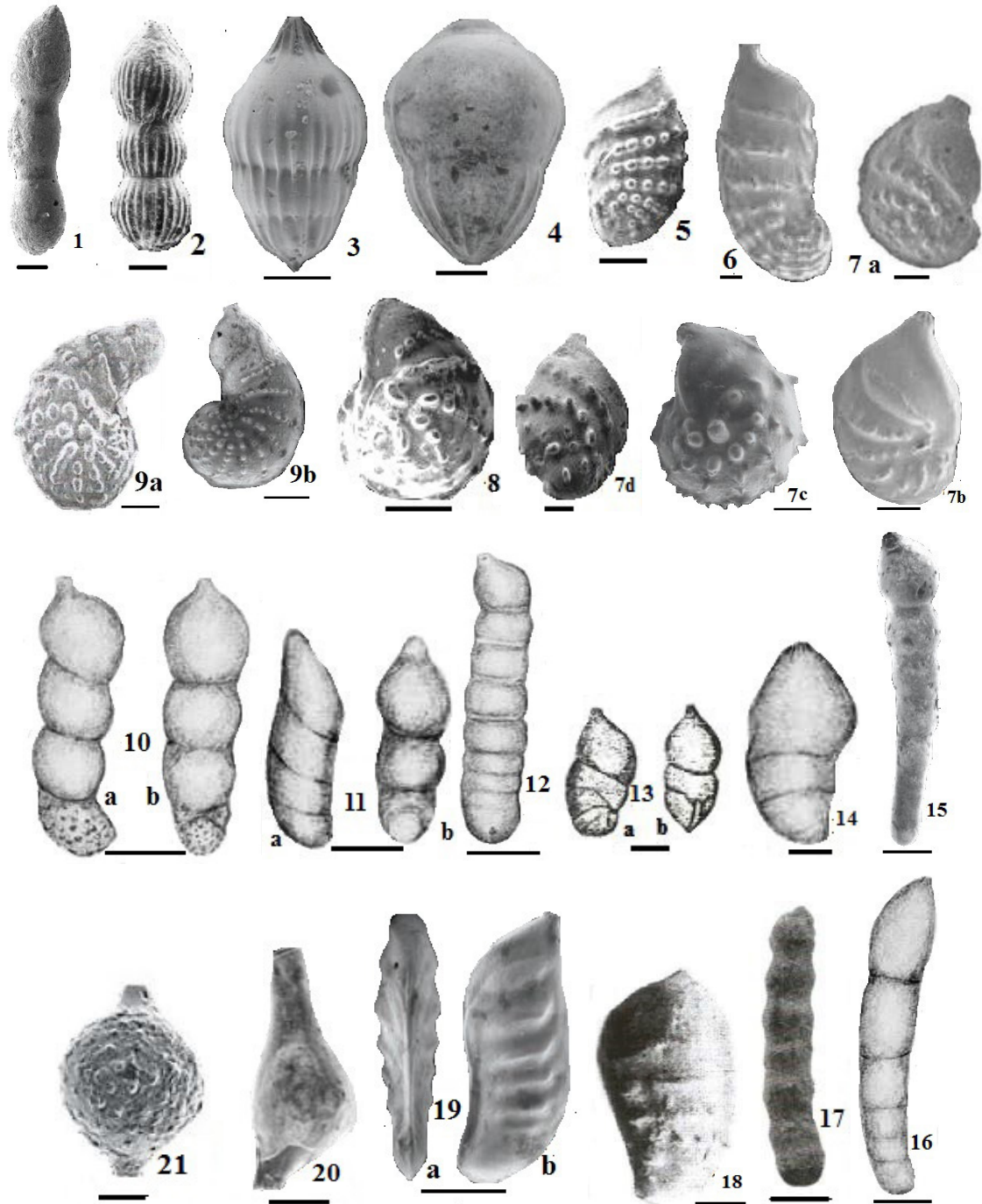


Plate 1. Figure 1. *Nodosaria catenula* (Reuss ^[3]), 2. *Pyramidulina robinsoni* (Futyan ^[4]), 3. *Tollmannia costata* (d'Orbigny ^[5]), 4. *Tollmannia fingeri* Anan, sp. nov., 5. *Percultazonaria fragaria* (Gümbel ^[6]), 6. *P. tuberculata* (Plummer ^[7]), 7a. *Lenticuzonaria argentinica* (Anan ^[8]), 7b. *Astacolus* sp.-Pearson et al. ^[9], 7c. *Percultazonaria* cf. *P. mamilligera* (Kar-rer)-Finger ^[1], 7d. *Marginulinopsis* sp.-Salahi ^[10], 8. *Lenticuzonaria misrensis* (Anan ^[8]), 9a,b. 9a. *Percultalina misrensis* (Anan ^[11]), 9b. *Percultazonaria vaughani* (Cushman)-Finger ^[1], 10a,b. *Hemirobulina comma* (Römer ^[12]), 10a. dorsal view, 10b. side view, 11a,b. *Hemirobulina curvatura* (Cushman ^[13]), 11a. dorsal view, 11b. side view, 12. *Hemirobulina humilis* (Reuss ^[14]), 13a,b. *Hemirobulina nammalensis* (Haque ^[15]), 13a. dorsal view, 13b. side view, 14. *Hemirobulina pachygaster* (Gümbel ^[16]), 15. *Vaginulinopsis argentinica* Anan, sp. nov., 16. *Vaginulinopsis deserti* (Said & Kenawy ^[17]), 17. *Vaginulinopsis emiratensis* (Anan ^[18]), 18. *Vaginulina boukharyi* (Anan ^[19]), 19a,b. *Vaginulina chilensis* Anan, sp. nov., 19a. side view, 19b. dorsal view, 20. *Ramulina shreiffae* Anan, sp. nov., 21. *R. pseudoaculata* (Olsson ^[20]). (Scale bars 100 µm)

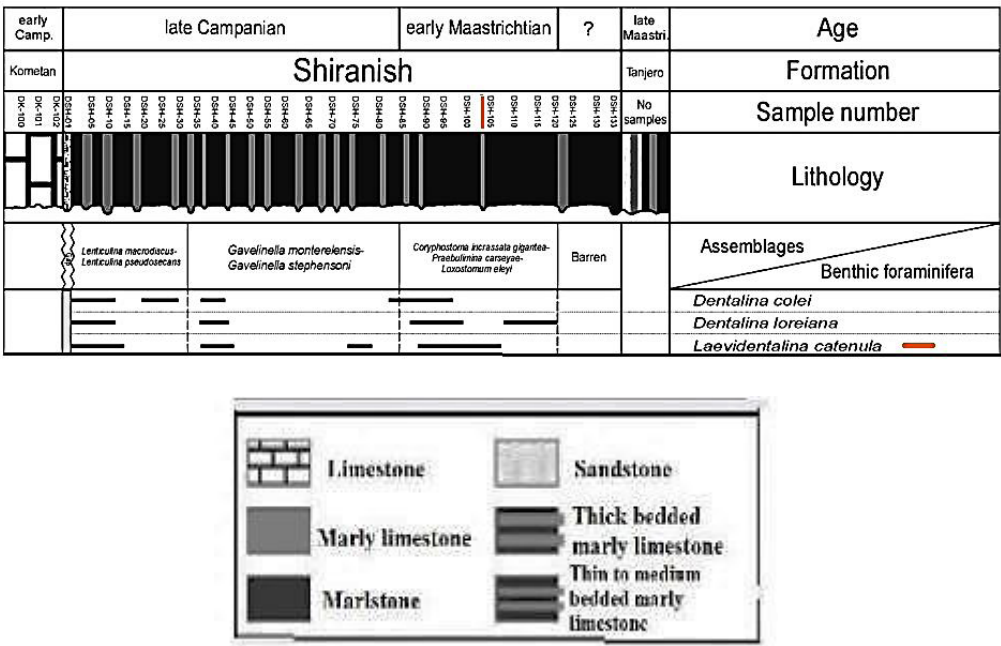


Figure 2. Stratigraphic log of the Dokan section, northeast Iraq, and the stratigraphic range of the *Nodosaria catenula* (Reuss) (after Jaff & Lawa [21]).

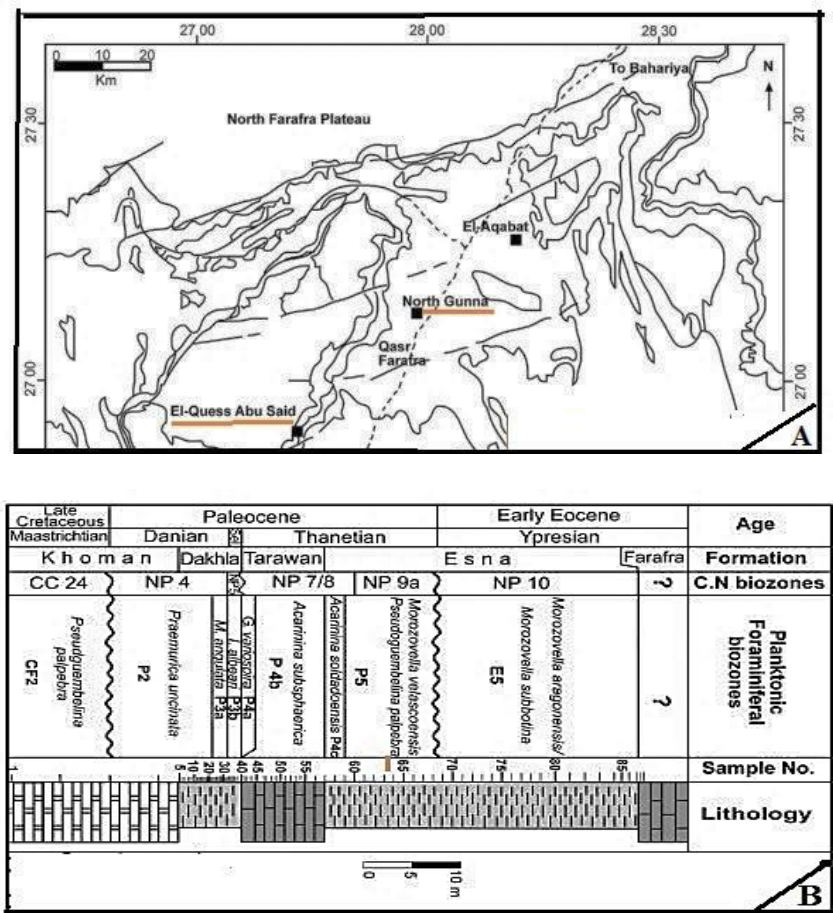


Figure 3. A. Location map of North Gunna and El-Guss Abu Said sections, Farafra Oasis, Egypt. B. Stratigraphy of North Gunna section, and the position of sample 65: Thanetian (after Orabi & Zaky [22]).

1965

Type species *Lingulina costata* subsp. *tricarinata* Tollmann, 1954 = *Lingulina costata* d'Orbigny.

***Tollmannia costata* (d'Orbigny, 1846)** (Plate 1, Figure 3)

2013 *Pseudonodosaria comatula* (Cushman)-Finger ^[1], p. 403, Plate 7, Figure 7.●

Type locality: Navidad Formation (in the vicinity of the name-bearing town located southwest of Capital Santiago), Central Chile, sample number and depositary: University of California Museum of Paleontology (UCMP50135), PPP (collected site in the Navidad Formation) (Figure 4).

Remarks: The test has fine to coarse longitudinal ribs, then an elongate test with a smooth surface. For that, the late Early Miocene Finger's specimen *P. comatula* is treated here to belong to *T. costata* (d'Orbigny ^[5]) (Table 1).

***Tollmannia fingeri* Anan, sp. nov.** (Plate 1, Figure 4)

2013 *Tollmannia costata* d'Orbigny-Finger ^[1], p. 404, Plate 7, Figure 11. ●

Holotype: Illustrated specimen in Plate 1, Figure 4.

Dimensions: Length 4.5 mm, width 3.2 mm.

Depositary: The University of California Museum of Paleontology (UCMP50135).

Etymology: After the micropaleontologist K.L. Finger, Univ. California Museum of Paleontology.

Type locality and sample: Navidad Formation, Central Chile, UCMP50135, PPP, PPT (Navidad area, Navidad Formation collecting sites) (Figure 5).

Stratigraphic level: Middle Miocene to Early Pliocene (Table 2).

Diagnosis: This new species is characterized by its fine to coarse surface longitudinal ribs, but die out distally in the last chamber, aperture terminal, slitlike, bordered by an elevated lip.

Remarks: *Tollmannia fingeri* Anan, sp. nov. differs

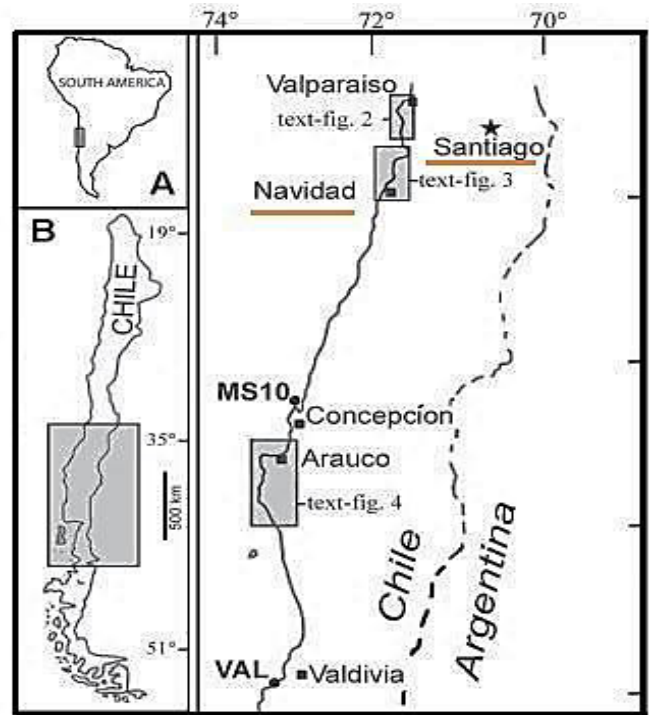


Figure 4. Location map of Navidad area, southwest the capital Santiago in central Chile (after Finger ^[1]).

from *T. costata* in its die out distally rib in the last chamber, and from *T. argentinica* Anan ^[25] in its shorter test, and without surface longitudinal ribs in the final globular chamber, than whole test. It is confined to Chile.

***Percultazonaria fragaria* (Gümbel, 1868)** (Plate 1, Figure 5)

1868 *Marginulina fragaria* Gümbel ^[6], p. 57, Plate 1, Figure 58.

2006 *Percultazonaria fragaria* (Gümbel)-Cimernan et al. ^[26], p. 24, Plate 5, Figures 4, 5.

2009 *Percultazonaria fragaria* (Gümbel)-Anan ^[27], p. 6,

Table 1. The stratigraphic range of *Tollmannia costata* in the Navidad Formation (Navidad area) and Ranquil Formation (Arauco area), Chile (VR = very rare, R = rare, F = frequent) (after Finger ^[1]).

Sector area	North												Central									
	Las Cruces		Navidad										Conc	Arauco						Vald		
Geologic unit	El Peral beds		Navidad Fm.												Ranquil Fm.						SDom	
Locality	NLP	LPER	MOS	RAP	PPP	PPT	PPN	LBZ	PTA	MAT	NAV5	MPUP	CPUP	MS10	FRA	FRM	ROT	ROK	RAN	MIB	LEB	VAL
<i>Pseudonodosaria aequalis</i>	VR				R	R											VR		R			
<i>Pseudonodosaria comatula</i> <div></div>			F		R	F			F		F		R		R		F					

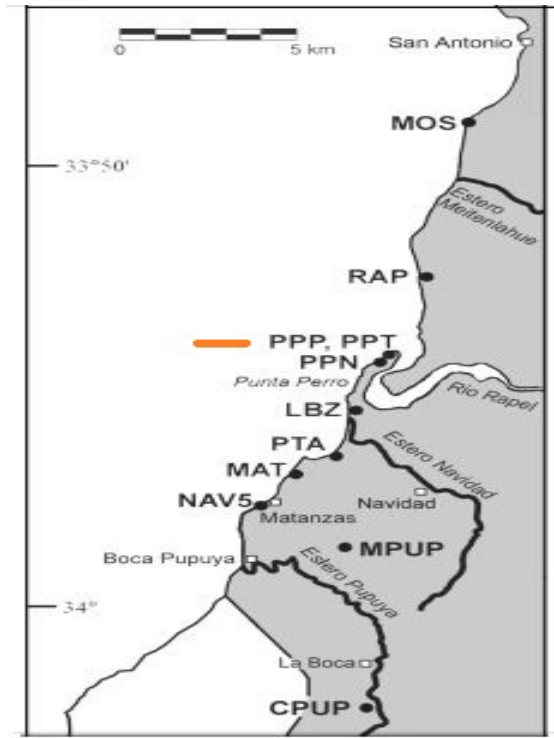


Figure 5. The sites of PPP and PPT in the Navidad Formation (Chile).

Plate 1, Figure 9.

2009 *Percultazonaria fragaria* (Gümbel)-Zlinská^[28], p. 306, Plate 1, Figure 2.

2013 *Percultazonaria fragaria* (Gümbel)-Valchev et al.^[29], p. 59, Plate 1, Figure 5.

2015 *Percultazonaria fragaria* (Gümbel)-Anan^[30], p. 21, Plate 1, Figure 9.

2016 *Lenticulina* sp.-VahdatiRad et al.^[31], p. 5 (of 13), Plate 2, Figure 8. ●

Type locality: Yaghol section, Khangiran formation, northeast of Iran (Figure 6).

Remarks: The Iranian specimen has closely characters with *P. fragaria*. It was recorded in France, Slovenia, Slovakia, Bulgaria, Egypt, UAE and Iran.

***Percultazonaria tuberculata* (Plummer, 1927)** (Plate 1, Figure 6)

1927 *Cristellaria subaculeata* var. *tuberculata* Plummer^[7], p. 101, Plate 7, Figure 2, Plate 14, Figure 1.

2004 *Vaginulinopsis waiparaensis* (Finlay)-Pearson et al.^[32], p. 40, Plate 5, Figure 8. ●

2021 *Marginulinopsis* sp. Salahi^[10], p. 316, Plate 5, Figures 31, 32.

Type locality: Tanzania Drilling Project (TPD 1, 2), and stratigraphic log of TDP2 (Figure 7).

Remarks: The Tanzanian specimen belongs here to the genus *Percultazonaria*, due to its rows of distinct beadlike tubercles best developed on the coiled portion of the test and giving place to more ridge-like elevations between later chambers with protruding radiate aperture.

***Lenticuzonaria argentinica* Anan, 2023** (Plate 1, Figures 7a-d)

2004 *Astacolus* sp.-Pearson et al.^[32], p. 40, Plate 5, Figure 9. ●

2013 *Percultazonaria* cf. *P. mamilligera* (Karrer)-Finger^[1], p. 412, Plate 9, Figure 8., UCMP 50169. ●

2021 *Marginulinopsis* sp.-Salahi^[10], p. 316, Plate 5, Figure 33. ●

2023 *Lenticuzonaria argentinica* Anan^[25], p. 37, Plate 1, Figure 9. ●

Type locality and sample of *L. argentinica*: Formación Punta Torcida, AV-5, SEGEMAR 2860 (Ypresian), (Figure 8).

Remarks: The specimens of Tanzania, Chile, Iraq have closely related to *L. argentinica* Anan^[25].

***Lenticuzonaria misrensis* Anan, 2021** (Plate 1, Figure 8)

2022 *Lenticulina tuberculata* (Plummer)-Farouk et al.^[34], p. 32, Figures 12, 14. ●

Type locality: Gharb El-Mawhob section, Dakhla Oasis (26°01'02" N, 28°13'18" E; Western Desert, Egypt) sample no. 255 (Figures 9a-c).

Remarks: The specimen of Farouk et al.^[34] has identical characteristics with the *Lenticuzonaria* Anan^[8].

***Percultalina misrensis* Anan, 2022** (Plate 1, Figure 9)

2012 *Marginulinopsis tuberculata* (Plummer)-Youssef & Taha^[35], p. 4289, Plate 2, Figure 18.

Table 2. The stratigraphic distribution of *Tollmannia fingeri* n. sp. in the Navidad Formation, Chile (VR = very rare, R = rare), (after Finger^[1]).

Sector area	North													
	Las Cruces				Navidad									
Geologic unit	EI Peral beds				Navidad Fm.									
Locality	NLP	LPER	MOS	RAP	PPP	PPT	PPN	LBZ	PTA	MAT	NAV5	MPUP	CPUP	
<i>Tollmannia costata</i>					R	VR								

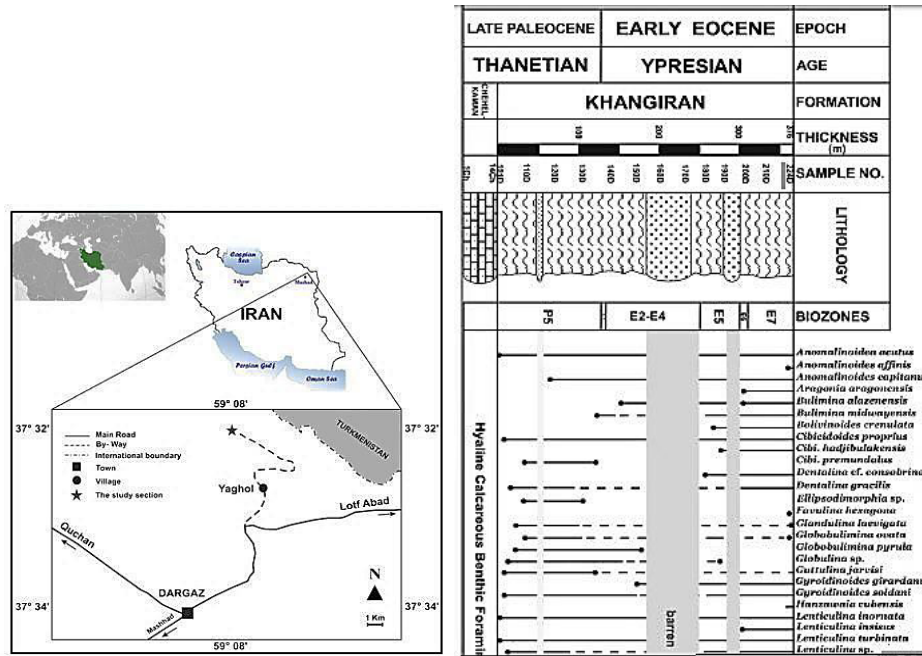


Figure 6. Location of the Yaghol section, sample location 224D (Ypresian) in the stratigraphic log of Yaghol section, North of Iran (after VahdatiRad et al. ^[31]).

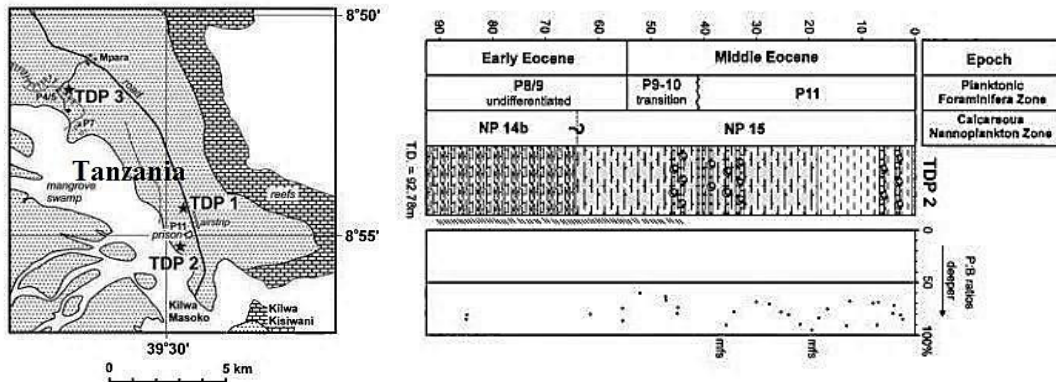


Figure 7. Location map of TPD 1, 2, and stratigraphic log of Early-Middle Eocene of Tanzania, East Africa (after Pearson et al. ^[32]).

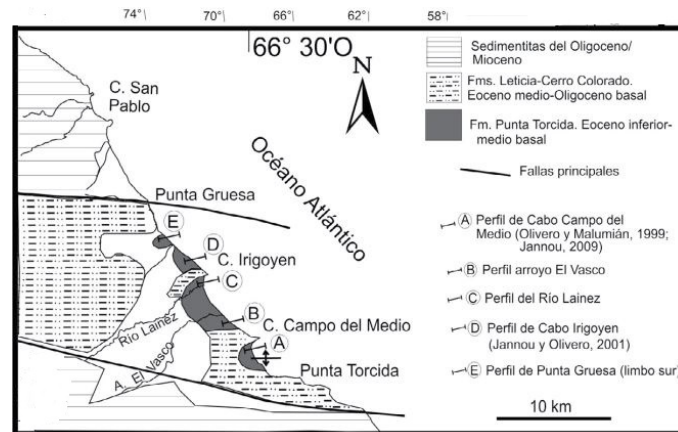


Figure 8. Geological map of de la Isla Grande de Tierra del Fuego (South Argentina), including the stratigraphy of the Punta Torcida Formation (after Jannou et al. ^[33]).

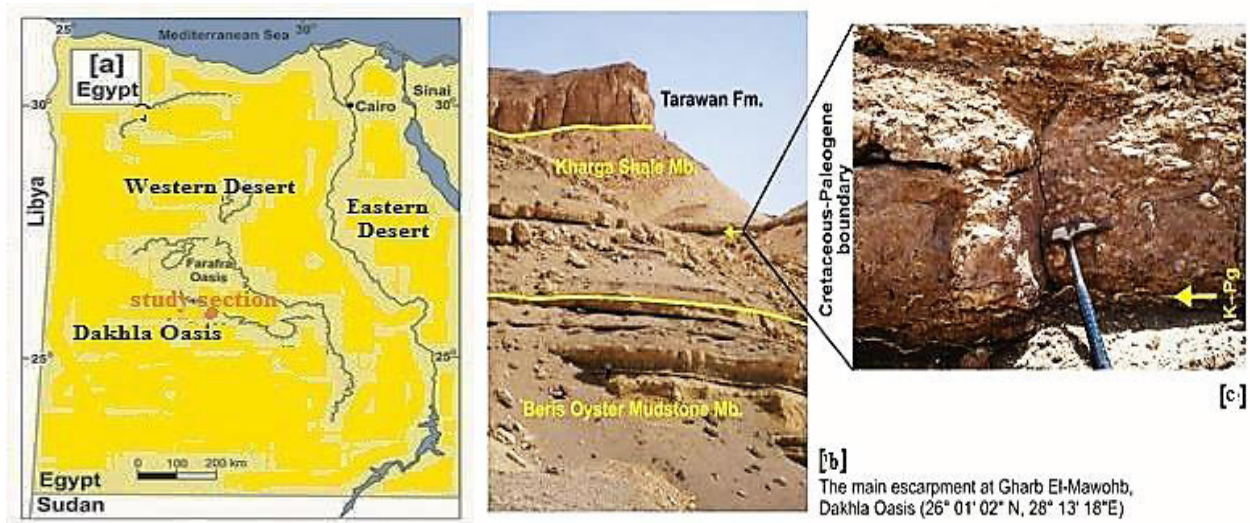


Figure 9. a) Location map of the Gharb El-Mawhob section, Dakhla Oasis, Western Desert of Egypt, b) stratigraphic log of the study section, c) the K/P boundary of the study section (after Farouk et al. ^[34]).

2013 *Percultazonaria vauhani* (Cushman)-Finger ^[1], p. 412, Plate 9, Figure 10.●

2015 *Marginulinopsis tuberculata* (Plummer)-Orabi & Hassan ^[36], Plate 1, Figure 13.

2022 *Percultalina misrensis* Anan ^[11], p. 32, Plate 1, Figure 2.

Type locality and depositary: Navidad Formation (North Chile), PPP, PPT, MPUP sites, UCMP 50171 (Figure 10).

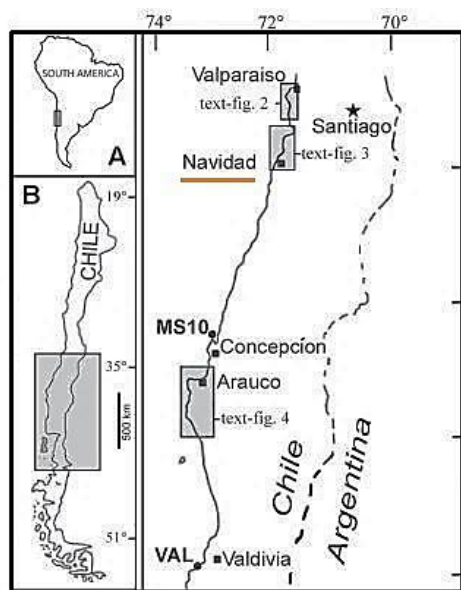


Figure 10. Location map of the Navidad section, Central Chile.

Stratigraphic range of Finger's specimen: Navidad Formation (VR = very rare, R = rare, C = common) (Table 3).

Remarks: The figured specimens of Finger ^[1], Youssef & Taha ^[35] and Orabi & Hassan ^[36] have closed characters

with *Percultalina misrensis* Anan ^[11]. This species was recorded in Egypt and Chile.

Genus *Hemirobulina* Stache, 1864

***Hemirobulina comma* (Roemer, 1841)** (Plate 1, Figure 10)

1841 *Marginulina comma* Römer ^[12], Plate 47, Figure 9.

1956 *Marginulinopsis comma* (Römer)-Said & Kenawy ^[17], p. 132, Plate 2, Figure 19.●

Type locality and stratigraphic log of Nekhl section, North Sinai, Egypt (Figure 11),

Stratigraphic level and sample no. of the species: Figure 12.

Remarks: The genus *Hemirobulina* differs from *Marginulina* in having a smooth rather than longitudinally costate wall, It also differs mainly from *Marginulinopsis* in slightly curved early chambers than close coiled and planispiral, and lacking ribbed ornamentation on the uniserial stage. *Hemirobulina comma* was recorded from the Maestrichtian of Germany, and later from Nekhl section, Sinai of Egypt.

***Hemirobulina curvatura* (Cushman, 1938)** (Plate 1, Figure 11)

1938 *Marginulina curvatura* Cushman ^[13], p. 34, Plate 5, Figures 13-14.


1956 *Marginulina curvatura* Cushman-Said & Kenawy ^[17], p. 132, Plate 2, Figure 20.●

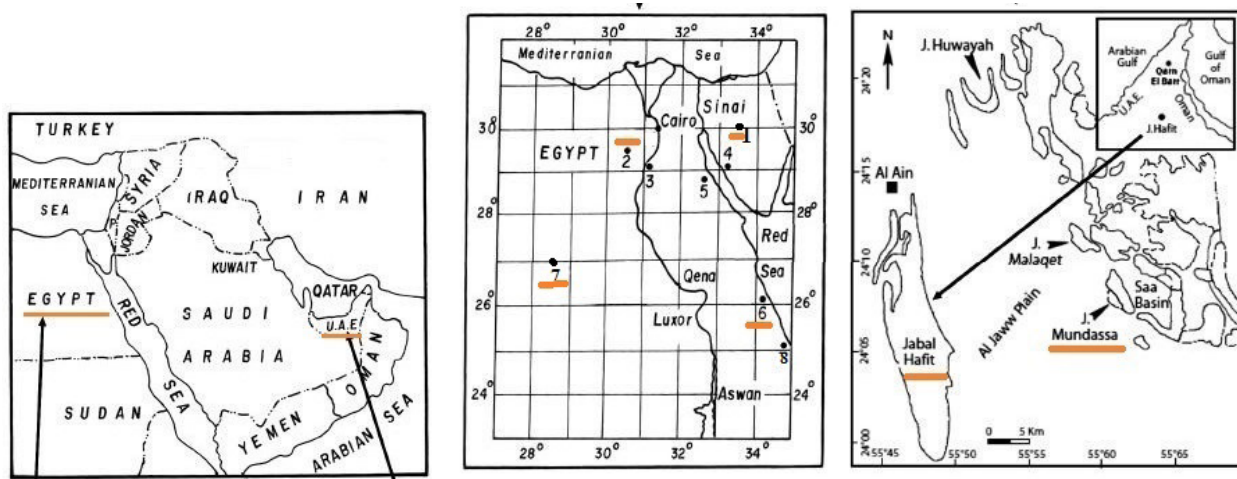
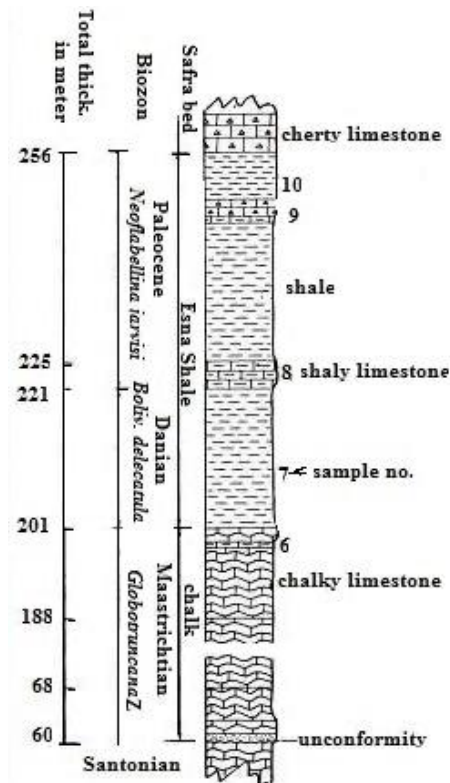
2003 *Marginulina curvatura* Cushman-Abdelghany ^[38], p. 394, Figure 3.

Type locality, Giddi section (no. 1), North Sinai, Egypt (see Figure 12).

Stratigraphic level and sample no.: Early Eocene, sample no. 859 (Figure 13).

Table 3: The stratigraphic ranges of the *Percultazonaria vaughani* of Finger (= *Percultalina misrensis* Anan) (after Figure ^[1]).

Sector area	North													
	Las Cruces		Navidad											
Geologic unit	EI Peral beds		Navidad Fm.											
Locality	NLP	LPER	MOS	RAP	PPP	PPT	PPN	LBZ	PTA	MAT	NAV5	MPUP	CPUP	
<i>Percultazonaria vaughani</i> 	VR				R				R			C		


Figure 11. The location map of some studied sections in Egypt (no. 1. Nekhl and Giddi sections in North Sinai, 2, Fayum area), 7 Maqfi section; and UAE (Jabal Hafit and J. Mundassa) (after Anan ^[37]).

Figure 12. Stratigraphic log of Nekhl section, North Sinai, stratigraphic level and sample no. 6 of the Maastrichtian *Hemirobulina comma* (after Said & Kenawy ^[17]).

Remarks: The figured specimens of Said & Kenawy^[17] and Abdelghany^[38] are closely related to the genus *Hemirobulina*. It was recorded from USA, and also Giddi section (Sinai of Egypt) and Qarn El Barr section (UAE).

***Hemirobulina humilis* (Reuss, 1863)** (Plate 1, Figure 12)

1863 *Cristellaria* (*Cristellaria*) *humilis* Reuss^[14], p. 65, Plate 6, Figures 16, 17.

1946 *Marginulina humilis* (Reuss)-Cushman^[39], p. 63, Plate 22, Figure 17.

1956 *Marginulina humilis* (Reuss)-Said & Kenawy^[17], p. 130, Plate 2, Figure 18. ●

Type locality and sample no.: Paleocene of Nekhl section (sample 7) and Giddi section (sample no. 834), North Sinai of Egypt (Figures 12, 13).

Remarks: The figured specimens of Cushman^[39] and Said & Kenawy^[17] are closely related to the genus *Hemirobulina*. It was recorded in the Cretaceous of Eu-

rope, USA and Mexico, while it was recorded from the Maastrichtian and Paleocene of Sinai of Egypt (Said & Kenawy^[17]).

***Hemirobulina nammalensis* (Haque, 1956)** (Plate 1, Figure 13)

1956 *Marginulina glabra* d'Orbigny var. *nammalensis* Haque^[15], p.74, Plate11, Figures 1-4. ●

2005 *Vaginulinopsis nammalensis* (Haque)-Sztrákos^[40], p. 186, Plate 14, Figure 28.

Type locality: Nammal Formation, Nammal Gorge area, Pakistan (Figure 14).

Remarks: *Hemirobulina* differs from *Vaginulinopsis* in the rounded cross section and curved but not distinctly enrolled early stage. It differs from *Marginulina* in having a smooth rather than longitudinally costate wall. For that, the figured specimens of Haque^[15] and Sztrákos^[40] belong to the genus *Hemirobulina*. *Hemirobulina nammalensis* was recorded from Pakistan (Southern Tethys), and France

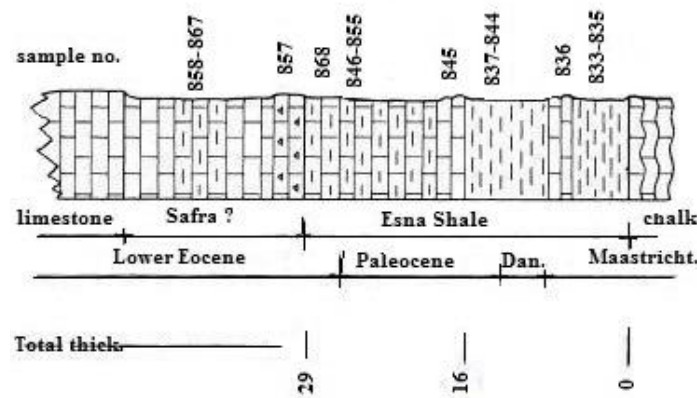


Figure 13. Stratigraphic log of Giddi section, North Sinai, Egypt (after Said & Kenawy^[17]).

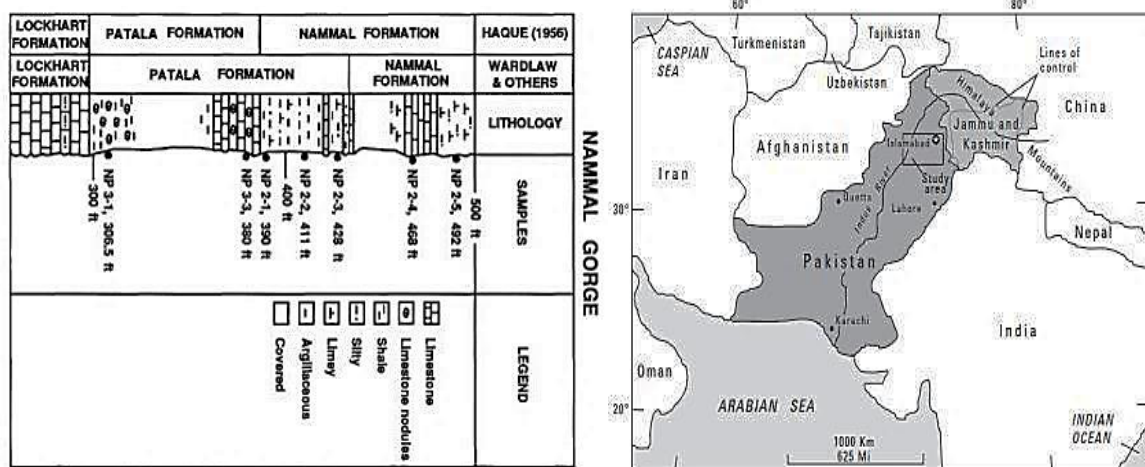


Figure 14. Lithostratigraphic section and location of Nammal Gorge at Nammal Dam: Patala and Nammal Formations of the Nammal Gorge, Salt and Sor Ranges of Pakistan (Gibson^[41]).

(Northern Tethys).

***Hemirobulina pachygaster* Gumbel, 1870** (Plate 1, Figure 14)

1870 *Marginulina pachygaster* Gumbel ^[16], 1868 (1870), p. 632, Plate 1, Figure 60.

1953 *Marginulina pachygaster* Gumbel-LeRoy ^[42], p. 38, Plate 8, Figure 11.

1956 *Marginulina pachygaster* Gumbel-Said & Kenawy ^[17], p. 132, Plate 2, Figure 21.●

Stratigraphic level and sample no.: Maastrichtian, Nekhl section, sample no. 6 (see Figures 12, 13).

Remarks: As noted before, *Hemirobulina* differs from *Marginulina* in having a smooth rather than longitudinally costate wall. For that, the Egyptian specimens belong to the genus *Hemirobulina*. It was originally described from the Eocene of Germany, Early Eocene in Maqfi section, Western Desert of Egypt (LeRoy ^[42]), and Maastrichtian in Sinai of Egypt (Said & Kenawy ^[17]).

Genus *Vaginulinopsis* Silvestri, 1904

***Vaginulinopsis argentinica* Anan, sp. nov.** (Plate 1, Figure 15)

2022 *Laevidentalina* sp. Jannou et al. ^[33], p. 21, Plate 2, Figure 5.●

Holotype: Illustrated specimen in Plate 1, Figure 15.

Diameter of the holotype: Length 0.62 mm, width 0.11 mm.

Depository: The Survey of Geology and Mineralogy of Argentina (SEGEMAR2849).

Etymology: After the State of Argentina.

Type locality and sample: Formación Punta Torcida, CI-20, SEGEMAR 2849, CM-145 (see Figure 8).

Stratigraphic level: Ypresian.

Diagnosis: This Early Eocene species has an elongate test and circular in section, early-stage planispirally enrolled and involute, the later stage includes numerous semi globular chambers added in a slight curve, sutures nearly horizontal, flush in the early stage, but depressed in the final three chambers, wall calcareous, hyaline, perforate radial, surface smooth and unornamented, aperture terminal at the dorsal angle, and produced on a neck.

Remarks: The genus *Vaginulinopsis* has a planispirally enrolled and involute early stage, which does not exist in the genus *Laevidentalina*. The *V. argentinica* Anan ^[12] is lacking an apiculate pro-loculus, which is characterized the genus *Laevidentalina*.

***Vaginulinopsis deserti* (Said & Kenawy, 1956)** (Plate 1, Figure 16)

1956 *Marginulinopsis deserti* Said & Kenawy ^[4], p. 132, Plate 2, Figure 23.

Remarks: This species Lacks the longitudinal ribs along the test surface as genus *Marginulinopsis*. It is

recognizable by its slender test and slightly inflated and elongated chambers. it was recorded from Maastrichtian, Nekhl section (Egypt), sample no. 6 (see Figures 12, 13).

***Vaginulinopsis emiratensis* (Anan, 1993)** (Plate 1, Figure 17)

1993 *Marginulinopsis emiratensis* Anan ^[18], p. 657, Plate 2, Figure 12.

Type locality: Qarn El Barr section, Al Dhayd area, no. 1 (about 80 km north of J. Hafit, no. 2), UAE (*Abathomphalus mayaroensis* Zone). (Figure 15)

Remarks: This Late Maastrichtian specimen belongs to the genus *Vaginulinopsis*. *V. emiratensis* was described from Qarn El Barr section, Al Dhayd area (about 80 km north of J. Hafit), UAE.

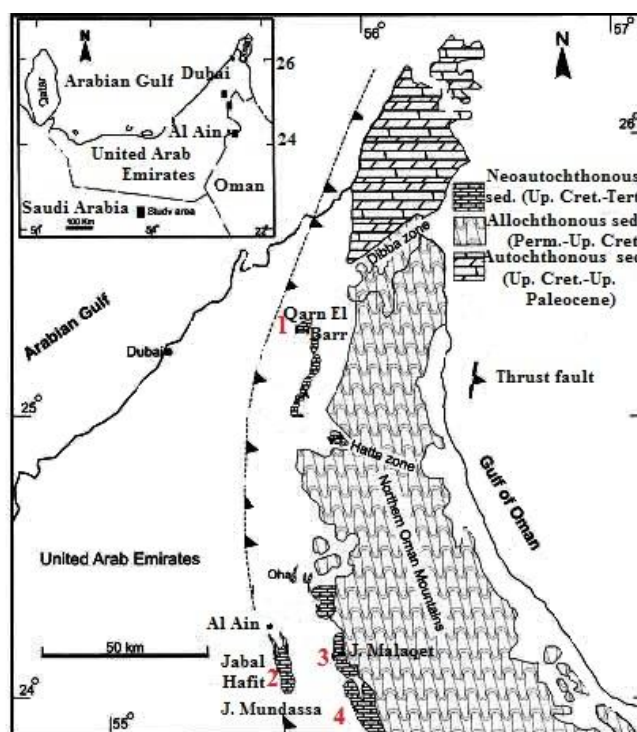


Figure 15. Location map of Qarn El Barr section (no.1) North UAE (after Abdelghany ^[38]).

Genus *Vaginulina* d'Orbigny, 1826

***Vaginulina boukharyi* (Anan, 2010)** (Plate 1, Figure 18)

2010 *Vaginulinopsis boukharyi* Anan ^[19], p. 30, Plate 1, Figure 12.

Type locality: Duwi section, Tarawan Chalk, Red Sea coast, Egypt (see Figure 12).

Remarks: This Paleocene species belongs here to the genus *Vaginulina* d'Orbigny ^[43] due to its thick raised sutures, then slightly depressed sutures in *Vaginulinopsis* Silvestri ^[44]. It is originally recorded from Duwi section, Egypt (Figure 16).

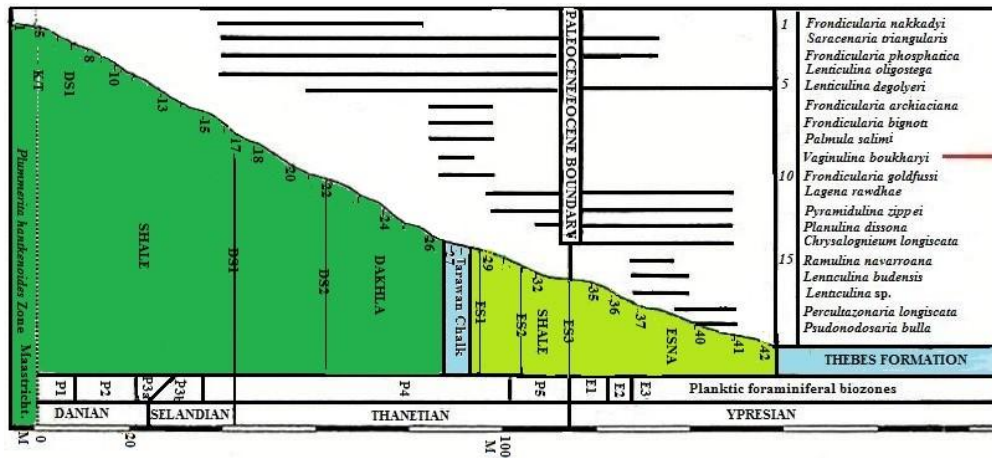


Figure 16. Stratigraphic log of Duwi section, including the stratigraphic range of the Thanetian *V. boukharyi* (after Anan^[45]).

Vaginulina chilensis Anan, sp. nov. (Plate 1, Figure 19)

2013 *Astacolus mexicanus* (Nuttall)-Finger^[1], p. 415, Plate 9, Figure 19.

Holotype: Illustrated specimen in Plate 1, Figure 19.

Diameter of the holotype: Length 0.55 mm, width 0.32 mm.

Depository: The University of California Museum of Paleontology (UCMP).

Etymology: After the State of Chile.

Type locality: Navidad Fm. (site CPUP), Ranquil Fm. (sites FRA, FRM), (Figure 17).

Stratigraphic level: Early Oligocene to Early Miocene (Table 4).

Diagnosis: This species has an elongate uniserial rectilinear laterally compressed test, septa horizontal to slightly oblique thickened and elevated, wall calcareous perforate, surface smooth, aperture radiate at the dorsal angle, and slightly produced.

Remarks: This new species differs from *V. boukharyi* Anan^[19] in its longer test, lesser and acuter width, with keel, and more elevated thick sutures.

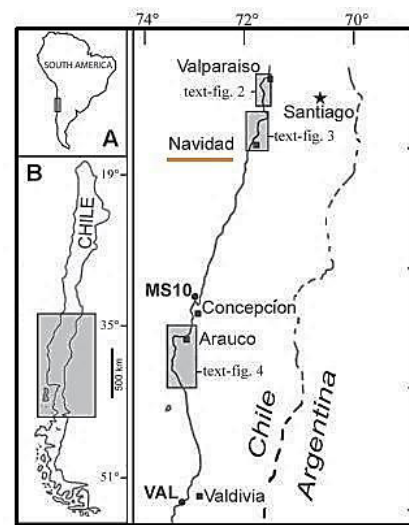


Figure 17. Location map of the Navidad section, Central Chile.

Genus *Ramulina* Jones, 1875

Ramulina shreifae sp. nov. (Plate 1, Figure 20)

2023 *Ramulina pseudoaculata* (Olsson)-Shreif et al.^[46], p. 115, Plate 6, Figure 8.

Table 4. Stratigraphic range of *Vaginulina chilensis* in both Navidad and Ranquil Formations, North and Central Chile (after Finger^[1]).

Sector area	North												Central									
	Las Cruces		Navidad										Conc	Arauco							Vald	
Geologic unit	EI Peral beds		Navidad Fm.												Ranquil Fm.							SDom
Locality	NLP	LPER	MOS	RAP	PPP	PPT	PPN	LBZ	PTA	MAT	NAV5	MPUP	CPUP	MS10	FRA	FRM	RQT	RQK	RAN	MIB	LEB	VAL
<i>Astacolus mexicanus</i> <div></div>													VR		R	F						

Holotype: Illustrated specimen in Plate 1, Figure 20.

Diameter of the holotype: Length 0.42 mm, width 0.18 mm.

Depository: Faculty of Education, Dept. Biological and Geological Sciences, Ain Shams Univ., Egypt.

Etymology: After the micropaleontologist Abeer Shreif, Ain Shams University, Faculty of Education, Department of Biological and Geological Sciences, Cairo, 11341, Egypt.

Type locality and sample no.: El Guss Abu Said, Western Desert, Egypt, samples 1, 2 (common), (after Shreif et al. ^[46]).

Stratigraphic level: Ypresian (E3, *Morozovella marginodentata* Zone), Figure 18.

Diagnosis: This Early Eocene species is characterized by its ovoid smooth test, with only two not concentric ends arms of the chamber.

Remarks: This new species differs from *R. pseudoaculata* (Olsson ^[20]) in having a smooth surface and not concentric two ends arms of the chamber, then ornamented surface and concentric two arms.

4. Paleogeography

The twenty identified species have wide geographic distribution in nine localities in the Southern Tethys: Chile (South Pacific), Argentina (South Atlantic), Egypt, Tanzania (Northeast Africa), Jordan, Iraq, UAE, Iran and Pakistan (Southwest Asia) (see Figure 1). The paleogeographic maps recorded by many authors ^[47-50] show the Tethyan realm had been connected with the Atlantic Ocean from the west to the Indo-Pacific Ocean to the east, via the Mediterranean Sea, crossing the Middle East region during the Paleogene time (Table 5).

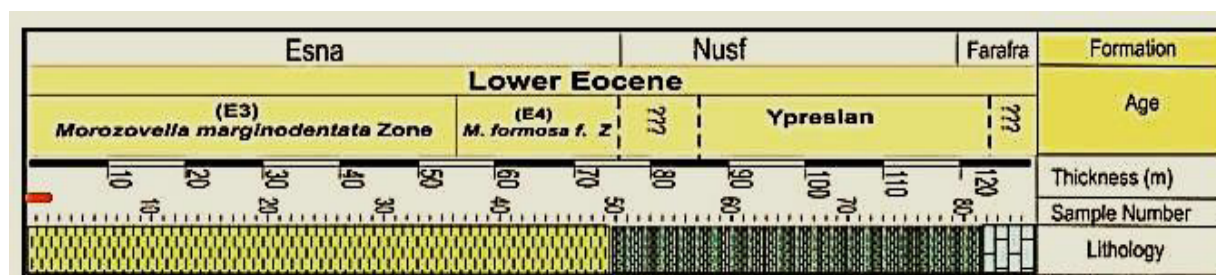


Figure 18. Stratigraphic log of El Guss Abu Said section, Farafra Oasis, Western Desert, Egypt, and the stratigraphic range of the new species *Ramulina shreifae*, samples (1, 2) (after Shreif et al. ^[46]).

Table 5. Paleogeographic distribution of the Early Eocene twenty Lagenid and Rotaliid benthic foraminiferal species in the different locations in the Southern Tethys, particularly the sp. nov. in this study: 1. Chile (*Tollmannia fingeri*, *Vaginulina chilensis*), 2. Argentina (*Vaginulinopsis argentinica*), 3. Egypt (*Ramulina shreifae*), 4. Tanzania, 5. Jordan, 6. Iraq, 7. UAE, 8. Iran, 9. Pakistan.

Sp. No.	species	countries	1	2	3	4	5	6	7	8	9
1	<i>Nodosaria</i>	<i>catenula</i>	-	-	x	-	-	●	-	-	-
2	<i>Pyramidulina</i>	<i>robinsoni</i>	-	-	x	x	●	-	-	-	-
3	<i>Tollmannia</i>	<i>costata</i>	●	-	-	-	-	-	-	-	-
4		<i>fingeri</i>	●	-	-	-	-	-	-	-	-
5	<i>Percultazonaria</i>	<i>fragaria</i>	-	-	x	-	-	-	x	●	-
6		<i>tuberculata</i>	-	-	x	●	-	-	-	x	x
7	<i>Lenticuzonaria</i>	<i>argentinica</i>	x	●	-	-	-	-	-	x	-
8		<i>misrensis</i>	-	-	●	x	-	-	-	-	-
9	<i>Percultalina</i>	<i>misrensis</i>	x	-	●	-	-	-	-	-	-
10	<i>Hemirobulina</i>	<i>comma</i>	-	-	●	-	-	-	-	-	-
11		<i>curvatura</i>	-	-	●	-	-	-	x	-	-
12		<i>humilis</i>	-	-	●	-	-	-	-	-	-
13		<i>nammalensis</i>	-	-	-	-	-	-	-	-	●
14		<i>pachygaster</i>	-	-	●	-	-	-	x	-	-
15	<i>Vaginulinopsis</i>	<i>argentinica</i>	-	●	-	-	-	-	-	-	-
16		<i>deserti</i>	-	-	●	-	-	-	-	-	-
17		<i>emiratensis</i>	-	-	x	-	-	-	●	-	-
18	<i>Vaginulina</i>	<i>boukharyi</i>	-	-	●	-	-	-	-	-	-
19		<i>chilensis</i>	●	-	-	-	-	-	-	-	-
20	<i>Ramulina</i>	<i>shreifae</i>	-	-	●	-	-	-	-	-	-

Note: ● = illustrated, x = recorded, - = not recorded.

5. Paleoecology and Paleoenvironment

Finger ^[1] noted that the presence of Neogene cosmopolitan deep-water benthic foraminifera in all of the assemblages supports the hypothesis that deep water masses derived from the Antarctic Circumpolar Current have enabled many Neogene deep-water foraminifera to disperse widely in the global ocean (Figure 19).

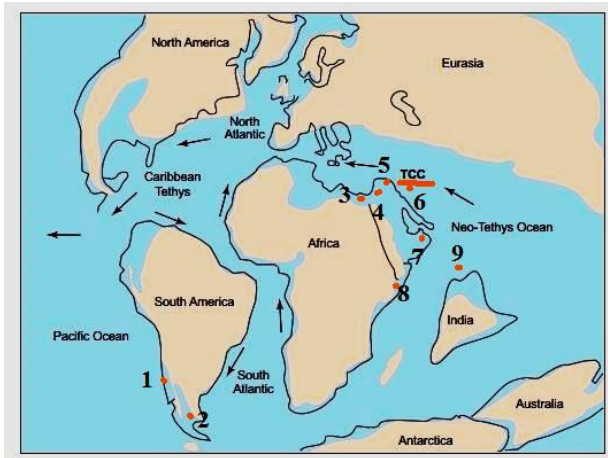


Figure 19. Paleogeography of the Neo-Tethys Ocean during the Maastrichtian showing the flow direction of the Tethyan Circumglobal Current (TCC) from east to west in the Southern Tethys (after Abed ^[51]); 1. Chile, 2. Argentina, 3. Egypt, 4. Jordan, 5. Iraq, 6. Iran, 7. UAE, 8. Tanzania, 9. Pakistan.

Jannou et al. ^[33] noted that the paleoenvironment of South Argentina would have been a shelf sea of normal salinity. LeRoy ^[42] noted that in certain respects the microfauna of the Esna Shale of Maqfi section (Figure 11, no. 7) exhibits an affinity with the Midway Type Fauna (MTF) of the American Gulf Coastal area, middle-outer neritic environment (50-200 m). Said & Kenawy ^[17] described and recorded more than twenty hundred benthic foraminiferal species from the Maastrichtian-Early Eocene strata of the two sections (Nekhl and Giddi) in northern Sinai, Egypt, and noted that these taxa showed an affinity with Midway faunas of American Gulf Coastal Plain, which indicate similarity with fauna of Trinidad and Tampico Embayment of Mexico. Anan ^[30] noted that the probable environment of northern Egypt is outer neritic-upper bathyal, while deeper in central Egypt, are deposited in the middle-outer neritic. Shreif et al. ^[46] noted that the abrupt decrease in the P/B ratio at the top of the Esna Formation and the erosional surface at the top of the Esna Formation indicate progressive or stepwise shallowing of the shelf through the succession of El Guss Abu Said, Western Desert, Egypt, and during the late Paleocene-Early Eocene. Berggren & Aubert ^[52] considered the Lower Tertiary

fauna of the Maqfi section, Western Desert of Egypt, and the northern part of Sinai Peninsula to be predominantly related to the “Midway-type fauna, MTF”, middle-outer neritic environment (50-200 m). Futyan ^[4] noted that the Jordanian faunal assemblage is predominantly considered here to be related to MTF (middle-upper neritic environment, 100-200 m). VahdatiRad et al. ^[31] noted that the changes in the relative abundance percentage of planktonic foraminiferal species in Yaghol section, Khangiran formation, northeast of Iran indicate the warm seawater and nearly oligotrophic condition in the late Paleocene-Early Eocene. Salahi ^[10] noted that the diverse benthic assemblages in the Kopet-Dag (KD) in northern Iran indicate a deeper environment in comparison with Late Paleocene fauna (middle-outer neritic based on the presence of Midway-type fauna, MTF), while a deep paleowater environment is evidenced by a high proportion of lenticulinids (= *Percultazonaria fragaria*) (Figure 20).

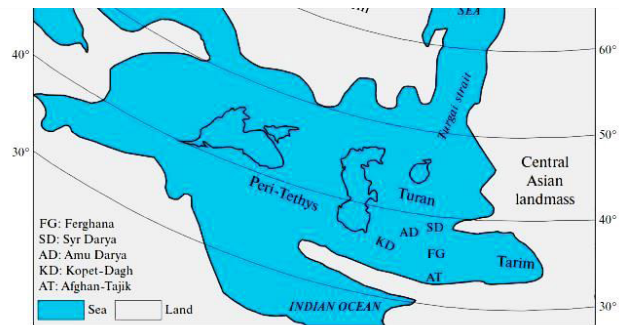


Figure 20. Peri-Tethys basin, includes Kopet-Dag area, KD (NE Iran) during the Early Paleogene (after Salahi ^[10]).

6. Conclusions

The modern taxonomical consideration is used for twenty Lagenid benthic foraminiferal species from nine countries in the Southern Tethys: Chile, Argentina, Egypt, Tanzania, Jordan, Iraq, United Arab Emirates (UAE), Iran and Pakistan. These species are: *Nodosaria catenula*, *Pyramidulina robinsoni*, *Tollmannia costata*, *Tollmannia fingeri*, *Percultazonaria fragaria*, *Percultazonaria tuberculata*, *Lenticuzonaria argentinica*, *Lenticuzonaria misrensis*, *Percultalina misrensis*, *Hemirobulina comma*, *Hemirobulina curvatura*, *Hemirobulina nammalensis*, *Hemirobulina humilis*, *Hemirobulina pachygaster*, *Vaginulinopsis argentinica*, *Vaginulinopsis emiratensis*, *Vaginulinopsis deserti*, *Vaginulina boukharyi*, *Vaginulina chilensis* and *Ramulina shreifae*. Nine species of these assemblage were recorded from Egypt (about 45%): *Lenticuzonaria misrensis*, *Percultalina misrensis*, *Hemirobulina comma*, *Hemirobulina curvatura*, *Hemirobulina humilis*, *Hemirobulina pachygaster*, *Vaginulinopsis deserti*, *Vagi-*

nulina boukharyi, *Ramulina shreiffae*; 3 species from Chile (about 15%): *Tollmannia costata*, *Tollmannia fingeri*, *Percultalina misrensis*; 2 from Argentina (about 10%): *Lenticuzonaria argentinica*, *Vaginulinopsis argentinica*; and one species (about 5%) from each of Tanzania: *Percultazonaria tuberculata*, Jordan: *Pyramidulina robinsoni*, Iraq: *Nodosaria catenula*, UAE: *Vaginulinopsis emiratenensis*, Iran: *Percultazonaria fragaria*, and Pakistan: *Hemirobulina nammalensis*. Four species are believed here to be new: *Tollmannia fingeri*, *Vaginulinopsis argentinica*, *Vaginulina chilensis* and *Ramulina shreiffae*. The identified species are marine fauna which indicates a middle neritic-deep paleowater environment. The identified species have wide geographic distribution in the Tethys, due to open and extended realms of the Tethys, which have extended from the Indo-Pacific to the Atlantic Oceans and Mediterranean Sea during the Late Cretaceous to Early Neogene times, and the fauna exhibit pronounced similarities. The unclosed number of the members of Lagenids in the study area may be due to a lack of available literature, different latitudes, differences in paleoenvironmental conditions (depth, temperature, salinity, dissolved oxygen, nutrient, land barriers, etc.) or misidentification.

Funding

This research received no external funding or internal funding.

Acknowledgement

The author would like to express his sincere appreciation to the editor of EPS and the unknown reviewers for their valuable comments. I am also indebted to my daughter Dr. Huda Anan for her help in the development of the figures, table and plate.

Conflict of Interest

There is no conflict of interest.

References

- [1] Finger, K.L., 2013. Miocene foraminifera from the south-central coast of Chile. *Micropaleontology*. 59(4-5), 341-492.
- [2] Loeblich, A.R., Tappan, H., 1988. Foraminiferal genera and their classification. Van Nostrand Reinhold (VNR): New York.
- [3] Reuss, A.E., 1860. Die Foraminiferen der Westphälischen Kreideformation (Germany) [The foraminifera of the westphalian cretaceous formation]. *Sitzungsberichte der Kaiserlichen Akademie der Wissenschaften in Wien, Mathematisch-Naturwissenschaftliche Classe*. 40, 147-238.
- [4] Futyan, A.I., 1976. Late Mesozoic and Early Cretaceous benthonic foraminifera from Jordan. *Palaeontology*. 19(3), 53-66.
- [5] Orbnig, A.D., 1846. Die fossilen Foraminiferen des Tertiären Beckens von Wien (French) [The fossil foraminifera of the Tertiary Basin of Vienna]. *Foraminifères fossiles du Bassin Tertiaire de Vienne*. pp. 312.
- [6] Gümbel, C.W., 1868. Beiträge zur Foraminiferenfauna der nordalpinen Eocäugebilde (Germany) [Contributions to the foraminiferal fauna of the northern Alpine Eocäugebilde]. *Abhandlungen der K. Bayerische Akademie der Wissenschaften, Cl. II*. 10(2), 579-730.
- [7] Plummer, H.J., 1926. Foraminifera of the midway formation in Texas. *Bulletin University of Texas: Austin*.
- [8] Anan, H.S., 2021. Lenticuzonaria: A new Tethyan Lagenid benthic foraminiferal genus. *Earth Sciences Pakistan (ESP)*. 5(1), 33-36.
- [9] Pearson, P.N., Nicholas, C.J., Singano, J.M., et al., 2006. Further Paleogene and Cretaceous sediment cores from the Kilwa area of coastal Tanzania: Tanzania drilling project sites 6-10. *Journal of African Earth Sciences*. 45(3), 279-317.
- [10] Salahi, A., 2021. Late paleocene-middle eocene planktonic and small benthic foraminiferal fauna from the type section of khangiran formation, Kopet-Dagh Basin (NE Iran), Southernmost Peri-Tethys. *Stratigraphy and Geological Correlation*. 29(3), 303-321.
- [11] Anan, H.S., 2022. Percultalina: A new lagenid benthic foraminiferal genus. *Earth Sciences Pakistan (ESP)*. 6(2), 43-48.
- [12] Römer, F.A., 1841. Die Versteinerungen des Norddeutschen Kreidegebirges/von Friedrich Adolph Roemer, Königlich-Hannoverschen Amts-Assessor. Mit 16 lithographirten Tafeln (Germany) [The fossils of the North German Chalk Mountains. With sixteen lithographed plates]. *Hahn'schen, Hofbuch-handlung, Hanover*. 4, 49-145.
- [13] Cushman, J.A., 1938. Additional new species of American Cretaceous foraminifera. *Contribution from the Cushman Laboratory for foraminiferal Research*. 14(2), 31-50.
- [14] Reuss, A.E., 1863. Beiträge zur Kenntniss der tertiären Foraminiferen-Fauna (Zweite Folge). (Germany) [Contributions to the knowledge of the tertiary foraminiferal fauna (second series)]. *Proceedings of the Imperial Academy of Sciences in Vienna, Mathematical-Natural Scientific Classe*. 48, 36-71.

- [15] Haque, A.F.M., 1956. The foraminifera of the Rankot and the Laki of the Namal Gorge, Salt Range. *Memoirs of the Geological Survey of Pakistan, Paleontologia Pakistanica*. 1, 1-300.
- [16] Gümbel, C.W., 1870. Beiträge zur Foraminiferenfau-na der nordalpinen Eocäugebilde. (Germany) [Con-tributions to the foraminiferal fauna of the northern Alpine Eocäugebilde]. Forgotten Books: London.
- [17] Said, R., Kenawy, A., 1956. Upper Cretaceous and Lower Tertiary foraminifera from northern Sinai, Egypt. *Micropaleontology*. 2(2), 105-173.
- [18] Anan, H.S., 1993. Maastrichtian-Paleocene micropa-leontology and biostratigraphy of Qarn El Barr sec-tion, Al Dhayd area, United Arab Emirates. *Al-Azhar Bulletin of Science*. 4(2), 639-670.
- [19] Anan, H.S., 2010. Contribution to the Egyptian benthic foraminifera around the Paleocene/Eocene boundary in Egypt. *Egyptian Journal of Paleontolo-gy*. 10, 25-47.
- [20] Olsson, R.K., 1960. Foraminifera of latest Cretaceous and earliest Tertiary age in the New Jersey Coastal Plain. *Journal of Paleontology*. 34, 1-58.
- [21] Jaff, R.B., Lawa, F.A., 2019. Palaeoenvironmental signature of the Late Campanian-Early Maastrichtian benthonic foraminiferal assemblages of Kurdistan, Northeast Iraq. *Journal of African Earth Sciences*. 151, 255-273.
- [22] Orabi, H.O., Zaky, A.S., 2016. Differential dissolu-tion susceptibility of Paleocene foraminiferal assem- blage from Farafra Oasis, Egypt. *Journal of African Earth Sciences*. 113, 181-193.
- [23] Anan, H.S., 2022. Stratigraphy, taxonomical con- sideration and evolutionary trends of futyan benthic foraminiferal Jordanian Species. *Earth Sciences Pa- kistan (ESP)*. 6(2), 66-71.
- [24] Anan, H.S., 2020. Taxonomic consideration and stratigraphic implication of the accelerated evolution of the Maastrichtian-Eocene transition of twenty benthic foraminiferal species in the Tethys. *Earth Sciences Pakistan (ESP)*. 4(1), 1-6.
- [25] Anan, H.S., 2023. Taxonomical Consideration, Phy- logeny and Paleobiogeography of Some Argentinian Ypresian Benthic Foraminiferal Species. *Earth and Planetary Science*. 2(1), 33-43.
- [26] Cimerman, F., Jelen, B., Skaberne, D., 2006. Late Eocene benthic foraminiferal fauna from clastic sequence of the Socka-Dobrna area and its chronostratigraphic importance (Slovenia). *Geologija*. 49(1), 7-44.
- [27] Anan, H.S., 2009. Paleontology, paleogeography, paleoenvironment and stratigraphical implications of the Nakkady's benthic foraminiferal fauna in Egypt and Tethys. *Egyptian Journal of Paleontology*. 9, 31-52.
- [28] Zlinská, A., 2009. Foraminiferové asociácie z lučenského súvrstvia vrtu FGRk-1 (Rimavská kotlina) (Slovak) [Foraminiferal associations from the Lučenec Formation in borehole FGRk-1 (Rimava kotlina basin)]. *Mineralia Slovaca*. 41, 291-312.
- [29] Valchev, B., Stojanova, V., Juranov, S., 2013. Pa- leogene hyaline benthic foraminifera (LAGENINA and ROTALIINA) from the Republic of Macedonia. *Review of the Bulgarian Geological Society*. 74(1-3), 81-110.
- [30] Anan, H.S., 2015. Paleogene Lagenid Percultazonarias (Foraminifera) in Egypt: paleontology, stratigraphy, paleogeography and some taxonomical considerations. *Egyptian Journal of Paleontology*. 15, 13-30.
- [31] VahdatiRad, M., Vahidinia, M., Sadeghi, A., 2016. Early Eocene planktonic and benthic foraminifera from the Khangiran formation (northeast of Iran). *Arabian Journal of Geosciences*. 9, 1-13.
- [32] Pearson, P.N., Nicholas, C.J., Singano, J.M., et al., 2004. Paleogene and Cretaceous sediment cores from the Kilwa and Lindi areas of coastal Tanzania: Tanzania Drilling Project Sites 1-5. *Journal of African Earth Sciences*. 39(1-2), 25-62.
- [33] Jannou, G.E., Nández, C.A., Malumián, N., 2022. Foraminíferos bentónicos de la Formación Punta Tor- cida, Eoceno inferior-medio (Ypresiano-Lutetiano in- ferior), Isla Grande de Tierra del Fuego y plataforma continental fueguina. *Serie Contribuciones Técnicas. Geología Regional (Spanish) [Benthic foraminifera from the Punta Torcida Formation, Lower-Middle Eocene (Lower Ypresian-Lutetian), Isla Grande de Tierra del Fuego and Tierra del Fuego continental shelf. Technical Contributions Series. Regional Geol- ogy]*. 9, 1-53. Available from: https://www.research-gate.net/publication/366052203_Foraminiferos_ben- tonicos_de_la_Formacion_Punta_Torcida_Eoceno_inferior-medio_Ypresiano-Lutetiano_inferior_Isla_Grande_de_Tierra_del_Fuego_y_plataforma_continental_fueguina
- [34] Farouk, S., Jain, S., Al-Kahtany, K., et al., 2023. Relationship of Maastrichtian-Thanelian benthic for- aminiferal species diversity, palaeooxygenation, and palaeoproductivity in shallow waters of the Western Desert, Egypt. *Geo-Marine Letters*. 43(1), 4.
- [35] Youssef, M., Taha, S., 2013. Biostratigraphy and Paleoecology of Paleocene/Eocene (P/E) interval of some geological sections in Central Egypt. *Arabian Journal of Geosciences*. 6, 4279-4298.

- [36] Orabi, O.H., Hassan, H.F., 2015. Foraminifera from Paleocene—early Eocene rocks of Bir El Markha section (West Central Sinai), Egypt: Paleobathymetric and paleotemperature significance. *Journal of African Earth Sciences*. 111, 202-213.
- [37] Anan, H.S., 2011. Paleontology, paleoenvironments, palaeogeography and stratigraphic value of the Maastrichtian-Paleogene and Recent foraminiferal species of Anan in the Middle East. *Egyptian Journal of Paleontology*. 11, 49-78.
- [38] Abdelghany, O., 2003. Late Campanian-Maastrichtian foraminifera from the Simsima Formation on the western side of the Northern Oman Mountains. *Cretaceous Research*. 24(4), 391-405.
- [39] Cushman, J.A., 1946. Upper Cretaceous Foraminifera of the Gulf Coastal Region of the United States and adjacent areas. United States Geological Survey, Professional Paper. 206, 1-241.
DOI: <https://doi.org/10.3133/pp206>
- [40] Sztrákös, K., 2005. Les foraminifères du Paléocène et de l'Éocène basal du sillon nord-pyrénéen (Aquitaine, France) (French) [Paleocene and lowest Eocene foraminifera from the north Pyrenean trough (Aquitaine, France)]. *Revue de Micropaléontologie*. 48, 175-236.
- [41] Gibson, T.G., 2007. Upper paleocene foraminiferal biostratigraphy and paleoenvironments of the Salt Range, Punjab, Northern Pakistan. *Regional Studies of the Potwar Plateau Area, Northern Pakistan*. p. 841-875.
- [42] LeRoy, L.W., 1953. Biostratigraphy of Maqfi section, Egypt. *Geological Society of American Memoir*. 54. 1-73.
- [43] Orbigny, A.D., 1826. Tableau méthodique de la classe des Céphalopodes. *Annals des Sciences de la Naturelles, Paris* (French) [Methodical table of the class Cephalopoda. *Annals of Natural Sciences, Paris*]. 7, 96-169, 245-314.
- [44] Silvestri, A., 1904. Ricerche strutturali su alcune forme dei Trubi di Bonfornella (Palermo). *Memorie della Pontificia Accademia Romana dei Nuovi Lincei* (Italian) [Structural research on some forms of Trubi di Bonfornella (Palermo). *Memoirs of the Pontifical Roman Academy of the New Lincei*]. 22, 235-276.
Available from: <https://archive.org/details/AttiDellAccademiaPontificiaLincei57/mode/2up>
- [45] Anan, H.S., 2020. Early Paleogene benthic foraminifera of Duwi section, Red Sea coast, Egypt. *Journal of American Science*. 16(2), 1-22.
- [46] Shreif, A., Obaidalla, N.A., Menoufy, S.A., 2023. Stratigraphic and paleoenvironmental studies on the lower eocene succession at El-Guss Abu Said Plateau, Farafra Oasis, Western Desert, Egypt. *Journal of Foraminiferal Research*. 53(2), 109-119.
- [47] Anan, H.S., 1995. Late Eocene Biostratigraphy of Jabals Malaqet and Mundassa of Al Ain region, United Arab Emirates. *Revue de Micropaléontologie*. 38(1), 3-14.
- [48] Haq, B.U., Aubry, M.P., 1978. Early Cenozoic calcareous nannoplankton biostratigraphy and palaeobiogeography of North Africa and the Middle East and Trans-Tethyan correlations. *The Geology of Libya*. Academic Press: London. pp. 271-304.
- [49] Mintz, L.W., 1981. *Historical geology, the science of a dynamic earth*, 3rd edition. Merrill Publication Company: Princeton. pp. 611.
- [50] Rosenbaum, G., Lister, G.S., Duboz, C., 2002. Relative motions of Africa, Iberia and Europe during Alpine orogeny. *Tectonophysics*. 359(1-2), 117-129.
- [51] Abed, A.M., 2013. The eastern Mediterranean phosphorite giants: An interplay between tectonics and upwelling. *GeoArabia*. 18(2), 67-94.
- [52] Berggren, W.A., Aubert, J., 1975. Paleocene benthonic foraminiferal biostratigraphy, paleobiogeography and paleoecology of Atlantic—Tethyan regions: mid-way-type fauna. *Palaeogeography, Palaeoclimatology, Palaeoecology*. 18(2), 73-192.



RESEARCH ARTICLE

Facies and Hydrocarbon Reservoir Rock Characterization of the Paleozoic Rocks of Peshawar Basin, Northwest Pakistan

Sajjad Ahmad*  Sohail Raza Suleman Khan

Department of Geology, University of Peshawar, Khyber Pukhtunkhwa, 25120, Pakistan

ARTICLE INFO

Article history

Received: 10 June 2023

Revised: 10 July 2023

Accepted: 20 July 2023

Published Online: 18 August 2023

Keywords:

Facies

Hydrocarbon reservoir

Paleozoic

Peshawar Basin

Pakistan

ABSTRACT

The present study details the facies description and hydrocarbon reservoir characterization of the Paleozoic rocks of Peshawar Basin, northwest Pakistan. The outcrop samples from the Cambrian-Devonian rocks along the famous Nowshera-Risalpur Road and Turlandi Village Section were investigated. The analysis of outcrop data revealed significant information regarding the facies and their depositional environments. Based on its detailed sedimentological data, it is believed that the Ambar Formation is deposited in shallow shelf-tidal flat settings, while the protolith of the Misri Banda Quartzite came from the wide beaches. The protolith of the Panjpir Formation was deposited in the shelf conditions, which shows an overall shallowing when moving up the section from the argillites and phyllites to crinoidal limestone. The Nowshera Formation was deposited as a reef complex on the shelf edge having reef core, reef breccia and a back-reef lagoon. The techniques of petrography, XRD and SEM were used for the bulk geochemical composition of the rocks focusing on their matrix, mineralogy, micro-porosity and pore-filling materials. The presence of micrite, goethite, kaolinite and illite as intergranular mass, dolomitization-induced porosity, twin cleavage plane and high dissolution porosity in the Ambar Formation can provide significant pore space to the reservoir fluids migration. Hematite with minor kaolinite, illite and chlorite as alteration products of unstable framework grains as intergranular mass and a deep seated burial diagenesis has minimized the reservoir potential in Misri Banda Quartzite. The coarse and fine calcite, dolomite, chlorite and kaolinite occur as pore-filling material between the framework grains while the high intensity of intragranular dissolution and micro intergranular connecting porosity in the Nowshera Formation makes it a promising reservoir.

*Corresponding Author:

Sajjad Ahmad,

Department of Geology, University of Peshawar, Khyber Pukhtunkhwa, 25120, Pakistan;

Email: dr.s_ahmed@uop.edu.pk

DOI: <https://doi.org/10.36956/eps.v2i2.874>

Copyright © 2023 by the author(s). Published by Nan Yang Academy of Sciences Pte. Ltd. This is an open access article under the Creative Commons Attribution-NonCommercial 4.0 International (CC BY-NC 4.0) License. (<https://creativecommons.org/licenses/by-nc/4.0/>).

1. Introduction

In the foothills of the Himalayas, the Peshawar Basin (Figure 1) includes the oldest exposed sequence of sedimentary and metasedimentary rocks. Marine evaporites (Salt Range Formation) can be found in the south, whereas deep water pelites can be found in the north. The entire sequence of Paleozoic-era strata can be found within the Peshawar Basin and along the hills that circle the basin on its eastern side. Waagen ^[1], Griesbach ^[2], Middlemiss ^[3], Wadia ^[4], Martin et al. ^[5], Davies and Ahmad ^[6], and Teichert and Stauffer ^[7] are credited with the first attempts to understand the stratigraphy of the Peshawar Basin. They also first reported the presence of Paleozoic rocks in the region. Burbank ^[8] described Pleistocene and Pliocene era sediments in 1983, and Tahirkheli and Burbank ^[9] did the same in 1985. In an effort to understand the local context of Himalayan stratigraphy, Fuchs ^[10] undertook a study in the Nowshera area. Hussain ^[11] created the regional geological map of the Nizampur region, which includes portions of the Attock, Mardan, and Peshawar districts. Pogue and Hussain ^[12] reconstructed the Nowshera region stratigraphy based on the discovery of Trilobite trace fossils. The structural events' timing in the foothills of the Himalayas was worked out by Yeats and Hussain ^[13]. Pogue and others ^[14] are responsible for the initial systematic attempt to understand the regionally applicable and coherent stratigraphy of the Peshawar Basin and surrounding regions. They completed a thorough sampling from several outcrops for a paleontological investigation, and as a result, they were able to modify the region's stratigraphic framework and carry out a regional correlation. The literature assessment makes clear that the petroleum geology of the study region has not yet been fully studied. Therefore, the assessment of the Peshawar Basin's hydrocarbon resource potential has received particular attention in this study.

2. Regional Tectonic Settings

A fairly large intra-mountain basin (more than 5500 km²) named the Peshawar Basin is located near the southernmost tip of the Himalayas, northwest of the Kohat Basin (Figure 1). It is situated where the northern and southern edges of the Indo-Gangetic fore-deep, as well as the southern limit of the Hindu Kush-Himalayan Ranges, converge. The Peshawar basin is delimited by the Khyber range in the northwest, the Attock-Cherat range in the south, and the Swat range in the northeast along the margin of the basin. Quaternary fanglomerates were seen. The majority of such deposits in the basin's central region are fluvial micaceous sand, gravel, and lacustrine depos-

its. Small outcrops within the basin are the only places where the Paleozoic and older strata have been exposed. Pre-Cambrian to Early Mesozoic metamorphosed and igneous rocks in the Peshawar Basin are highly deformed and tightly folded. According to Treloar and Others ^[15] these rocks are thrust over the Kurrum-Cherat-Margalla ranges in the south. More than 300 meters of floodplain mudstone and siltstones with minor sandstone intercalations occupy the basin, which is overlaid by eroded Eocene limestone or Murree sandstone fanglomerates which are moving northward. Intruding metamorphosed Paleozoic sediments along fault zones are a few alkaline rock complexes that emerge towards the western edge of the Peshawar basin. The heavily deformed Murree sediments that make up the northern part of the Peshawar Basin indicate that the pre-existing fore-deep basin experienced severe deformation prior to the start of sedimentation in the newly created Peshawar Basin. At least 2.8 million years ago, sediments that filled the basin piled at a pace of 15 cm/1,000 years, totaling more than 300 m. The juxtaposition of metasediments from the Lesser Himalaya in the north and sediments from the Mesozoic to Neogene fold-belt in the south characterizes the southern edge of the Peshawar Basin. Ahmad and others ^[16] hypothesized that the marine shelf sedimentation of the Indus Basin was extended up to the Peshawar Basin during the Mesozoic. Under the Pre-Paleocene thrust nappes in the submerged Mesozoic marine strata, it is anticipated that a potential petroleum system may be present in the Peshawar Basin.

3. Stratigraphic Setup

In a younging up stratigraphic sequence, the Peshawar Basin contains the Cambrian (Ambar Formation), Mid Ordovician (Misri Banda Quartzite), Late Silurian (Panjpir Formation), and Late Devonian (Nowshera Formation) (Figure 2). Of particular mention is the absence of Precambrian (Manki, Shekhai and Dakhner Formations), Cambrian (Darwaza Formation), Early Ordovician (Hisartang Formation) and early-Mid Devonian (Inazari Formation) from the Peshawar Basin and characterizes the adjacent Attock-Cherat Ranges in the south of Peshawar Basin (Table 1).

3.1 Ambar Formation

It is a thick rock unit that is exposed in the form of isolated hillocks between the Nowshera and Swabi areas. The dominant lithology of the formation is thick bedded to massive sandy dolomite, having ripple marks, mud cracks and salt pseudomorphs (Figures 2-3). Minor shale and siltstone intercalations are also present.

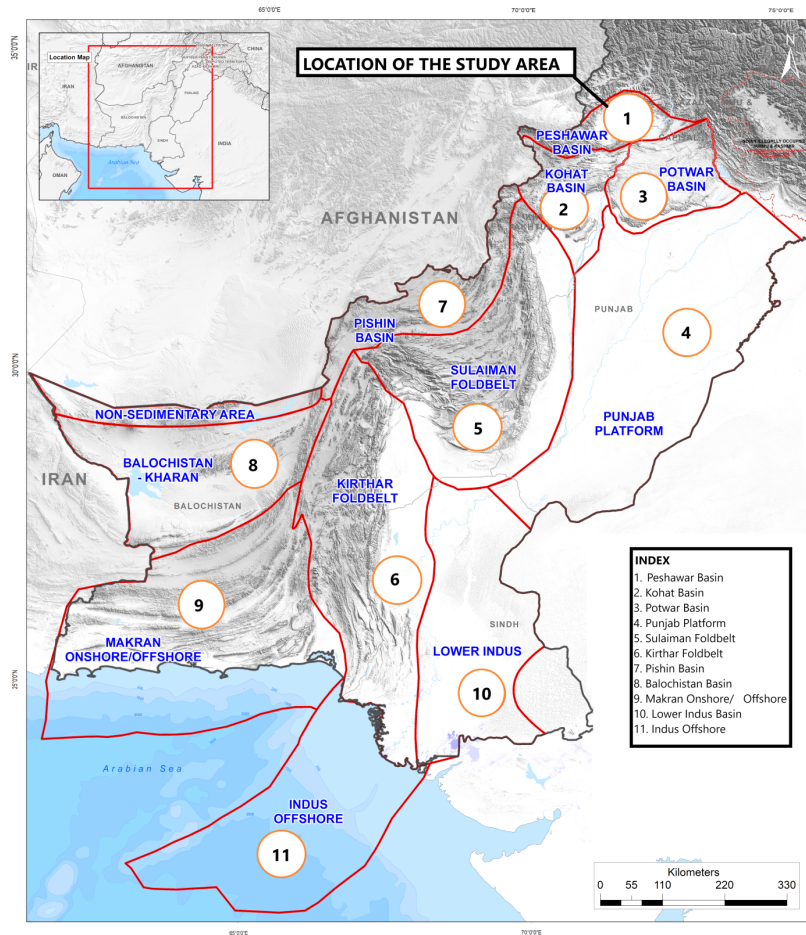


Figure 1. The map shows major sedimentary basins and actinomorphic terrains of Pakistan. The Peshawar Basin is located in the northwest of the Kohat Basin.

Table 1. The Paleozoic Stratigraphic framework of the Peshawar Basin and adjoining Attock Cherat Ranges, in north Pakistan.

Era	Epochs	Peshawar Basin and adjoining Attock-Cherat Range		
		Formation	Lithology	Thickness
Paleozoic	Devonian	Nowshera	Limestone, dolomite,	30-215 m
		Panjpir	argillie, phyllite, limestone, meta-sediments & quartzite	400-600 m
	Ordovician	Missri Banda	Quartzite	200-500 m
		Hissar-Tang	Argillites & quartzite	400-600 m
	Cambrian	Darwaza	Limestone, dolomite and maroon shale	500-760 m
		Ambar	Dolomite, quartzite and argillite	425 m

3.2 Misri Banda Quartzite

It is a dominantly arenaceous unit, bounded by unconformities, and lies between the underlying Ambar Formation (Figure 4) and overlying the Panjpir Formation. The formation contains feldspathic quartzite with thin intervals of argillites. The quartzite is cross bedded, and ripple marks are common. The lower contact is marked by

argillites of the Ambar Formation whereas the upper contact is represented by a basal conglomerate. Based on the *Cruziana rugosa* fossils Ordovician age is assigned to this rock unit.

3.3 Panjpir Formation

This is dominantly an argillaceous unit lying between the Misri Banda Quartzite and the overlying Nowshera

Formation. The formation consists of argillites and phyllites; with interbeds of limestone in the upper part having crinoids (Figure 5). The lower contact was not exposed while its upper contact is gradational with the Nowshera Formation.

3.4 Nowshera Formation

The Nowshera Formation is the youngest stratigraphic unit in the Peshawar Basin. The dominant lithology of the Nowshera Formation includes recrystallized limestone, dolomitic limestone (Figure 6), sandstone and calcareous quartzite and minor argillite. The Nowshera Formation is subdivided into reef core, reef breccia, and unfossiliferous carbonates. The Nowshera Formation has an unconformable contact with the overlying Jafar Kandao Formation in the north of Swabi. The unconformity is marked by cobbles of argillite in the quartzite-argillite matrix and a discontinuous conglomerate bed composed of pebbles.



Figure 2. Salt pseudomorphs can be seen in the dolomite of Ambar Formation in the Ambar Village Section.



Figure 3. A view of the ripple marks in the Ambar Formation in the Ambar Village Section.



Figure 4. The contact relationship of the Ambar Formation and Misri Banda Quartzite in the Turlandi Village Section.



Figure 5. A close view of the Panjpir Phyllites is exposed along the Nowshera-Risalpur Road Section.

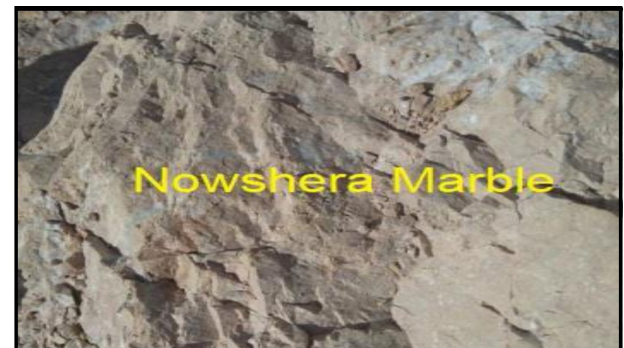


Figure 6. The outcrop of Nowshera Formation, shows the marble facies along the Nowshera-Risalpur Road Section.

4. Material and Methods

A total of twenty-eight outcrop samples from the Nowshera-Risalpur Road Section, the Turlandi Section, and the

Ambar Village Section, were thoroughly investigated for the assessment of the hydrocarbon reservoir rocks in the Peshawar Basin. At the Central Resource Laboratory of the University of Peshawar, all the samples were analyzed. The techniques of thin section petrography, X-ray diffraction (XRD) analysis, and Scanning Electron Microscopy (SEM) were used and the results were integrated to better understand the hydrocarbon reservoir characterization in the study area.

5. Results and Discussion

5.1 Facies and Depositional Environments

Ambar Formation

Siltstone Facies: This facies is dominantly composed of silty siliceous matrix (Plate 1, A) with some muscovite grains (Plate 1, B). Some iron stains and heavy minerals (pyrite) are also obvious in the facies. The Ambar Village section has more sandy/siliciclastic content that is fine-grained (Plate 1, C). The facies is characterized by veins filled with low Mg calcite crystals (Plate 1, D). The facies shows signs of a low grade of metamorphism. The facies is very fine-grained, have some heavy mineral concentrations and is devoid of any fauna. The facies therefore represents the inner parts of a restricted environment. The sand content, present only in the Ambar Village Section is derived from the fine sand beaches.

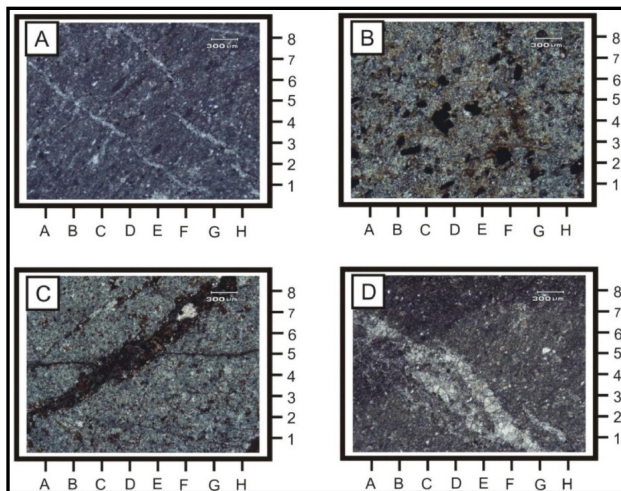


Plate 1. A: Photomicrograph showing the silty matrix in the siltstone facies of the Ambar Formation; B: the ferruginous mineral D4 and Muscovite mineral (D6); C: the ferruginous mineral filled fracture (D4); D: the calcite filled echelon fracture (D3).

Siliciclastic Lime Mudstone Facies: The facies is characterized by the dominance of lime mud (Plate 2, A) with varying amounts of siliciclastic input, in the form of quartz

(Plate 2, B) and minor muscovite flakes, some unrecognizable bioclasts and ore minerals. The quartz grains are fine and sub angular to sub rounded (Plate 2, C). The facies is laminated (Plate 2, D) in one portion in the Ambar Village Section. The facies has a network of calcite filled vein that cross cut each other. Ferruginous stains and stylolites with ferruginous and clayey material are also obvious in the facies at different horizons. The facies contains an overall visual porosity of 2% in the thin section. The facies is mud supported and is almost devoid of any fauna and it seems to have been deposited in the restricted parts of the ocean with elevated salinities and less circulation. The presence of lamination in the facies is an indication of the slow nature of deposition in this environment. This lagoon was supplied with siliciclastic input by fluvial and aeolian processes. The undulose extinction, displayed by quartz grains, is because of low grade metamorphism.

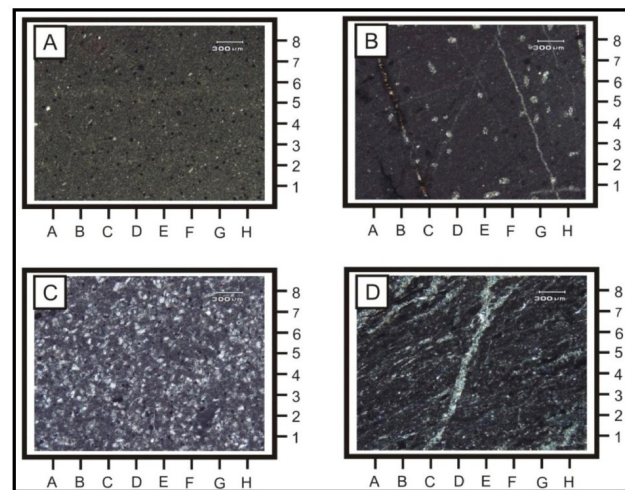


Plate 2. A: Photomicrograph showing the Lime Mudstone Facies of the Ambar Formation; B: the siliciclastic material (E4); C: fine silt size grains (B4); D: Photomicrograph showing the laminated fabric.

Dolomitized Ooidal-Peloidal Limestone Facies: The facies is characterized by the presence of carbonate allochems that include ooids and peloids (Plate 3, A). These grains are bounded by sparry cement along with intervening lime mud at places. The facies has packstone to grainstone textures. The ooids are radial with peloidal nuclei and some are micritized and converted into peloids. Both the micritized peloids and fecal pellets are present in the facies. In some horizons, the cementing material is replaced by dolomite of secondary origin (Plate 3, B). Some siliciclastic material in the form of angular to sub-rounded quartz is also present, some of which show undulose extinction. Ferruginous stains, stylolites and calcite filled veins are obvious in the facies at different places.

The facies is grain supported and are bounded by spar-

ry calcite cement, some of which have been replaced by secondary dolomite (Plate 3, C) and some sand grains (Plate 3, D). The general absence of fauna, presence of faecal pellets, micritized nature of the grains and radial habit of the ooids indicate that deposition took place on hyper saline beaches of the lagoons. The presence of lime mud in some sections shows that this environment was subjected to fluctuating energy.

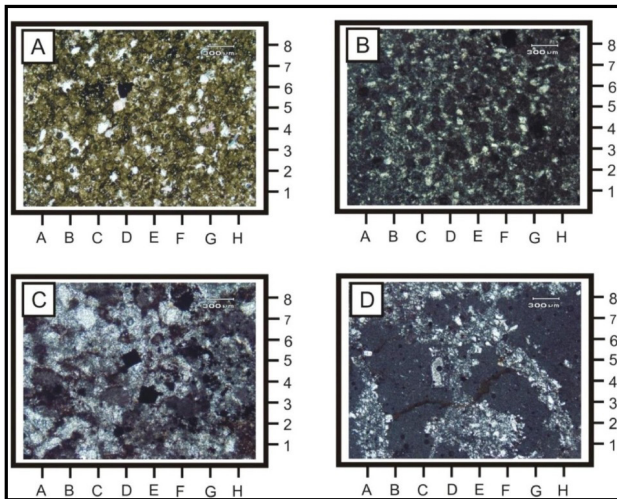


Plate 3. A: Photomicrograph showing the Ooids (C3) in the dolomitized Ooidal Peloidal Limestone Facies of the Ambar Formation; B: Peloids (D5) and siliciclastics (D4); C: Photomicrograph showing the dolomitized cement and pyrite (D5); D: siliciclastic material within the Ooidal Peloidal Limestone Facies.

Sandy Siliciclastic Mudstone Facies: The facies is a siliciclastic mudstone (Plate 4, A) that has some sandy patches of fine grained nature. It contains some amounts of muscovite, recrystallized biota and altered clays. The muscovite grains are aligned preferentially and show micro folding (Plate 4, B). The facies have some iron rich heavy minerals that exhibit a network of silica filled fractures.

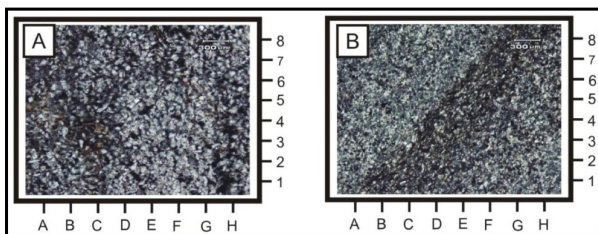


Plate 4. A: Photomicrograph is showing Fine Grained Sandstone Facies showing the siliciclastic input (E5); B: Muscovite flakes (D4).

The facies is siliciclastic mud supported and is devoid of fauna, except for some recrystallized bioclasts. The deposition took place in the inner parts of a lagoon. The

minor siliciclastic input is probably derived from the fine grained siliciclastic beaches. The absence of planktons suggests an inner shelf lagoon environment rather than an outer shelf.

Missri Banda Quartzite

At the outcrop, this facies is composed of medium-thick bedded quartzose sandstone having ripple marks and cross beds at certain intervals. At the thin section level, this facies is dominantly composed of monocrystalline (90%) and polycrystalline (2%) quartz (Plate 5, A). The quartz is angular to subrounded, moderate to well sorted, tightly packed with straight to sutured contacts. A few quartz grains show undulose extinction. The feldspars (alkali feldspar and plagioclase) constitute about 10% of the facies. Altered clay lithic fragments constitute about 2% of the facies. A trace amount of muscovite (1%) is also present in the facies. Fracture porosity is present in the facies. The well sorted, sub rounded to rounded, rippled and cross bedded quartzose sandstone of the Misri Banda Quartzite is deposited on high energy beaches and fore-shore environments.

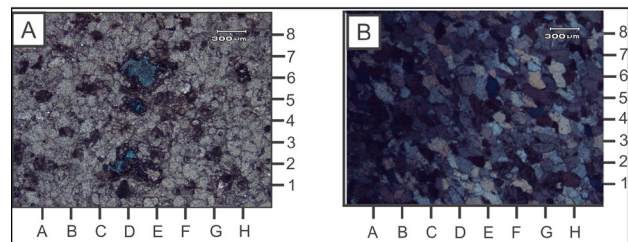


Plate 5. A: Photomicrograph is showing moderately sorted quartz, Dissolution porosity (EC57), Intraclasts (D1) within the Quartzite of Misri Banda Formation; B: Photomicrograph showing moderately the contacts between the quartz grains (XPL).

Panjpir Formation

Phyllites: The phyllites of the Panjpir Formation are dominantly composed of quartz and clays. The segregation of quartz and clays into separate layers is quite well developed but not to the degree of schistosity. Very fine mica is developed in the clay rich layers (Plate 6, A-D). Prominent segregation and the development of mica suggest that the Panjpir Phyllites have undergone the peak of low grade metamorphism.

Bioclastic Wackestone Facies: The facies is composed of grains to matrix ratio of 1.5:8.5. The grains consist mainly of bioclasts of echinoderms (Plate 7, A), pelecypods (Plate 7, B), brachiopods, ostracods (Plate 7, C). The other grains include siliciclasts (Plate 7, D) of fine sand

and have angular to sub rounded shapes. These grains are embedded in a matrix of lime mud. The facies is mud supported and contains diverse fauna in the form of brachiopods and echinoderms. The facies thus represents a normal salinity low energy environment of the middle shelf environment.

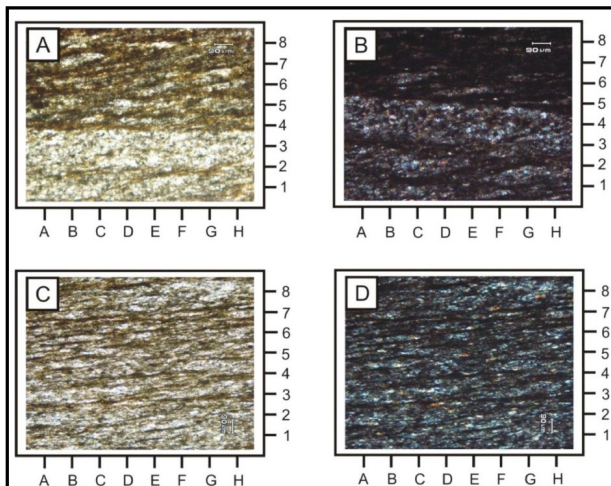


Plate 6. A, B: Photomicrograph showing the quartz, clays and mica rich layers in the Panjpir Phylites (PPL, XPL); C, D: preferred orientation of the quartz and clay layers (PPL, XPL).

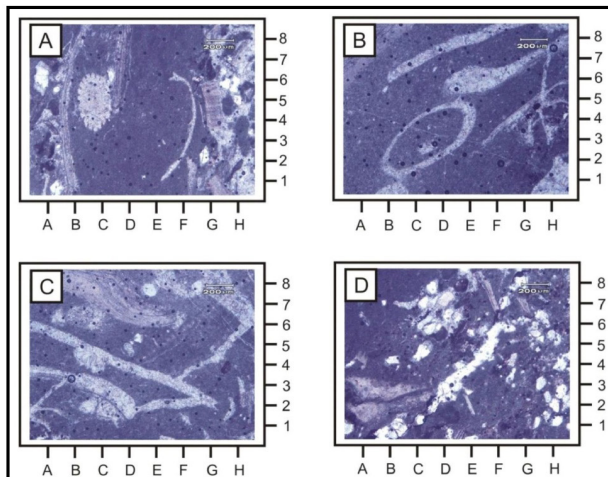


Plate 7. A: Photomicrograph showing the Bioclastic Wackestone Facies, confirming echinoderm spine (C5) within the Panjpir Formation; B: bivalve (E6); C: ostracode (F2) and brachiopod (C7); D: siliciclasts (H2) are common.

Nowshera Formation

Dolostone Facies: The dolostone is the most prevalent facies across the formation in both the Nowshera and Pir Sabak Village Sections. The dolomite (Plate 8, A) ranges in size from fine to medium sand and it is often pervasive,

sometimes selective as well. The dolomite has replaced either the matrix or the grains or both. In some cases, the signs of the original precursor material are still obvious (Plate 8, B). Most of the dolomitization has taken place in the fine grained lime mudstones and wackestones. Some of the dolomite crystals are euhedral (Plate 8, C), ferroan and zoned. Silt size siliciclasts are found in some of the samples. Fracturing, though not common, is found in some parts of the facies (Plate 8, D).

The facies is characterized by fine to medium dolostones, some of which have euhedral crystals. The original precursor material, in some cases, is still obvious. The facies is therefore considered secondary in nature replacing the matrix and bioclasts of the mudstones and wackestones. The Magnesium rich fluids might have been circulated through the reef complex, particularly in the back reef portion.

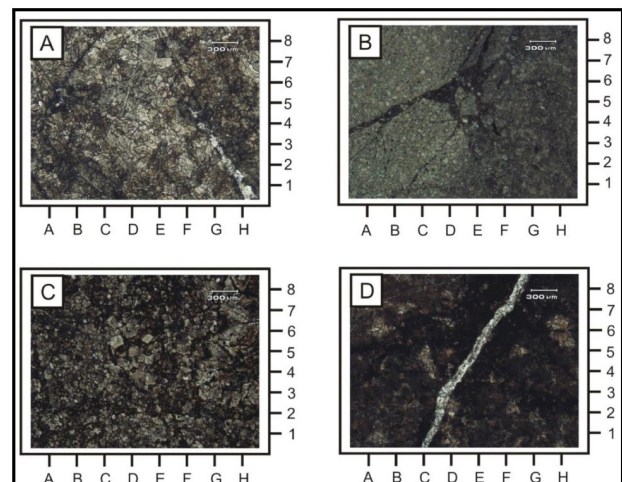


Plate 8. A: Photomicrograph showing the presence well developed dolomite crystals (D5) in the Dolostone facies of the Nowshera Formation; B: the original precursor (D5); C: Euhedral dolomites (DE56); D: Photomicrograph is showing the fractures (E5).

Recrystallized Bioclastic Wackestone/Mudstone Facies: The facies is represented by mud supported nature and have grains in the form of bioclasts. The facies is dolomitized (Plate 9, A) but the precursor facies is still evident. The bioclasts consist of crinoid's ossicles (Plate 9, B), bivalves (Plate 9, C), and gastropods. Most of these bioclasts are recrystallized but their outlines are still obvious (Plate 9, D). The facies is fractured in some horizons and stylolites are also obvious.

The facies is supported by lime mud and bioclasts such as crinoids and mollusks. The crinoids are found in the reef flank beds^[17]. The facies thus represent the reef flank/ upper slope depositional environment.

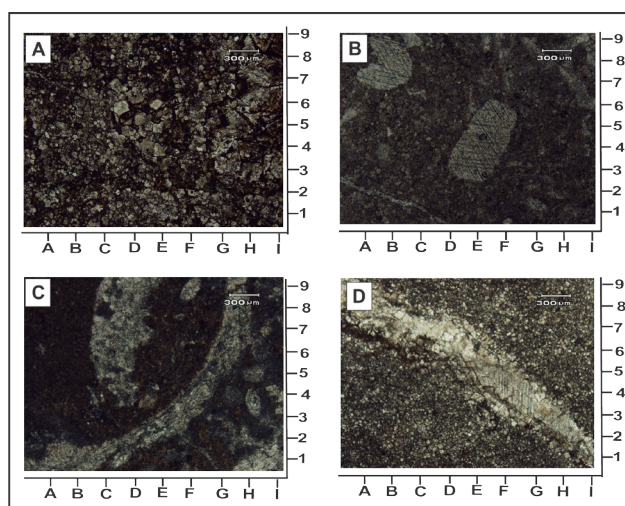


Plate 9. A: Photomicrograph shows the precursor dolomite within the Recrystallized Bioclastic Wackestone/Mudstone facies (E5); B: A view of the Crinoid ossicle (E4); C: Photomicrograph showing the bivalve fragment (F4); D: Photomicrograph is showing the recrystallized bioclast (E5).

Siliciclastic Dolostone Facies: This facies is restricted to the Pir Sabak Village Section and is composed of dolostones with substantial amounts of siliciclasts (Plate 10, A) in the form of quartz. The quartz grains, some of which are fractured (Plate 10, B), are fine-medium sand size, moderately sorted and range from sub-angular to rounded (Plate 10, C). These grains are set in a mix of fine grained dolomite and coarse calcite (Plate 10, D). The facies has a preponderance of quartz grains set in secondary dolomite and calcite. The secondary calcite is formed as a result of the circulation of Mg rich lagoon waters^[18]. The facies represents the lagoon facies with some clastic input from the land area.

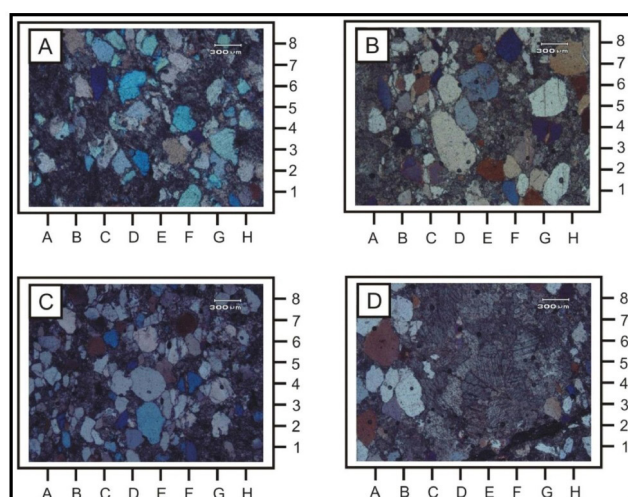


Plate 10. A: Photomicrograph showing the Siliciclastics Dolostone Facies; B: siliciclastic quartz (G5); C: well rounded quartz (E4); D: A view of the recrystallized calcite.

6. Hydrocarbon Reservoir Characterization

6.1 Ambar Formation

The Ambar Formation is mainly comprised of dolomite and argillite. The matrix is composed of ferruginous-clay, dolomite and micrite while the spar is present as fracture filling and as a product of neomorphism (Plate 11, A, B, C, D, and E). The XRD analysis indicates that the ferruginous clay matrix constitutes quartz, dolomite, goethite, kaolinite, albite and illite (Plate 11, F).

Dolomitization may increase the secondary porosity and is connected to the ferruginous matrix. When rocks are exposed sub-aerially to meteoric fluids in an exogenic environment, porosity enhancement owing to dissolution may also happen to make up for this early porosity loss^[19-21]. Twin cleavage plane and high dissolution porosity which is evident from the SEM images can provide significant pore space to the migrating hydrocarbons thus making it an excellent reservoir (Plate 11, G and H).

6.2 Misri Banda Quartzite

The feldspathic quartzite with subordinate argillite is the main lithology in Misri Banda Quartzite. The quartzite is tightly packed with concavo-convex to sutured contacts. Grains are mostly sub-rounded to rounded having the ability to adopt the closest packing upon increased pressure. At places, a small amount of ferruginous matrix is present along the fractures. Secondary dissolution porosity has been developed at the expense of the much unstable sedimentary lithics (Plate 12, A and B). A high concentration of quartz and a minor occurrence of microcline and hematite is also evident from the XRD analysis. A minor amount of kaolinite, illite and chlorite as alteration products of unstable framework grains (feldspar) are present which can affect the porosity (Plate 12, C). All naturally occurring smectite clays including kaolinite are susceptible to chlorite alteration^[22,23]. In situations with high pH values and high Fe and Mg ion levels, smectite changed into chlorite. Chlorite-smectite mixed layer stage is when the transition typically takes place^[24,25]. This process takes place at a low diagenetic temperature at a relatively shallow depth. In an environment with abundant Fe and Mg supply, kaolinite changed to chlorite with increasing burial depth and temperature^[26,27]. Illite is present in the form of flaky pore lining material and partially covers a few of the pore spaces thus minimizing its reservoir potential (Plate 12, D). Being tightly packed, still there exists intergranular porosity between the stable grains (Plate 12, E) because the mineralogical, mature sandstone has the ability to retain a high amount of intergranular porosity at greater

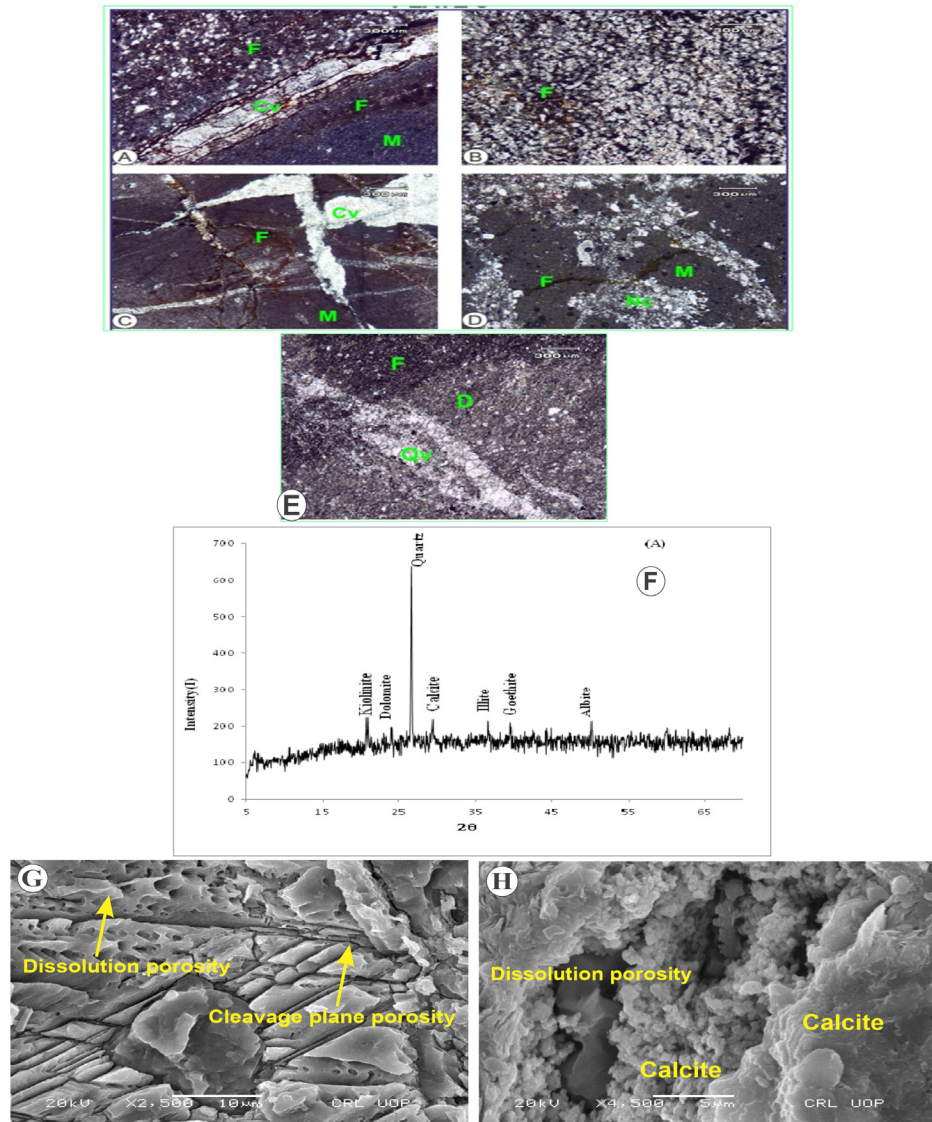


Plate 11. A, B, C, D, and E are representing the Photomicrographs of Ambar Formation, various blocks of cement matrix types, Ferruginous clays (F). Micrite (M), Calcite filled Veins (CV), Dolomite (D) and calcite; F: The XRD results showing the bulk rock geochemistry of the Ambar Formation; G, H represent the SEM images focusing the Dissolution and cleavage plane porosities and calcite mineral.

burial depth. According to earlier research, chlorite coatings, particularly in deeper reservoir sandstones are significant contributors to anomalous porosity and permeability. The Presence of chlorite and sutured contacts between quartz grains are indicative of deep burial diagenesis and very low grade metamorphism, which may have obliterated the depositional porosities to a great extent.

6.3 Nowshera Formation

Limestone, dolomite, and quartzite are the main lithologies in the Nowshera Formation. Between the framework grains, coarse and fine calcite, dolomite, and ferruginous clays are present as pore fillers (Plate 13, A and B). Chlo-

rite and kaolinite may have been created by the alteration of alkali feldspar or unstable clastic framework grains, as shown by the XRD study in Plate 13, C. According to Foscolos ^[28], certain fluids produced during burial diagenesis aid in the alteration of clay minerals, such as the transformation of smectite to illite. The burial depth and temperatures had a significant impact on how quickly kaolinite turned into chlorite. Almost no porosity is present at the thin section level. However, SEM analysis shows that the carbonate of the Nowshera Formation possesses a high amount of intragranular dissolution porosity and micro intergranular connecting porosity (Plate 13, D and E). The primary porosity has been reduced as a result of high tem-

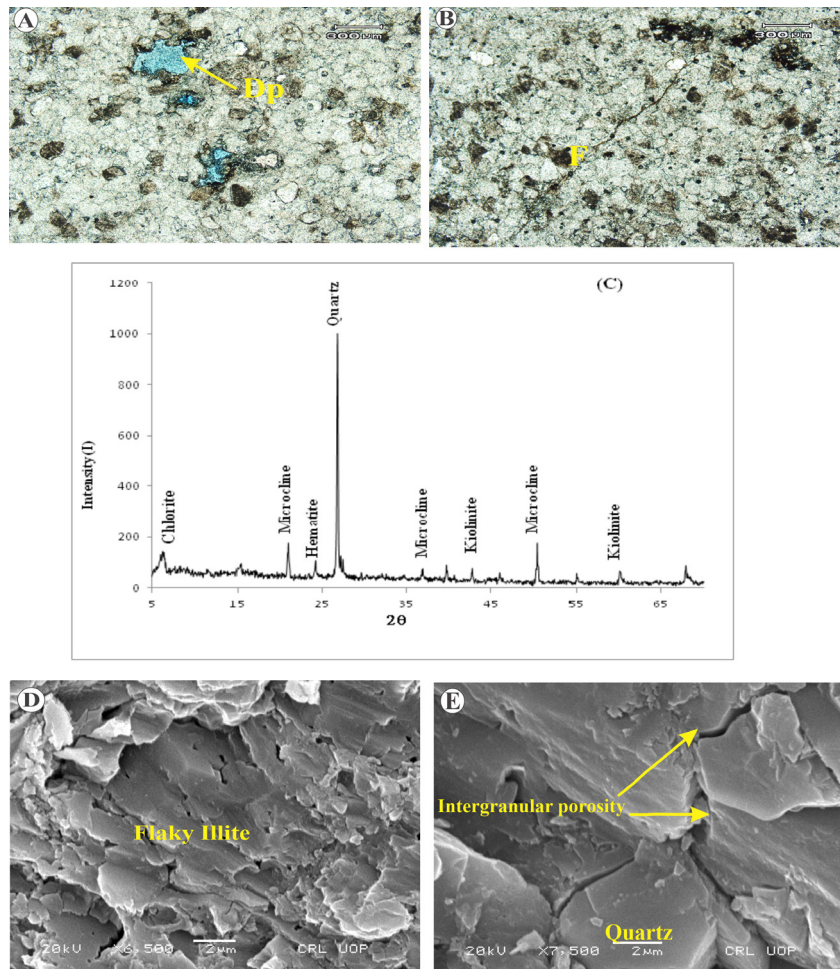


Plate 12. A, B: Photomicrographs of the Misri Band Quartzite showing tightly packed quartzite with dissolution porosity (Dp) and ferruginous clays (F); C: The XRD data are showing the bulk rock geochemistry of the Quartzite rocks; D, E: represent the SEM images showing the pore filling illite and inter-granular porosity.

perature recrystallization, which alters the size, shape, and lattice of the crystals without altering their mineralogy.

7. Conclusions

Hydrocarbon reservoir characterization has gained significance as numerous oil fields are getting mature around the world. The development of petroleum geology and reservoir characterization over time provides insight into how these issues have been overcome and what new methods and technologies will be used in the future. Integrated sedimentological, mineralogical and Nano porosity analysis of the Cambrian-Devonian clastic-carbonate mixed lithofacies of the Peshawar Basin in Pakistan has been seen as a significant tool in characterizing the hydrocarbon reservoirs in the study area.

The following conclusions are drawn from current investigations.

- The Ambar Formation is characterized by a mix of

siliciclastics and carbonates. The siliciclastic lime mudstones and ooidal peloidal limestones represent the carbonate portion of this shelf in the form of hyper saline lagoons and beaches. Whereas the fine grained sandstone, siltstone and sandy siliciclastic mudstone occupied the clastic dominated beach and lagoon environments. The deposition of formation, therefore, took place in the clastic and carbonate dominated near shore waters of the shelf.

- The XRD analysis indicated the presence of dolomite, micrite; goethite, kaolinite and illite are present as an intergranular mass while calcitic spar is present as fracture filling and a product of neomorphism in Ambar Formation. Dolomitization induced porosity, twin cleavage plane and high dissolution porosity confirmed from SEM image can provide significant pore space to the fluids creating it good reservoir.
- The deposition of the Misri Banda Quartzite oc-

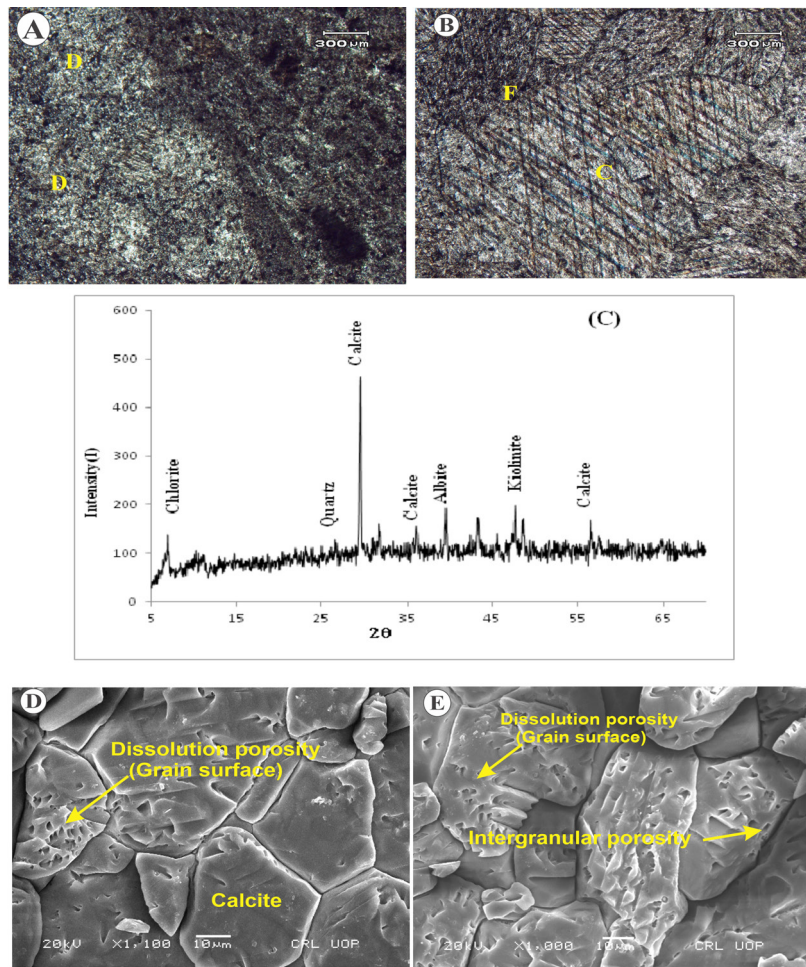


Plate 13. A, B: Photomicrographs of the Nowshera Formation illustrating its pore filling material, Calcite (C) Ferruginous clay (Fc) and dolomite D; C: The XRD data showing the bulk rock geochemistry of the Nowshera Formation lithologies showing the bulk geochemistry; D, E: represent the SEM images of the Nowshera Fm illustrating the dissolution and inter-granular porosities.

curred on the sandy beaches. The thin section of Misri Banda Quartzite shows lithic fragments dissolution. Hematite with some minor amount of kaolinite, illite and chlorite as alteration products of unstable framework grains as an intergranular mass in Misri Banda Quartzite confirmed from XRD analysis. Deep seated burial diagenesis has minimized the reservoir potential of the unit. It is concluded that Misri Banda Quartzite is a moderate Reservoir.

- The reefal buildups (Dolomites and carbonates) of the Nowshera Formation contain both coarse and fine calcite, dolomite, chlorite and kaolinite that occur as pore filling material between the framework grains. The SEM images display a high amount of intragranular dissolution and micro intergranular connecting porosity in the Nowshera Formation which makes it a promising reservoir.

Authors Contributions

Sajjad Ahmad conceptualized this research and drafted this manuscript. Sohail Raza completed his MS Geology research in this area of investigation while Suleman Khan's Contribution in the geological fieldwork and subsequent laboratory work are highly appreciated. All authors have read and agreed to the published version of the manuscript.

Funding

This research received no external funding.

Acknowledgement

The authors acknowledge the help of Rashed Maseh, Lab Attendant at the Department of Geology, University of Peshawar.

Data Availability Statement

Data will be made available on request.

Conflict of Interest

There is no conflict of interest.

References

- [1] Waagen, W., 1884. Section along Indus from Peshawar valley to the Salt Range. Geological Survey of India Records. 17, 118-123.
- [2] Griesbach, G.L., 1892. The geology of the Safed Koh. Records of the Geological Survey, India. 25(3), 59-109.
- [3] Middlemiss, C.S., 1896. The geology of Hazara and the Black Mountains. Memoir Geological Survey, India. 26, 302.
- [4] Wadia, D.N., 1931. The syntaxes of the north-west Himalaya: Its rocks, tectonics and orogeny. Records of the Geological Survey of India. 65, 190-220.
- [5] Martin, N.R., Siddiqui, S.F.A., King, B.H., 1962. A geological reconnaissance of the region between the lower Swat and Indus Rivers of Pakistan. Panjab University Geological Bulletin. 2, 1-13.
- [6] Davies, R.G., Ahmad, R., 1963. Fossils from the Hazara Slate Formation at Baragali, Hazara, West Pakistan. Punjab University Geological Bulletin. 3, 29-30.
- [7] Teichert, C., Stauffer, K.W., 1965. Paleozoic reef discovery in Pakistan. Science. 150, 1287-1288.
- [8] Burbank, D.W., 1983. Multiple episodes of catastrophic flooding in the Peshawar basin during the past 700,000 years. Geological Bulletin of the University of Peshawar. 16, 43-49.
- [9] Burbank, D.W., Tahirkheli, R.K., 1985. The magnetostratigraphy, fission-track dating, and stratigraphic evolution of the Peshawar intermontane basin, northern Pakistan. Geological Society of America Bulletin. 96(4), 539-552.
- [10] Fuchs, G., 1975. Contributions to the geology of the North-Western Himalayas. Geologische Bundesanstalt: Vienna.
- [11] Hussain, A., 1984. Regional geological map of Nizampur covering parts of Peshawar. Mardan and Attock Districts, Geological Survey of Pakistan, Geological Map Series. 14(1), 50,000.
- [12] Pogue, K.R., Hussain, A., 1986. New light on stratigraphy of Nowshera area and the discovery of early to middle Ordovician trace fossils in NWFP Pakistan. Geological Survey of Pakistan Information Release. 135, 15.
- [13] Yeats, R.S., Hussain, A., 1987. Timing of structural events in the Himalayan foothills of northwestern Pakistan. Geological Society of America Bulletin. 99(2), 161-176.
- [14] Pogue, K.R., Wardlaw, B.R., Harris, A.G., et al., 1992. Paleozoic and Mesozoic stratigraphy of the Peshawar basin, Pakistan: Correlations and implications. Geological Society of America Bulletin. 104(8), 915-927.
- [15] Treloar, P.J., Broughton, R.D., Williams, M.P., et al., 1989. Deformation, metamorphism and imbrication of the Indian plate, south of the Main Mantle Thrust, north Pakistan. Journal of Metamorphic Geology. 7(1), 111-125.
- [16] Ahmad, S., Khan, I., Khan, S. (editors), 2015. An insight into the southern fringe of Peshawar Basin as a new frontier for hydrocarbon exploration in North Pakistan. International Conference & Exhibition; 2015 Sep 15; Melbourne, Australia.
- [17] Flugel, E., 1989. Typen und wirtschaftliche Bedeutung von Rifkallen (German) [Types and economic importance of reef reefs]. Archiv fur Lagerstättenforschung der Geologischen Bundesanstalt Wien. 10, 25-32.
- [18] Scholle, P.A., Halley, R.B., 1985. Burial diagenesis: Out of sight, out of mind! Carbonate Sedimentology and Petrology. 4, 135-160.
- [19] Bathurst, R.G.C., 1972. Carbonate sediments and their diagenesis. Elsevier: Amsterdam.
- [20] Longman, M.W., 1980. Carbonate diagenetic textures from nearsurface diagenetic environments. AAPG Bulletin. 64(4), 461-487.
- [21] Harris, P.M., Kendall, C.G.S.C., Lerche, I., 1985. Carbonate cementation—a brief review. SEPM Special Publication. 36, 79-95.
- [22] Grigsby, J.D., 2001. Origin and growth mechanism of authigenic chlorite in sandstones of the lower Vicksburg Formation, south Texas. Journal of Sedimentary Research. 71(1), 27-36.
- [23] Berger, A., Gier, S., Krois, P., 2009. Porosity-preserving chlorite cements in shallow-marine volcanoclastic sandstones: Evidence from Cretaceous sandstones of the Sawan gas field, Pakistan. AAPG Bulletin. 93(5), 595-615.
- [24] Chang, H.K., Mackenzie, F.T., Schoonmaker, J., 1986. Comparisons between the diagenesis of dioctahedral and trioctahedral smectite, Brazilian offshore basins. Clays and Clay Minerals. 34, 407-423.
- [25] Tian, J.F., Chen, Z.L., Fan, Y.F., et al., 2008. Sha yan zhong zi sheng lu ni shi de fu cun, sheng zhang ji zhi ji fen bu (Chinese) [The occurrence, growth mecha-

- nism and distribution of authigenic chlorite in sandstone]. *Kuang Wu Xue, Yan Shi Xue He Di Qiu Hua Xue Tong Bao*. 27(2), 200-205.
- [26] Moraes, M.A., De Ros, L.F., 1992. Depositional infiltrated and authigenic clays in fluvial sandstones of the Jurassic Sergi Formation, Reconcavo Basin, northeastern Brazil. *Origin, Diagenesis and Petrophysics of Clay Minerals in Sandstones*, Society of Economic Paleontologists and Mineralogists Special Publication. 47, 197-208.
- [27] Hunt, J.M., 1979. *Petroleum geochemistry and geology*. W. H. Freeman and Company: San Francisco. pp. 617.
- [28] Foscolos, A.E., 1984. Diagenesis 7. Catagenesis of argillaceous sedimentary rocks. *Geoscience Canada*. 11(2), 67-75.



RESEARCH ARTICLE

Interpretation of Geothermal Magnetic Depths, Physicochemical Parameters and Heavy Metals Determination of Lamurde Hot-spring in the North-Eastern Benue Trough, Nigeria

Mukaila Abdullahi^{1*} Yunis B. Valdon² Fartisincha P. Andrew¹ Adamu Usman Abba³
Ibrahim Maigari⁴

1. Department of Science Laboratory Technology, Modibbo Adama University, P.M.B. 2076, Yola, Nigeria
2. Department of Geology, Modibbo Adama University, P.M.B. 2076, Yola, Nigeria
3. Nigerian Geological Survey Agency (NGSA), Abuja Office, 900108, Nigeria
4. Office of the Surveyor General, Adamawa State, Jimeta-Yola, 640001, Nigeria

ARTICLE INFO

Article history

Received: 2 May 2023

Revised: 17 August 2023

Accepted: 22 August 2023

Published Online: 30 August 2023

Keywords:

Aeromagnetic data

Lamurde hot-spring

Geothermal potential

Physicochemical parameters

Heavy metals

ABSTRACT

An integrated interpretation of the magnetic data and the analysis of physicochemical parameters and heavy metals from Lamurde hot spring has been done for the first time. The temperature of the hot spring was measured to be at 44 °C while the normal surface temperature is 25 °C. Three prominent magnetic anomalies were found at bottom depths of 11.379 ± 0.253 km, 13.015 ± 2.120 km and 9.161 ± 1.200 km suggesting that the Lamurde hot-spring is heated at deep mantle (13.015 ± 2.120 km) and issued to the surface through either local or regional fault system or both. The physicochemical analysis gave pH (7.93 ± 0.06), total chlorine (125.0 ± 2.89 µg/L), total dissolved solids TDS (202.0 ± 2 ppm), hardness (64 ± 1.73 µg/L), alkalinity (210 ± 4 µg/L) and nitrate (1.3 ± 0.3 µg/L). In comparison with that of WHO standards, the results indicated that all the physicochemical parameters studied except for alkalinity fall within the permissible limits. Heavy metals were identified and analyzed in the sampled water: lead (0.1501 ± 0.0007 mg/L), chromium (0.0729 ± 0.0007 mg/L), nickel (0.1987 ± 0.1476 mg/L), cadmium (0.0115 ± 0.0003 mg/L), copper (0.0442 ± 0.0008 mg/L), arsenic (0.0456 ± 0.0003 mg/L), iron (0.8016 ± 0.0005 mg/L), cobalt (0.0274 ± 0.0004 mg/L), selenium (undetectable), manganese (5.31 ± 0.0361 mg/L) and zinc (0.1629 ± 0.0004 mg/L). The concentrations of heavy metals observed in the area with the exception of Zn, Cu and Se are all above the standards for drinking water. Their concentrations are in the order of Mn > Fe > Ni > Zn > Pb > Cr > As > Cu > Co > Cd > Se. These results suggest that the Lamurde hot spring is a potential zone for Mn, Fe, Ni, Zn and Pb deposit.

*Corresponding Author:

Mukaila Abdullahi,

Department of Science Laboratory Technology, Modibbo Adama University, P.M.B. 2076, Yola, Nigeria;

Email: mukailaa.agp@mau.edu.ngDOI: <https://doi.org/10.36956/eps.v2i2.852>

Copyright © 2023 by the author(s). Published by Nan Yang Academy of Sciences Pte. Ltd. This is an open access article under the Creative Commons Attribution-NonCommercial 4.0 International (CC BY-NC 4.0) License. (<https://creativecommons.org/licenses/by-nc/4.0/>).

1. Introduction

The study of geothermal energy reserves of hot springs, from different geophysical data and methods, has been the interest of geophysicists to interpret the thermo-tectonics of a region [1-4]. Spatial mapping of thermally potential zones from a geophysical point of view requires prior information that could be in connection with the tectonic orogeny of the region [5]. Hot water from inside the ground as a result of naturally occurring geological or tectonic phenomena of the past is what is known as 'hot spring'. A study of the Lamurde thermal (hot) spring was recently conducted using geophysical data [3,6]. Hot water from springs habitually contains huge volumes of dissolved minerals in it with low pH [7,8].

The geochemistry of hot springs provides a better understanding of the physicochemical constituents of water under study as well as its origin, re-charging circumstances and heavy metals present. In a region under an intense volcanic regime, the physicochemical characteristics of hot spring in such regions are altered.

Lamurde hot spring is a sedimentary-volcanic region, which is expected to have huge concentrations of unlikeable and more toxic elements like arsenic, iron, lead, manganese and so on whose presence is guided by pH value

and other chemical conditions [9].

In the present work, analysis and interpretation of geothermal potential from magnetic signature and physicochemical parameters and heavy metals from sampled water of Lamurde hot spring has been done.

2. Geology of the Study Area

The Lamurde hot spring has a measured area of approximately 13.465 km square. The region (Figures 1 and 2) is characterized by undulating surfaces [6]. The area has a maximum sedimentary thickness of 6.5 km [10,11].

The Tertiary-Recent sediment of the study area has been compressionally folded, faulted and uplifted in several places during the mid-Santonian tectonic episode, producing a series of deformational structures including the Lamurde anticline as one of the major deformational structures in the Upper Benue Trough [6]. The major fracture associated with the Lamurde anticline is the Barashika fault which cross-cut the Cretaceous sediment. The Barashika fault provided the post-depositional zones that are favourable for uranium concentration in the area [10,6]. Hence, the area of Lamurde hot spring is associated with heat-generating lithological factors with a measured hot spring temperature of 44 °C while the normal surface temperature is 25 °C.

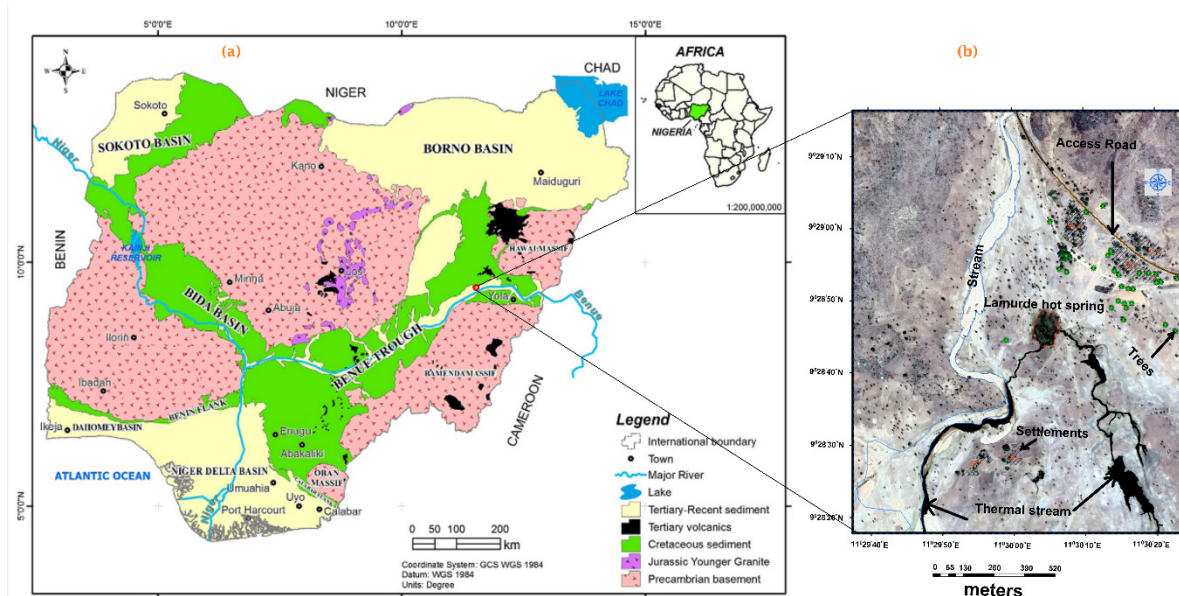


Figure 1. (a) The geological map of Nigeria shows the location of study. (b) The ground Google map, depicting the location of the Lamurde hot spring (Ruwan Zafi) measured approximately 13.465 km square and two channels through which the water from the hot spring run into the main water of the river Benue (i.e., named the thermal streams). These are shown in a distinctive black.

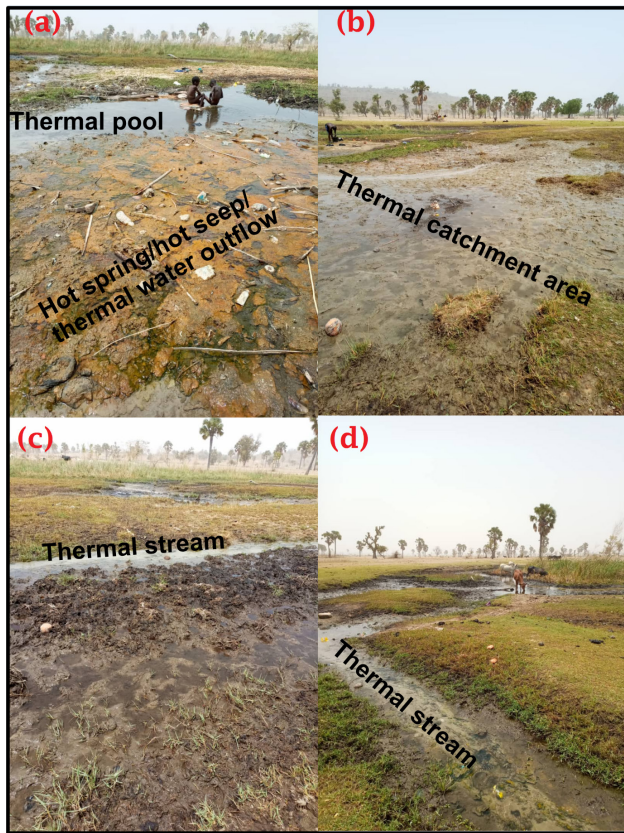


Figure 2. The Physical photographs of the Lamurde hot spring and environs. The hot spring temperature is measured to be 44 °C from the central hot-spring/hot-seep/thermal-water-outflow zone (a) and thermal-catchment area (b) while the normal surface temperature is 25 °C. The thermal-pool (a) is relatively warm around 39 °C where people from the near village called Kwanan Ruwan Zafi sit in to take their baths. Discussions with people from the village revealed that the area of the hot spring/hot-seep/thermal-water-outflow is very dangerous in fact is a no-go zone. The two channels through which the water from the hot spring run into the main water of the river Benue are named the thermal streams (c and d).

3. Data and Methods of Study

The magnetic anomaly of the area of study is shown in Figure 3. On the anomaly map, observed three prominent anomalies. By implication, the zone of low magnetic value could be associated with thick sediment or basin structure and the zones of high magnetic values are in connection with the near surface features or basement. From the prominent high anomaly marked (C2), the signature of the Lamurde hot is delineated and shown by a black star mark. The selected window cells (C1, C2 and C3) are the sizes of anomaly taken for the power spectrum of the calculation of bottom magnetic depths in the area under study.

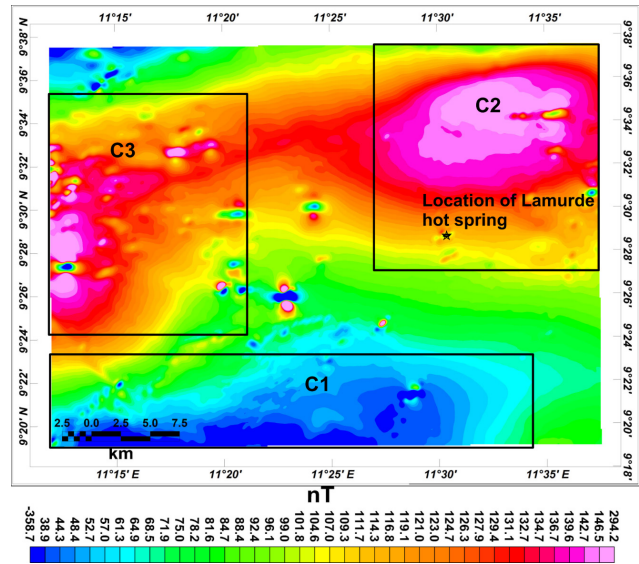


Figure 3. TMI map of the study area delineating the location of Lamurde hot-spring (shown with black star mark). The three prominent anomalies are taken as cells (C1, C2 and C3) for the spectral power spectrum for the calculation of the geothermal parameters.

3.1 Method of Estimation of Bottom (Curie) Depths

Curie depth with the utilization of the centroid method has been done in detail, application of the aeromagnetic data of the SW region of the Benue trough^[3]. The approach is the modification of Spector and Grant^[12] on the basis of a power law, to describe geologically, the heterogeneity of magnetization within a region^[13-18,3].

Simultaneous calculations of depth and ‘a parameter’ of scaling exponent from magnetic anomaly for the interpretation of the geology of a region are usually non-consistence^[19-21]. The scaling exponent for a region of known geology assumed a fixed value^[21,22]. Hence, in this study, the unity value of the scaling exponent for the regions’ geology is used for the depth computations.

3.2 Chemical Analysis of Water Sample from the Lamurde Hot-spring

All the chemicals and reagents used in this study were of analytical grade. Ethylene diamine tetra acetic acid (EDTA), sulphuric acids (H₂SO₄), methyl red indicator, ammonium buffer, ethanol and phenolphthalein indicator were purchased from commercial sources. Deionized water was used for the preparation of the sample and the standard solutions of the heavy metal ions.

The water sample was collected in a washed and cleaned polyethylene bottle. During sampling, the bottle was rinsed thrice with the water to be sampled. The col-

lected sample was transported to the laboratory and kept in a refrigerator for further analysis. The water sample was digested and prepared by methods [23].

Alkalinity and hardness were determined by EDTA titration, while nitrate, chlorine and heavy metals were determined by instrumental methods using a HACH Benchtop DR3900 spectrophotometer DR3900 and BUCK scientific 205 Atomic Absorption Spectrophotometer.

4. Results and Discussion

4.1 Geothermal Properties from High-resolution Aeromagnetic Data

Figure 4 shows the calculated depths from window cell C1 whereas. Table 1 presents the result of depths estimate of the top (Z_t) depths (km) and centroid (Z_0) depths (km) and bottom (Curie) depths (Z_b) in the area under study for the three window cells (C1, C2 and C3). These depths can be considered only provisional because the area of study is small for good resolution of depth interpretations [3]. The top depths have been calculated between 0.507 ± 0.0416 km and 0.966 ± 0.0576 km. These depths could be interpreted as the thickness of the tertiary-recent sediment within the region of study. The centroid depths as calculated between 4.46 ± 0.5790 km and 5.80 ± 0.0976 km are found comparable and inconsistent to the magnetic basement [18] calculated from the south-western region (middle and lower Benue trough). The present result of the bottom (Curie) depths between 9.161 ± 1.200 km and 13.015 ± 2.120 km are comparable with those calculated in the combined middle and lower Benue trough [3]. A higher calculated Curie depth of 13.015 ± 2.120 km is found over the location of Lamurde hot-spring which also interpreted a higher magnetic basement of 6.43 ± 1.0400 km. The intermediate Curie depth of 11.379 ± 0.253 km and magnetic basement of 5.80 ± 0.0976 km is calculated over the low magnetic zone in the study area. It could be expected that high magnetic basement as well as Curie depth to have been calculated over the low magnetic value [18,3]. In this case, it could be that basement is high but possibly intruded by low susceptibility material. The depth differences (approximately 2 km) from the three anomalies could indicate or suggest that the geothermal manifestation of the Lamurde hot spring is structurally controlled by local and regional deep fault systems.

4.2 Physicochemical Parameters of Water Sample

The important physicochemical parameters namely pH, total chlorine, total dissolved solids, total hardness and nitrate in comparison with that of WHO are presented in Table 2. The result indicates that all the physicochemical

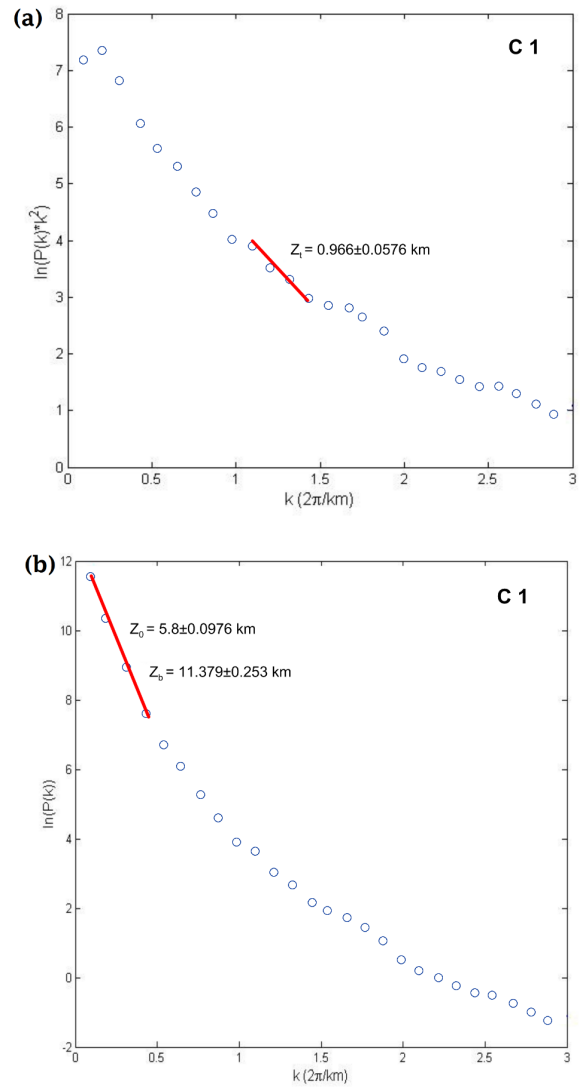


Figure 4. Plots of power spectra for the computation (a) of the top (Z_t) and (b) centroid (Z_0) and bottom (Z_b) depths with standard errors with the red lines showing the selected best fit in the C1 window cell.

Table 1. Estimated geothermal parameters with standard error from the high-resolution aeromagnetic data of the study area.

Cell number	Depth to top (Z_t) in km	Depth to centroid (Z_0) in km	Depth to bottom (Z_b) in km
C1	0.966 ± 0.0576	5.80 ± 0.0976	11.379 ± 0.253
C2	0.600 ± 0.0311	6.43 ± 1.0400	13.015 ± 2.120
C3	0.507 ± 0.0416	4.46 ± 0.5790	9.161 ± 1.200

parameters studied except for alkalinity fall within the WHO permissible limits. The pH of the water was found to be 7.93 ± 0.06 , which is within the WHO permissible limit. This indicates that according to the pH, the water is fit for drinking, recreation, agricultural and aquatic uses [24].

The total dissolved solids (TDS) consist of both ionized and unionized matter in water. The desirable limit of TDS in drinking is in accordance with WHO ranges (500-1000 ppm). The TDS of the water sample analyzed was found to be 202.0 ± 2 ppm which is within the WHO permissible limit.

The mean value of chloride, hardness and nitrate in the water sample were 125.0 ± 2.89 mg/L, 64 ± 1.73 mg/L and 1.3 ± 0.3 mg/L which is within the WHO values of 250 mg/L, 200 mg/L and 3 mg/L respectively. However, that of alkalinity (210 mg/L) is slightly above the WHO permissible limit (200 mg/L). High alkalinity has some positive effect of buffering acid rain and other acid waste that may have been washing off into the water body, thereby preventing pH changes that may be harmful to aquatic lives [25].

Table 2. Physicochemical parameters of the water sample and WHO permissible limit.

Parameters	Water sample	WHO permissible limit
pH	7.93 ± 0.06	6.5-8.5
Chloride ($\mu\text{g/L}$)	125.0 ± 2.89	250
Total Dissolved Solids (ppm)	202.0 ± 2	1000
Hardness (mg/L)	64 ± 1.73	200
Alkalinity (mg/L)	210 ± 4	20-200
Nitrate (mg/L)	1.3 ± 0.3	3

4.3 Heavy Metal Analysis

The heavy metals analyzed include lead, chromium, nickel, cadmium, copper, arsenic, iron, cobalt, selenium, manganese and zinc. The concentration of the heavy metals observed is shown in Figure 5 except for Zn, Cu and Se, all the metals analyzed are beyond the WHO permissible limit. The concentration of lead was averagely found to be 0.1501 ± 0.0007 mg/L higher than the 0.01 mg/L WHO permissible limit. The concentration of nickel and iron were found to be 0.1987 ± 0.1476 mg/L and 0.8016 ± 0.0005 mg/L which are above the WHO permissible limit of 0.07 and 0.3 mg/L respectively. Similarly, the concentration of chromium, cadmium and arsenic were found to be 0.0729 ± 0.0007 mg/L, 0.0115 ± 0.0003 mg/L and 0.0456 ± 0.0003 mg/L also above the WHO limit of 0.05 mg/L, 0.003 mg/L and 0.01 mg/L respectively. The concentration of manganese was the highest 5.31 ± 0.0361 mg/L above the 0.5 mg/L WHO permissible limit, while selenium was below the detectable limit. Cobalt was found to be 0.0274 ± 0.0004 mg/L, although, there is no any WHO prescribed guideline value for cobalt. For zinc and copper, the concentration was found to be 0.1629

± 0.0004 mg/L and 0.0442 ± 0.0008 mg/L which is within the WHO permissible limit of 3 mg/L and 2 mg/L respectively. The concentration follows the order $\text{Mn} > \text{Fe} > \text{Ni} > \text{Zn} > \text{Pb} > \text{Cr} > \text{As} > \text{Cu} > \text{Co} > \text{Cd} > \text{Se}$.

These results suggest that the Lamurde hot spring is a potential zone for Mn, Fe, Ni, Zn and Pb deposit. The concentration of Mn is the highest followed by Fe. Water with high concentrations of Fe and Mn is not healthy for human consumption [9]. Manganese (Mn) is not found as a free element in nature but in combination with iron and other minerals. It is a metal with important alloy uses and specifically in stainless steel. Iron and manganese are similar in chemistry and the manner; they are distributed and concentrated in rocks [9]. They originate from the Earth's crust and mantle and are usually described as the products of continental weathering, seafloor hydrothermal activity and sediment diagenesis [8,9]. The fraction of the iron and manganese from the continental weathering of which the volcanic Lamurde hot spring is one is more geologically recycled than that from the oceanic crust and the sediment diagenesis in this regard is the process for further recycling of the metals (Mn and Fe) within the sediment's column [9].

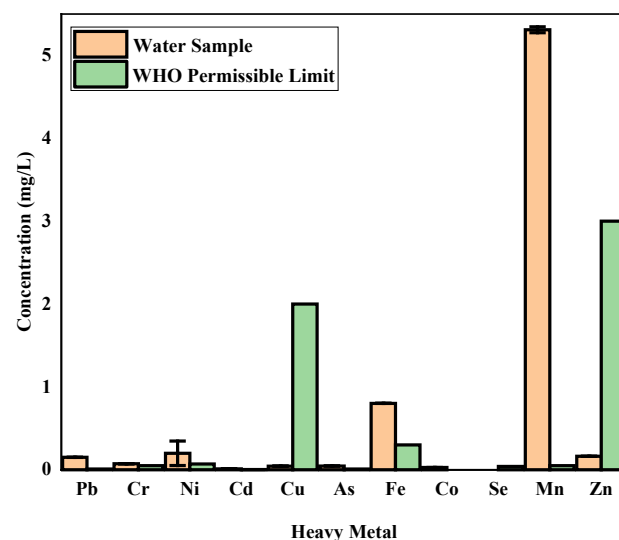


Figure 5. The mean value of the heavy metals compared with WHO Standard permissible limit.

5. Conclusions

The high-resolution aeromagnetic data of this region is analyzed. From the magnetic data, we see a fault signature from the location of the Lamurde hot spring. The large differences of geothermal depths (which is beyond 2 km) calculated over the three magnetic anomalies in the region are also an indication that the water from the Lamurde hot-spring is heated from deep (13.015 ± 2.120

km) Earth's mantle and issued at the surface through a volcanic fault system.

The Lamurde volcanic hot-spring content concentrations of metals in the order: Mn > Fe > Ni > Zn > Pb > Cr > As > Cu > Co > Cd > Se. Determination of the amount of these elements in the hot spring is in order to protect public health. This study showed that the concentration of Fe and Mn are significantly higher than acceptable standards in drinking water.

Author Contributions

Mukaila Abdullahi (MA), Yunis B. Valdon (YBV), Fartisincha P. Andrew (FPA), Adamu Usman Abba (AUA), Ibrahim Maigari (IM).

MA, FPA were responsible for project conceptualization, administration, data collection, analysis, literature work, funding acquisition and writing of the original draft of the article. MA, YBV, AUA and IM were responsible for the geological survey of the study area, data generation, review and final editing. Additionally, FPA and MA were responsible for the chemical analysis of the water sample from the study area and correspondence respectively.

Acknowledgement

The aeromagnetic data of this location was obtained from the Nigerian Geological Survey Agency (NGSA), Abuja office. The research was funded by Tertiary Education Trust Fund (TETFund), Nigeria under the Institutional Based Research (IBR) fund. The authors also acknowledge the Research and Development (R&D) office of Modibbo Adama University Yola, Nigeria through which the research fund was released, and the Departments of Science Laboratory Technology and Chemistry where the research was conducted.

Data Availability Statement

The data used in the work is readily available on request from the corresponding author.

Funding

The research was funded by Tertiary Education Trust Fund (TETFund), Nigeria under the Institutional Based Research (IBR) fund.

Conflict of Interest

The authors declare that they have no conflict of interest.

References

- [1] Obande, G.E., Lawal, K.M., Ahmed, L.A., 2014. Spectral analysis of aeromagnetic data for geothermal investigation of Wikki Warm Spring, north-east Nigeria. *Geothermics*. 50, 85-90.
- [2] Nwankwo, L.I., 2015. Estimation of depths to the bottom of magnetic sources and ensuing geothermal parameters from aeromagnetic data of Upper Sokoto Basin, Nigeria. *Geothermics*. 54, 76-81.
- [3] Abdullahi, M., Kumar, R., 2020. Curie depth estimated from high-resolution aeromagnetic data of parts of lower and middle Benue trough (Nigeria). *Acta Geodaetica et Geophysica*. 55(4), 627-643.
- [4] Ngansom, W., Pirarai, K., Dürrast, H., 2020. Geological setting and hydrogeothermal characteristics of the Kapong non-volcanic hot spring area in Southern Thailand. *Geothermics*. 85, 101746.
- [5] Wang, Z., Jiang, G., Zhang, C., et al., 2019. Thermal regime of the lithosphere and geothermal potential in Xiong'an New Area. *Energy Exploration & Exploitation*. 37(2), 787-810.
- [6] Idi, B.Y., Maiha, A.I., Abdullahi, M., 2022. Spatial mapping and monitoring thermal anomaly and radiative heat flux using Landsat-8 thermal infrared data—A case study of Lamurde hot spring, upper part of Benue trough, Nigeria. *Journal of Applied Geophysics*. 203, 104654.
- [7] Shanker, R., Thussu, J.L., Prasad, J.M., 1987. Geothermal studies at Tattapani hot spring area, Sarguja district, central India. *Geothermics*. 16(1), 61-76.
- [8] Chandrasekharam, D., Antu, M.C., 1995. Geochemistry of Tattapani thermal springs, Madhya Pradesh, India—field and experimental investigations. *Geothermics*. 24(4), 553-559.
- [9] Esteller, M.V., Kondratenko, N., Expósito, J.L., et al., 2017. Hydrogeochemical characteristics of a volcanic-sedimentary aquifer with special emphasis on Fe and Mn content: A case study in Mexico. *Journal of Geochemical Exploration*. 180, 113-126. DOI: <https://doi.org/10.1016/j.gexplo.2017.06.002>
- [10] Haruna, I.V., Ahmed, H.A., Ahmed, A.S., 2012. Geology and tectono-sedimentary disposition of the Bima sandstone of the Upper Benue Trough (Nigeria): Implications for sandstone-hosted Uranium deposits. *Journal of Geology and Mining Research*. 4(7), 168-173.
- [11] Abdullahi, M., Singh, U.K., 2018. Basement geology derived from gravity anomalies beneath the Benue Trough of Nigeria. *Arabian Journal of Geosciences*.

- 11, 1-8.
- [12] Spector, A., Grant, F.S., 1970. Statistical models for interpreting aeromagnetic data. *Geophysics*. 35(2), 293-302.
- [13] Tanaka, A., Okubo, Y., Matsubayashi, O., 1999. Curie point depth based on spectrum analysis of the magnetic anomaly data in East and Southeast Asia. *Tectonophysics*. 306(3-4), 461-470.
- [14] Bansal, A.R., Gabriel, G., Dimri, V.P., 2010. Power law distribution of susceptibility and density and its relation to seismic properties: An example from the German Continental Deep Drilling Program (KTB). *Journal of Applied Geophysics*. 72(2), 123-128.
- [15] Bansal, A.R., Gabriel, G., Dimri, V.P., et al., 2011. Estimation of depth to the bottom of magnetic sources by a modified centroid method for fractal distribution of sources: An application to aeromagnetic data in Germany. *Geophysics*. 76(3), L11-L22.
- [16] Bansal, A.R., Dimri, V.P., Kumar, R., et al., 2016. Curie depth estimation from aeromagnetic for fractal distribution of sources. *Fractal solutions for understanding complex system in earth sciences*. Springer: Berlin. pp. 19-31.
- [17] Kumar, R., Bansal, A.R., Anand, S.P., et al., 2018. Mapping of magnetic basement in Central India from aeromagnetic data for scaling geology. *Geophysical Prospecting*. 66(1), 226-239.
- [18] Abdullahi, M., Kumar, R., Singh, U.K., 2019. Magnetic basement depth from high-resolution aeromagnetic data of parts of lower and middle Benue Trough (Nigeria) using scaling spectral method. *Journal of African Earth Sciences*. 150, 337-345.
- [19] Ravat, D., Pignatelli, A., Nicolosi, I., et al., 2007. A study of spectral methods of estimating the depth to the bottom of magnetic sources from near-surface magnetic anomaly data. *Geophysical Journal International*. 169(2), 421-434.
- [20] Bouligand, C., Glen, J.M., Blakely, R.J., 2009. Mapping Curie temperature depth in the western United States with a fractal model for crustal magnetization. *Journal of Geophysical Research: Solid Earth*. 114(B11).
- [21] Li, C.F., Lu, Y., Wang, J., 2017. A global reference model of Curie-point depths based on EMAG2. *Scientific Reports*. 7(1), 45129.
- [22] Fedi, M., Quarta, T., De Santis, A., 1997. Inherent power-law behavior of magnetic field power spectra from a Spector and Grant ensemble. *Geophysics*. 62(4), 1143-1150.
- [23] Gerenfes, D., Teju, E., 2018. Determination of some selected heavy metals in water, *Oreochromis niloticus* and *Labeobarbus intermedius* samples from Abaya and Chamo Lakes. *World*. 10(6), 1-11.
- [24] World Health Organization, 2004. Guidelines for drinking-water quality (Vol. 1). World Health Organization: Geneva.
- [25] Texeira, L., Calisaya-Azpilcueta, D., Cruz, C., et al., 2023. Impact of the use of seawater on acid mine drainage from mining wastes. *Journal of Cleaner Production*. 383, 135516.



RESEARCH ARTICLE

Results of the Application of Direct-search Mobile Technology in the Exploration Blocks of Shakal and Halabja (Kurdistan)

Mykola Yakymchuk¹ Arzu Javadova^{2*} Ignat Korchagin³

1. Institute for Applied Problems of Ecology, Geophysics and Geochemistry, Laboratory Lane, 1, Kyiv, 01133, Ukraine

2. MicroPro GMBH, st. Magdeburg 26, b, Gommern, 39245, Germany

3. Subbotin Institute of Geophysics of the NAS of Ukraine, Palladin Ave., 32, Kyiv, 03680, Ukraine

ARTICLE INFO

Article history

Received: 12 May 2023

Revised: 16 August 2023

Accepted: 21 August 2023

Published Online: 8 September 2023

Keywords:

Oil and gas

Exploration model

Breakthrough technology

Remote sensing

Mobile technology

Kurdistan

ABSTRACT

Using experimental studies of mobile exploration technology, which includes modified methods of frequency-resonance processing, decoding of satellite and photographic images, vertical electron resonant scanning of the geological section, and the method of integral assessment of oil and gas content, the authors identified the potential of large prospecting blocks and licensed areas within the Shakal and Halabja blocks in Kurdistan. In the Shakal exploration area, the authors received oil responses from 3 intervals: 1) 2771-2794 m, 2) 2795.3-2815.45 m, and 3) 2834.40-2854 m in limestone sections. In Halabja exploration area, oil responses were obtained from 12 intervals: 1) 297-311.5 m, 2) 328-330 m, 3) 1190-1260 m, 4) 2018-2020 m, 5) 2059-2061 m, 6) 2132-2133 m, 7) 2192-2201 m, 8) 2249-2276 m, 9) 2307-2310 m, 10) 2317-2321 m, 11) 2326-2329 m and 12) 3310-3340 m. These results suggest that the proposed alternative exploration model can provide a more direct means of assessing the hydrocarbon potential of large exploratory areas, even before other geophysical investigations provide detailed information on possible targets.

1. Introduction

The Kurdistan Region of Iraq opened to foreign investors through licence awards in 2002 and 2004. However, the main influx started in 2006 with the award of the first Production Sharing Contract (PSC) in the region ^[1]. The approval of the Kurdistan Oil and Gas Law in 2007 coincided with a further fifteen licence awards. A larger

number and more diverse range of companies operate in Kurdistan than in federal Iraq. Initial entrants consisted mainly of European and North American small caps along with private investment firms. Significant discoveries by these companies including DNO (Bastora & Tawke), Gulf Keystone (Shaikan), Heritage Oil (Miran West), HKN Energy (Swara Tika) and Western-Zagros (Kurdamir) have proven Kurdistan to be a prolific exploration region. In

*Corresponding Author:

Arzu Javadova,

MicroPro GMBH, st. Magdeburg 26, b, Gommern, 39245, Germany;

Email: javadova@micropro.de

DOI: <https://doi.org/10.36956/eps.v2i2.857>

Copyright © 2023 by the author(s). Published by Nan Yang Academy of Sciences Pte. Ltd. This is an open access article under the Creative Commons Attribution-NonCommercial 4.0 International (CC BY-NC 4.0) License. (<https://creativecommons.org/licenses/by-nc/4.0/>).

October 2011, ExxonMobil became the first major IOC to be awarded contracts in Kurdistan. It signed six PSCs to become the largest acreage holder in the region. Chevron and Total have since also entered the region with two/three M & A deals and one licence award each. Significant new oil and gas discoveries have recently been made in Kurdistan in northern Iraq, which has emerged as one of the Middle East's most active exploration provinces (Figure 1). Continued activity in these areas is expected to lead to reserves growth, even as oil production increases. Kurdistan continues to be an active exploration play involving the largest independent oil companies in the region, including Hess, Hunt, Marathon, Murphy, Oil Search, Repsol, Talisman, OMV and MOL (through its subsidiary Kalegran). There are also two Asian NOCs, Sinopec (through Addax) and KNOC operating in Kurdistan, while Dana Gas and Crescent Petroleum operate the

two gas fields, Kormor & Chemchemical.

The Shakal exploration block area is 632 km² with target study horizons of Paleocene and Miocene carbonate deposits. Shakal-2 (ST-1) was spudded on 23 June 2014 and reached the total depth (TD) of 2950 mMD on 31 December 2014. Shakal-3 well was spudded on 6 August 2014 and reached TD 3355 mMD on 23 December 2014.

The Halabja exploration block area is 1519 km² with target study horizons of Cretaceous and Paleocene carbonate and terrigenous deposits. It is believed that Kurdistan has significant yet-to-find reserves, but these two exploration block areas' geologies are more complex than they seem. After the geological and geophysical survey and drilling in the Shakal exploration block area, it needs to understand facies variation and structural evolution. Regardless of complex geology, both areas are located in a proven oil and gas zone.

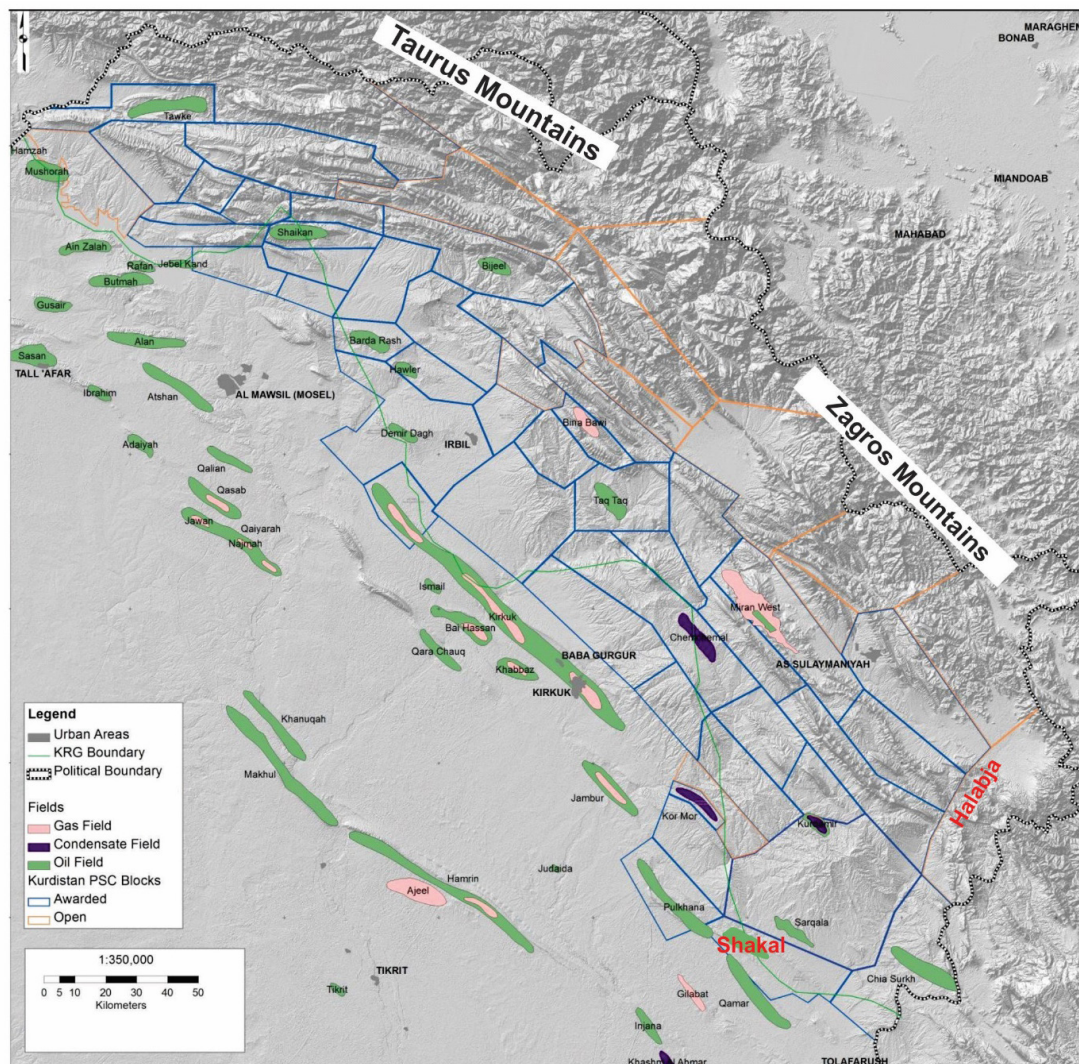


Figure 1. Shakal and Halabja area. Surrounding discoveries. Shakal & Halabja blocks are in the vicinity of significant oil and gas discoveries.

2. An Overview of the Regional Geological Background

From a regional geology point of view, the Zagros folded region occupies the extreme eastern region along the border with Iran within Iraqi Kurdistan and has a width not exceeding 50 km. Sedimentary-volcanogenic formations of the Mesozoic and Paleogene take part in the geological structure of the Zagros folded area. Mesozoic deposits are mainly represented by globigerina marls and radiolarites. Paleogene deposits—flysch and clastic rocks with a total thickness of over 5000 meters. The entire territory is characterized by a complex thrust structure. The angles of inclination of the fold along the overthrust vary from 20° to 50°.

According to tectonic the Iraqi Kurdistan lies on the border between two main geo-structural units—The Arabian part of the African platform and the Asian branches of Alpine. In general, three major tectonic zones ^[2] are developed in Northern Iraq (N-S):

- Thrust Zone
- Imbricated Zone
- High Folded Thrust Zone (Figure 2)
- Low Folded Thrust Zone (Figure 3)



Figure 2. High-folded thrust zone.

The occurrences of sediments and traps that generated and preserved hydrocarbons are linked to the history of the Arabian plate margin evolution ^[3]. The thick sedimentary cover of the Zagros orogenic belt records all the stages of evolution of the basin, evolving from a rift and passive continental shelf to a foreland basin associated with several stages of deformation related to obduction and collisions.



Figure 3. Low-folded thrust zone.

The Kurdistan Foreland basin has a complex geology and tectonostratigraphic framework which is not the subject of this paper. In the general geology map of Kurdistan (Figure 4) exploration blocks of Shakal and Halabja are located in the SE area of Iraqi Kurdistan.

According to seismic data, the geological feature of the surface expression is an NW-SE trending thrust fault that extends approximately 35 km in the strike direction and up to 8 km in the dip direction. Rocks of Tertiary age (Upper Fars and Lower Fars formations) are exposed in outcrop and are underlined by a Lower Tertiary to Cretaceous anticline that acted as a buttress and caused the younger rocks to be displaced by thrusts due to compressional tectonics (Figure 5). The structure extends from the town of Kalar to the SE and appears to continue the NW Pulkhana discovery completed in 2006. The producing fields of Jampur and Kirkuk are on trend and were originally thought to be structurally analogous to the Pulkhana and Shakal complex of structural closure. A review of drilling indicated that it should be possible to drill all of the primary objectives (Jeribe, Dhiban, Euphrates, Jaddala, and Shiranish formations) and potentially reach the secondary targets (Balambo and Qamchuga formations) as well. The closest analogue for the southern part of the Shakal block is Qara Dagħ field's, productive Mio-Oligocene and Cretaceous deposits. There are no analogues for the northern part, all the nearest blocks are at the same stage (Figure 6).

Halabja area is characterized by complex dissected relief. More than 50% of the area is occupied by medium-altitude mountains with absolute elevations of 1200-1600 m, and in the extreme east and north on the border with Iran up to 2000 m, only a small part of the territory has hilly and elevated relief. The northern part of the block is composed of rocks of the Mesozoic age. The Cenozoic section is completely absent. Cretaceous deposits of the Balambo, Kometan, Shiranish, Tanjero, and Qulqula formations outcrop occur at the surface. The southern part of the block is composed of rocks of the Meso-Cenozoic age. Deposits

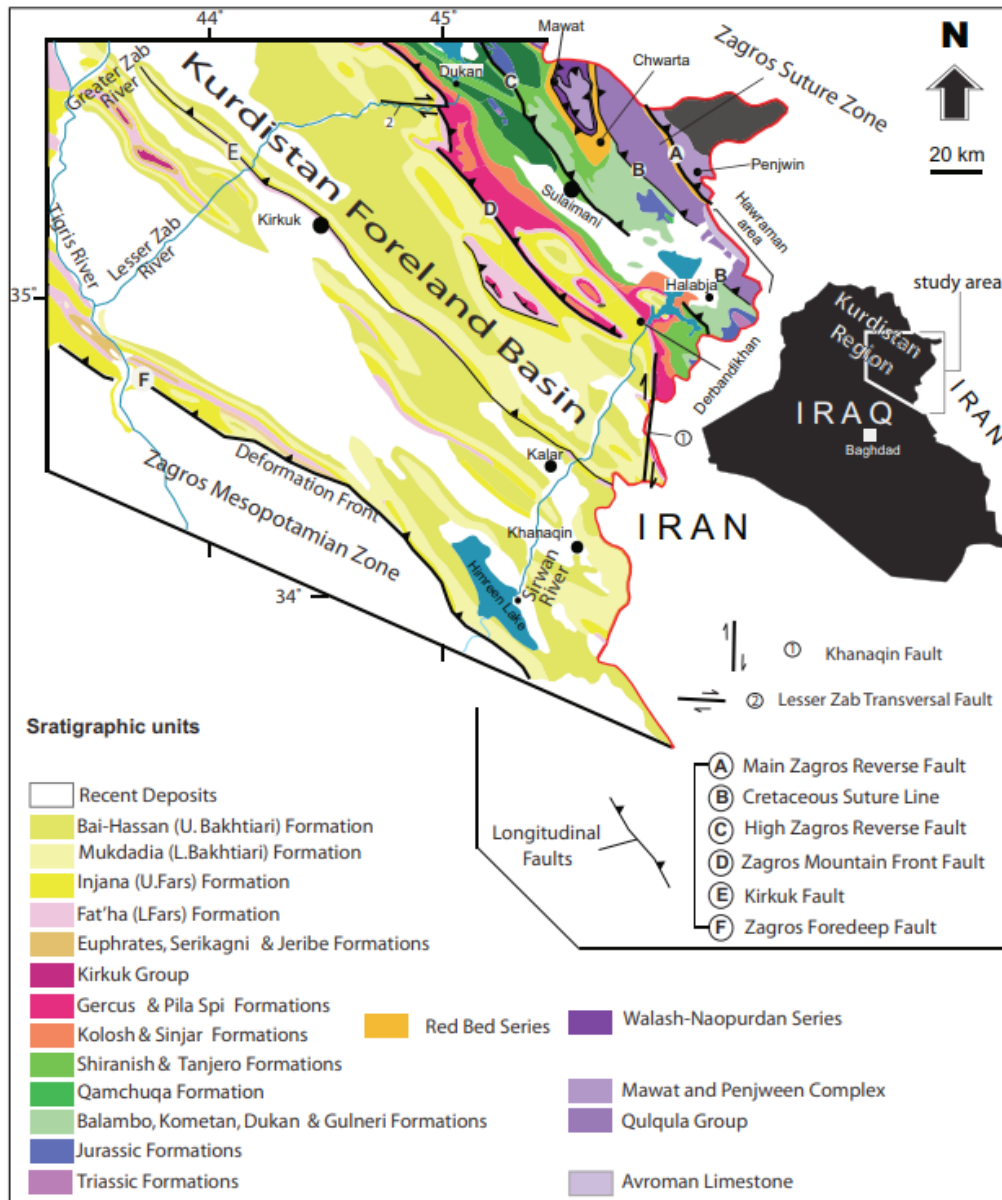


Figure 4. Geological map of the study area in the Kurdistan segment of the Zagros fold-thrust belt (modified from [4]).

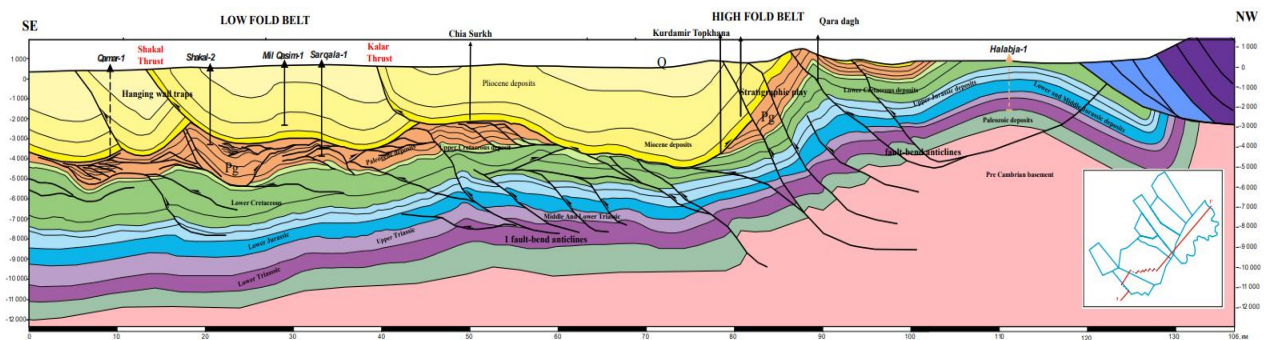


Figure 5. Geological features of the Shakal and Halabja blocks [5].

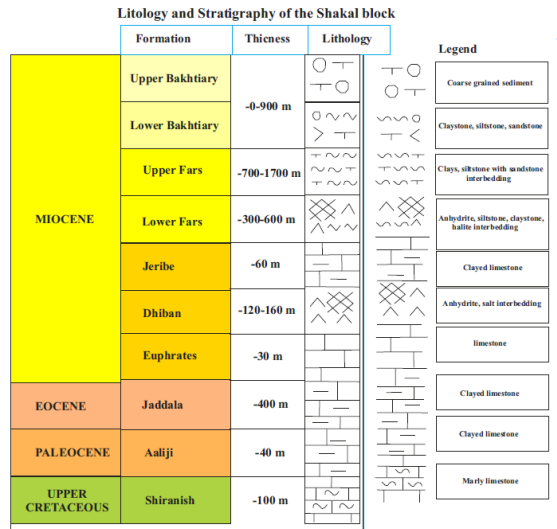


Figure 6. Lithology and Stratigraphy of Shakal block.

of the Paleocene, Eocene, and Miocene ages of the Kolosh, Sinjar, Gercus, Pila-Spi, and Fars formations occur at the surface. The Halabja block can be divided into two subblocks Upper Sirwan sub-block and Lower Sirwan sub-blocks. The Upper Shiwan Blocks occur within the Imbricated zone and consist of two Main subzones (a. Allochthonous part: consisting of Triassic and Jurassic Units with igneous intrusions; b. Autochthonous parts: consisting of the Triassic to Cretaceous rocks). Lower Sirwan sub-blocks consist of the Highly Folded Thrust zone of the foreland basin, and Low -Folded thrust zone whole Tertiary rocks are exposed on the surface (Figure 7).

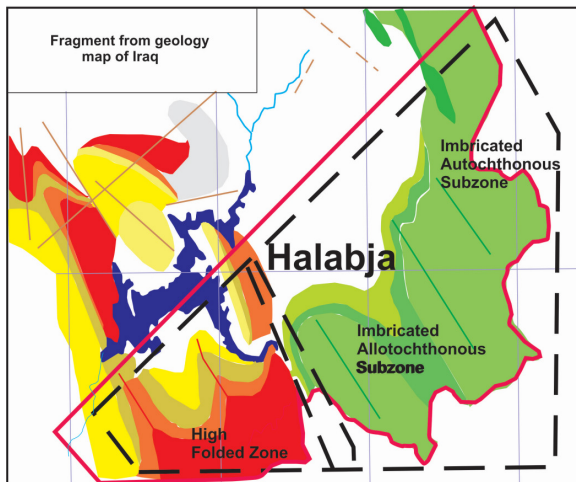


Figure 7. Halabja area. Tectonic zone. (Low Fold Belt: 36 total identified structures; 27 structures with HC shows; 3 failed structures; 6 undrilled blocks; Geologic Success Rate = 90%; High Fold Belt: 25 total identified structures; 11 structures with shows; 4 failed structures; 2 structures currently being tested; 9 undrilled blocks; Geologic Success Rate = 73.3%; Thrust belt: Remains untested).

Based on regional data (Figure 8) and neighbouring blocks (Qara-Dagh, SanGaw) the following potential reservoirs are expected in the Halabja area; 1) Cretaceous reservoirs: Qamchuqa, Kometan (Figure 9A) Shiranish; 2) Jurassic reservoirs: Barsarin (Figure 9B) Mus, Butman.

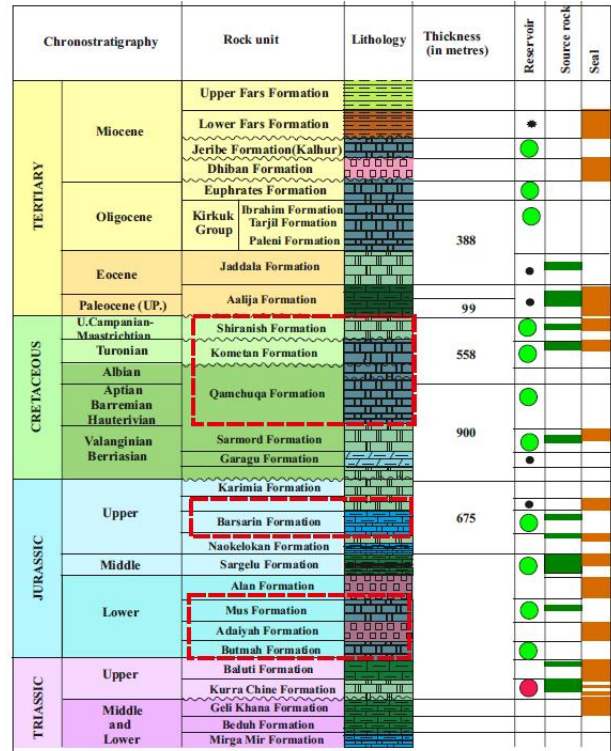


Figure 8. Stratigraphy of Halabja area. Oil reservoirs: Fars-N1, Jeribe-N1, Euphrates-Pg3, Kirkuk Group-Pg3, Jaddala-Pg2, Shiranish-K2, Gas reservoirs: Shiranish-K2, Chia Gara-J3, Kurra Chine-T3.



Figure 9. A: Limestones of the Kometan formation; B: Stromatolite limestones/dolomites of the Barsarin formation.

Halabja Block is a frontier acreage with no wells yet. Target horizons of the study: Carbonate and terrigenous sediments of the Cretaceous and Paleocene ages. The closest analogue for the southern part of Halabja is a Qara Dag, productive deposits of the Mio-Oligocene and Cretaceous. There are no analogues for the northern part, all the nearest blocks are in the same stage. According to geophysical data, the deep junction of structures in the south of the Halabja and Qara Dag blocks is still unclear,

but it is possible that they form a single zone. In terms of surface geology, it is assumed that Jurassic, Triassic, and possibly Upper Paleozoic deposits are promising.

3. Research Method

In geophysics, special attention is paid to electromagnetic (or so-called geoelectric) methods of oil and gas exploration. To date, there are advanced instruments for geophysical research, which can practically be considered direct indicators of hydrocarbons. These devices theoretically prognosis the presence of oil and gas accumulations, which even the best seismic methods still cannot do consistently and reliably. This is a direct reconnaissance method based on frequency-resonant processing and interpretation of remote sensing data. Direct-search mobile technology is carried out using frequency-resonance processing of satellite data and interpretation of space and photo images. The method also includes vertical electro-resonant sounding (scanning) of any studied section with the integral assessment of the prospects for the oil and gas (or ore) potential of search areas^[6]. Shortly we named it Mobile technology. Mobile technology successfully detects any subsurface substance (hydrocarbons, water, or other) with a 100% guarantee. The developed method is an effective express technology for the prompt solution of environmental, engineering-geological, and geological-geophysical problems. A phenomenological description of the technological features of mobile technology, in general, is as follows: “It is based on the latest achievements in astrophysics, mathematics, knowledge of electromagnetic radiation, computer technology, and software.”

From basic physics, it is known that the wave can be travelling or standing. A standing wave is an oscillatory (wave) process in distributed oscillatory systems with a characteristic spatially stable arrangement of alternating maxima (antinodes) and minima (nodes) of the amplitude. Such an oscillatory process occurs when several coherent waves interfere. An antinode is the section of a standing wave in which the oscillations have the greatest amplitude. When do standing waves occur? When primary and reflected sound waves meet in space, they overlap and interact. The result is a standing wave! It got its name because the distribution of nodes and antinodes in it is constant in time. Nikola Tesla was the first to discover standing electric waves in the deep horizons of the Earth, and Dr. Yakimchuk developed the appropriate equipment, which, based on Tesla’s theory, works as a direct reconnaissance method. So, the theoretical basis of the mobile technology method is based on “standing” electric waves, discovered by Nikola Tesla in 1899. The bottom line is

when we shout and hear a return echo, we know that the sound has reached a wall or other obstacle, reflected, and returned. Just like sound, an electrical wave is reflected, this phenomenon is known as a “standing wave”, that is, a wave with fixed nodes and antinodes. Tesla wrote: Instead of sending sound vibrations to a distant wall, I sent electrical vibrations deep into the Earth, and instead of a wall, the Earth answered me. Instead of an echo, I received a standing electrical wave reflected from the distant depths. The model of the structure of a fragment of the earth’s crust can be represented as a set of flat capacitors. N. Tesla believed that the Earth is a spherical capacitor formed by different layers (from the core to the surface of the Earth) with different parameters—thickness, permittivity, density, and contact potential difference. The model of the structure of a fragment of the earth’s crust can be represented as a set of flat capacitors. The dielectric constant of the formations is designated as ϵ_1 , ϵ_2 , ϵ_3 (respectively). Between the layers, a contact potential difference ΔU is formed and exists, the sign of which depends on the sign of the differences in the dielectric permittivity of the two contact layers. Thus, N. Tesla for the first time experimentally substantiated the possibility of sounding and studying the entire Earth using standing electric waves (Figure 10).

The theoretical substantiation of this technology is based on the fact that the atoms in all molecules have a certain spatial position and their electromagnetic field with a characteristic spatial-frequency intensity distribution. The spatial-frequency structure of electromagnetic fields of any substance is determined by the chemical composition and spatial structure of the molecules. A large amount of a homogeneous substance will create a collective electromagnetic field characteristic of this substance, the radiation power of which is proportional to the concentration of the substance in a given direction. We can assume that a linear polarization wave with a given frequency response, which carries information about the structure of matter, is not absorbed by the medium (environment) and its intensity does not decrease with distance. Then a homogeneous substance at a random depth of the Earth will create a field similar to how this substance would be on the surface. It turned out that the characteristic of electromagnetic waves of a large amount of hydrogen, oil, gas, water, and other substances is fixed in a certain way on a satellite image.

When carrying out instrumental measurements using the developed computerized complexes, the spectra of satellite, aerial, and other photographs of objects of study are sequentially compared with the spectra of rock samples, the desired minerals, and chemical elements. In modified versions of the methods of frequency-resonance process-

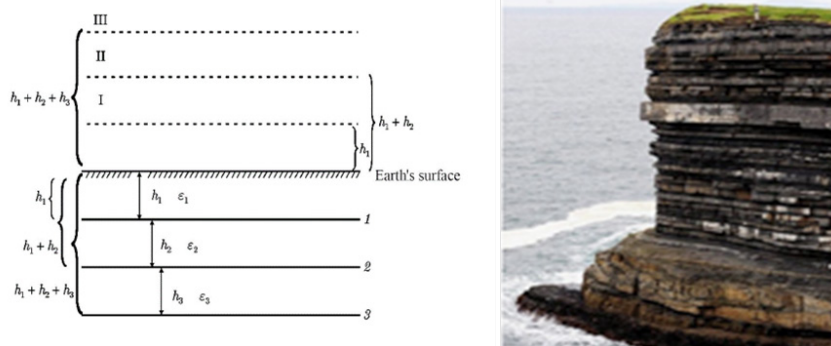


Figure 10. Model of the standing electric waves formation in the deep horizons of the Earth. Model (fragment) of the Earth's crust: h_1 - h_3 : thickness of sedimentary rock strata; ϵ_1 - ϵ_3 : their dielectric constant; 1-3: the boundaries of the layers; I-III: antinode of standing waves the length of the main waves has the following values: $\lambda_1 = 2h_1$; $\lambda_2 = 2(h_1 + h_2)$; $\lambda_3 = 2(h_1 + h_2 + h_3)$. The length of other waves is $4 = 2h_2$, $5 = 2h_3$, $6 = 2(h_2 + h_3)$, but they may not have antinodes on the earth's surface and their effect on the voltage on this plate will be minimal.

ing of satellite images and photographs, as well as vertical sounding (scanning) of the cross-section, existing databases (sets, collections) of sedimentary, metamorphic, and igneous rocks (<http://rockref.vsegei.ru/petro/>), minerals and chemical elements are used. Features and capabilities of the used method, as well as the measurement technique, are described in more detail ^[6-9]. Unlike classical geophysical methods, the mobile method used makes it possible to investigate the composition of the studied section. In each specific case, we obtain information on what the studied section consists of; what rock complexes are in it - sedimentary, metamorphic, or igneous? And we determine in the first approximation (and clarify at the stage of detailing) the intervals of the section that are promising for the detection of combustible and ore minerals, immediately, in the process of measurements (signal registration) by the developed instrumentation (i.e., without additional stages of modelling and geological interpretation of the results of instrumental measurements).

4. Results of Instrumental Measurements

The drilled wells within the Shakal exploration area were discovered by seismic studies shown in Figure 11. Shakal-3 well targeted the Jaddala-Aaliji reservoir interval which was encountered at a depth of 3280 mMD. The well was perforated behind the 7" liner against the reservoir intervals of Jaddala Fm. No hydrocarbon flow was found in the Jaddala-Aaliji interval. Shakal-2 well was initially planned to test by perforating behind the 7" liner against the reservoir intervals of Upper Jaddala and Euphrates formations. However, the interval of Dhiban formation was kept as an optional case to be reviewed and decided according to the results of the first two drill steam tests (DSTs). It was later tested as well and found oil shows in

the Upper Jaddala and Euphrates formations. Formation water was received from the Dhiban interval. In Shakal-1 well three DSTs tested in the Jaddala-Aaliji formations, which resulted also in oil shows. In the Dhiban interval was received formation water.

Signals from oil, condensate and sedimentary rocks of very weak intensity were recorded from the surface of the local area indicated in Figure 12. In this regard, further work was not carried out to fix the intervals of responses from hydrocarbons. However, within the entire block, intense signals were recorded from diamonds and graphite, as well as from the kimberlite volcano. The root of the kimberlite volcano was determined to be at a depth of 723 km. The upper edge of the kimberlite volcano was fixed at a depth of 120 m. Signals at diamond frequencies were recorded from 152 m.

4.1 Local Fragment within the Shakal Area

In the area of the drilled wells (rectangular contour in Figure 12), responses from oil, condensate, bacteria, phosphorus, dead water, diamonds and graphite, limestones and kimberlites were recorded from the surface. The lower limit of limestones as a potential hydrocarbon reservoir is fixed at a depth of 4676 m. At 2770 m, we determined the boundaries of the lower and upper parts of the productive section, which consists mainly of limestones. When scanning the section from a depth of 2770 m and further, we obtained responses of oil from limestones from 3 intervals: 1) 2771-2794 m, 2) 2795.3-2815.45 m, and 3) 2834.40-2854 m. Below 2854 m was missing oil responses. It should also be noted that there are no signals from oil at the surface of 2771 m from the upper part of the section. From this, it follows that the productive hydrocarbon intervals are between 2771 and 2854 meters.

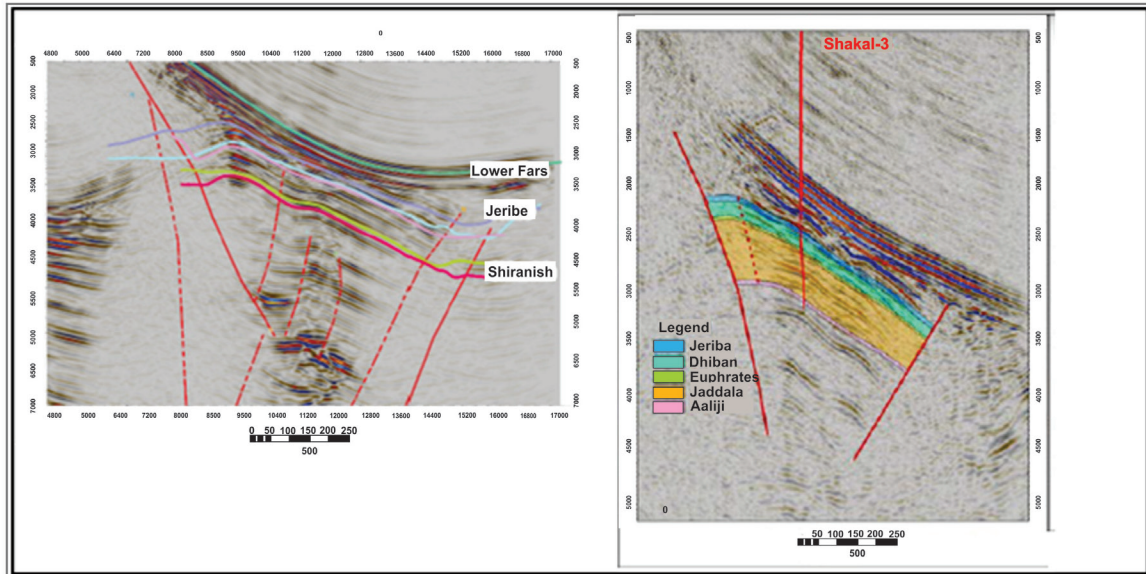


Figure 11. Seismic profiles through the Shakal structure.

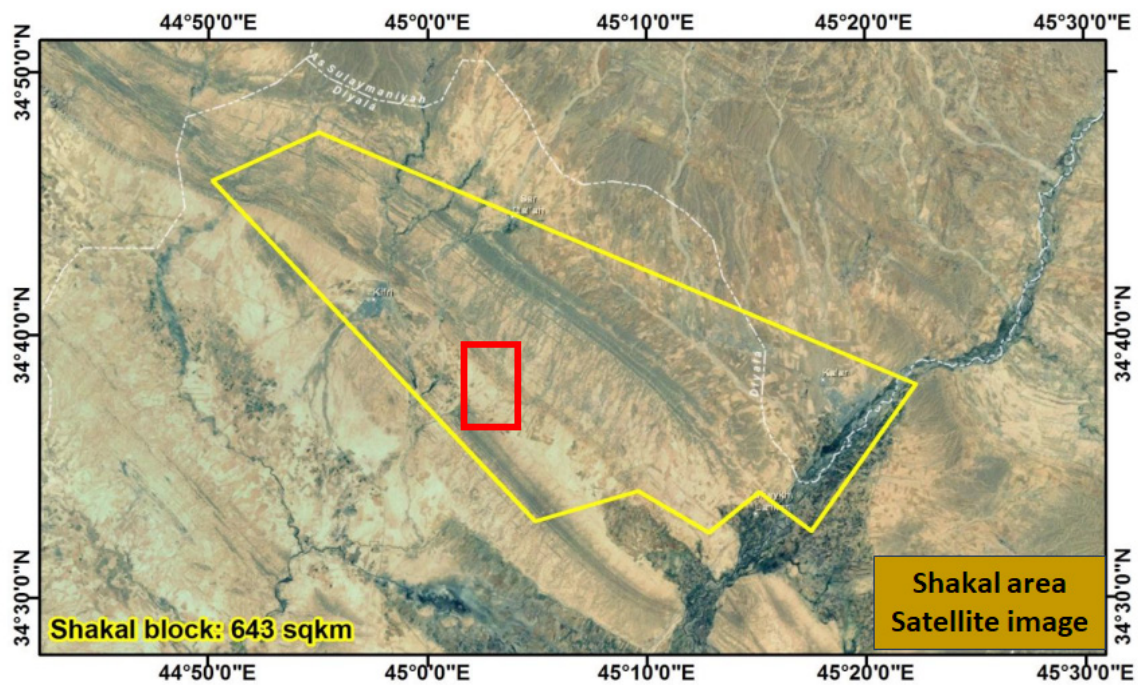


Figure 12. Satellite image of the Shakal area.

4.2 Halabja Exploration Area

No exploration drilling took place in the Halabja area. Based on analysis of regional data the expected reservoirs are carbonate. Local development of the seal is Lower Fars formation. On the adjacent block, oilfields are identified. High uncertainties in the Halabja area are structures at target formations; facies distribution and petrophysical properties of expected reservoirs; seal at the areas where

Lower Fars is absent and effective hydrocarbon maturation. All blocks around the Halabja area are in the exploration stage. In complex topography, large areas are under minefields.

Frequency resonance processing of a satellite image of the Halabja block (Figure 13) from the surface of recorded responses (signals) at the frequencies of oil, condensate, gas, phosphorus, bacteria, sodium chloride and dolomites.

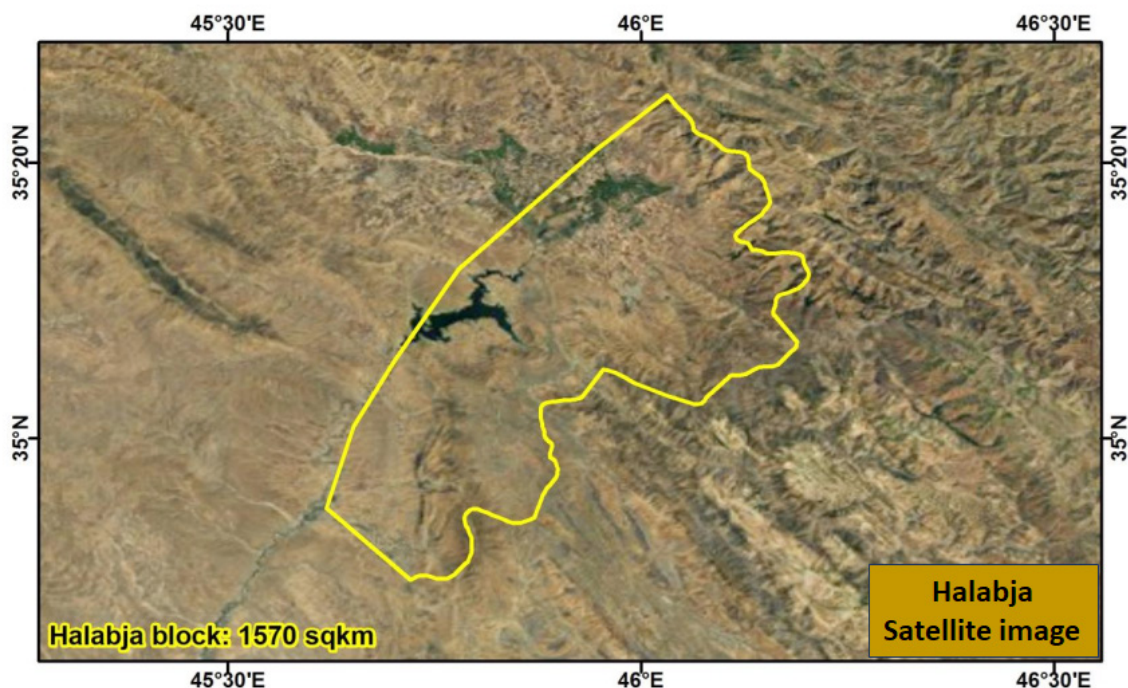


Figure 13. Satellite image of the Halabja area.

We adhere to the abiogenic-mantle origin of hydrocarbons. In the studied blocks of Kurdistan, the synthesis of hydrocarbons occurs at the 57-kilometre border. The applied mobile technology made it possible to register responses at the frequencies of oil, condensate, and gas in the Halabja area. In this area, the responses of a salt volcano were recorded. Scanning of the section made it possible to determine the upper boundary of the salt at a depth of 480 m. Oil responses were also received from 12 intervals:

1) 297-311.5 m, 2) 328-330 m, 3) 1190-1260 m, 4) 2018-2020 m, 5) 2059-2061 m, 6) 2132-2133 m, 7) 2192-2201 m, 8) 2249-2276 m, 9) 2307-2310 m, 10) 2317-2321 m, 11) 2326-2329 m and 12) 3310-3340 m. We traced the section up to 4 km (Figure 13). Below 3340 m there were no HC responses.

5. Discussions

Pilot studies on the territory of Kurdistan were carried out with the aim of additional testing, as well as improving the methodological methods of mobile technology. In fact, this was a continuation of earlier work, the results of which are presented in Yakimchuk et al., 2019^[4] and Yakimchuk et al., 2020^[5-7]. The obtained values of the cross-sectional parameters at the survey sites in Kurdistan are integral estimates, not point ones. To obtain point estimates, it is necessary to conduct a study with a dense grid over the entire area. A minimum survey grid should be carried out every 5 meters. Electromagnetic, resonant frequency signals must

travel vertically and horizontally as is common in conventional seismic surveys. The distinguishing feature is that mobile technology deals with satellite imagery and photographic images. In the study in the integrated mode, the object under study carries approximate predictive values, and in individual objects, it is performed by a limited number of measurement procedures.

The selected intervals of responses at the frequencies of oil and gas are areas for searching for oil and gas deposits. I would also like to note the fact that a kimberlite volcano with a root at a depth of 723 km and an upper edge at a depth of 120 m was discovered within the Shakal block. When scanning the section, responses at diamond frequencies began to be recorded from 152 m. a very interesting object for the search for diamond ore. The position of a diamond-bearing kimberlite volcano within the block can be determined by detailed processing of a satellite image of the block. This means that the scanning procedure must be performed with a scanning step of at least 1 meter with a dense horizontal grid. This allows us to get more detailed information about the distribution of the diamond.

The materials presented above also testify to the expediency of using direct exploration methods at the stages of site selection for laying exploration wells. It is also expedient to carry out an additional survey of the identified structures using mobile geological exploration methods at the stages of planning on drilling exploration wells within them. It can be assumed that an increase in drilling suc-

cess by at least two times will contribute to a significant increase in the efficiency of the exploration process. This is also evidenced by the results of the approbation of mobile technology in areas of exploratory wells in various regions of the world. Studies of this nature were carried out on drilling rigs in the Black Sea (Maria-1, Melnik-1, within block 1-14 Khan-Kubrat, Tuna-1 area), in the North Sea (57°10.644'N, 01°07.066'E), South African shelf (Brulpadda-1AX), Angola shelf (6°19'4.8" S, 10°53'33" E), Pakistan shelf ("Kekra-1"), shelf Alaska (Mukluk, the most expensive in history), Peru shelf (Marina-1), Uruguay shelf (Raya-1), Lebanon shelf (Block 4), Azerbaijan shelf (SAX01), Omelkovschinskoye oil field (Republic of Belarus), at the Shebelinskaya-888 well, at the Zapadno-Krestishchenskoye field (emergency well) (Yakimchuk and Korchagin^[5-7]). Experiments carried out in Kurdistan have been added to the database, which testifies in favour of the deep (endogenous) genesis of hydrocarbons in the process of hydrogen degassing of the Earth.

6. Conclusions

The results of the conducted experimental investigations of an intelligence nature within two blocks in Kurdistan allow us to state the following:

A) Fixation of SW responses during frequency-resonance processing of satellite images of blocks indicates the expediency of carrying out a detailed search in their search work.

B) According to the results of the study of the section within the local section of the Shakal block, the interval of section 2760-2860 m is the most promising for the search for oil deposits.

C) Within the Halabja block, the most promising for oil exploration are intervals from 295 to 3340 m.

Research materials conducted at sites in Kurdistan demonstrate the operability and effectiveness of mobile technology in the search for hydrocarbon accumulations on land. Low-cost technology in general, can be used in various regions for a preliminary assessment of the oil and gas potential of little-studied and unexplored prospecting blocks and local areas. Promptly conducted additional studies by direct methods in local areas of drilling exploration wells will contribute to increasing the success of drilling (increasing the number of wells with industrial hydrocarbon inflows). Well, placement in the areas of vertical channels of fluid migration can lead to an increase in the inflow of hydrocarbons.

Author Contributions

Mykola Yakymchuk is an author of the mobile technol-

ogy methods. Arzu Javadova took an active participation in exploration drilling and G&G analysis of Shakal and Halabja area. Ignat Korchagin participated in different approbation of mobile technology in areas of exploratory wells in various regions.

Funding

There was no funding for this research.

Conflict of Interest

There is no conflict of interest.

References

- [1] Javadova, A., 2015. Kurdistan Operator Activity Updates [Internet]. ResearchGate. Available from: https://www.researchgate.net/publication/373489995_Kurdistan_Operator_Activity
- [2] Lawa, F.A., Koyi, H., Ibrahim, A., 2013. Tectono-stratigraphic evolution of the NW segment OF the Zagros fold-thrust belt, Kurdistan, NE Iraq. *Journal of Petroleum Geology*. 36(1), 75-96.
- [3] Berberian, M., 1995. Master "blind" thrust faults hidden under the Zagros folds: Active basement tectonics and surface morphotectonics. *Tectonophysics*. 241(3-4), 193-224.
- [4] Sissakian, V.K., 2000 Geological map of Iraq, scale 1:1000000, 3rd edition. Iraq Geological Survey Publications: Baghdad.
- [5] Javadova, A., 2016. Geological Features of South-west-North East Kurdistan [Internet]. LinkedIn Post. Available from: <https://www.linkedin.com/pulse/geological-feature-south-west-north-east-kurdistan-dr-arzu-javadova/>
- [6] Якимчук, Н.А., Корчагин, И.Н., Бахмутов, В.Г., et al., 2019. Геофизические исследования в Украинской морской антарктической экспедиции 2018 г.: мобильная измерительная аппаратура, инновационные прямопоисковые методы, новые результаты (Russian) [Geophysical research in the Ukrainian Marine Antarctic Expedition 2018: mobile measuring equipment, innovative direct search methods, new results]. *Геоинформатика*. 1, 5-27.
- [7] Якимчук, Н.А., Корчагин, И.Н., 2020. Технология частотно-резонансной обработки данных ДЗЗ: Результаты практической апробации при поисках полезных ископаемых в различных регионах земного шара. Часть 1. УДК 528+550.837+553.98. *Геоинформатика*, №. 3, pp. 29-51, 2019; Часть II. *Геоинформатика*. № 4, pp. 30-58, 2019; Часть III. *Геоинформатика*. № 1, pp. 19-41, 2020; Часть IV.

- Geoinformatika*. № 3, pp. 29-62 (Russian) [Technology of frequency-resonance processing of remote sensing data: Results of practical testing in the search for minerals in various regions of the globe. Part 1. UDC 528+550.837+553.98. *Geoinformatics*, no. 3, pp. 29-51, 2019; Part II. *geoinformatics*. No. 4, pp. 30-58, 2019; Part III. *geoinformatics*. No. 1, pp. 19-41, 2020; Part IV. *geoinformatics*. No. 3, pp. 29-62]. Available from: <http://dspace.nbuv.gov.ua/handle/123456789/125236>
- [8] Якимчук, Н.А., Корчагин, И.Н., 2020. О целесообразности дополнительного применения мобильных прямопоисковых методок на участках бурения скважин на нефть и газ (Russian) [On the feasibility of additional use of mobile direct search methods in the areas of drilling wells for oil and gas]. *Azerbaijan Geologist*. 24. 49-66.
- [9] Якимчук, Н.А., Корчагин, И.Н., 2020. Аprobация прямопоисковой технологии частотно-резонансной обработки спутниковых снимков и фотоснимков на известных месторождениях углеводородов в различных регионах (Russian) [Approbation of direct search technology for frequency-resonance processing of satellite images and photographs at known hydrocarbon deposits in various regions]. *Геоінформатика*. 2, 3-38.



REVIEW

Origin of the Moon and Lunar Water

Nick Gorkavyi*

Science Systems and Applications, Inc., Lanham, MD 20706, USA

ARTICLE INFO

Article history

Received: 31 August 2023

Revised: 11 October 2023

Accepted: 16 October 2023

Published Online: 20 October 2023

Keywords:

Moon

Mega-impact

Water

Asteroid satellites

ABSTRACT

Three principal concepts regarding lunar formation have been examined: the accretion hypothesis, the mega-impact theory, and the multi-impact model. The multi-impact model amalgamates the salient facets of the mega-impact theory and the accretion hypothesis. As per this model, fragments of the terrestrial crust are ejected into space during collisions with numerous planetesimals (proto-asteroids) with diameters around 10-100 kilometers. In the vicinity of Earth's orbit, this ejecta interacts with the accretion disk, augmenting its mass. Numerical computations demonstrate that particles within the prograde-rotating accretion disk effectively capture prograde-rotating ejecta while shedding retrograde-rotating ejecta onto the planetary body. The multi-impact theory provides an explanation for the creation of not just the Moon and Charon but also the satellites of asteroids. Several predictions regarding the parameters of asteroid satellites posited by this theory have already been validated through statistical analysis of binary asteroids. Different models of lunar formation yield varied conclusions regarding the quantity of lunar water, its subsurface distribution, and isotopic composition. The mega-impact theory postulates the genesis of a largely desiccated Moon. Consequently, the modest lunar water content may arise from comets, solar wind, or the transport of water from Earth's atmosphere. These mechanisms for lunar water formation imply its superficial occurrence in polar regions and substantial deviation of the deuterium-to-hydrogen (D/H) ratio from terrestrial norms. Conversely, the multi-impact theory posits lunar water's origin from planetesimals, akin to terrestrial water. Thus, a significant quantity of lunar water is inferred, expected to be pervasive across the lunar surface at varying depths, and possessing isotopic composition analogous to terrestrial water. Geomorphological structures in the lunar polar regions (smoothed craters, landslides, regular patterns) suggest the presence of a substantial permafrost layer with an approximate thickness of a kilometer.

1. Introduction

In recent years, various lunar exploration programs

have been actively advancing. The most ambitious among them are the programs of the United States^[1] and China,

*Corresponding Author:

Nick Gorkavyi,

Science Systems and Applications, Inc., Lanham, MD 20706, USA;

Email: nick.gorkavyi@ssaihq.com

DOI: <https://doi.org/10.36956/eps.v2i2.940>

Copyright © 2023 by the author(s). Published by Nan Yang Academy of Sciences Pte. Ltd. This is an open access article under the Creative Commons Attribution-NonCommercial 4.0 International (CC BY-NC 4.0) License. (<https://creativecommons.org/licenses/by-nc/4.0/>).

yet Russia, India, and Japan also have their lunar initiatives. As part of the Indian project “Chandrayaan-3”, on August 23, 2023, a lander along with a mobile rover successfully touched down in the vicinity of the Moon’s southern pole. The “Smart Lander for Investigating Moon” (SLIM), developed in Japan, was launched to the Moon on September 6, 2023. In November 2024, the American lunar rover “VIPER” (Volatiles Investigating Polar Exploration Rover) is planned to touch down in the vicinity of the Moon’s southern pole. One of the primary objectives facing these lunar landers is the search for and study of lunar water. The investigation of lunar water sheds light on the Moon’s origin, making it intriguing to analyze the lunar water predictions of different lunar origin models. Early descriptions of lunar formation models (such as capture and fission due to centrifugal force) can be found in Ringwood’s book [2]. Herein, our focus centers on three pivotal theories of lunar formation: the accretion model, the mega-impact theory, and the multi-impact model.

2. Accretion Model of Lunar Formation and Its Challenges

The Safronov group successfully formulated an accretion theory for the formation of terrestrial planets [3]. Ruskol proposed a similar accretion theory for the Moon’s formation from near-Earth protosatellite swarms [4]. Such a swarm around Earth was envisioned to accumulate from particles moving along heliocentric orbits, colliding within Earth’s gravitational field, and transitioning to near-Earth orbits, thus forming a protosatellite swarm or disk. The accretion model faces two significant challenges:

- a. The accretion mechanism leads to a relatively low mass fraction (10^{-3} to 10^{-4} of the planet’s mass) for the protosatellite swarm, which is inadequate to account for the Moon’s substantial mass fraction (1/81 or 1.2% of Earth’s mass, a record in the Solar System as of 1975);
- b. There is no explanation for the Moon’s average chemical composition, including its low density (3.3 g/cm^3) and iron deficiency (13% FeO) [5]. If the accretion theory holds, the Moon, formed similarly to Earth from planetesimals, should exhibit analogous parameters: a density of 5.5 g/cm^3 and an average iron content of 31% FeO [6].

3. Mega-Impact Model of Formation and Its Challenges

Until 1610, the Moon was perceived as a singular celestial body; no other natural satellites were known within the Solar System. However, four centuries ago, Galilei’s

observations revealed the presence of four new moons around Jupiter, marking the initiation of a new era of Solar System exploration. In terms of relative mass, the Moon exceeded all previously known satellites before 1978.

The Moon’s distinct status as a one-of-a-kind natural satellite led to the development of a unique theory about its origin: the mega-impact theory. This theory was initially proposed by R. Daly in 1946 and was further detailed in a 1975 publication by W. Hartmann and D. Davis [7]. According to this theory, larger celestial bodies that were forming near Earth’s orbit could have collided with Earth during the first 10^7 - 10^8 years, approximately 4.5 billion years ago. If a planetesimal with a radius of about 1200 km struck Earth’s surface at a speed of 13 km/sec, it could have provided enough kinetic energy to eject two lunar masses at nearly escape velocities [7]. Hartmann and Davis concluded that this model could explain the Moon’s characteristics, such as its reduced iron content, increased abundance of refractory elements, and depletion of volatile substances. In accordance with the Hartmann-Davis hypothesis, the protosatellite disk, and subsequently the moon, are postulated to form from ejected fragments of Earth’s crust and upper mantle, possessing a density similar to that of the Moon, approximately 3 g/cm^3 . This explanation also addresses the Moon’s iron deficiency, as Earth’s crust and mantle exhibit diminished iron content (6% FeO) [6] due to its concentration within the molten Earth’s core, where FeO constitutes 83% [6].

Hartmann and Davis employed a very moderate impactor mass estimate of 6.7×10^{-3} of Earth’s mass, merely half the mass of the Moon, for their calculations. However, Hartmann and Davis’s qualitative model did not account for the intricate issue of retaining material in near-Earth orbit. Within a two-body problem context, matter ejected from Earth due to impact cannot persist in near-Earth orbit. This ejecta must acquire hyperbolic velocity and escape onto heliocentric orbits or enter elliptical orbits around Earth, returning to Earth’s surface within a single revolution due to the lower part of such an orbit intersecting Earth’s surface.

Consequently, when scientists embarked on detailed calculations, they significantly deviated from the original Hartmann and Davis estimates. They augmented the impactor mass to the extent that the dynamics of smaller fragments conformed to the three-body problem, as fragments moved between Earth and the surviving part of the impactor. This adjusted model presented the possibility of retaining at least a fraction of the ejected material in orbit.

In accordance with this model, there was a colossal collision around 4.5 billion years ago involving Earth and a massive celestial body named Theia. Theia was approx-

imately the size of Mars, with a diameter of around 7,000 km. This extraordinary event resulted in fragments from the collision being placed into an orbit around Earth.

In the most contemporary calculations, the mass of the impacting planet has reached approximately half of the proto-Earth's mass^[8]. As a result of this catastrophic impact around Earth, a protolunar disk with significant angular momentum emerged. The model featuring a massive impactor resolved the issue of retaining a small amount of ejected material in near-Earth orbit but gave rise to another predicament: it was revealed that, under such a scenario, the Moon is formed not only from Earth's crust and mantle but also from material derived from the impacting Theia. Since Theia's isotopic composition is expected to differ from that of Earth, this implies that the isotopic composition of the Moon, which comprises a substantial portion of Theia's material, must also differ from that of Earth. However, as demonstrated in a series of studies, the isotopic composition of oxygen, titanium, and tungsten in lunar and terrestrial rocks aligns entirely.

The uniformity of isotopes implies that the material found on the Moon originated from the mantle of the early Earth^[9].

There are additional arguments against the mega-impact model. Geochemical analyses have led to the following conclusions regarding the catastrophic impact model^[5]:

- a. The Moon, which originated from Earth, must be younger than Earth;
- b. Due to the mega-impact, both the Moon and Earth should have experienced melting. This suggests that both Earth and the Moon likely had oceans of molten magma;
- c. The Moon's lack of volatile elements can be attributed to the heating of Earth's material ejected into orbit during the mega-impact.

However, empirical data from these geochemical analyses provide a somewhat different perspective^[5]:

- a. The Moon is older than Earth or, to be more precise, the Moon's core may have formed before Earth's core;
- b. The Moon appears to have been relatively cool and might not have been entirely covered in molten magma. Furthermore, geochemical data contradicts the idea of a molten mantle ocean on Earth. For instance, the Earth's current mantle shows less differentiation than it would if there had been a molten magma ocean in the distant past;
- c. The composition of volatile elements found on the Moon doesn't align with the mega-impact theory. These elements cannot be explained as originating from Earth's mantle through heating processes.

As a result, in the year 2000, geochemists J.H. Jones and H. Palme supported the model of lunar formation

from a near-Earth protosatellite disk generated through accretion^[5].

Charon, one of Pluto's moons, was discovered in 1978. Despite Pluto being a small, cold dwarf planet on the outskirts of the Solar System, Charon is relatively massive compared to its parent body, accounting for 12 percent of Pluto's mass. In contrast, the Moon only makes up 1.2 percent of Earth's mass, thereby diminishing the Moon's status as a unique satellite in terms of its relative mass. Furthermore, the phenomenon of substantial (approximately 10%) duplicity was observed among small solid-surfaced celestial bodies—asteroids and trans-Neptunian objects^[10]. In 1994, the first satellite of an asteroid (Ida) was photographed, followed by the discovery of the first triple asteroid (Sylvia) in 2005. Additionally, apart from Charon, four smaller and more distant satellites were detected around Pluto. It is noteworthy that the origin of Charon and asteroidal satellites within the framework of the mega-impact model appears highly implausible. This is due to the fact that collisions among bodies in the asteroid belt occur at speeds of several kilometers per second, while the initial escape velocity for asteroids is lower by 2-3 orders of magnitude. The matter ejected by a massive impactor is simply unfeasible to retain in orbit around an asteroid with weak gravity.

In 1989, Ringwood published an article^[11] in which he noted that the current version of this hypothesis is unlikely to be true for several reasons:

- 1) The probability of such an event is low.
- 2) If such a collision had occurred, it would have melted and separated the Earth's materials, resulting in chemical compositions different from what we observe.
- 3) The mechanics of this collision suggest that the Moon's composition would primarily come from the mantle of the impacting body, while the evidence from geochemistry strongly suggests that most of the Moon's material originated from the Earth's mantle instead.

Ringwood concludes that in the Moon's creation, impactors with masses of 0.001 to 0.01 times that of Earth were involved.

As far back as 1986, Ruskol introduced the concept that the Moon didn't originate from a single massive impact but rather from a series of "macro-impacts", which are essentially the same phenomenon but on a somewhat smaller scale. In these impactful events involving significant celestial bodies, the developing Earth isn't entirely obliterated. Instead, the ejections from the impact craters in the Earth's mantle are so forceful that they partially escape Earth's gravitational pull and spread into the nearby space, forming a swarm of materials^[12].

4. The Multi-Impact Model and Its Predictions

We maintain that the Hartmann and Davis model^[5] was accurate in its assessments of the maximum impactor mass. These assessments aligned with calculations by the Safronov group, which indicated that the mass of the second-largest body within Earth's vicinity should be close to 1% of Earth's mass. The issue of retaining material in near-Earth orbit, which remained unresolved in the Hartmann-Davis model, needed to be addressed not by doubling the impactor mass, but by considering an accretion disk that would inevitably accumulate near Earth. The interaction between the propelled ejecta and particles of the circumplanetary disk altered the trajectory of the ejecta, taking its dynamics beyond the scope of the two-body problem.

In 2004, Gorkavyi proposed the multi-impact model for the formation of celestial bodies like the Moon, Charon, and binary asteroids, which doesn't involve catastrophic events^[13]. Here are the key elements of this new model:

1) Moon Material from Earth: The majority of the Moon's material came from the Earth's mantle through multiple impacts by large asteroids (approximately 1-100 km in size). This explains why the Moon has a "low-iron" composition, similar to the single-impact model proposed by Hartmann and Davis.

2) Prograde Protosatellite Disk: Initially, there was a low-mass prograde protosatellite disk orbiting around the proto-Earth, similar to those seen around other planets.

3) Debris Collection: Collisions between Earth debris and particles in the prograde protosatellite disk played a crucial role in collecting the debris into stable orbits. Prograde Earth debris effectively joined the prograde protosatellite disk, while retrograde debris returned to Earth. Due to the prograde rotation of the Earth, the volume of prograde debris exceeds the volume of retrograde ejecta.

4) Optimal Ring Radius: Calculations regarding the transfer of angular momentum showed that the protosatellite ring should have an optimal radius, close to the average semi-major axis of debris orbits (A.M. Fridman, N.N. Gorkavyi "Physics of Planetary Rings", Springer, 1999, p.222-233). Earth debris pushed away a smaller ring and decreased the angular momentum of a larger ring.

5) Formation of Massive Ring: A massive, low-iron ring near Earth eventually accreted onto the Moon. In the final stages, Earth debris bombarded the newly formed Moon, resulting in a dichotomy of crater populations.

Predictions from this new multi-impact model include:

a. Satellite Orbits: Most satellites of asteroids should have prograde and circular orbits that are close to the equator of the central body, similar to the Moon-Earth and

Charon-Pluto systems.

b. Asteroid Rotation: Asteroids with satellites should rotate faster than single asteroids.

c. Satellite Absence: Low-rotating asteroids (or Earth-like planets) should generally lack satellites, as is the observed case with Venus and Mercury.

d. Satellite Mass: All else being equal, the relative mass of satellites can be larger for smaller asteroids.

e. Crater Dichotomy: The dichotomy of craters should be a common feature of Charon, Pluto, and large asteroid satellites.

f. Moon Signatures: The Moon should exhibit chemical, isotopic, and geological signatures of many different asteroid impacts from Earth.

This model provides an alternative explanation for the formation of these celestial bodies without the need for catastrophic events.

This qualitative hypothesis needs to be substantiated through detailed calculations. The most challenging issue pertains to the stability of the protosatellite disk, which is bombarded by ejecta propelled from Earth's surface by impacts from planetesimals. These impacts expel ejecta onto both prograde and retrograde orbits. Neglecting Earth's rotation, the cumulative angular momentum of the ejecta is zero. How does a low-mass protosatellite swarm with positive angular momentum interact with an intense stream of zero-net-momentum ejecta? Can the ejecta precipitate the protosatellite swarm to Earth?

To address these inquiries, a numerical model was developed, which investigated the interaction between protosatellite disk particles and bodies ejected from the Earth's surface^[14].

The article by Gorkavyi^[14] addresses the planar two-body problem in the case of Earth and a particle under the following conditions (neglecting the influence of the Sun and Earth's rotation effects):

1) The elliptical trajectory of the ejecta particle intersects the circular orbit of the satellite particle in the ascending branch (point A) and descending branch (point B).

2) The major axis and eccentricity of the intersecting orbits are specified, enabling us to readily determine the azimuthal and radial components of velocity for each particle at points A and B.

3) The collision of the two particles forms a cloud of debris, the center of mass of which moves away from the collision point with velocities determined by the conservation of momentum and the mass ratio between the ejecta and satellite particles.

4) With knowledge of the velocity vector of the center of mass of the debris, we determine the major axis and eccentricity of its trajectory and analyze:

a. How the debris orbit changes based on the mass ratio of particles, the orbit parameters of the ejecta, and the radius of the protosatellite swarm particle's orbit.

b. Whether the debris impacts the planet's surface or remains in a stable satellite orbit.

c. Whether the protolunar disk's mass decreases or increases under the influence of planet-originated ejecta. Does the disk maintain its orbital stability?

We postulate that the distribution of ejecta is symmetric with respect to the direction of Earth's revolution—meaning that for a certain number of particles ejected from the planet's surface onto prograde near-Earth orbits, an equal number of particles are ejected onto retrograde orbits. Two primary scenarios exist for the interaction between the disk particles and ejecta:

1) Ejecta with retrograde orbital rotation interacts with particles from the prograde disk, thus inevitably impacting Earth and carrying along a disk particle, if its mass is smaller or comparable to that of the ejecta particle.

2) Ejecta with prograde orbital rotation interacts with particles from the prograde disk and is highly likely to transition to a stable satellite orbit. Even a slight perturbation from a disk particle is sufficient to induce an increase in the ejecta's perigee, thus avoiding collision with Earth.

Figure 1 illustrates the growth and degradation profiles of a disk extending above the Earth's surface by 10,000 km. A study was conducted involving 1000 distinct values for ejecta particle masses ranging from 0.1 to 10 relative to the mass of disk particles. The number of particles is inversely proportional to their mass. Additionally, 1000 disk orbits (with a step of 10 km) of varying radii and 400 ejecta orbits with uniformly distributed eccentricities from nearly circular to 1 were examined. All ejecta orbits are tangential to the Earth's surface, thus their semi-major axes are consistent with this condition. The probability of ejecta interaction with each disk orbit was conventionally set at 1%. It is assumed that the debris cloud contributes to the disk orbit with a radius equal to the semi-major axis of the debris cloud orbit. The debris cloud distribution was examined within a space twice the size of the disk, up to 20,000 km above the Earth's surface. A total of 400 million debris cloud trajectories were analyzed.

It is evident that the parts of the protosatellite disk closest to the planet are vanishing (due to particle outward migration or collision with the planet), while in the rest of the disk, a confident growth (gain) is observed, dominating over the reduction (loss). The disk's growth is attributed to the accretion of prograde ejecta, which compensates for the disk's reduction caused by bombardment from retrograde ejecta. The examined mechanism effectively selects ejecta trajectories that align with the pro-lunar disk's

orbital motion. The qualitative results remain unchanged under substantial variations in the size distribution law of the ejecta particles or when considering an extensive disk extending up to 100,000 kilometers from the planet's surface. These calculations compellingly demonstrate the dynamic efficiency of the discussed lunar formation mechanism.

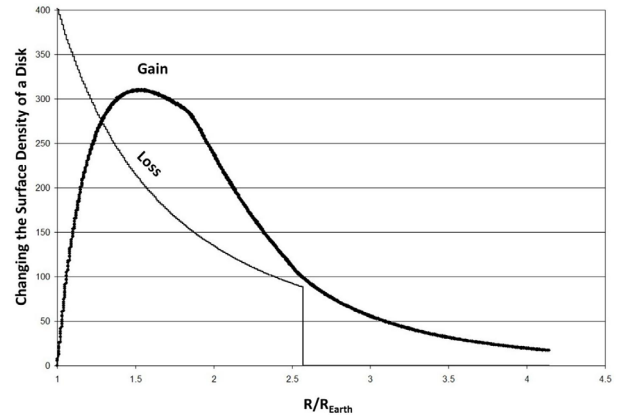


Figure 1. (From the article ^[14]). This graph illustrates the changes in surface density within the protosatellite disk caused by its interaction with the material ejected from Earth, with values measured in arbitrary units. Initially, the disk, which extends 10,000 kilometers above Earth's surface, is considered to be uniform in composition. The slender curve shows how the surface density of the disk decreases over time due to the material being expelled onto Earth after interactions with both prograde and retrograde ejecta trajectories. On the other hand, the bold curve depicts how the surface density of the disk increases over time as a result of material accreting onto it from the direct ejecta. The most favorable conditions for satellite formation occur within the zone of 2-3 Earth radii, where the increase (gain) in disk surface density significantly surpasses the losses.

In 2017, Rufu, Aharanson, and Perets published a similar article in *Nature-Geoscience* on the multi-impact formation of the Moon, demonstrating that the Moon's origin could be attributed to numerous moderate impacts rather than a single mega-impact event ^[15]. In their study, they examined a sequence of 20 impacts from bodies with masses ranging from 0.1 to 0.01 times that of Earth, which generated disks and subsequently formed satellites. These 20 satellites eventually merged to form a single larger Moon. The structure of the protosatellite disk presented in the Rufu, Aharanson, and Perets article ^[15] aligns well with Figure 1 from the article ^[14].

The lunar formation model, which combines the existence of an accretion disk around Earth along with the continuous replenishment of this disk through multiple macro-impact events, is actively developed within the

Moscow Safronov group. See, for instance, the work by Adushkin et al. ^[16] and the references therein. Ruskol discusses the asymmetry of craters and maria on the visible and far sides of the Moon ^[4]. The higher concentration of lunar maria (dark, flat plains) on the side of the Moon that faces Earth, particularly in the leading quarter of the lunar disk, could suggest that the Moon has been impacted by material ejected from Earth. Thus, the “maria” asymmetry suggests the occurrence of numerous and temporally distributed strong asteroid impacts, transporting material from Earth to the Moon.

Hence, the multi-impact theory of lunar formation combines the strengths of both the accretion theory and the original Hartmann-Davis mega-impact model. This model is independently developed by three groups of researchers, yielding similar outcomes. It remains consistent with contemporary geochemical data and avoids dynamic issues. A significant advantage of the multi-impact theory lies in its applicability not only to the Moon’s formation but also to the formation of Charon and asteroid satellites ^[17]. This broadens the opportunities for testing the theory against a substantial volume of observational data.

5. Comparison of Moon Formation and Binary Asteroids

In the study by Gaftonyuk and Gorkavyi, a database containing 113 binary asteroids was examined, with rotational periods and diameters of the primary components determined ^[18]. The predictions of the multi-impact model ^[13,14,17] were fully corroborated. The average rotation rate of single asteroids amounts to 3.54 rotations per day, whereas the average rotation rate of the primary bodies of binary asteroids was found to be nearly twice as high: 6.56 ± 0.28 rotations per day.

Furthermore, it has also been demonstrated that:

- 1) The satellites of asteroids exhibit solely direct orbits, typically characterized by low eccentricities and inclinations relative to the equator of the central body, thereby falling within the class of regular satellites.

- 2) The duality of asteroids (percentage of bodies with satellites) rapidly increases with the rotational speed of the primary body.

- 3) The percentage of duality among asteroids depends on the size of the main asteroid, and there is a minimum number of binary asteroids found among those sized between 10-100 km. Asteroids with satellites are most commonly observed in two size ranges: those smaller than 10 km and those larger than 100 km.

Consequently, asteroid satellite systems are regular and akin to satellite systems of typical planets. When considering mass relative to their respective primary bodies, the

Moon is positioned somewhere in the middle of the distribution of asteroid satellites, thereby definitively shedding the aura of uniqueness. Models of Moon formation in proximity to Earth and satellites around solid-surfaced planets must be unified, elucidating both the Moon and asteroid satellites. A potential question might arise: if the mechanism of asteroid satellite formation lacks substantial constraints on its efficacy, then why do only about 10% of asteroids manifest as binaries or possess satellites?

We posit that the actual percentage of duality among asteroids and trans-Neptunian objects is considerably higher; however, when the protosatellite disk transforms into an actual satellite, the mechanism of selection exclusively by direct ejection ceases to operate. A substantial satellite absorbs ejected material with a net zero angular momentum and converges with the primary body. The orbital velocity of the satellite is contingent upon the mass of the central body. Depending on the rotational velocity of the central body, the satellite can gently merge with it, thereby forming a binary system. Notably, certain asteroids, such as 486958 Arrokoth, exhibit a dumbbell shape or that of two agglomerated bodies (Figure 2).



Figure 2. The most detailed images of 486958 Arrokoth (Wenu $21.20 \times 19.90 \times 9.05$ km; Weeyo $15.75 \times 13.85 \times 9.75$ km ^[19]). New Horizons spacecraft, 1 January 2019 (<https://www.nasa.gov/feature/new-horizons-spacecraft-returns-its-sharpest-views-of-ultima-thule>).

The formation of another satellite on an outer orbit around such a binary system is also possible. A third body, undergoing a similar evolution, may decelerate and become incorporated into the already merged pair of bodies. This appears to be how the triple body of asteroid 9969 Braille was formed.

In the scenario where the moon follows a circular orbit and collides tangentially with a large, quasi-spherical

asteroid, it would leave an elongated trench (fossa) on the surface of the primary body. The asteroid Vesta, a large and fast-rotating celestial object with a diameter of 525 km, is an example of this phenomenon. Despite its size, Vesta does not possess any moons. However, a distinctive series of enormous fossae were discovered on its surface (indicated by blue arrows in Figure 3). These fossae are found in two formations: one near the equator (Divalia Fossae Formation) and another at approximately 30°N (Saturnalia Fossae Formation). These grooves extend to lengths of 300-400 km, widths of 10-20 km, and depths of up to 5 km (Figure 3). A moon orbiting Vesta would need to travel at a velocity of 900 km/h. If its orbital rotation aligns with the direction of Vesta's rotation, the moon would move relative to Vesta's surface at approximately 600 km/h. According to calculations, a moon with a mass roughly 10^{-3} times that of Vesta, having the same density, would possess enough kinetic energy before it completely breaks apart to create a canyon. This canyon would be 5 kilometers deep, 10 kilometers wide, and 1,000 kilometers long, even if the material it is moving through is as tough as durable granite. The specific energy required for this fragmentation process would be approximately 10^9 erg/cm³. The presence of two distinct sets of grooves suggests that Vesta encountered and incorporated two moons with inclined orbits. The author of this theory first introduced this concept in an interview with "New Scientist" ^[20] in 2015 and later elaborated on it in a more comprehensive discussion published in 2019 ^[21].

Attention is drawn to intriguing spiral structures in the polar regions, particularly prominent in the vicinity of the southern pole (indicated by yellow arrows). As calculations reveal, the absorption of a 50-kilometer-diameter satellite, moving in the direction of the blue arrows at a velocity of approximately 200 m/s, should lead not only to the formation of deep valleys, expanding the satellite's energy, but also to a global acceleration of the asteroidal crust in the equatorial region, utilizing the angular momentum of the satellite. Following the satellite's absorption, the crust with a thickness of around 10 km should acquire additional rotation at a rate of about one meter per second relative to the satellite's core and its polar regions. This additional angular momentum may induce a displacement of the crust with respect to the asteroid's main mass by ~100 km, resulting in the appearance of spiral structures in the polar region.

Another scenario that should be considered is a gentler interaction between an asteroid and its satellite. This scenario assumes that the moon has relatively low energy and cannot create a canyon or crater that is larger in volume than the moon itself. In such situations, for the creation

of a dumbbell-shaped asteroid, certain conditions must be met. These conditions include a constrained orbital velocity for the moon, represented as V , where $V^2 < 2E_v/\rho$. Here, E_v signifies the specific volumetric energy required for the asteroid's breakup, and ρ represents the moon's density. This velocity threshold is approximately 100 meters per second. Consequently, rapidly rotating asteroids with diameters of several hundred kilometers or less can display equatorial grooves, which essentially serve as the impact scars left by their moons. For asteroids with diameters less than one hundred kilometers, the interaction with a moon should result in the formation of a dumbbell-shaped structure.

In the issue of lunar formation, the primary question revolves around the source of material required for the creation of such a satellite. In the issue of asteroid belt formation, the key query pertains to the whereabouts of 99.97% of the mass of the belt. Interestingly, these two questions are intricately interconnected.

The actual masses of Mars and the asteroid belt differ significantly from the values that would be expected based on theoretical predictions derived from extrapolating the density of solid materials present in the protoplanetary disk near Venus and Earth. During collisions of planetesimals, a significant amount of dust is generated. A more detailed analysis has revealed that 10% of dust particles ranging in size from 0.2 to 40 micrometers acquire a significant eccentricity in their orbits due to the pressure of solar radiation. Eventually, Jupiter's gravitational field scatters these particles, causing them to exit the Solar System, on average, within about 30,000 years ^[22]. This process could explain a substantial loss of mass in both the asteroid belt and the Martian region ^[23]. The effectiveness of removing dust particles from asteroids, despite their weak gravitational pull, is supported by observations from spaceborne images. These images show that the surfaces of small asteroids exhibit rocky features, while the larger Moon's surface is covered by fine dust, which remains in place due to the Moon's gravitational forces (Figure 4).

The isotopic composition of noble gases found in surface regolith samples taken from asteroid 25143 Itokawa suggests that over a span of more than one million years, this asteroid, with an average diameter of around 330 meters, experiences a loss of surface material equivalent to a layer several tens of centimeters thick ^[24].

Hence, asteroids experience a reduction in mass as they lose a significant portion of their substance, while simultaneously generating a region conducive to satellite formation around them. It is the satellites that capture a fraction of the material ejected from the asteroid's surface and thereby grow. Following a similar mechanism, the

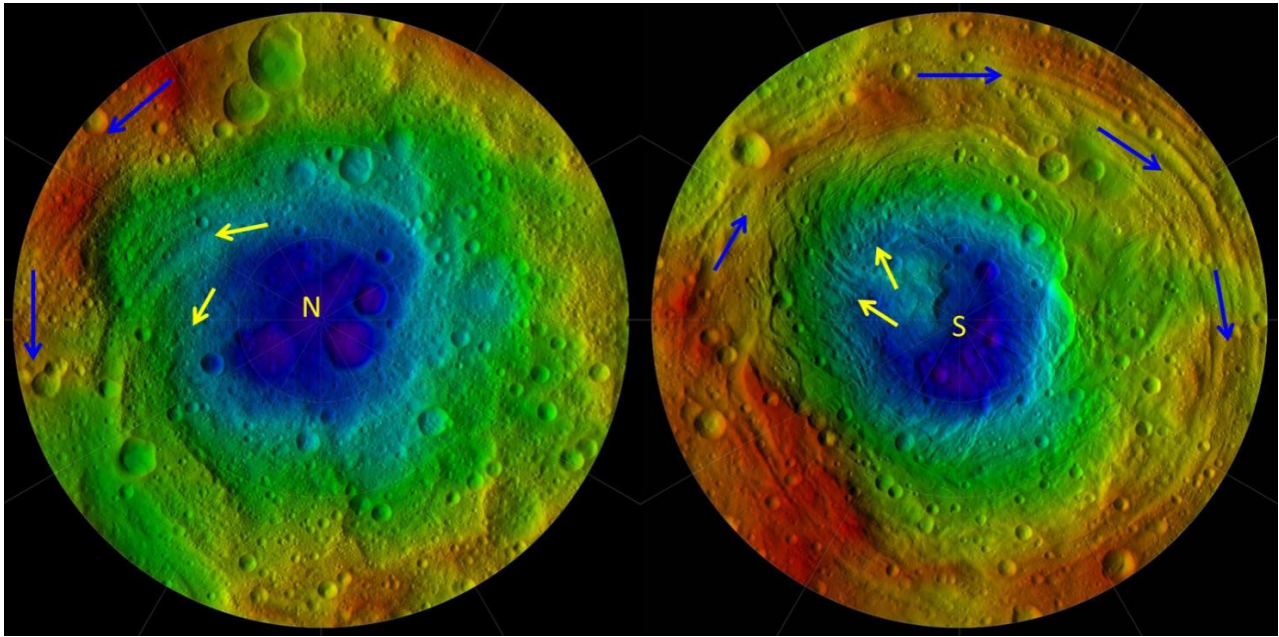


Figure 3. The relief map depicts the northern (left) and southern (right) hemispheres of asteroid 4 Vesta. The equatorial region is omitted from the map. The color scheme corresponds to the distance from Vesta's center, with lower elevations represented in violet and higher elevations in red. This map is a result of the Dawn mission and was created using data from NASA, Johns Hopkins Applied Physics Laboratory, Southwest Research Institute, and the National Optical Astronomy Observatory. Blue arrows on the map indicate the direction of the satellite's orbital movement, while yellow inner arrows highlight spiral structures present in the polar regions.

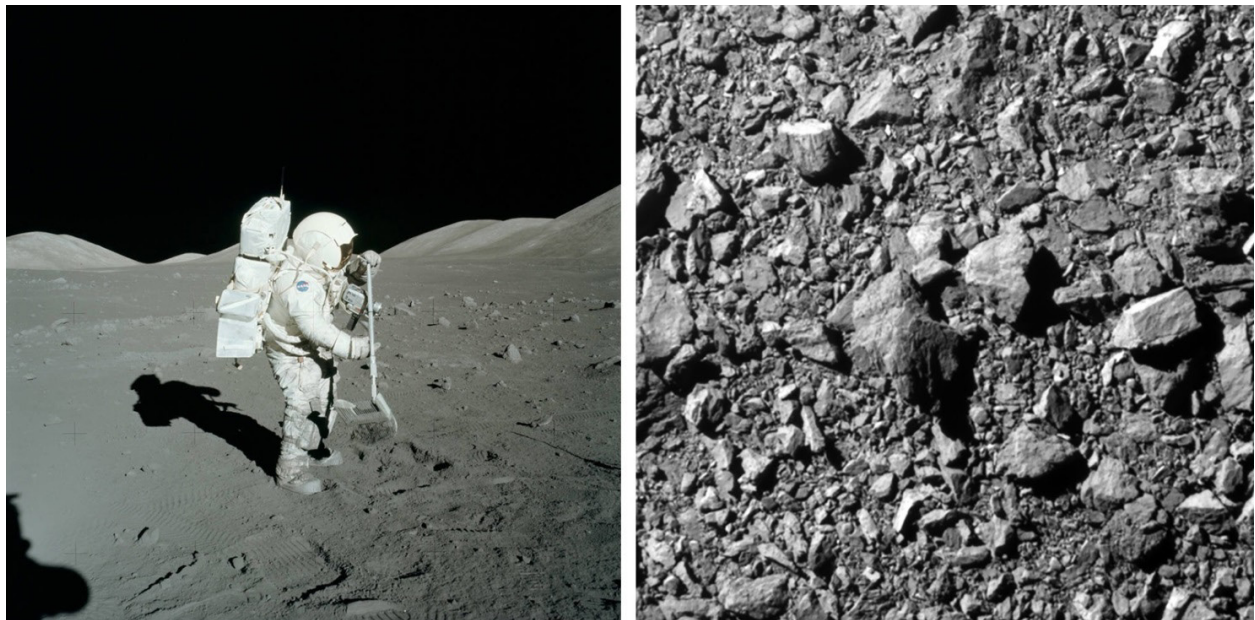


Figure 4. The image on the left displays the surface of the Moon, which is coated with a layer of regolith and dust. It captures the moment when NASA astronaut Harrison Schmitt was gathering lunar samples as part of the Apollo 17 mission at the Taurus-Littrow landing site on December 11, 1972. The photo credit goes to Eugene A. Cernan/NASA. On the right side, there is a picture of the rocky surface of the asteroid moonlet Dimorphos, which has a diameter of 150 meters (with a field of view spanning 31 meters across). This image was captured on October 26, 2022, from the DART spacecraft and is credited to NASA/Johns Hopkins APL.

Moon also expands, drawing sustenance from the debris expelled from the Earth's surface.

The distinction between the formation of the Moon and Charon compared to Phobos, Deimos, and binary asteroids lies primarily in the fact that the Moon and Charon are substantial satellites that have moved considerably away from their respective planets due to tidal interactions. In this context, the relatively faster and longer-lasting Moon, characterized by a higher rate of radial drift, likely absorbed the smaller outer satellites of Earth over time, whereas the slower and younger Charon did not have the opportunity to do so. It is conceivable that the extensively discussed enigmatic intense lunar bombardment 3.9 billion years ago, which lacks corresponding evidence on Earth^[24], might have resulted from collisions between external smaller satellites and the Moon, which was drifting outward.

It is noteworthy that the transfer of material from a solid-surfaced planet to a satellite disk is absent in the case of gas giant planets. All matter falling from heliocentric orbits onto a gas giant planet becomes incorporated into the planet upon any contact with its surface. Material arriving from heliocentric orbits—both gases and solid bodies—can not only fall onto the planet's surface but can also remain in satellite orbits through fortuitous self-interactions, rather than interactions with the planet itself. This process of gas accretion is extensively elucidated by Ruskol^[4]. The typical mass of a satellite system of a gas giant planet is approximately $\sim 10^{-4}$ of the planet's mass and is found in usually regular and massive satellites, such as Galilean satellites. This gas accretion from heliocentric orbits presumably imparts the planet's rotation rate. An interesting fact emerges: for Jupiter, the equatorial speed of self-rotation is 12.6 km/s, while its orbital speed around the Sun is 13.07 km/s (a difference of 3.7%). This implies that the lower part of Jupiter facing the Sun is almost stationary—similar to the bottom point of a swiftly moving train wheel remaining still relative to the rail. For Saturn, the equatorial rotation speed around its axis is 9.87 km/s, while its orbital speed is 9.68 km/s (a difference of 1.9%). These occurrences are likely not coincidental.

Small and irregular outer satellites of gas giant planets exhibit distinct characteristics from the massive inner satellites. However, their emergence is also linked to quasi-accretionary capture of particles and asteroids from heliocentric orbits. Gorkavyi and Taidakova demonstrated in a series of articles from 1993 to 1995 (references in paper^[25]) that the interaction between impacting solid bodies from heliocentric orbits and a protosatellite disk can elucidate the formation of groups of irregular satellites—both prograde, such as the Himalia and Nereid groups, and

retrograde, like the Pasiphae and Phoebe groups, along with the massive retrograde Triton. In the 1995 article, a prognostication was put forth concerning the existence of an as-yet-undiscovered outermost cluster of retrograde satellites encircling Saturn. Utilizing numerical simulations involving 256 thousand clusters of debris within the context of the three-body problem, it was determined that the realm occupied by retrograde satellites encompasses approximately 19 to 31 million kilometers, exhibiting a focal concentration of around 25 to 26 million kilometers. The computations indicated that the retrograde satellite Phoebe (positioned at 12.9 million kilometers) should, on the contrary, be predominantly encircled by prograde satellites^[26].

In the year 2000, the predicted family of outer retrograde satellites of Saturn was discovered through telescopic observations. By 2023, within the region spanning from 15 to 27 million km, 96 retrograde satellites and only 16 prograde satellites were detected. In the vicinity of Phoebe, ranging from 11 to 15 million km, the reverse trend was observed, with 6 prograde satellites and merely 3 retrograde satellites being identified. Gorkavyi and Taidakova discussed the alignment between theoretical and observational results concerning Saturn's irregular satellites in December 2001. Based on the 1995 model, they inferred an additional outcome that a group of numerous undiscovered satellites likely exists beyond Triton's orbit (> 0.5 million km) around Neptune: "Nereid is probably the largest member of the family of prograde satellites mixed with more numerous family of smaller retrograde satellites"^[27]. Observers announced the discovery of such a new Neptune satellite group several months later in 2002. Within the range of 15.7-48.4 million km, 2 prograde and 3 retrograde satellites of Neptune were found. Thus, the formation of satellite systems around gas giant planets is broadly understood and well-described by an accretion model involving interactions between planetesimals from heliocentric orbits and the gaseous protosatellite disk.

6. Predictions Regarding Lunar Water

The giant impact theory posits the complete melting of the Moon, followed by its gradual cooling, resulting in a state of near-complete dryness. Jewitt and Young discussed the scenario in which Earth experienced a collision with a Mars-sized object about 4.5 billion years ago. This collision resulted in the ejection of material, which eventually cooled and came together to form the Moon. The immense energy from this colossal impact would have removed a significant portion of Earth's atmosphere, evaporated any existing oceans, and created a deep ocean of molten rock. Whether Earth initially had water or not, the

powerful impact that led to the Moon's formation likely removed most, if not all, of the planet's original water^[28].

Observations have confirmed the presence of a substantial amount of water on the Moon, prompting the search for mechanisms that deliver new water to the arid lunar surface. Comets appear as the most plausible candidates due to their high ice content and potential encounters within the lunar and terrestrial vicinity. The exact quantity of water brought by comets to the Moon remains uncertain, although their contribution to Earth's oceans has been established. Notably, comets have introduced approximately a quarter of the noble gases, such as xenon, into Earth's atmosphere. Consequently, the contribution of comets to Earth's oceans is estimated to be less than 1%^[29]. Furthermore, cometary water exhibits a distinct isotopic composition, with three times the amount of deuterium compared to terrestrial water^[30].

He et al. investigate different origins of water on the Moon and perform an examination of the amount, hydrogen isotope makeup, and variations from the core to the rim of water present in impact glass beads obtained from lunar soil samples collected during the Chang'e-5 mission^[31]. Their calculations suggest that the amount of water trapped within these impact glass beads within lunar soil could possibly be as high as 2.7×10^{14} kilograms^[31].

Recently, a model proposing the transfer of water from Earth's atmosphere to the Moon has emerged^[32]. The Moon periodically traverses through the Earth's magnetic tail containing terrestrial hydrogen and oxygen ions,

suggesting that the Earth's atmosphere could be a contributing source of lunar water. This interaction allows for the accumulation of terrestrial water on the Moon, with a potential capacity of approximately 3000 km^3 ^[32].

Mechanisms related to the solar wind and material transport to polar regions are realistic, but they can only saturate the surface layer with water to a depth of several decimeters or meters. The multi-impact model posits that lunar water shares a common origin with Earth's water—arising from planetesimals that contributed to the formation of both Earth and the Moon. Consequently, water should be present not only in polar but also in equatorial regions of the Moon, where it resides at greater depths. The isotopic composition of lunar water is expected to mirror that of terrestrial water. The surface layers of regolith can contain water from the solar wind, which has a different isotopic composition.

The presence of lunar water should manifest in the lunar geomorphology^[33,34]. At the LCROSS impact site (Cabeus crater, approximately 85°S), the concentration of water ice within the regolith is estimated to be 5.6% by mass^[35], or potentially even higher^[36]. The existence of a permafrost layer beneath the lunar surface can induce alterations in crater shapes, akin to observations in the permafrost zones of Mars^[37]. Notably, near certain craters within the Moon's South Pole region, signs of landslides are evident (Figure 5a), exhibiting diverse scale structures^[34]—reminiscent of landslides within Earth's permafrost areas (Figure 5b).

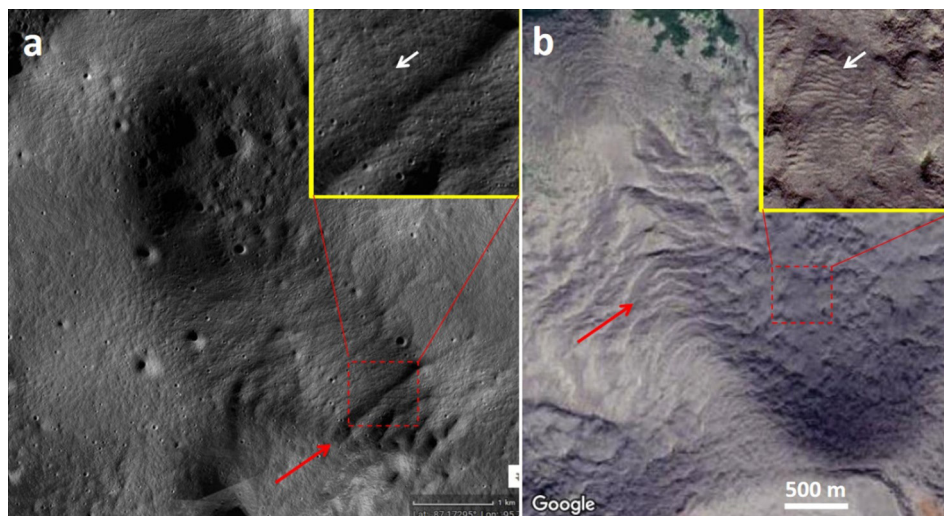


Figure 5. (a) The image shows a landslide occurrence along the edge of a crater situated in the region of 87.1°S and 95.0°W on the lunar surface. Notably, visible are cracks spanning many hundreds of meters, as indicated by the red arrow. Additionally, smaller folds measuring tens of meters are denoted by the white arrow (refer to the inset). This figure employs MOONTrek Version: 3.4.140 (source: <https://trek.nasa.gov/moon/>). (b) This part of the figure displays a patterned ground formation composed of substantial folds, indicated by the red arrow, alongside smaller wrinkles shown by the white arrow. This geomorphic feature occurs within the permafrost melting zone on Earth, situated at coordinates 67.4°N and 134.8°E , and is sourced from Google Maps.

The depth and morphology of craters located at the lunar South Pole may exhibit distinctive characteristics attributed to the presence of a layer of water ice and volatile compounds. These substances are expected to undergo both melting and sublimation processes during impact events and over subsequent periods (refer to Figures 5-6). An examination of photographs depicting the polar regions reveals several notable attributes associated with small craters in proximity to the lunar poles (as illustrated in Figures 5-6):

- 1) These craters tend to possess smoother contours, and the surrounding terrain displays a distinctive pattern^[34].
- 2) The occurrence of patterned ground is frequently observed within the craters and their immediate vicinity^[34].
- 3) Notably, landslides and cracks are discernible in areas outside the craters^[34].
- 4) Layers or steps are often apparent on the inner slopes of these craters^[34].

These characteristics closely resemble those found in craters within the permafrost regions on Mars^[38], as well

as analogous zones on Earth^[39] (refer to Figure 5b). Our hypothesis posits that the observed traits of lunar craters in the South and North Polar regions of the Moon are indicative of the presence of permafrost^[34].

When contrasting the topography of the equatorial and polar regions of the Moon, the latter display notably distinctive features (see Figure 6): smoothed craters (Figure 6a) and numerous intricate relief patterns (Figures 6b-6d). It is evident that such features cannot be exclusively attributed to meteoritic impacts. Consequently, an alternative factor is at play, influencing geological activity in the polar zones. This likely involves a substantial layer of perpetual frost, the evolving dynamics of which give rise to the distinct relief patterns known as solifluction structures. The estimated thickness of this layer is on the order of kilometers, as its influence is observable in the shapes of craters of kilometer-scale dimensions (see Figure 6a). Notably, it is improbable for sources of lunar water such as solar wind or Earth's atmospheric tail to create permafrost layers thicker than a few meters.

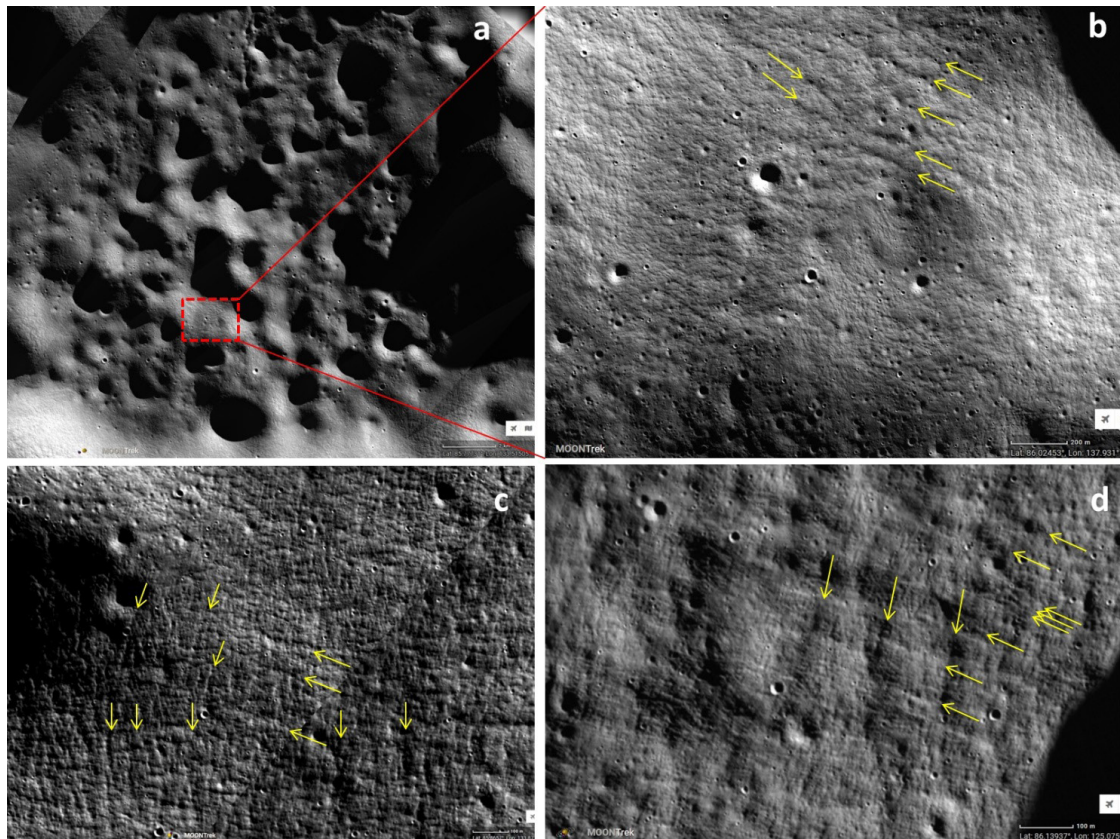


Figure 6. (a) Lunar reliefs in the vicinity of the Moon's North Pole exhibit distinctive features, characterized by smoothed forms (the lower left corner of the photograph has coordinates 85.8°N, 133.5°E). (b) Landslide at the edge of a crater (86.0°N, 137.9°E). (c) Patterned surface in the region of 85.9°N, 133.9°E. (d) Regular structures of various scales in the area of 86.1°N, 125.1°E. The yellow arrows in (b, c, d) indicate quasi-regular structures, often with different orientations, which are typical for relief features in permafrost zones^[38,39].

Source: NASA/MOONTrek Version: 3.4.140.

7. Conclusions

We have demonstrated that ejecta generated by large-scale impacts on a planet's surface readily transition to stable satellite orbits, even when interacting with smaller particles in the protosatellite disk, which are 10-100 times less massive than the ejecta. A protosatellite disk with prograde rotation effectively captures and incorporates ejecta with prograde rotation, destabilizing and returning ejecta with retrograde rotation to the planet. The initial protosatellite disk is not destroyed by the impact of ejecta with a net zero angular momentum, but instead rapidly grows by absorbing prograde ejecta carrying mass and additional angular momentum.

The discussed multi-impact model represents a natural extension of the Hartmann-Davis idea^[5] and combines it with the accretion model. The concept of a mega-impact has significantly contributed to understanding lunar formation by emphasizing the importance of a mantle material flow induced by collisions of large planetesimals with the planet. The accretion model explores the formation and evolution of the other crucial element in lunar cosmogony—the protosatellite disk around Earth. These two models—accretion and mega-impact—can be united into a comprehensive multi-impact theory applicable to the formation of a wide spectrum of satellite systems, from large planets like Earth to small asteroids with dimensions of a few hundred meters. From the multi-impact model of lunar formation, significant insights regarding lunar water can be drawn. The mega-impact theory would have completely vaporized water from lunar rocks and necessitated the introduction of new mechanisms for lunar water formation—involving comets, solar wind particles, or Earth's atmosphere. Such mechanisms imply shallow subsurface lunar ice in relatively small quantities. The multi-impact model posits that the Moon possesses substantial water reserves from planetesimals that also contributed to Earth's formation. The material from Earth's crust that contributed to the Moon likely held a considerable amount of water as well. It is plausible that lunar water is distributed beneath the surface at all latitudes, albeit at different depths. This can lead to the formation of regular geomorphological structures, particularly in polar regions, (see, for example, ^[33,34,38,39]). Determining the isotopic composition of lunar water will provide a definitive answer about its origin and the most probable scenario of lunar formation.

Funding

This research received no external funding.

Acknowledgement

The author expresses gratitude to Tanya Taidakova for years of fruitful collaboration; John Mather for support and valuable advice, and astronaut Harrison Schmitt for his insightful lecture at the Goddard Space Flight Center in May 2017.

Data Availability Statement

The data supporting these findings are publicly available.

Conflict of Interest

The author declares no conflicts of interest.

References

- [1] Artemis III Science: Definition Team Report [Internet]. Available from: <https://www.nasa.gov/sites/default/files/atoms/files/artemis-iii-science-definition-report-12042020c.pdf>
- [2] Ringwood, A.E., 2012. Origin of the Earth and Moon. Springer Science & Business Media: Berlin. pp. 1-295.
- [3] Safronov, V.S., 1972. Evolution of the Protoplanetary Cloud and Formation of the Earth and the Planets [Internet]. Available from: <https://philpapers.org/rec/SAFEOT>
- [4] Ruskol, E.L., 1975. Origin of the moon. Nauka: Moscow. pp. 1-188.
- [5] Jones, J.H., Palme, H., 2000. Geochemical constraints on the origin of the Earth and Moon. Origin of the Earth and Moon. University of Arizona Press: Tucson. pp. 197-216.
- [6] Wang, H.S., Lineweaver, C.H., Ireland, T.R., 2018. The elemental abundances (with uncertainties) of the most Earth-like planet. *Icarus*. 299, 460-474. DOI: <https://doi.org/10.1016/j.icarus.2017.08.024>
- [7] Hartmann, W.K., Davis, D.R., 1975. Satellite-sized planetesimals and lunar origin. *Icarus*. 24(4), 504-515. DOI: [https://doi.org/10.1016/0019-1035\(75\)90070-6](https://doi.org/10.1016/0019-1035(75)90070-6)
- [8] Cameron, A.G.W., 2000. Higher-resolution simulation of the giant impact. Origin of the Earth and Moon. University of Arizona Press: Tucson. pp. 133-144.
- [9] Zhang, J., Dauphas, N., Davis, A.M., et al., 2012. The proto-Earth as a significant source of lunar material. *Nature Geoscience*. 5(4), 251-255. DOI: <https://doi.org/10.1038/ngeo1429>

- [10] Prokof'eva, V.V., Tarashchuk, V.P., Gor'kavyi, N.N., 1995. Satellites of asteroids. *Physics-Uspekhi*. 38(6), 623.
DOI: <https://doi.org/10.1070/PU1995v038n06ABEH000092>
- [11] Ringwood, A.E., 1989. Flaws in the giant impact hypothesis of lunar origin. *Earth and Planetary Science Letters*. 95(3-4), 208-214.
DOI: [https://doi.org/10.1016/0012-821X\(89\)90097-6](https://doi.org/10.1016/0012-821X(89)90097-6)
- [12] Ruskol, E.L., 1986. Natural satellites of the planets. *VINITI: Moscow*. pp. 1-116.
- [13] Gorkavyi, N.N., 2004. The new model of the origin of the Moon. *Bulletin of the American Astronomical Society*. 36, 861.
- [14] Gorkavyi, N.N., 2007. The origin of the Moon and binary asteroids. *Izvestiya Astrophysicheskoy Observatorii*. 103(2), 143-155.
- [15] Rufu, R., Aharonson, O., Perets, H.B., 2017. A multiple-impact origin for the Moon. *Nature Geoscience*. 10(2), 89-94.
DOI: <https://doi.org/10.1038/ngeo2866>
- [16] Adushkin, V.V., Vityazev, A.V., Pechernikova, G.V., 2014. В развитие теории происхождения и ранней эволюции Земли (Russia) [Development of the theory of the origin and early evolution of the Earth]. *Problems of Biosphere Origin and Evolution*. 2, 3-39.
- [17] Gorkavyi, N.N., 2008. Regular Mechanism of the Formation of Asteroid Satellites [Internet]. Available from: <https://www.lpi.usra.edu/meetings/acm2008/pdf/8357.pdf>
- [18] Gaftonyuk, N.M., Gorkavyi, N.N., 2013. Asteroids with satellites: Analysis of observational data. *Solar System Research*. 47, 196-202.
DOI: <https://doi.org/10.1134/S0038094613020032>
- [19] Keane, J.T., Porter, S.B., Beyer, R.A., et al., 2022. The geophysical environment of (486958) Arrokoth—A small Kuiper belt object explored by new horizons. *Journal of Geophysical Research: Planets*. 127(6), e2021JE007068.
DOI: <https://doi.org/10.1029/2021JE007068>
- [20] Hecht, J., 2015. Vesta has no moons—is it unlucky or did it eat them? [Internet]. *New Scientist*, 2015 May 21. Available from: <https://www.newscientist.com/article/dn27576-vesta-has-no-moons-is-it-unlucky-or-did-it-eat-them>
- [21] Gorkavyi, N.N., Taidakova, T.A., 2019. The lonely Moon, double asteroids, and multiply collisions. *Chelyabinsk superbolide*. Springer: Berlin. pp. 287-300.
- [22] Trofimov, P.M., Gorkavyi, N.N., 2022. The mass loss of the main asteroid belt and Mars' zone caused by the impact of solar radiation and Jupiter: I: Numerical calculations of the dust evolution. *Solar System Research*. 56(3), 183-190.
DOI: <https://doi.org/10.1134/S0038094622030078>
- [23] Gorkavyi, N.N., Trofimov, P.M., 2022. Reduction of the mass of the main asteroid belt and the Mars zone due to solar radiation and the influence of Jupiter—II: Scenario of the evolution of the residual disk density. *Solar System Research*. 56(4), 225-232.
DOI: <https://doi.org/10.1134/S0038094622040049>
- [24] Nagao, K., Okazaki, R., Nakamura, T., et al., 2011. Irradiation history of Itokawa regolith material deduced from noble gases in the Hayabusa samples. *Science*. 333(6046), 1128-1131.
DOI: <https://doi.org/10.1126/science.1207785>
- [25] Ryder, G., Koeberl, Ch., Mojzsis, S.J., 2000. Heavy bombardment on the Earth at ~3/85 Ga: The search for petrographic and geochemical evidence. *Origin of the Earth and Moon*. University of Arizona Press: Tucson. pp.475-492.
- [26] Gorkavyi, N.N., Taidakova, T.A., 1995. A model for the formation of the satellite systems of Jupiter, Saturn, and Neptune. *Astronomical Journal Letters*. 21(6), 846-851.
- [27] Gorkavyi, N.N., Taidakova, T.A., 2001. Discovered Saturnian and undiscovered Neptunian retrograde satellites. *American Astronomical Society Meeting Abstracts*. 199, 63-06.
- [28] Jewitt, D., Young, E.D., 2015. Oceans from the Skies. *Scientific American*. 312(3), 36-43.
- [29] Marty, B., Altwegg, K., Balsiger, H., et al., 2017. Xenon isotopes in 67P/Churyumov-Gerasimenko show that comets contributed to Earth's atmosphere. *Science*. 356(6342), 1069-1072.
DOI: <https://doi.org/10.1126/science.aal3496>
- [30] Altwegg, K., Balsiger, H., Bar-Nun, A., et al., 2015. 67P/Churyumov-Gerasimenko, a Jupiter family comet with a high D/H ratio. *Science*. 347(6220), 1261952.
DOI: <https://doi.org/10.1126/science.1261952>
- [31] He, H., Ji, J., Zhang, Y., et al., 2023. A solar wind-derived water reservoir on the Moon hosted by impact glass beads. *Nature Geoscience*. 16(4), 294-300.
DOI: <https://doi.org/10.1038/s41561-023-01159-6>
- [32] Kletetschka, G., Klokočník, J., Hasson, N., et al., 2022. Distribution of water phase near the poles of the Moon from gravity aspects. *Scientific Reports*. 12(1), 4501.
DOI: <https://doi.org/10.1038/s41598-022-08305-x>
- [33] Ding, Z.X., Wang, D., 2018. The Discovery of the “Freezing and Thawing Landform” of Tycho Impact Crater of the Moon [Internet]. Available from: <https://>

- www.hou.usra.edu/meetings/lpsc2018/pdf/1367.pdf
- [34] Gorkavyi, N., 2022. Investigation of Geomorphological Signatures of Permafrost in the Polar Lunar Areas with VIPER [Internet]. Available from: <https://ntrs.nasa.gov/citations/20220018310>
- [35] Colaprete, A., Schultz, P., Heldmann, J., et al., 2010. Detection of water in the LCROSS ejecta plume. *Science*. 330(6003), 463-468.
DOI: <https://doi.org/10.1126/science.1186986>
- [36] Stopar, J.D., Robinson, M.S., Barnouin, O.S., et al., 2017. Relative depths of simple craters and the nature of the lunar regolith. *Icarus*. 298, 34-48.
DOI: <https://doi.org/10.1016/j.icarus.2017.05.022>
- [37] Bramson, A.M., Byrne, S., Putzig, N.E., et al., 2015. Widespread excess ice in arcadia planitia, Mars. *Geophysical Research Letters*. 42(16), 6566-6574.
DOI: <https://doi.org/10.1002/2015GL064844>
- [38] Johnson, A., Reiss, D., Conway, S., et al., 2015. Small-scale Lobes in the Southern Hemisphere on Mars: Implications for Transient Liquid Water in the Recent Past [Internet]. Available from: <https://elib.dlr.de/101155/1/EPSC2015-882.pdf>
- [39] Painter, S.L., Coon, E.T., Khattak, A.J., et al., 2023. Drying of tundra landscapes will limit subsidence-induced acceleration of permafrost thaw. *Proceedings of the National Academy of Sciences*. 120(8), e2212171120.
DOI: <https://doi.org/10.1073/pnas.2212171120>

